EXAMINATION OF GRANULAR MATERIAL BEHAVIOR IN A LAMINAR-TYPE DIRECT SIMPLE SHEAR DEVICE USING LABORATORY VALIDATED DISCRETE ELEMENT METHOD SIMULATIONS

A Dissertation

by

MICHELLE LEE BERNHARDT

Submitted to the Office of Graduate and Professional Studies of
Texas A&M University
in partial fulfillment of the requirements for the degree of

DOCTOR OF PHILOSOPHY

Chair of Committee,	Giovanna Biscontin
Committee Members,	Jean-Louis Briaud
	Stefan Hurlebaus
	Catherine O'Sullivan
	Robert B. Warden
Head of Department,	Robin L. Autenrieth

December 2013

Major Subject: Civil Engineering

ABSTRACT

Simple shear testing is used to study a number of practical geotechnical problems including: soil conditions directly below a loaded surface, adjacent to a driven pile shaft, soils deposited on a slightly inclined slope, and most notably the response of soils subjected to earthquake-type loading. While each of these problems still have important questions to be answered, earthquakes and earthquake triggered geohazards are the most complex and also pose the highest risk.

An important aspect of assessing the risk associated with earthquakes is the need to accurately predict soil behavior. True field loading conditions involve multi-directional shearing and the rotation of principal planes and are much more complex than the triaxial laboratory testing methods and models often used to describe them. Simple shear testing allows for the in situ conditions to be replicated; however, several limitations of the device make data interpretation difficult. The inability to apply complementary shear stresses and the inability to measure the horizontal normal stresses results in non-uniform stresses across the boundaries, as well as an undefined stress state during shearing. This, in turn, requires assumptions to be made about the failure conditions before any state parameters can be determined. Even when only monotonic testing is conducted, there are still many important questions to be answered about the actual severity of the non-uniform stresses on the boundaries, as well as the internal stresses and the microscopic response of granular soils.

Discrete element method (DEM) modeling has the advantage of being able to examine particle-to-particle interactions. Once validated with the measured laboratory data, these models provide a vast quantity of information about the fundamental mechanisms underlying the observed complexity of the response of the soil mass as

a whole.

The goal of this research is to gain insight into the particle-to-particle interactions driving the overall response of granular samples subjected to multi-directional cyclic simple shear conditions. The main objectives of this proposed project are to (1) characterize the macroscopic response of metal ballotini representing idealized sand under simple shear loading conditions and (2) model the physical element tests using DEM simulations to gain insight into the microscopic response of the granular material. Findings from this study showed that the DEM simulations could be successfully validated by laboratory data and that the overall trends observed agreed reasonably well with the experimental data from this study, as well as previous studies by other researchers. Analyses showed that density not only influences shear strength of a sample, it also affects the angle of shearing resistance, the magnitude of principal stress rotation, the angle of non-coaxiality, and the orientation of the principal fabrics for strains below those needed to reach critical state. Vertical effective stress was instead shown to have very little influence on these parameters. The initial fabric appears to play the largest role in the behavior of samples tested at different vertical stresses. The simulations also showed the non-coaxial behavior of the granular samples in terms of principal stress and strain rate orientations, as well as particle displacements. A number of other sensitivity studies were conducted to examine the influence of the model simplifications on the observed response. Several of these simplifications were shown to affect the shear strength obtained and should be included in future analyses.

DEDICATION

Destitutus ventis, remos adhibe.

If the wind will not serve, take to the oars. - Latin Proverb

To all those who helped me paddle.

ACKNOWLEDGEMENTS

First and foremost, I would like to thank my advisors Dr. Giovanna Biscontin and Dr. Catherine O'Sullivan for their continued guidance and encouragement during the course of this project. It has been an honor to work with these two brilliant and dedicated researchers and mentors, and I will forever be grateful for the things I have learned and the opportunities that they have bestowed on me over the past few years. It is hard to put into words how thankful I am for all that they have done. I could not have asked for a better pair of advisors.

I would also like to thank Dr. Jean-Louis Briaud, Dr. Stefan Hurlebaus, and Dr. José M. Roësset for their time and support as members of this dissertation committee, but also for their guidance throughout my time here at Texas A&M. Additionally, I would like to thank Robert Warden for his advice and recommendations as a committee member and for taking the time to learn a little Geotech and DEM. I would also like to thank him for allowing me to explore the historic preservation world and for the chance to get out of the office every now and again. I have had so many opportunities that were not directly related to this dissertation, but they have helped make my PhD experiences unforgettable. The members of my dissertation committee, as well as the other professors at Texas A&M have all impacted my education and my life and have set examples that I will strive to reach. For this, I am thankful.

Without the technical and mechanical expertise of Mike Linger and Charles Pivonka, none of the laboratory testing would have been possible. Whether it was machining a part, troubleshooting a problem for the umpteenth time, or even fixing the A/C at my house, they were always there to help me when things in the lab,

or in life, were not working like they should. I would also like to thank the staff at Texas A&M, especially Kay Choate, for their support over the years, as well as Troy Brown and Thomas Mather for their patience and for helping me keep my computer simulations up and running. I am grateful for all that they have done.

I would especially like to thank Cassandra Rutherford for her help with the device and her mentorship throughout my PhD, but also for her friendship. A special thanks is also extended to my fellow graduate students and friends, Stacey Tucker, Vishal Dantal, Maddy Murali, and Ryan Beemer, who contributed at times to this research. I am also thankful for the time I spent abroad working with the group at Imperial College. For their help and friendship I am truly grateful. Most importantly, I wish to extend my gratitude to all of my friends and family who contributed to the parts that make up life. I am forever grateful for their support and encouragement in good times and in bad, and for making is whole experience great.

Lastly, I would like to acknowledge and thank the National Science Foundation for their financial support of this research through the Graduate Research Fellowship Program and Grant No. 0449021.

TABLE OF CONTENTS

LIST OF FIGURES

FIGURE Page

LIST OF TABLES

TABLE Page

1. INTRODUCTION

1.1 Research Motivation

Simple shear testing is used to study a number of practical geotechnical problems including: soil conditions directly below a loaded surface, adjacent to a driven pile shaft, soils deposited on a slightly inclined slope, and most notably the response of soils subjected to seismic loading. While each of these problems still have important questions to be answered, earthquakes and earthquake triggered geohazards are the most complex and also pose the highest risk.

Seismic events can result in large ground displacements/accelerations, liquefaction, and slope failure causing infrastructure damage or collapse, foundation subsidence or failure, debris flow, and tsunamis. In fact, in the last decade alone, several large events across the globe have shown the destructive nature of earthquakes and earthquake-triggered geohazards. Over 630,000 deaths are estimated to have occurred solely due to the earthquakes in Sumatra, Sichuan China, Haiti, and Japan (USGS, 2010). Even in developed urban settings where loss of life may not occur, liquefaction induced ground failures result in billions of US dollars in damages to buildings and other infrastructure, potentially making liquefaction the most destructive and highest risk phenomenon associated with earthquakes. The most recent literature and experimental studies have mainly focused on liquefiable soils, however, even when soils do not liquify, large settlements can still occur. Ohsaki (1969), Seed and Silver (1972), and Pyke (1973) each describe a number of cases in which non-saturated soils settled during seismic shaking, leading to costly infrastructure damage. As urban population densities continue to increase, so does the risk associated with these geohazards.

An important aspect of assessing the risk associated with these events is the ability to accurately predict soil behavior. Numerous experimental and numerical investigations have been conducted over the last 40 years to study liquefaction, as well as the basic behavior of sand and silt soils subjected to earthquake conditions. While cyclic triaxial testing accounts for a number of these studies, it is simple shear testing which most accurately replicates the loading conditions expected during an earthquake. Testing in simple shear not only allows the smooth rotation of the principal directions, the three principal stresses remain independent, providing a better understanding of the stress-strain behavior of soils.

Simple shear testing on granular soils has progressed with the development of a number of devices including: direct simple shear (DSS) devices, shake-table devices, and torsional shear devices. The majority of simple shear testing to date consists of uni-directional loading and very few have focused on multi-directional shearing paths (Pyke, 1973; Ishihara and Yamazaki, 1980; Boulanger, 1990; Boulanger and Seed, 1995; Kammerer, 2002). One issue limiting testing is the fact that very few devices exist in the world that are able to subject the soil sample to controlled, multi-directional, complex stress paths. This type of loading can only truly be achieved in the multi-directional direct simple shear devices (MDSS). Not only are the number of these types of devices limited, the documented MDSS studies have highlighted the difficulty in inherently interpreting the 3-D results. Unlike triaxial and hollow cylinder devices, standard DSS laboratory devices are unable to control and measure the horizontal normal stress, making it impossible to fully describe the current stress state of the specimen during testing. This feature makes it very difficult to clearly define the stress-strain relationships of soil based on laboratory data alone. Also, the laboratory data obtained only represents boundary information, which has been criticized for its non-uniformities. Little information is available regarding the inter-

nal stress and strain conditions and the particle scale interactions. The limitations of the device and the inability to measure these stresses and strains have left important questions to be answered about the actual severity of the non-uniform stresses on the boundaries, as well as the internal stresses and the microscopic response of granular soils.

A relatively new type of modeling technique, the discrete element method (DEM) or more specifically the distinct element method, has the advantage from a geotechnical perspective to be able to simulate large deformation problems, as well as be used to examine particle-to-particle interactions. By using laboratory validated DEM simulations, information such as localized stress and strain values, inter-particle contact orientations, and contact force magnitudes can be recorded. Such information cannot be obtained in even the most sophisticated laboratory tests. The DEM data also allows for statistical analysis of the soil fabric, and the ability to determine and track the principal stress and strain axes during shearing. These particulate mechanics parameters have the potential to provide insight on the fundamental mechanisms underlying the observed complexity of the response of the soil mass as a whole. They also provide the potential to better understand the DSS device itself, as well as the stress-strain conditions imposed on the physical element.

DEM has been used to model a number of soil laboratory tests and other soil related simulations including triaxial and direct shear testing (Thornton and Antony, 1998; Thornton, 2000; Cui et al., 2007; O'Sullivan et al., 2008; Cheung and O'Sullivan, 2008). Li and Yu (2010) used DEM to study the fundamental mechanisms underlying non-coaxial material response by simulating the two dimensional response of the material to controlled variation of the principal stress orientation. In terms of liquefaction simulations, Ng and Dobry (1994) and Sitharam et al. (2009) used DEM to study cyclic response using the constant volume approach. Zeghal and El Shamy

(2008) used a coupled DEM model to study liquefaction in which an averaged Navier-Stokes approach was employed. Shen et al. (2010) presented a study of the use of two dimensional DEM models to simulate simple shear testing. Two configurations were used in the study to simulate the various boundary conditions present in existing simple shear apparatus: hinged rigid lateral walls, and laminar sidewalls. Dabeet et al. (2011) present the only documented three-dimensional validated DEM study on simple shear response, in which glass bead experimental data is used to validate DEM simulations of idealized granular material under uni-directional direct simple shear loading.

True field conditions are very complex and understanding the particle scale response of granular soils under multi-directional loading is important. The limitations of direct simple shear devices, however, make data interpretation difficult even for granular soils under uni-directional simple shear conditions, leaving a large number of questions unanswered. Understanding granular behavior under these types of shearing paths is crucial in order to improve existing and future constitutive models. Validated DEM models can provide the microscopic information necessary to better understand the basic fundamentals which govern the overall granular response.

1.2 Scope of Current Research

This research focuses on the macro- and micro-scale behavior of idealized granular media subjected to uni-directional (monotonic) simple shear loading. Several issues arise in the collection and interpretation of DSS laboratory data due to the complexity of the results and the limitations of the device. For example, Pyke (1973) and Pyke et al. (1974) showed that volumetric differences are observed for the uni-directional and multi-directional loading cases, however, little evidence is available regarding the particle scale mechanisms driving these differing responses. While the

overall goal is to someday understand the cause of these differences, the goal of this particular research study is to evaluate only the uni-directional response, in an effort to better understand the basic mechanisms of granular soils and the DSS device conditions. Even when considering only monotonic testing, researchers have criticized DSS devices for their non-uniformity of stresses and strains and the fact that the stress state is undefined (Saada and Townsend, 1981; LaRochelle, 1981; Airey et al., 1985; Talesnick and Frydman, 1991; Jardine and Menkiti, 1999). Using DEM simulations of the physical element test to study the microscopic response not only allows for improved understanding of the fundamental mechanisms driving of granular material response, they also provide the potential to better understand the DSS device itself. Because granular assemblies are highly indeterminate systems, DEM models must be validated by experimental data. By using metal ballotini samples, the material parameters are known and the DEM models can be directly compared to and validated with the laboratory results.

This dissertation presents a study comprised of four main objectives which are summarized as follows:

- Laboratory Testing: Characterize the metal ballotini under monotonic simple shear using the TAMU-MDSS. Limited data is available on the response of metal spheres subjected to simple shear conditions. The laboratory results are used to validate the DEM simulations.

- DEM Model Development: Develop DEM simulations which replicate the experimental testing program. Developments include sample preparation and numerous sensitivity studies to examine the influence of various testing conditions and simulation differences.

- DEM Model Validation: Validate the DEM simulations with the laboratory

data. The results from the laboratory and DEM simulations are directly compared for similar test conditions.

- Data Analysis: Analyze the micro-scale information obtained from the DEM simulations. A large amount of information is available in the DEM simulations that cannot be obtained in the laboratory including: boundary stress distributions, localized measurements of stress and strain, angle of shearing resistance, stress path, and a statistical description of the fabric.

1.3 Dissertation Organization

This dissertation is comprised of seven chapters. Chapter 2 presents a review of the relevant literature including: a description of simple shear, a comparison of available simple shear devices and their limitations, a review of previous simple shear testing on granular material, non-coaxiality, an overview of DEM, and previous DEM validation and simple shear studies. Chapter 3 provides information related to the experimental testing program. Sample specifications, a description of the device, sample preparation and setup, as well as the testing procedure are given. This chapter also presents the experimental results for a number of different testing conditions. Chapter 4 covers the development of the DEM model simulations. The DEM model development consisted of a study on various sample preparation procedures, the development of the control algorithms, and the initial prototype development and sensitivity studies. This chapter also presents the DEM simulation data for various testing conditions chosen to replicate the experimental testing program. Chapter 5 presents the validation of the DEM simulations using the experimental results, including a number of additional studies to examine possible explanations for differences in the initial stiffness of the two data sets. The microscopic information is a main feature of this dissertation. This information is derived from the validated

DEM simulations and is described in Chapter 6. Finally, Chapter 7 presents the conclusions from the previous chapters, as well as a description of ongoing work and suggestions for future research.

2. LITERATURE REVIEW

2.1 Relevance of Simple Shear Testing

Simple shear testing has been conducted for well over 60 years, but has lost some popularity due to the fact that the test set up and data interpretation are more complicated compared to the triaxial device. One criticism of the triaxial testing, however, is that the stress path imposed is not well representative of true field conditions, especially in the case of earthquake loading. In triaxial devices, the intermediate principal stress, σ_2, can only be equal to the major principal stress (extension tests), or the minor principal stress (compression tests). Therefore, in a cyclic triaxial test, σ_2 changes instantaneously and the principal stress axes flip by 90°. For in situ soils, however, the loading histories are extremely complex and often involve a change in magnitude of the principal stresses, as well as the smooth rotation of the principal planes (e.g. in the case of a soil element subjected to an earthquake, traffic loading, wave loading). A number of researchers have shown that the behavior of sand is influenced by not only this smooth principal stress rotation (Symes et al., 1984; Miura et al., 1986; Nakata et al., 1998; Wijewickreme and Vaid, 1993), but also by the magnitude of the intermediate principal stress (Lade and Duncan, 1973; Yamada and Ishihara, 1979; Budhu, 1984b; Sayão and Vaid, 1996). Yang et al. (2007) and Zhang et al. (2008) investigated the combined effects of the intermediate principal stress parameter and cyclic principal stress axis rotation and found that pore pressure generation (in the case of undrained response in Yang et al. (2007)) and volumetric strain (in the case of drained response in Zhang et al. (2008)) increased with increasing magnitudes of the intermediate principal stress parameter. In terms of strength parameters, Kjellman (1951) showed that the internal friction angle of

sand is also dependent on the intermediate principal stress. Cornforth (1964), Bolton (1986), Sayão and Vaid (1996) and Lade et al. (2008) also showed that both the yield and critical state friction angles were most likely affected by the intermediate principal stress. Therefore, to obtain laboratory results truly representative of the in situ conditions, it is important to replicate the shearing mechanism properly (i.e. smooth rotation of the principal directions), as well as the strength dependency of all three principal stresses. Triaxial testing does not allow either of these conditions to be fulfilled.

The simple shear mechanism, however, does allow the principal planes to rotate smoothly, while all three principal stresses remain independent. Simple shear is a plane strain condition in which a uniform shear strain is applied to the soil. In the case of undrained or constant volume testing, no other strains are allowed. For drained testing where a constant vertical stress is maintained, the vertical strain, ϵ_{zz}, is nonzero. The in situ soil conditions and mode of soil deformation for many practical geotechnical problems can be most appropriately replicated through simple shear testing (Bjerrum and Landva, 1966; Randolph and Wroth, 1981; Budhu, 1984a; Shaw and Brown, 1986; Malek, 1987; Ng and Donald, 1988; Lacasse et al., 1988). For example, simple shear conditions exist for soils within the foundation of an embankment, soils deposited on a slightly inclined slope, soils below a loaded pavement surface, soils adjacent to a driven pile shaft, and foundation soils subjected to cyclic wind or wave loading (Figs. 2.1 through 2.4).

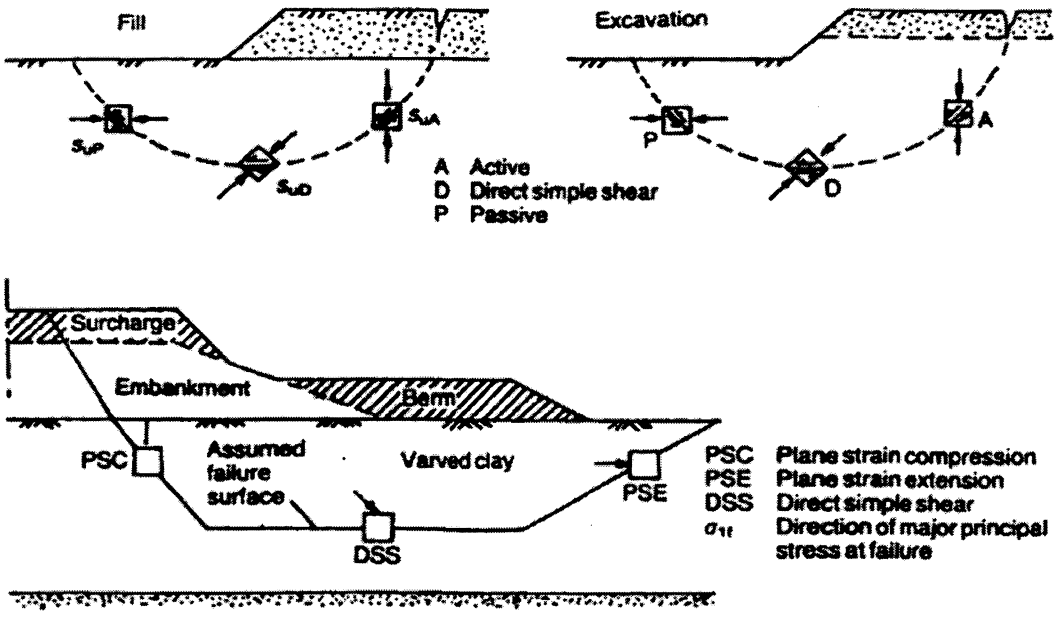

Fig. 2.1. Example of simple shear conditions within an embankment foundation (after Lacasse et al., 1988)

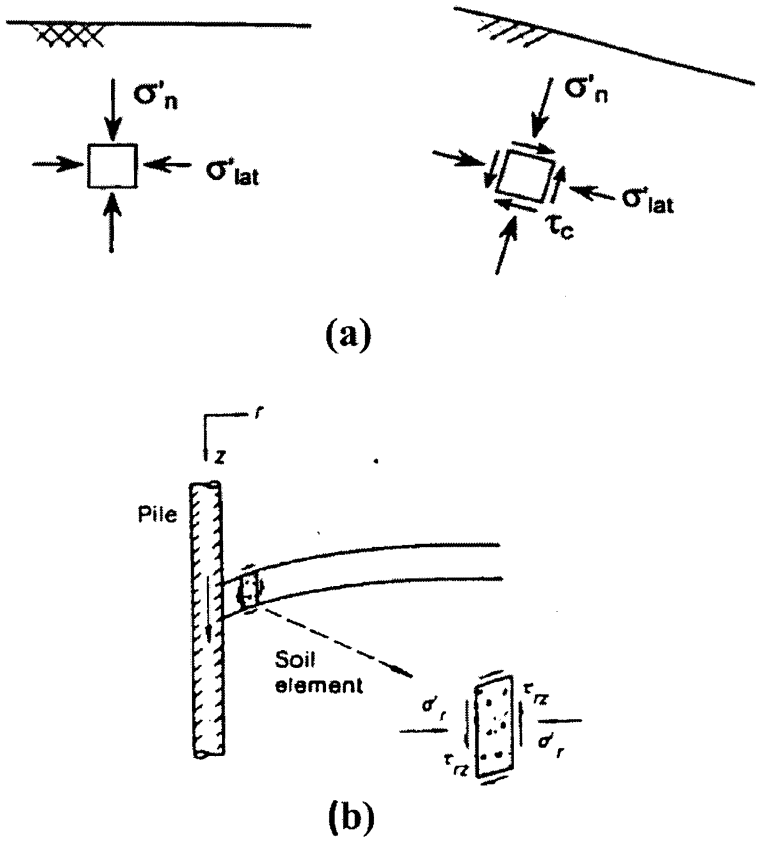

Fig. 2.2. Examples of simple shear conditions in geotechnical engineering (a) soils on an inclined slope (after Kammerer, 2002) (b) soils next to an axially loaded pile (after Randolph and Wroth, 1981)

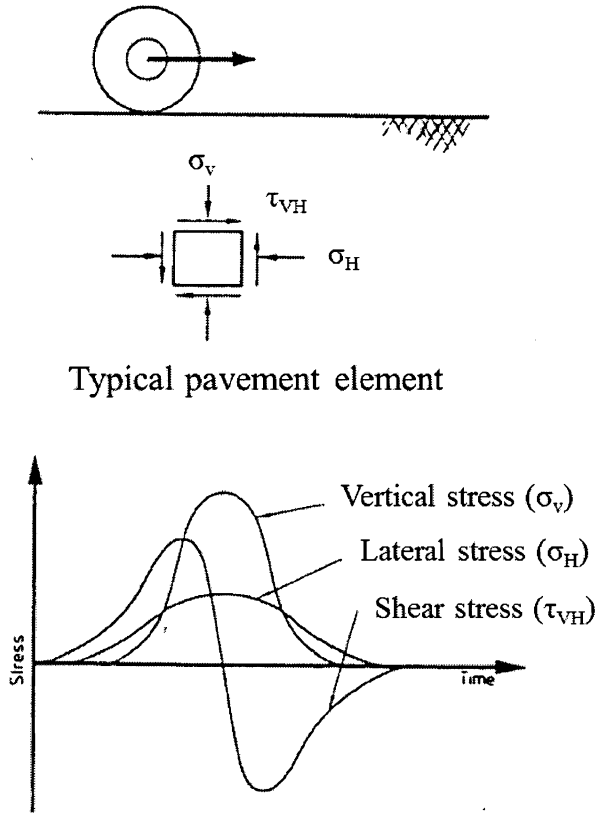

Fig. 2.3. Example of simple shear conditions below a loaded pavement (after Shaw and Brown, 1986)

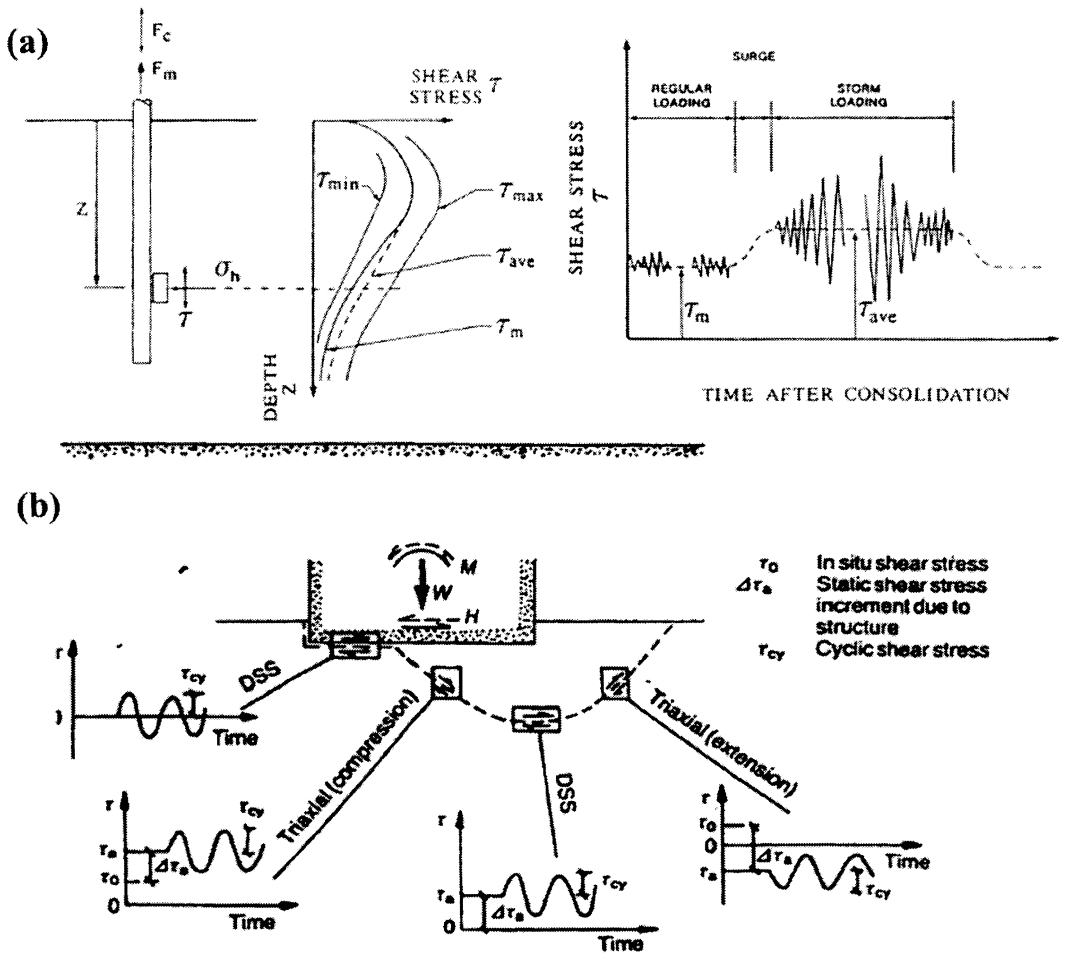

Fig. 2.4. Examples of simple shear conditions under wave loading (a) cyclic loads on offshore foundation piles (after Malek, 1987) (b) cyclicly loaded shallow foundation (after Lacasse et al., 1988)

Soils are also subjected to simple shear conditions during seismic events if the earthquake is idealized as vertically propagating horizontally polarized shear waves moving through the soil mass (Fig. 2.5). The in situ soils experience a stress behavior characterized by the smooth rotation of the principal stress/strain axes, while the specimen is kept in a plane strain condition (Fig. 2.6). The points shown on Fig. 2.6 represent the cyclic rotation experienced by an in situ soil element as the propagating shear wave passes through.

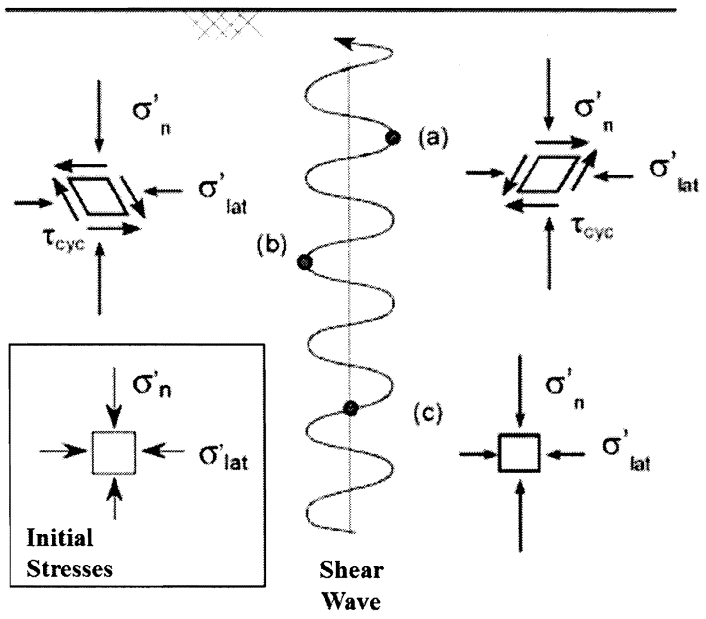

Fig. 2.5. Idealized in situ conditions for soil elements experiencing seismic loading (after Kammerer, 2002)

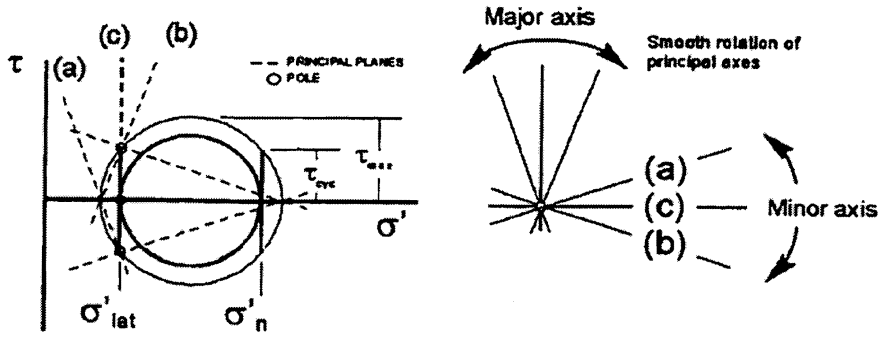

Fig. 2.6. Rotation of principal stresses during seismic loading (after Kammerer, 2002)

2.2 Devices used to Investigate Soil Strength in Simple Shear

Simple shear devices aim to impose a uniform shear strain field within the soil element and were originally created to try and overcome some of the issues that exist with the direct shear box apparatus. Two main types of testing devices exist: direct simple shear (DSS), consisting of either a cuboidal or cylindrical sample, and torsional shear, consisting of either a solid or hollow cylinder sample. These devices are able to characterize soils in terms of their stress-strain behavior, as well as their dynamic properties. While both device types subject the sample to simple shear and replicate in situ loading conditions, they each have advantages and disadvantages that make them suitable for various testing scenarios.

2.2.1 Torsional Shear Apparatus

Torsional shear testing originally began with a solid cylinder sample. Due to large non-uniformities in strain across the sample, the data was not seen as an ideal representation of the actual physical case. To overcome this problem, the hollow cylinder configuration was developed (Saada and Baah, 1967). The hollow

cylinder apparatus has since been widely used to study the behavior of sands and remolded clay specimens (e.g. Lade, 1975; Saada et al., 1983; Shibuya and Hight, 1987; Tatsuoka et al., 1989; Gutierrez et al., 1991; Cai, 2010). Because of the difficulty involved in sample preparation, as pointed out by Vucetic and Lacasse (1984), relatively few torsional tests have been conducted on undisturbed clay specimens (Macky and Saada, 1984; Saada and Macky, 1985; Tatsuoka and Hara, 1987; Talesnick and Frydman, 1991). Hollow cylinder torsional samples are subjected to an axial force, inner and outer cell pressures, and torque applied by rigid end platens. A number of hollow cylinder apparatuses have been developed through the years, each similar to and expanding upon an early device presented in Hight et al. (1983). An example test configuration and stress schematic of the Imperial College Hollow Cylinder Apparatus (HCA), as described in Hight et al. (1983), Menkiti (1995), and Jardine and Menkiti (1999), is shown in Fig. 2.7. This particular apparatus tests hollow cylinder specimen 254 mm in height with inner and outer diameters of 203 mm and 254 mm, respectively. The HCA allows for the application and monitoring of four boundary controls (torque, axial load, internal pressure, and external pressure) giving it the ability to control σ_1, σ_2, σ_3, and α independently.

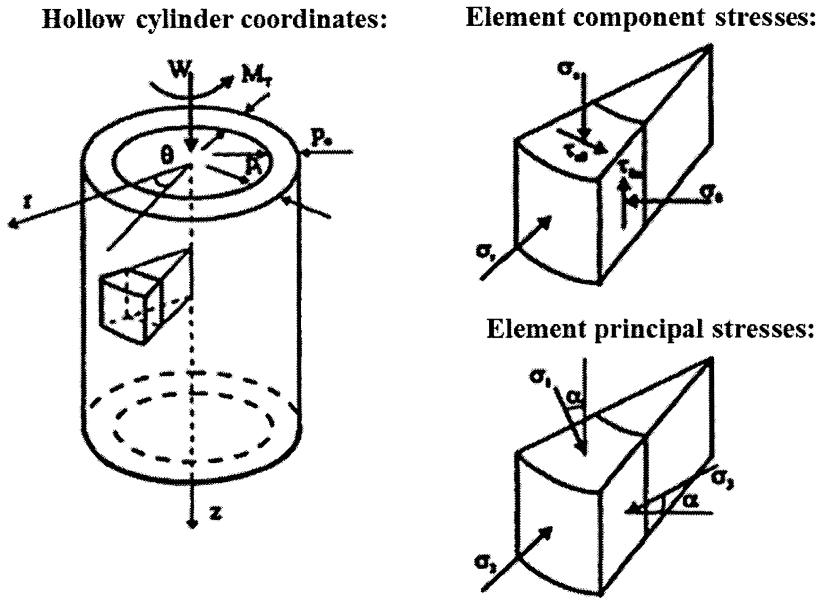

Fig. 2.7. Hollow Cylinder Apparatus (HCA) configuration and stress schematic (after Jardine and Menkiti, 1999)

A similar hollow cylinder torsional shear device, described in Nakata et al. (1998), was used to study the undrained deformation behavior of sand subjected to cyclic principal stress rotation. This apparatus tests slightly different dimensioned samples of 200 mm height, and an internal and external diameter of 60 mm and 100 mm, respectively. Fig. 2.8 shows a schematic representation of the device and the soil element where the principal stress and principal strain values are calculated as:

$$\sigma_1 = (\sigma_z + \sigma_\theta)/2 + sqrt((\sigma_z - \sigma\theta)/2)^2 + \sigma_{z\theta}^2 \tag{2.1}$$

$$\sigma_2 = \sigma_r \tag{2.2}$$

$$\sigma_3 = (\sigma_z + \sigma_\theta)/2 - sqrt((\sigma_z - \sigma\theta)/2)^2 + \sigma_{z\theta}^2 \tag{2.3}$$

$$\epsilon_1 = (\epsilon_z + \epsilon_\theta)/2 + sqrt((\epsilon_z - \epsilon\theta)/2)^2 + \epsilon_{z\theta}^2 \tag{2.4}$$

$$\epsilon_2 = \epsilon_r \tag{2.5}$$

$$\epsilon_3 = (\epsilon_z + \epsilon_\theta)/2 - sqrt((\epsilon_z - \epsilon\theta)/2)^2 + \epsilon_{z\theta}^2 \tag{2.6}$$

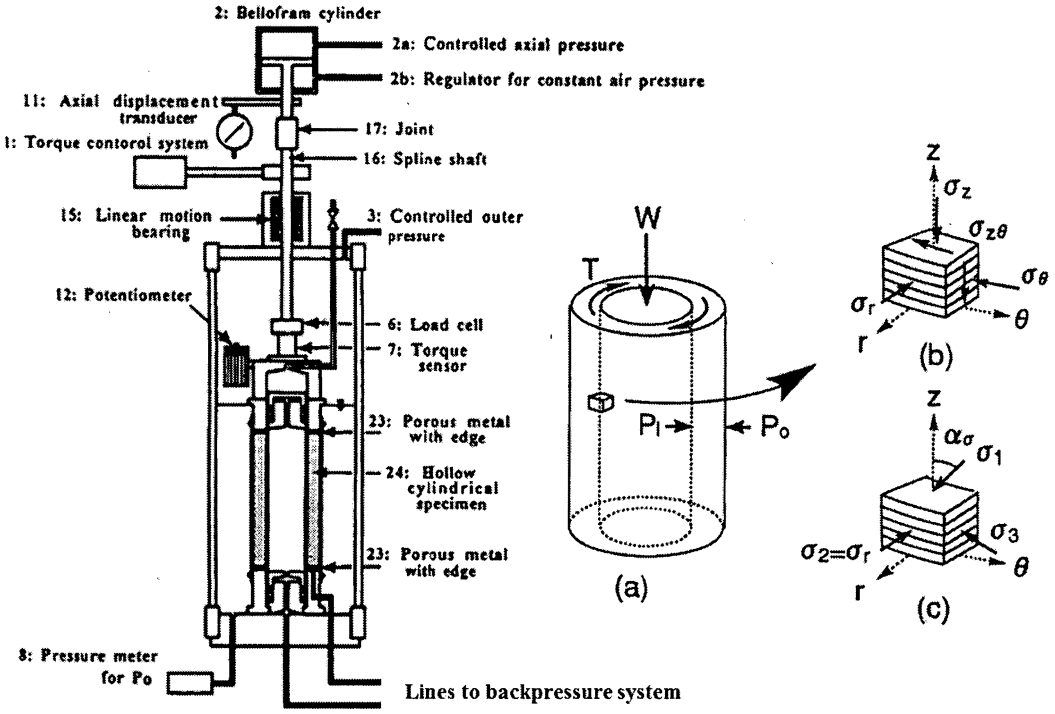

Fig. 2.8. Automatic hollow cylinder torsional shear apparatus and sample stress diagram (after Nakata et al., 1998)

Similar to Hight et al. (1983), the axial, radial, circumferential, and shear stresses and strains are calculated as follows:

$$\sigma_z = (W/(\pi(r_o^2 - r_i^2))) + (P_o(r_o^2 - d_r^2) - P_i r_i^2)/(r_o^2 - r_i^2) \tag{2.7}$$

$$\sigma_r = P_o r_o + P_i r_i/(r_o + r_i) \tag{2.8}$$

$$\sigma_\theta = P_o r_o - P_i r_i/(r_o - r_i) \tag{2.9}$$

$$\sigma_{z\theta} = 1/2[3T/(2\pi(r_o^3 - r_i^3)) + 4(r_o^3 - r_i^3)T/(3\pi(r_o^2 - r_i^2)(r_o^4 - r_i^4))] \tag{2.10}$$

$$\epsilon_z = z/H \tag{2.11}$$

$$\epsilon_r = -u_o - u_i/(r_o - r_i) \tag{2.12}$$

$$\epsilon_\theta = -u_o + u_i/(r_o + r_i) \tag{2.13}$$

$$\epsilon_{z\theta} = \theta(r_o^3 - r_i^3)/(3H(r_o^2 - r_i^2)) \tag{2.14}$$

where r_o and r_i are the outer and inner radii, respectively, H is the specimen height, d is the radius of the rod, z is the measured axial deformation, θ is the torsional deformation, and u_o and u_i are the outer and inner radius deformation, respectively.

A third hollow cylinder torsional (HCT) device, developed at the University of British Columbia and described in Vaid et al. (1990), has been also used to explore the stress path dependency of soil behavior, as well as the non-uniformities that exist across the wall of the specimen. While the definitions of strain are exactly the same, the equations used for axial, radial, circumferential, and shear stress differ slightly from those presented in Hight et al. (1983). Because the stress distribution of the cylinder varies based on the soil's constitutive law, the authors compute the stresses and strains by averaging them over the volume of the specimen rather than across the wall. Although the differences reported are less than 2%, averaging over the volume more accurately considers the curvature of the wall. Unlike the previous studies where both elastic and plastic constitutive laws are used, Vaid et al. (1990) assumes a linear elastic isotropic material behavior for all of the stress components

that are dependent on a material constitutive law (σ_r, σ_θ,and $\tau_{z\theta}$). Neglecting the effects of end constraint and assuming a linear elastic isotropic material, the average stresses are given by:

$$\sigma_z = (F_z + \pi(P_e r_e^2 - P_i r_i^2))/(\pi(r_e^2 - r_i^2)) \tag{2.15}$$

$$\sigma_r = P_e r_e^2 - P_i r_i^2/(r_e^2 + r_i^2) - 2(P_e - P_i) r_e^2 r_i^2 ln(r_e/r_i)/(r_e^2 - r_i^2)^2 \tag{2.16}$$

$$\sigma_\theta = P_e r_e^2 - P_i r_i^2/(r_e^2 + r_i^2) + 2(P_e - P_i) r_e^2 r_i^2 ln(r_e/r_i)/(r_e^2 - r_i^2)^2 \tag{2.17}$$

$$\sigma_{z\theta} = 4T_[H](r_e^3 - r_i^3)/(3\pi(r_e^4 - r_i^4)(r_e^2 - r_i^2) \tag{2.18}$$

where r_e and r_i are the external and internal specimen radii, $T_[H]$ is torque, F_z is vertical force, and P_e and P_i are external and internal pressures, respectively.

The hollow cylinder torsional shear apparatus allows for the smooth rotation of principal stress axes, closely replicating the true field conditions. The main advantage of the device is that it allows for direct control and measurement of all three principal stresses and therefore, a full description of the stress state of the sample at any point during testing. These features, unique to torsional testing alone, enable stress path dependent studies to be carried out to examine inherent and evolving anisotropy, as well as the flow deformation characteristics of soils. With this type of information, a more complete picture of stress-strain relationships can be developed. Another benefit of torsional devices is their ability to achieve very large shear strains, making them the preferred device for gaining residual soil strengths (Kammerer, 2002). They also allow for examination of the non-coaxial behavior of granular soils, an important feature of sand behavior which is discussed in more detain below.

While this torsional device has many advantages related to stress path control and has been said to provide more reliable and useful data than that obtained from

direct simple shear devices, it also has several disadvantages. First, with the application of torque to a finite sample thickness, a non-uniform distribution of stresses and strains exists across the wall. As described in Vaid et al. (1990), the degree of this stress non-uniformity depends on the stress state, specimen dimensions, and constitutive law assumed. Because the stresses vary across the wall, it is necessary to present the stress and strain definitions in terms of average values. As presented above, there are several issues and inconsistencies with the way in which these expressions are derived. The averaging can be carried out across the wall (Hight et al., 1983; Nakata et al., 1998), or over the volume of the specimen (Vaid et al., 1990). An additional complication arises with the assumed constitutive laws used to describe the variation in stress across the sample thickness. Vaid et al. (1990) assumed a linear elastic isotropic material while others have assumed plastic or elastic-plastic behavior for some stress components. Depending on the material behavior assumed, a slightly different definition of stress is given.

A second non-uniformity develops due to the device end constraints. Because the shearing is applied to the specimen ends, a fully frictional contact must be developed between the sample and the loading platens. Most equipment uses ridges, thin blades, or nails to satisfy this requirement. As consolidation progresses, non-uniform stresses and strains develop at the specimen ends. The platens also limit lateral strains at the specimen ends during shearing, further increasing the non-uniformities. These non-uniformities can be partially minimized by making the sample thickness as small as possible and increasing the ratio of the specimen height to thickness. Saada et al. (1983) recommends that the ratio of inner to outer specimen radius exceed 0.65, and that the length of the specimen exceed $5.44\sqrt{(r_o^2 - r_i^2)}$. While this may reduce the severity of the non-uniformity, it does not eliminate it and coefficients and corrections must be applied to the raw data. Vaid et al. (1990) gives a more in

depth description of the non-uniformities present and a study of their severity for various stress paths.

Another problem with torsional testing arises in maintaining simple shear conditions for certain stress path scenarios. In simple shear, both the vertical and lateral strains are zero. For undrained torsional testing, this can be achieved on a global scale by maintaining the specimen height, volume, and the bore volume constant. The only way to develop a homogeneous stress condition in the sample is to apply equal inner and outer pressures to the specimen. As described in Wood (2004), setting the inner and outer pressures equal eliminates one of the four degrees of freedom of control for the device (i.e. $\sigma_r = \sigma_\theta = \sigma_2$). Based on the Mohr circle geometry, the relationship of the intermediate principal stress to the major and minor principal stress is now a function of α and cannot be controlled independently. This, in turn, limits the stress paths that can be studied.

Also, for torsional testing, setting $\sigma_r = \sigma_\theta$ is essentially the same as setting $\sigma_x = \sigma_y$ for cartesian coordinates, which is very unlikely the case in true simple shear conditions. Most torsional testing in the literature, maintains this equality in cell and bore pressures; however, very few comment on the fact that it may deviate from true simple shear conditions, or in the difficulty of ensuring plane strain requirements under these conditions. Shibuya and Hight (1987) did conduct studies where $\sigma_r \neq \sigma_\theta$ by imposing different internal and external pressures on the sample. These conditions further increase the non-uniformities through the sample, making the stress-strain relationships questionable. Gutierrez (1989) carried out a study of the relationship between the non-uniformity of stress and strains due to internal and external pressure differences. The stress paths tested were limited based on a difference in internal and external pressures of 0.75 to 1.3. Nakata et al. (1998) also followed this convention. Talesnick and Frydman (1991) presents a comparison of

direct simple shear and torsional shear results on clay samples, as well as a detailed discussion on the aforementioned points.

In addition to stress non-uniformities and the possibility of neglecting true simple shear conditions, several other problems exist with hollow torsional testing. Due to the complex geometry and setup, undisturbed samples are very difficult to test. Kammerer (2002) also discusses a number of issues including: possible pore pressure redistribution, difficulty of maintaining zero lateral strains, and the large surface area to volume ratio which exists for hollow cylinder samples. This is usually a value that is minimized in equipment design in an effort to minimize the boundary effects and influences. Despite the problems listed, many researchers prefer use of the torsional shear device over that of the NGI DSS device tested because of its ability to give a full description of the stress state/tensor of the soil being tested.

For this study, even though the device has the added benefit of stress path control, the major limitation in the hollow cylinder apparatus is its inability to impose multi-directional loading paths. The specimen geometry restricts testing to one-directional loading paths. True field conditions are extremely complex and there is a need for the ability to perform element testing under multi-directional simple shear conditions. While this particular dissertation only considers monotonic simple shear, the idea and overall goal is to move to multi-directional shearing in future studies using the same device. Only MDSS devices are capable of loading in two independent horizontal directions, and thus, are the device of choice for this particular research study.

2.2.2 Direct Simple Shear Devices

These devices originated with uni-directional monotonic testing and have progressed to multi-directional cyclic capabilities. The first direct simple shear (DSS)

device capable of deforming a soil specimen in simple shear was developed in 1936 at the Royal Swedish Geotechnical Institute (SGI) (Kjellman, 1951). This device (Fig. 2.9) overcame several of the issues associated with the direct shear box apparatus and provided the first information on the stress-strain behavior of soils subjected to uni-directional simple shear conditions. Following this development, came two main direct simple shear devices, which all of the subsequent devices are essentially modeled after: the Cambridge device and the NGI or Geonor device (Fig. 2.10).

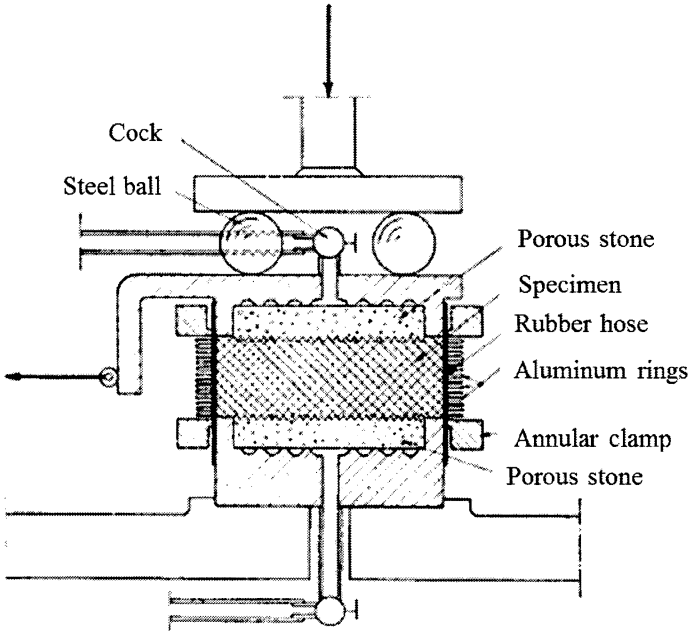

Fig. 2.9. Cambridge DSS and NGI DSS type samples (after Kjellman, 1951)

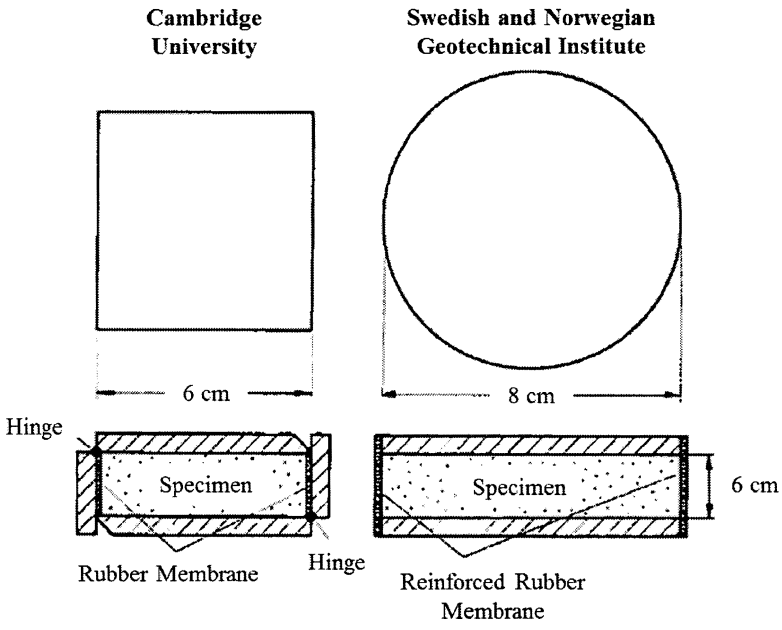

Fig. 2.10. Cambridge DSS and NGI DSS type samples (after Franke et al., 1979)

The Cambridge device, developed at the University of Cambridge by Roscoe (1953), accepts 6 cm cuboidal samples within hinged rigid metal plates. Knowing that inducing pure shear would be difficult with any device, Roscoe chose to instead impose a condition of uniform shear strain. Even though this was achievable under large normal loads, it did not result in a uniform stress field. Several adaptations have been made since the original creation of the device to improve some of its limitations for dry and saturated granular soils (Roscoe et al., 1967; Peacock and Seed, 1968; Stroud, 1971; Ansell and Brown, 1978). Additionally, the device has been continuously developed at Cambridge adding elaborate external and internal instrumentation which allows for the measurement of all three principal stresses, as well as gives internal stress distribution information for the samples. Stroud (1971) conducted several pilot tests on Leighton Buzzard sand to show successful

improvements to the device, correcting some of the previous issues discussed in Cole (1967). Fig. 2.11 shows a comparison of the tests results before and after the device modifications for measurements taken on the central third of the sample, where test 42ERC is from Cole (1967). The improvement to the top boundary measurements are the most pronounced. Additionally, Stroud showed that the stresses acting over the central third of the samples were essentially the same as those acting in the sample core up to the peak stress ratio, after which only a slight difference was observed (Fig. 2.12).

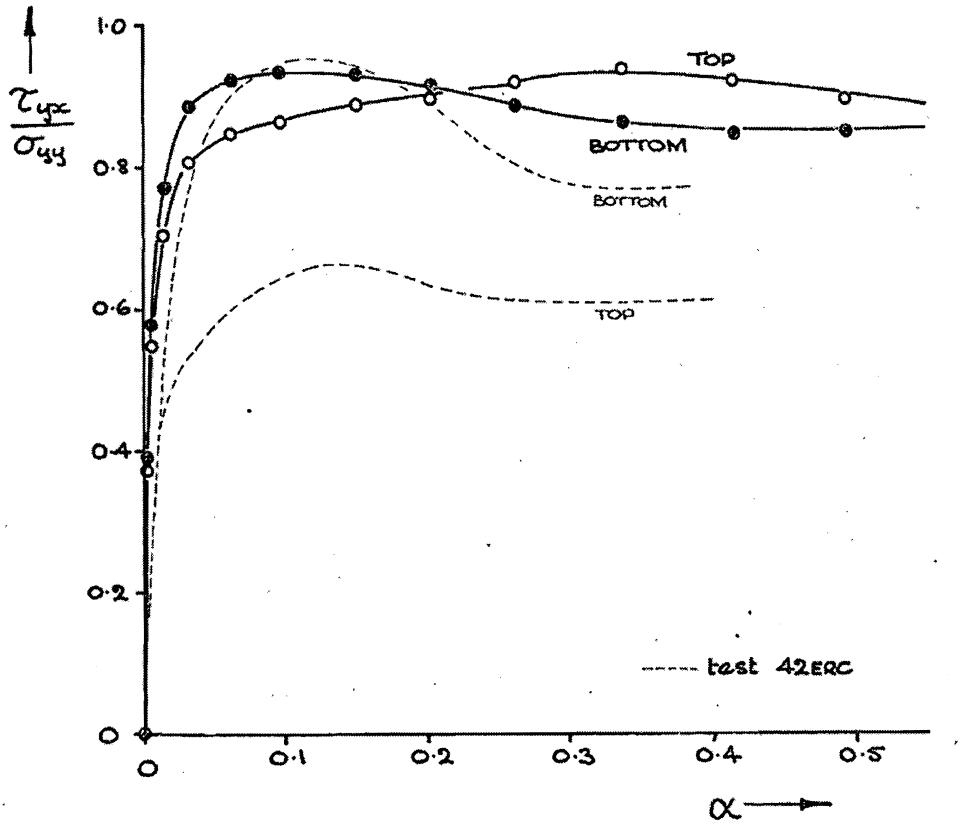

Fig. 2.11. Comparison of stress ratios at the top and bottom boundaries of the central third of the sample for pre- and post-modification tests in the Cambridge device (Stroud, 1971)

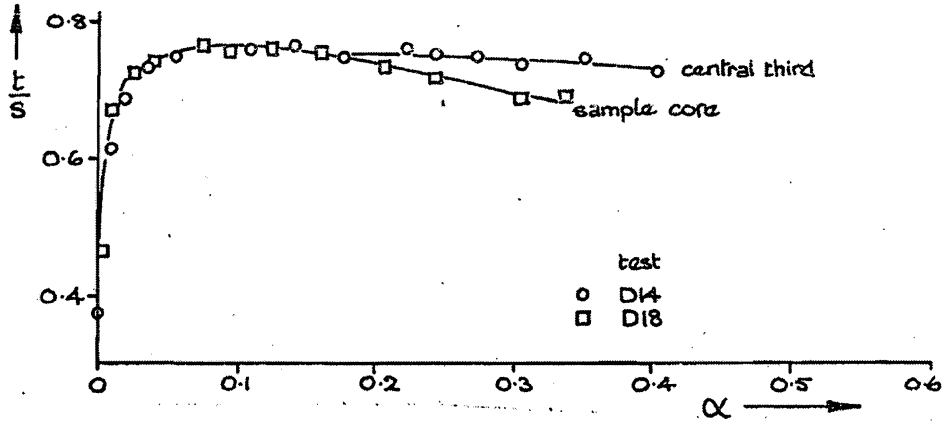

Fig. 2.12. Comparison of stress ratios at the central third and the sample core (Stroud, 1971)

Stroud also states that this region strained uniformly up to this point for the dense tests and somewhat so for the loose tests. Budhu (1979) and Budhu (1984a) present a detailed comparison of the Cambridge and NGI devices, including a discussion on the results obtained from sand tests using both devices. Budhu reports that even though the characteristic responses are different, both the Cambridge device and the NGI-type devices accurately capture the behavior of sand in simple shear if the sample core measurements are used. The sample core is under the most uniform conditions in terms of both stress and strain and it is removed from any boundary or geometrical effects that alter the overall boundary measurements.

The NGI device was developed at the Norwegian Geotechnical Institute by Bjerrum and Landva (1966). This device uses a short cylindrical specimen wrapped in a wire reinforced membrane. This steel wire prevents any significant changes in lateral expansion ideally maintaining k_0 conditions throughout the test. This apparatus was originally designed to study the shear strength of quick clay for which the wire membrane was adequate. For testing on sand, however, issues can arise

with maintaining the cross-sectional area and with membrane penetration. The alternative SGI-type confinement system using a stack of metal rings has, in turn, become very popular. Along with using a stack of thin rings, several modifications have been made through the years to try and correct these issues. These include a gyratory apparatus designed by Casagrande (1976) where a flat spiral spring takes the place of the wire, and the use of liquid rubber in Franke et al. (1979) to minimize membrane penetration effects. The device is manufactured and sold commercially by Geonor and will be referred to as the NGI-type device for the remainder of the discussion. Extensive reviews and comparisons of the devices are presented in Lucks et al. (1972), Shen et al. (1978), Saada et al. (1983), Budhu (1985), Amer et al. (1987), Airey and Wood (1987), Budhu and Britto (1987), Budhu (1988), and Boulanger et al. (1993) .

In terms of bi-directional and multi-directional loading, several devices have been developed following and expanding upon these original designs. Most notably are the University of Tokyo device described by Ishihara and Yamazaki (1980), the U.C. Berkeley bi-directional device described by Boulanger (1990) and Boulanger et al. (1993), and the multi-directional direct simple shear (MDSS) apparatus developed at the Massachusetts Institute of Technology and described by DeGroot (1989) and DeGroot et al. (1996). Of these devices, the most documented in terms of multi-directional cyclic simple shear testing on sands is the University of California, Berkeley bi-directional simple shear device (Boulanger, 1990; Boulanger et al., 1993; Boulanger and Seed, 1995; Kammerer, 2002). This device follows the NGI-type model; however, it allows bi-directional loading in the horizontal plane and additional lateral confinement provided by an enclosed pressurized chamber. Improvements to this device include an increased stiffness to minimize rocking motions and reduced friction to improve performance. The system also runs on computer feedback control

with an integrated data acquisition system. One limitation of this device, however, is its inability to apply broadband earthquake-like loadings at a rapid rate due to the pneumatic control system.

The Texas A&M University multi-directional direct simple shear device (TAMU-MDSS), as described in Rutherford (2012), is the latest NGI-type device that has been developed. This device is capable of loading along three independent axes, allowing for application of vertical load and complex stress or strain controlled paths in the horizontal plane. The servo-hydraulic control system allows testing at frequencies up to 20 Hz, as well as the ability to test at displacement amplitudes of $\pm$ 10 mm. This device also offers several improvements and additional features including: increased stiffness to further reduce rocking, a pressure chamber allowing for backpressure saturation and additional radial confinement, and a sensitive multi-axis load cell. The device is discussed further in Chapter 3.

Direct simple shear devices are relatively straightforward in terms of sample preparation and testing procedure. Unlike torsional devices, however, where three and even four degrees of freedom can be controlled, DSS devices only allow for control of two degrees of freedom: axial stress/strain and shear stress/strain. The device design has several limitations, which have made exact interpretation of the test data somewhat difficult (Saada and Townsend, 1981; LaRochelle, 1981; Airey et al., 1985). First, the intermediate principal stress, σ_y, is not independently controlled and must adjust to maintain the plane strain requirements. Although elaborate instrumentation in the research based Cambridge device now allows for measurement of the intermediate principal stress (Budhu, 1984b), there is still no practical means to measure k_0, or the horizontal normal stresses during shearing in the more common and commercially sold cylindrical sample/NGI-type devices. This leads to an unknown σ_2 and only a partial description of the stress state for the specimen. Budhu

(1985) and Budhu (1988) describe studies in which the core of both the cuboidal and cylindrical specimen were elaborately instrumented to determine the lateral stresses and the failure state of sands in simple shear. With this instrumentation, the stress state is fully defined for the Cambridge cuboidal sample; however, the stress state is still undefined in the cylindrical sample. The measured radial stresses in the NGI-type device were not equal to the intermediate principal stresses nor the horizontal normal stresses perpendicular to the plane of shearing deformation.

Secondly, for the sample to be in simple shear, three conditions must be satisfied: the soil unit should be subjected to compressive stresses and shear stresses at each face, there should be zero lateral strains, and the horizontal displacements at diagonal corners should be equal. For this to hold true, the top and bottom horizontal faces remain a constant length, but the side or vertical faces are forced to lengthen during shearing. One issue with all of these devices, and another main criticism of DSS, is the inability to effectively apply the complementary shear stresses on the vertical faces (Fig. 2.13).

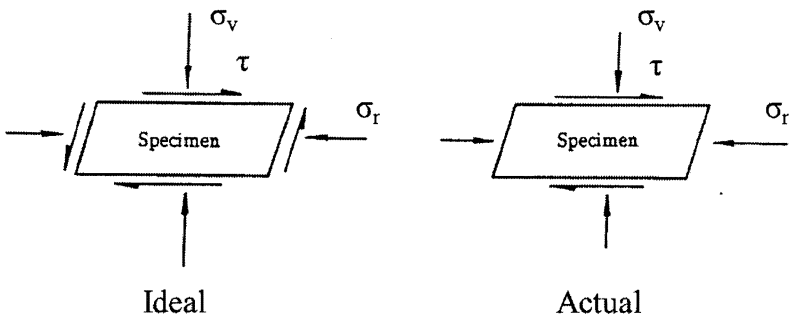

Fig. 2.13. Comparison of the ideal set of simple shear stresses and the stresses actually imposed by available devices (after DeGroot, 1989)

Because of this deficiency, possible rocking or pinching can occur and a non-uniform stress distribution occurs across the top and bottom faces (Fig. 2.14). Kjellman (1951) points out that the shear stresses are unevenly distributed because they must be zero at the edges. Also, in order for equilibrium to be satisfied, the normal forces must also be unevenly distributed. Numerous studies, both experimental (Wright et al., 1978; Franke et al., 1979; Seed, 1979; Vucetic, 1981; Vucetic and Lacasse, 1982; Amer et al., 1987) and numerical (Prevost and Hoeg, 1976; Lucks et al., 1972; Shen et al., 1978; Saada et al., 1983; Budhu and Britto, 1987; Dounias and Potts, 1993), have investigated the effects of this non-uniformity on the measured soil response. Prevost and Hoeg (1976) showed the non-uniform distribution of stresses across the boundaries of a cuboidal Cambridge sample for various values of slippage (λ) using an analytical approach (Fig. 2.15).

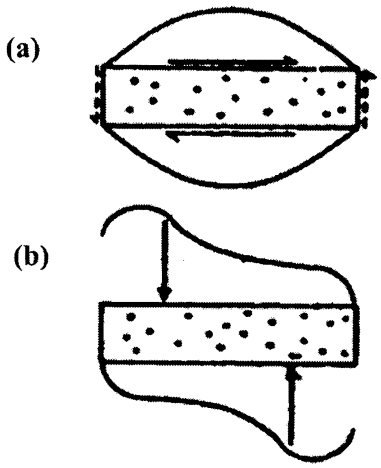

Fig. 2.14. Distribution of stresses across the top and bottom sample caps due to the absence of applied complementary shear stresses (a) Shear stress distribution during shearing (b) Normal stress distribution during shearing (after Airey et al., 1985)

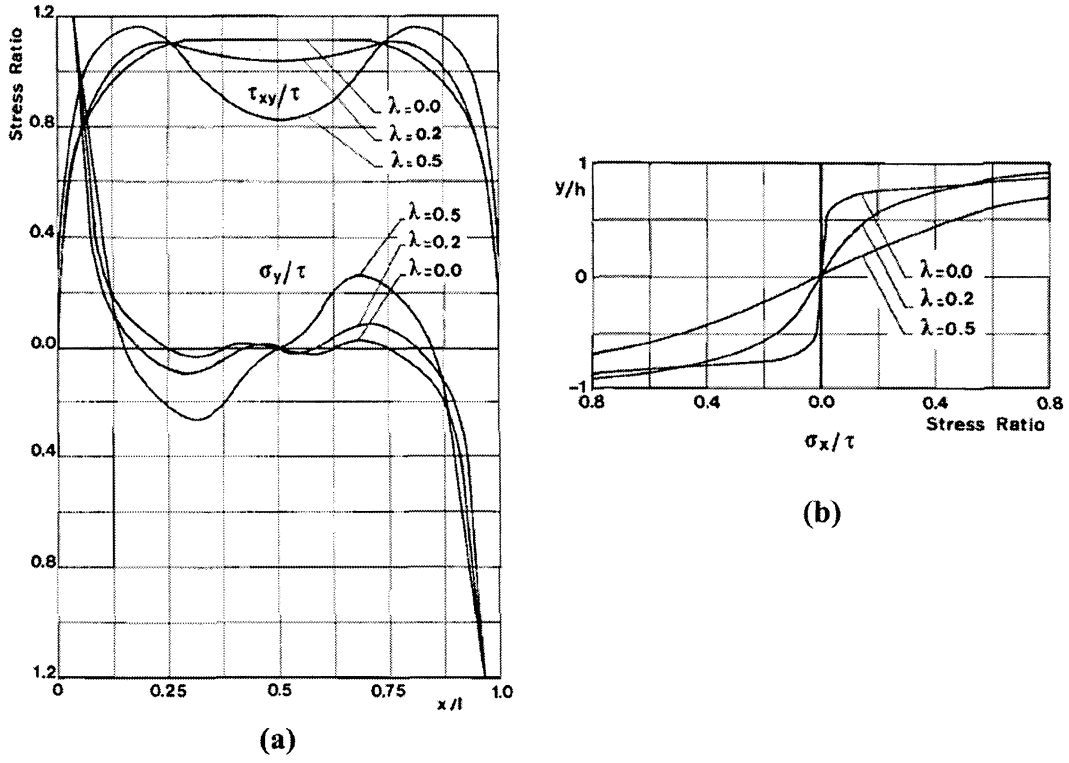

Fig. 2.15. Distribution of stresses across the boundaries of a sample in the Cambridge device for various values of slippage (λ=0, no slippage) (a) stresses on upper and lower faces (b) stresses on end of sample (Prevost and Hoeg, 1976)

In two separate discussions of a state of the art paper, however, Lacasse and Vucetic (1981) and Christian (1981) both state that the distribution of stresses is actually relatively uniform for the majority of the sample face and that the case is much less severe than presented in Prevost and Hoeg (1976) and Saada and Townsend (1981), especially for the most likely case of no slippage. It is also pointed out that Prevost and Hoeg assumed an isotropic elastic material. For an elastic-plastic material, the non-uniformities are even less and continue to decrease as yielding occurs. Wright et al. (1978) experimentally examined the non-uniformities by using a three-

dimensional photoelastic method. Fig. 2.16 shows the non-uniform distribution of stresses determined for the cuboidal and cylindrical samples. As mentioned by Christian (1981), however, the horizontal shear stresses are asymmetric about the center of the sample, which is impossible for an isotropic elastic soil under such a loading. The author comments that the resulting strains may be due to the photoelastic setup and not the actual DSS test apparatus.

According to Shen et al. (1978), the area over which these non-uniformities exist can be minimized if the diameter to height ratio is large. Franke et al. (1979) showed that for saturated sand samples, no differences in load resistance occurred for diameter to height ratios (D/H) of 3.75 to 7.5. Vucetic (1981) showed a similar result for Haga clay, in which the differences measured in horizontal shear stresses were less than the expected scatter due to the non-homogeneity of undisturbed samples (Figure 2.17). Additionally, Airey and Wood (1987) point out that the stress and strain distributions in the DSS samples are more uniform than in the standard triaxial device where bulging occurs due to the end constraints.

While non-uniformities exist overall, most studies show that the core region of the sample is under uniform stress and strain conditions (Roscoe, 1953; Duncan and Dunlop, 1969; Lucks et al., 1972; Prevost and Hoeg, 1976; Shen et al., 1978; Budhu and Britto, 1987; Dounias and Potts, 1993). Duncan and Dunlop (1969) showed through finite element analysis that shear stress varies along the height of the sample with the stresses being the largest at the center. In Roscoe's analysis using an elastic material, there is approximately a 7% difference between the top and mid height values. For the nonlinear and anisotropic case used by Duncan and Dunlop, the difference ranges from 4 to 8%. The difference was also shown to decrease with increasing shear strain. In a different finite element based study, Dounias and Potts (1993) showed that the stress measurements taken at the core of the sample closely

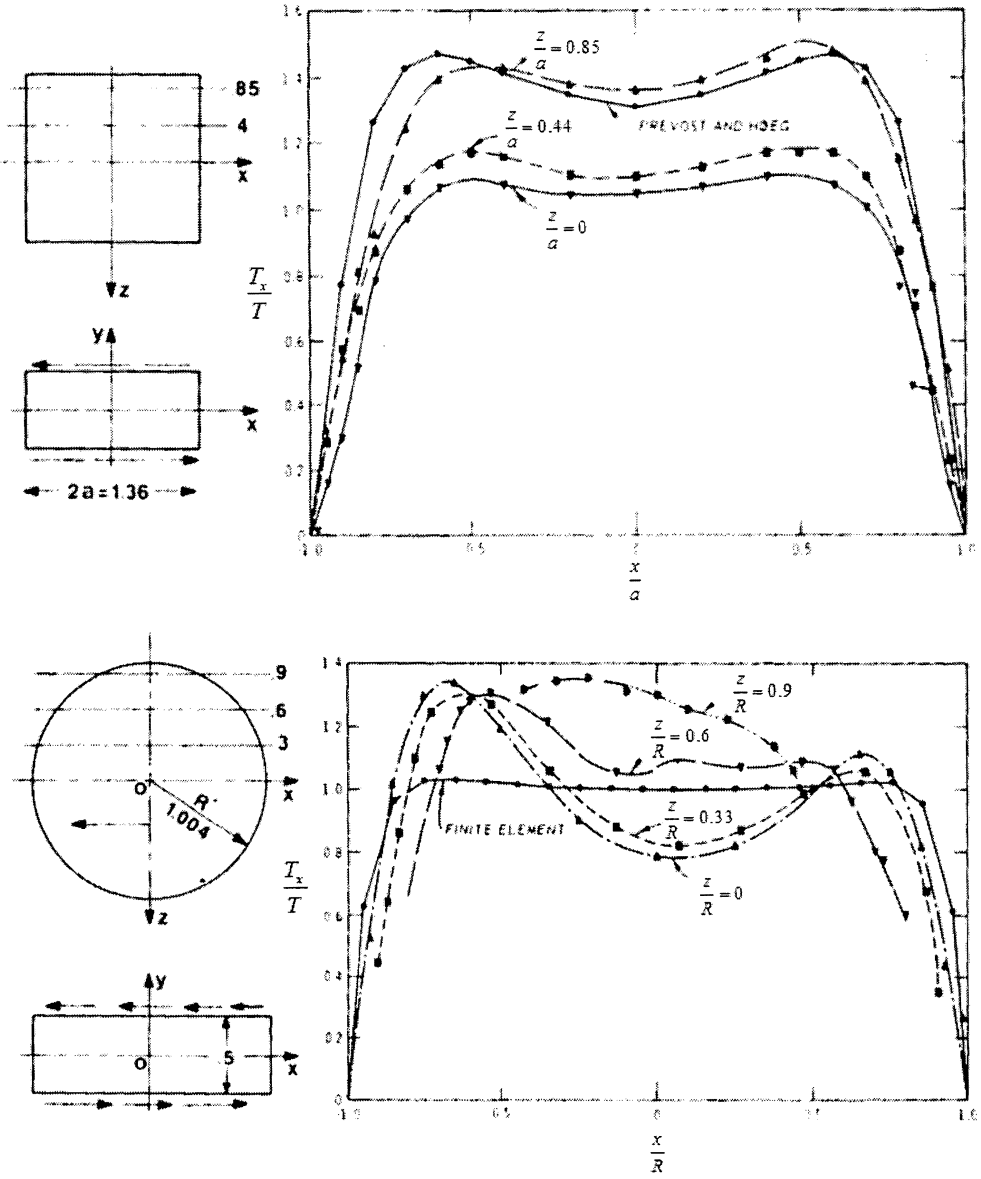

Fig. 2.16. Distribution of stresses determined from photoelastic analysis (after Wright et al., 1978)

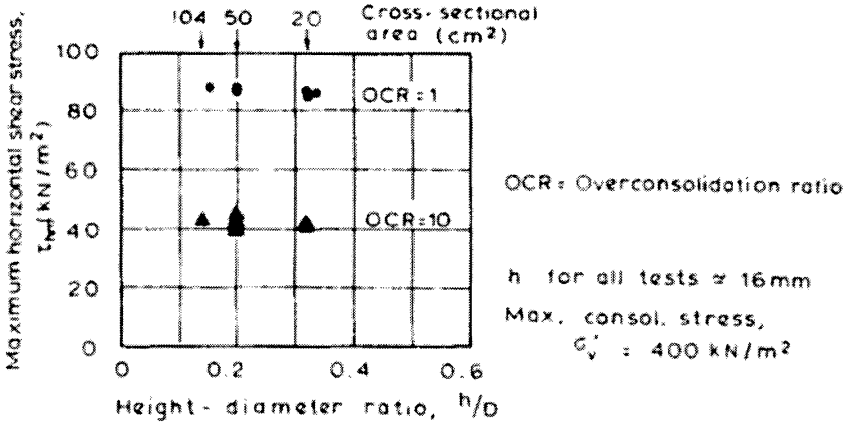

(a) Maximum horizontal shear stress

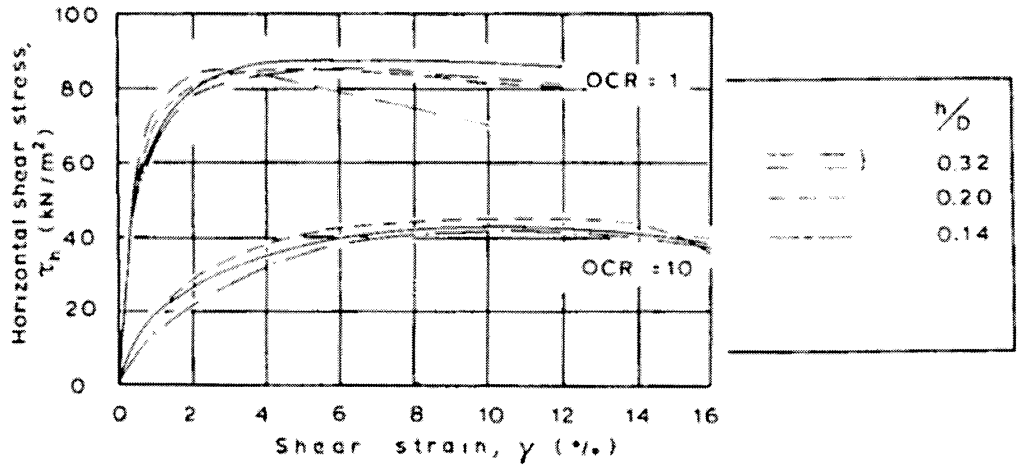

(b) Stress – strain curves

Fig. 2.17. Effect of height to diameter ratio on DSS test results (after Vucetic, 1981)

approximate the ideal simple shear conditions (Fig. 2.18). They also showed that the average values measured on the boundary underestimate the initial stiffness and the peak strength by as much as 20% for the various cases tested, while the sample core values tend to give the best overall approximations to the ideal simple shear

case.

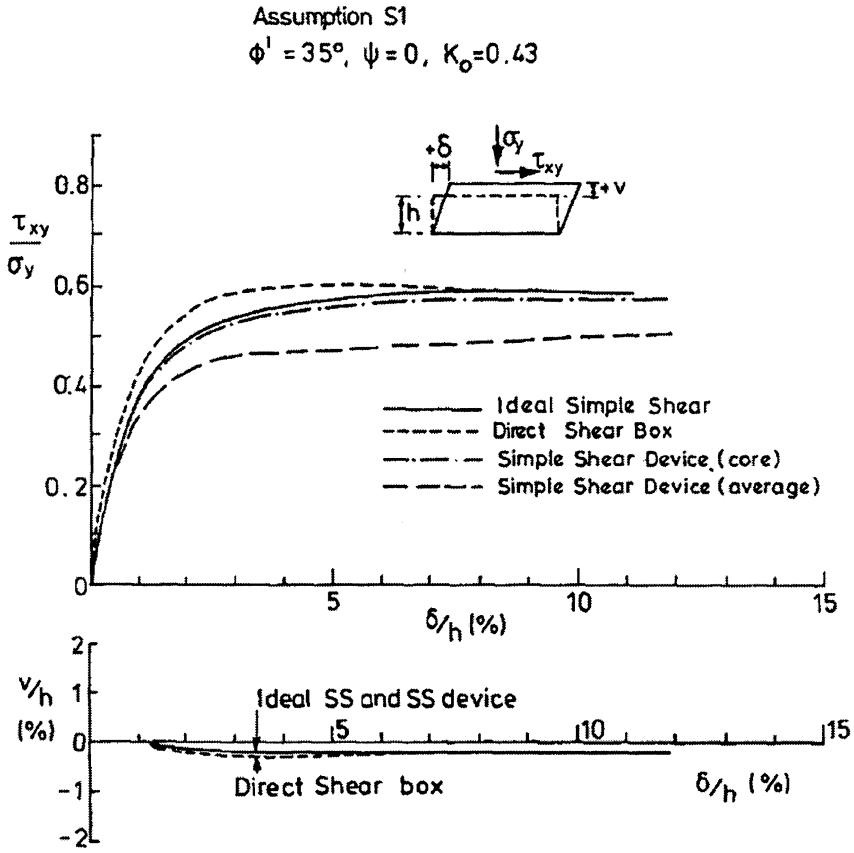

Fig. 2.18. Comparison of stress-strain curves for various cases (Dounias and Potts, 1993)

As discussed above, both the torsional shear and direct simple shear devices apply forces to the soil element replicating the in situ soil conditions (i.e. forces that enact the simple shear mechanism and allow for smooth rotation of the principal planes). The major advantage of DSS devices over torsional devices for this study, is their ability to apply two independent horizontal shear stresses allowing for multi-directional complex stress paths not achievable in torsional testing. Additionally,

as pointed out in Kammerer (2002), because of their large diameter to height ratio (D/H = 4) and overall relatively small size, direct simple shear samples have relatively uniform stress distributions across the active zone of the sample and more closely replicate the element-level case. For the simple shear testing in this study the ratio of D/H is slightly less than 4. The TAMU-MDSS device also has an increased stiffness to help minimize any rocking or pinching and further decrease the non-uniformities across the top and bottom boundaries.

2.3 Direct Simple Shear State of Stress at Failure

The goal of simple shear laboratory testing is to gain information about the stress-strain response of a particular soil subjected to loading conditions which closely replicate the true field conditions. As is the case with other apparatuses, the stress state of the material at failure and the corresponding strength parameters are ultimately derived from the test data in order to characterize the material and aid in design. The continuously developed and elaborately instrumented Cambridge device is capable of measuring the complete set of data needed to fully describe the stress state during testing, but due to its configuration, it is primarily used for research purposes only. The cylindrical sample used in the NGI-type device, however, is simple to prepare and well suited for trimmed natural samples. The device itself is also simple to operate and is commercially available, making it the most commonly used DSS device in practice. Even when the samples are elaborately instrumented and the sample core is measured to minimize the non-uniformities, one major drawback still exists for the NGI-type device. Budhu (1985) showed that the radial stresses measured in an instrumented cylindrical NGI-type sample are not equal to the intermediate principal stress nor the horizontal normal stresses perpendicular to the plane of shear deformation. Therefore, even if the stresses are measured, the com-

plete stress state still cannot be defined and the Mohr's circle cannot be constructed without making several assumptions of the failure conditions.

For the NGI-type devices, only the vertical normal stress (σ_{zz}) and the average horizontal shear stresses (τ_{xy} and τ_{yx}) are measured. Therefore, the full stress tensor $\begin{bmatrix} \sigma_{xx} & \tau_{xy} & \tau_{xz} \\ \tau_{yx} & \sigma_{yy} & \tau_{yz} \\ \tau_{zx} & \tau_{zy} & \sigma_{zz} \end{bmatrix}$ cannot be fully defined. The device cannot apply shear to the vertical sample faces and even if friction is minimized on these walls, and the assumption is made that τ_{yz} is zero, (σ_{xx}) and (σ_{yy}) still remain unknown. Because the horizontal normal stresses cannot be easily measured during shearing, a failure mode must be assumed in order to draw a complete Mohr's circle and derive the strength parameters from the test results. It should be noted that using a Mohr's circle of stress to determine the strength parameters only takes into account the major and minor principal stresses and does not consider any influence that the intermediate principal stress may have on the overall soil strength. Davis (1968), Roscoe (1970), de Josselin de Jong (1971), Wood et al. (1979) and Budhu (1988) each proposed various methods to interpret test results for simple shear devices. DeGroot (1989) and Shen (2013) both provide detailed reviews of the more common methods proposed. DeGroot showed that for a single normally consolidated test on Boston Blue clay, the calculated strength parameters varied greatly for the seven different failure assumptions presented. For example, the friction angle could range from 19.3° to 90° and the orientation of the major principal stress could range from 19.3° to 45° depending on the failure criterion used. The following sections summarize several of the assumed failure criterion described in Budhu (1988), DeGroot (1989), and Shen (2013).

Each method assumes a particular orientation of the major principal stress at failure, while the initial stresses follow K_o conditions and the Mohr-Coulomb failure criteria is considered valid. The most conventional approach assumes that the hor-

izontal planes are the planes of maximum stress obliquity (i.e. failure plane). For this case, the measured shear and vertical stresses are the failure stresses. The major principal stress is, therefore, oriented at $45 + \phi'/2$ with respect to the horizontal (Fig. 2.19). This is the general assumption for the direct shear box tests, but it is not correct for simple shear testing as shown by several researchers. Roscoe et al. (1967) conducted drained testing on sand in the Cambridge device and found that the failure plane was not horizontal. Airey et al. (1985) conducted tests on Kaolin samples impregnated with lead paste and found that rupture occurred at the peak shear stress and the rupture plane was oriented at an angle of 5-15° to the horizontal.

A second approach assumes that the horizontal planes are planes of maximum shear stress (Fig. 2.20). For this case, the measured peak horizontal and shear stresses are plotted on the Mohr's circle at the location of maximum shear stress. The major principal stress is oriented at 45° from the horizontal. Roscoe et al. (1967) showed that this failure criteria is valid for drained tests on medium-loose sand; however, it was not valid for dense sands.

Three failure hypotheses, as presented by Shen (2013), are shown in Fig. 2.21. Fig. 2.21a shows the previously discussed case in which the horizontal plane is assumed to be the failure plane or plane of maximum obliquity. This approach holds only for materials that follow an associated flow rule (i.e. the angle of internal friction and the angle of dilation are equal) and may not be the most applicable for granular soils which are generally treated as non-associated flow materials.

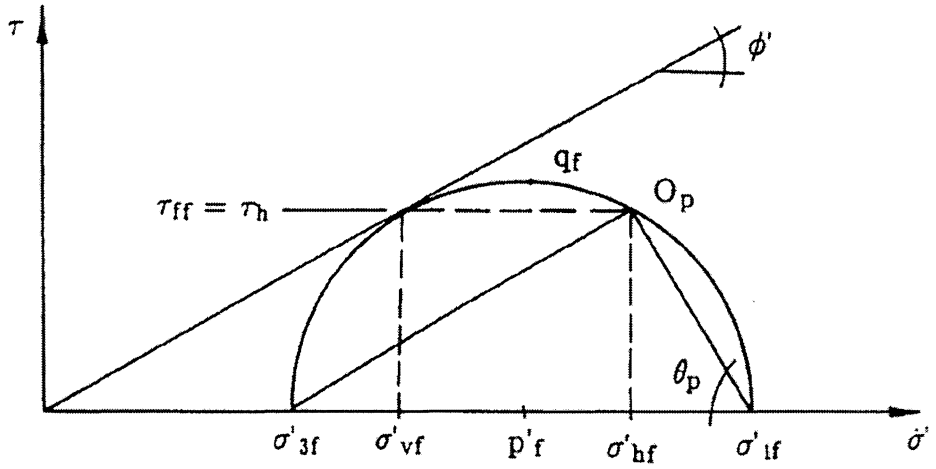

$$q_f/\sigma'_{vc} = \frac{\tau_h/\sigma'_{vc}}{\cos\phi'} \qquad \tau_{ff} = \tau_h$$

$$p'_f/\sigma'_{vc} = \sigma'_{vf}/\sigma'_{vc} + (\tau_h/\sigma'_{vc})\tan\phi'$$

$$\sigma'_{hf}/\sigma'_{vf} > 1 \qquad \tan\phi' = \tau_h/\sigma'_{vf}$$

$$\theta_p = 45^\circ + \phi'/2 \qquad \theta_f = 0^\circ$$

Fig. 2.19. Failure mode: horizontal plane is the plane of maximum obliquity (DeGroot, 1989)

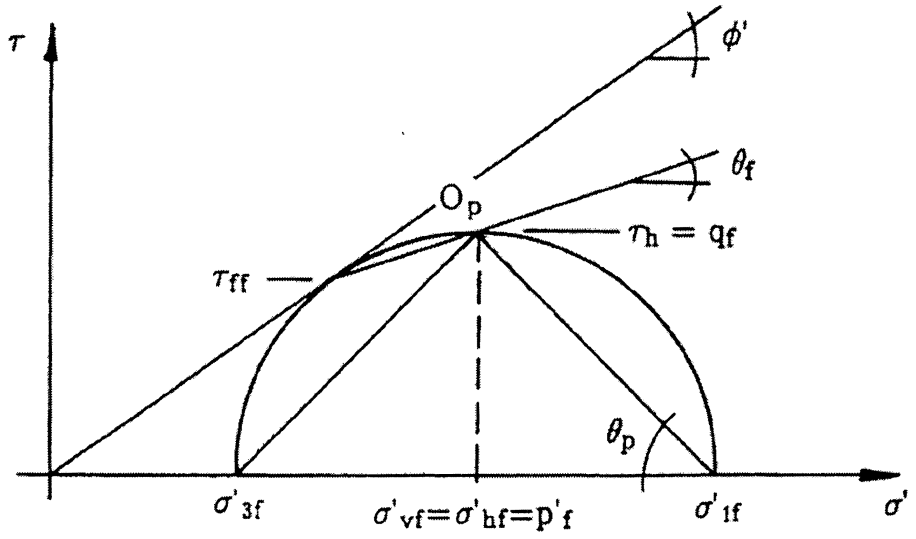

$q_f/\sigma'_{vc} = \tau_h/\sigma'_{vc}$ $\qquad$ $\tau_{ff} = q_f \cos\phi'$

$p'_f/\sigma'_{vc} = \sigma'_{vf}/\sigma'_{vc}$

$\sigma'_{hf}/\sigma'_{vf} = 1$ $\qquad$ $\sin\phi' = \tau_h/\sigma'_{vf}$

$\theta_p = 45°$ $\qquad$ $\theta_f = \phi'/2$

Fig. 2.20. Failure mode: horizontal plane is plane of max shear stress (DeGroot, 1989)

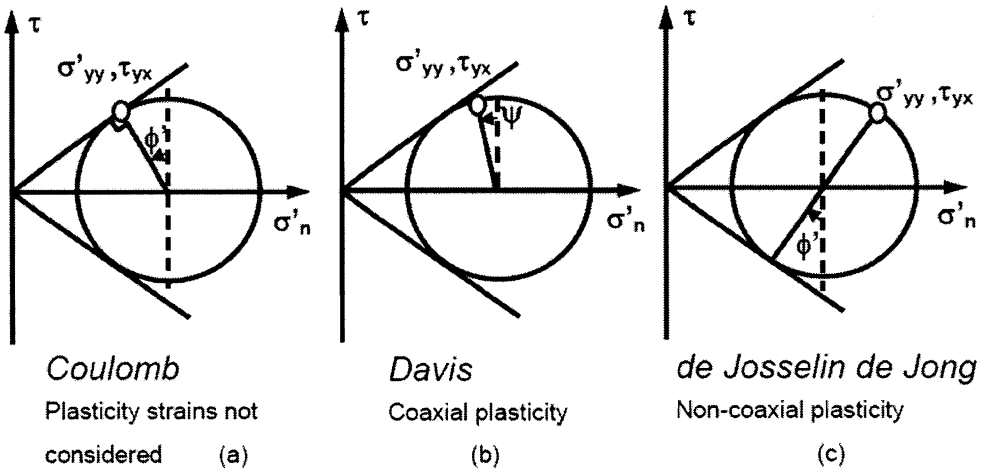

Fig. 2.21. Common assumed failure modes for simple shear samples (Shen, 2013)

Davis (1968) proposed a different approach assuming coaxial plasticity, in which the internal friction and dilatancy angles do not have to be equal (Fig. 2.21b). For most situations, the dilatancy angle is less than the internal friction angle, therefore, Davis suggests that the real failure plane occurs at an angle less than that of maximum obliquity. One issue arises with the use of coaxial plasticity theory for this approach. Coaxial plasticity represents the case where the principal stress axes coincide with the plastic strain-rates. A number of researchers have shown both experimentally and numerically (Roscoe et al., 1967; Roscoe, 1970; Drescher and de Josselin de Jong, 1972; Arthur et al., 1977b; Zhang, 2003; Jiang and Yu, 2006; Yu, 2006; 2008) that this is not always the the case for granular soils, especially when principal stress rotation occurs. The non-coaxial behavior of granular materials is further discussed below. Additionally, non-coaxial plasticity is discussed in detail in Yu (2006).

Recognizing the potential for an additional failure mode, de Josselin de Jong

(1971) proposed the possibility of failure occurring on either horizontal planes (as discussed previously) or a combination of sliding and rotation on vertical planes (Figs. 2.22 and 2.23).

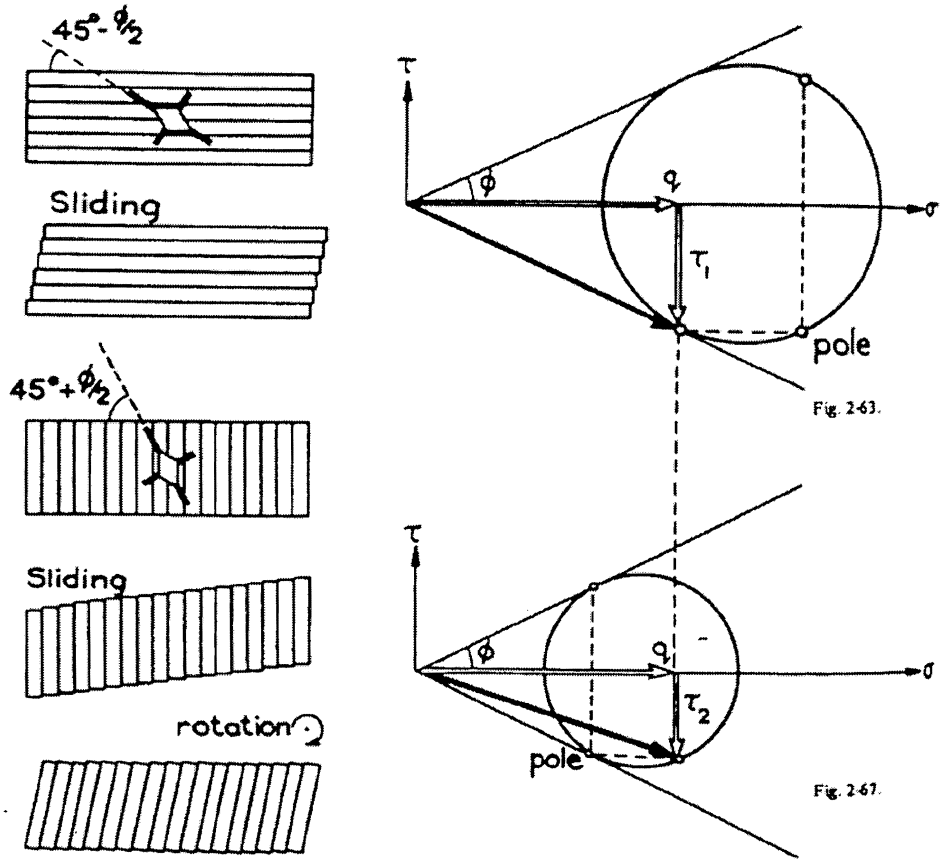

Fig. 2.22. Possible failure modes for simple shear samples with sliding on (a),(b) horizontal planes and (c),(d) vertical planes (Wood, 1990) (after de Josselin de Jong, 1971)

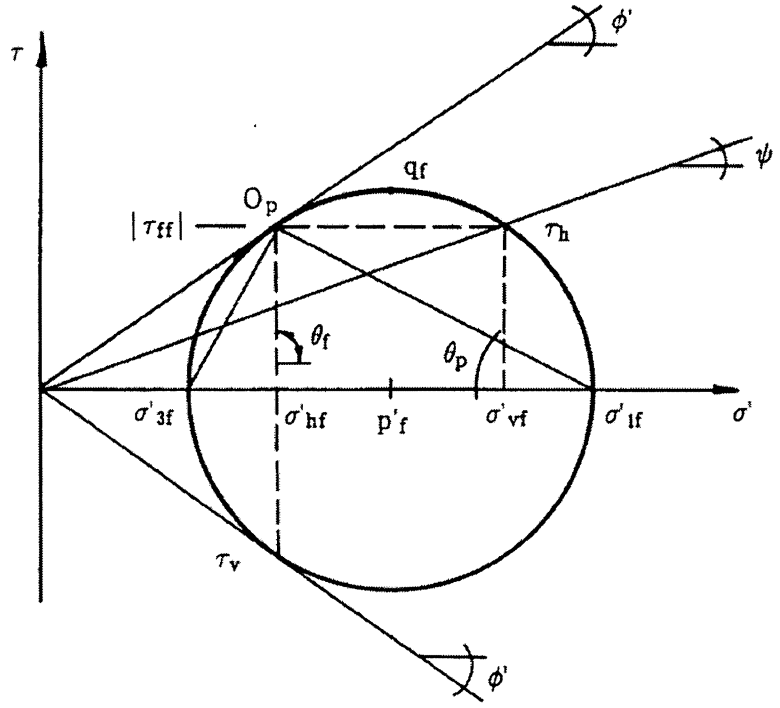

$$q_f/\sigma'_{vc} = \frac{\tau_h/\sigma'_{vc}}{\cos\phi'} \qquad \tau_h/\sigma'_{vf} = \frac{\sin\phi'\cos\phi'}{1+\sin^2\phi'}$$

$$\tau_{ff} = q_f\cos\phi' \qquad p'_f/\sigma'_{vc} = \sigma'_v/\sigma'_{vc} - (\tau_h/\sigma'_{vc})\tan\phi'$$

$$\theta_p = 45^\circ - \phi'/2 \qquad \psi = \arctan(\tau_h/\sigma'_{vf})$$

$$\theta_f = 90^\circ$$

Fig. 2.23. Failure mode: vertical plane is failure plane as proposed by de Josselin de Jong (1971) (after DeGroot, 1989)

For common boundary conditions, the sample will fail in the mode of least resistance. The vertical case produces the smaller shear stresses of the two and is thus the most probable failure mode. This proposed method takes into account the non-coaxial behavior of granular soils with the idea that failure can first be initiated on vertical planes even when shearing is progressing in a different direction. The

major principal stress plane is oriented at $45° - \phi'/2$ with respect to the horizontal plane. Airey et al. (1985) state that this theory is only valid if rupture occurs along the directions of zero extension and if these planes are the planes of maximum obliquity. Budhu (1988) showed that for drained tests on sand, the failure is initiated on vertical planes; however, these nor the horizontal planes are planes of maximum obliquity. Notice in Fig. 2.24 that the stresses on the vertical plane reach a peak much earlier (at lower strains) than the stresses on the horizontal plane. Budhu also points out that additional assumptions of constant volume and uniform stress conditions are assumed by de Josselin de Jong which are not correct in actual drained tests.

Additional failure criterion have been proposed through the years; however, each has shortcomings due to their neglect of important features of granular soil behavior. In a study on the state of stress in DSS tests using Discrete Element Method (DEM) models, Wijewickreme et al. (2013) show that the planes of maximum stress obliquity rotate as shearing progresses. At the peak mobilized friction angle, it is valid to assume the maximum shear stress acts on the horizontal plane. The planes of maximum stress obliquity are then at angles of $\phi_{mob}/2$ and $\pi/2 - \phi_{mob}/2$ with respect to the horizontal. In the post peak range at large shear strains, however, it is more appropriate to assume the horizontal plane is a plane of maximum stress obliquity. Overall, these findings suggest that there is not just one interpretation for the stress state of a granular soil in simple shear that suffices for all strain levels. It is instead a very complex problem in which the planes of maximum stress obliquity seem to rotate as the principal planes rotate and shearing progresses. This becomes a very important feature when considering the validity of some continuum approaches and development of constitutive models that intend to capture this type of strain-dependent behavior.

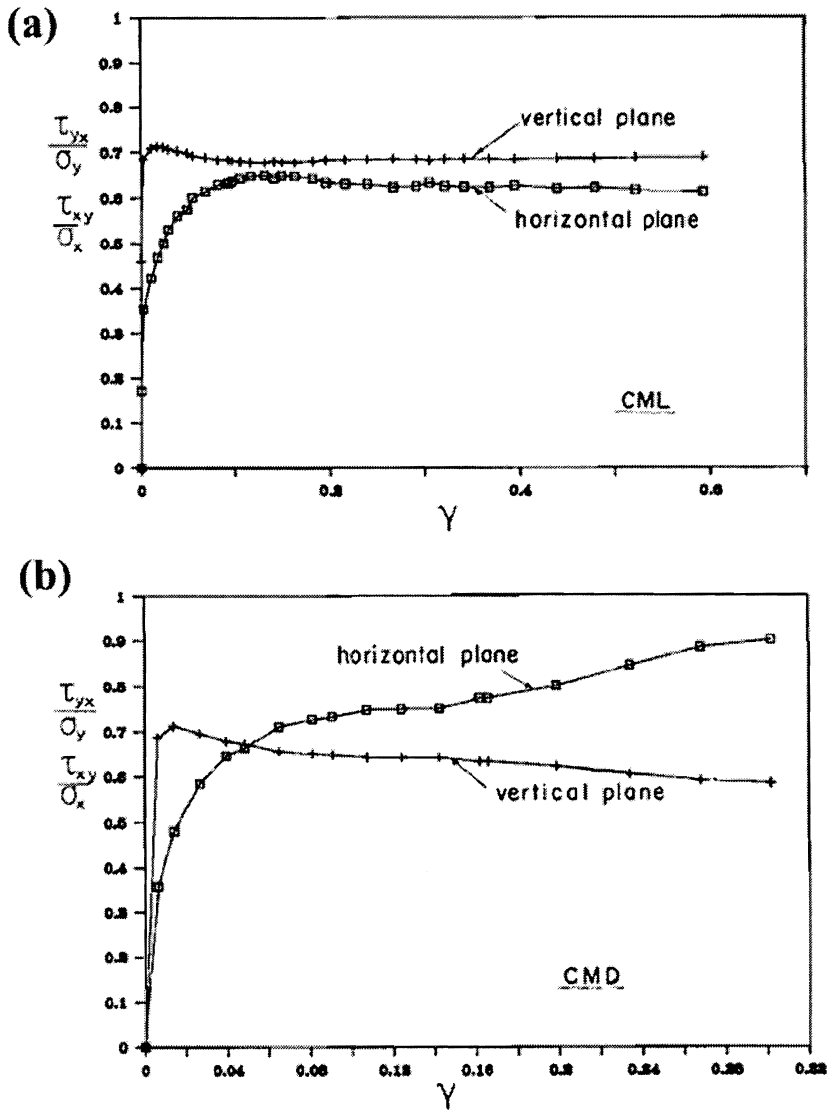

Fig. 2.24. Shear stress ratio versus shear strain in the specially instrumented NGI-type device (a)loose sand (b)dense sand (Budhu, 1988)

2.4 Anisotropy and Non-coaxial Behavior of Granular Materials

Besides being used to examine the basic stress-strain behavior of soils, simple shear testing has been used to study two important factors affecting granular material

behavior during principal stress rotation, anisotropy and non-coaxiality. To date, very few models are able to incorporate their effects. Roscoe (1970) and Oda and Konishi (1974) showed experimentally that principal stresses rotate up to 60° during shearing with the majority of the rotation occurring at the lower strain stages. The effects on soil response due to this rotation have often been neglected in models concerned with only the post-peak behavior, and it is only recently that an accurate pre-failure description of soil behavior has been examined. Additionally, the majority of continuum models available for granular soils are based on continuum mechanics and follow coaxial plasticity theory (Yu, 2006). While this may be a reasonable assumption for isotropic soils, it may lead to unsafe design strengths for soils with inherent anisotropy, especially those experiencing principal stress rotation (Yu, 2008).

Anisotropy is present in soils which exhibit directionally dependent properties. Two types of anisotropy are possible for soils: inherent and induced. Inherent anisotropy defines a physical characteristic that is inherent in the material and is independent of the applied strains, while induced anisotropy is dependent upon the applied stress and strain history (Arthur and Menzies, 1972). Natural sand deposits have inherent anisotropy due to their gravity based depositional processes and the fact that they are comprised of many small particles (Oda, 1972; Arthur and Menzies, 1972; Symes et al., 1982; Shibuya and Hight, 1987; Vaid et al., 1990). This in turn means that the shear deformation and strength of these soils is dependent on both the magnitude and direction of the principal stresses. This type of anisotropy influences the mechanical behavior of granular soils in triaxial and other tests, but it becomes an extremely important key feature when considering simple shear tests in which the principal stresses rotate. In other words, even under constant shear stress and constant mobilized friction angle, granular soils will still deform during principal stress rotation due to anisotropy (Arthur et al., 1980; Miura et al., 1986; Gutierrez

et al., 2009). The effects of principal stress rotations on inherently anisotropic sands has been studied both experimentally and numerically by a number of researchers (Arthur et al., 1980; Towhata and Ishihara, 1985; Miura et al., 1986; Symes et al., 1988; Gutierrez et al., 1993; Nakata et al., 1998; Gutierrez et al., 2009). Most of the recent studies on principal stress rotation have been conducted using the hollow cylinder apparatus due to the ease of monitoring and controlling the principal stress magnitudes and directions. The experimental data is used to explore the effects of principal stress rotation on granular soil behavior in an effort to develop more advanced constitutive models that account for these effects.

Another factor affecting the behavior of granular soils subjected to principal stress rotation is non-coaxiality. Non-coaxiality is defined as the non-coincidence of the principal stress directions and the directions of the corresponding principal plastic strain rates. The first experimental indication of this behavior was noted by Roscoe during early simple shear tests on sand using the Cambridge device (Roscoe et al., 1967; Roscoe, 1970). The test data indicated an initial difference in the principal stress and principal strain rate directions. As the major principal stress direction rotated, the major principal strain rate direction also rotated, however, it continued to lag behind the principal stress rotation (Fig. 2.25).

It was not until very large strains and essentially critical state before the two were coincident. A number of other researchers have also observed this experimentally (Drescher and de Josselin de Jong, 1972; Oda and Konishi, 1974; Arthur et al., 1986; Matsuoka et al., 1988; Gutierrez et al., 1991; Joer et al., 1998; Cai, 2010). Using a Directional Shear Cell (DSC) to study anisotropy and non-coaxiality under principal stress rotation, Arthur et al. (1986) showed that the angle between the principal stress and strain rate directions, or angle of non-coaxiality ζ, decreased with increasing shear stress ratios as straining progressed (Fig. 2.26c).

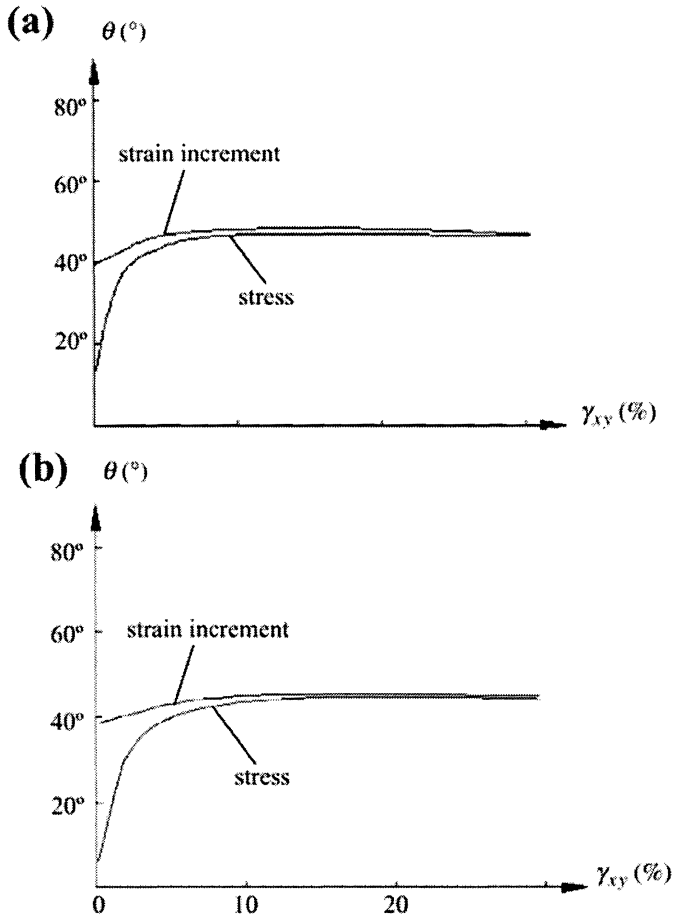

Fig. 2.25. Principal stress and principal strain increment rotations during simple shear test (Roscoe, 1970)

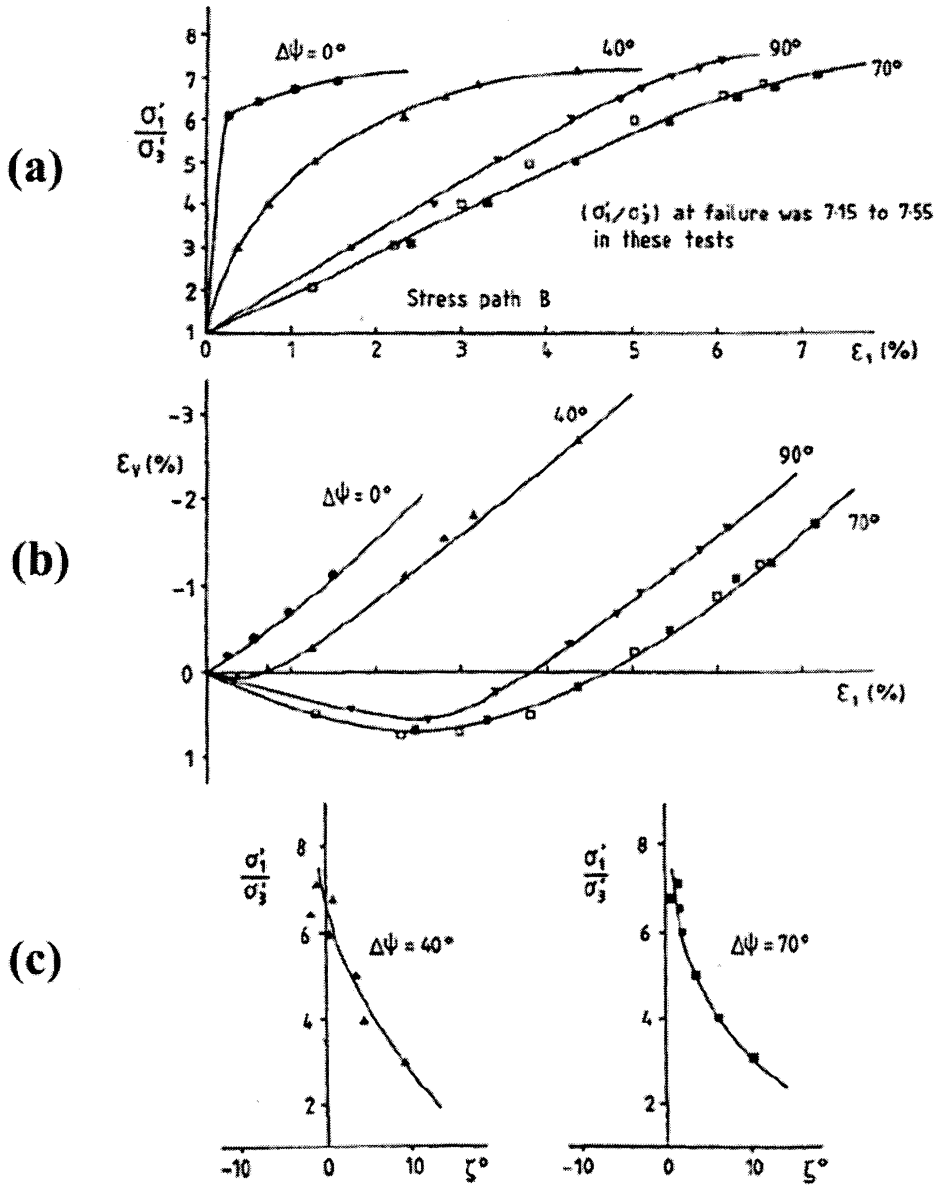

Fig. 2.26. Decreasing angle of non-coaxiality with increasing stress ratios (Arthur et al., 1986)

Gutierrez et al. (1991) also observed this type of non-coaxial behavior while conducting a study using the hollow cylinder apparatus. Samples were subjected to three different loading schemes, one with fixed or non-rotating principal stresses, and the other two with rotating principal stresses under constant and increasing stress ratios. Fig. 2.27 shows the total and plastic strain rate vectors for the pure principal rotation case at constant stress ratios.

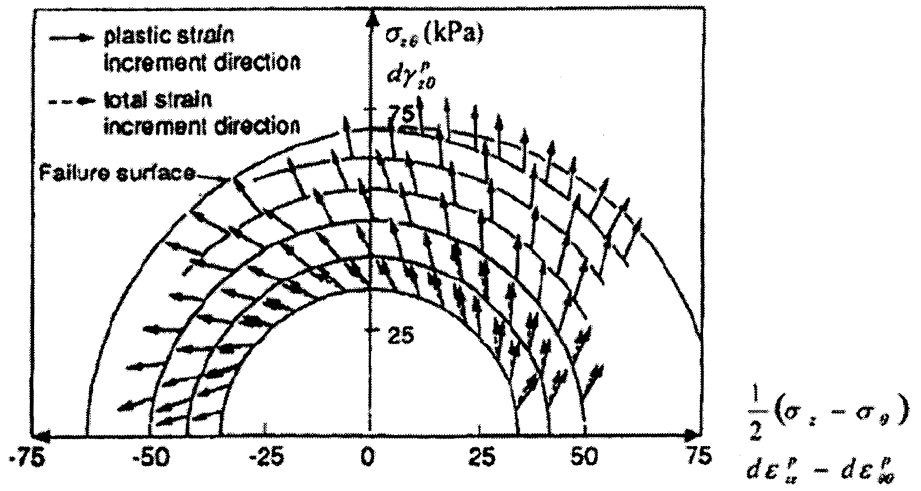

Fig. 2.27. Total and plastic principal strain increment vectors during pure principal stress rotation and constant stress ratio (Gutierrez et al., 1991)

It should be noted from the figure that the difference in total and plastic strain increments is very small and further decreases with increasing stress ratios (Gutierrez et al., 1991; Yu, 2008). Additional experimental evidence of non-coaxial behavior was observed by Cai (2010) in hollow cylinder tests on Leighton Buzzard and Portaway sands. Cai states that the degree of non-coaxiality is relatively small for monotonic loading, but becomes more significant during pure rotation and combined loading

tests. Cai also showed that the degree of non-coaxiality is influenced by sample density, stress path, stress level, and the inherent material properties.

Very few models are able to account for the above mentioned effects due to principal stress rotation. As described in numerous papers by Yu, most continuum based models use plastic potential theory and do not account for this type of behavior. Various modeling methods have been proposed in an effort to account for principal stress rotation (Dafalias et al., 2004; Lashkari and Latifi, 2007; Osinov and Wu, 2006; Yang and Yu, 2006; Gutierrez et al., 2009). Many of these models are based on complex theories and still lack the ability to capture all aspects of granular soil behavior in simple shear. Most recently, Gutierrez et al. (2009) presented a simple constitutive model that accounts for the two effects, anisotropy and non-coaxiality, resulting from principal stress rotation. The model incorporates an anisotropic failure criterion, and cross-anisotropic elasticity. It also incorporates a plastic flow rule and a stress-dilatancy relationship that accounts for the effects of non-coaxiality. Because continuum based modeling is out of the scope of this research, only a very short discussion of the current state of modeling is presented. A more in depth summary can be found in Yu (2006), Yu and Yuan (2006), and Yu (2008). A short discussion of the discrete methods used for investigating the effects of principal stress rotation is presented in Chapter 6.

2.5 Behavior of Granular Materials in Previous Direct Simple Shear Studies

Testing can be conducted under two different sets of conditions. One approach maintains the vertical stress (σ_{zz}) by varying the vertical strain (ϵ_{zz}). This allows the sample to contract and dilate freely simulating drained conditions. Alternatively, a constant volume approach can be used, in which the specimen height is maintained

($\delta\sigma_{zz} = 0$) by allowing the vertical stress (σ_{zz}) to vary, simulating undrained soil conditions. In both cases, all other strains are zero (ϵ_{xx}=ϵ_{yy}=γ_{xz}=γ_{yz}=0).

Direct simple shear testing has progressed from uni-directional or monotonic paths to bi-linear cyclic and multi-directional cyclic paths. As mentioned previously, monotonic DSS testing is used to gain general stress-strain relationships for a soil, as well as strength parameters to be used in design. Monotonic simple shear testing has been used extensively over the last 60 years to study the behavior of soils. The findings discussed below represent only a very small fraction of the available studies, and are intended to serve simply as a short review of granular behavior in simple shear.

2.5.1 Monotonic Direct Simple Shear Testing on Sand

2.5.1.1 Drained or constant vertical stress testing

The majority of the early reported simple shear tests on granular materials were carried out using the Cambridge device developed by Roscoe. Wroth (1958) conducted simple shear tests on a number of different types of granular materials including: Hauxton sand (< No.14 and > No.25 B.S. sieve), Leighton Buzzard sand (< No.18 and > No.25 B.S. sieve), glass beads, and steel ball bearings. The tests on Hauxton and Leighton Buzzard sand served as pilot tests to assess the additional developments to the device and provide interpretable results comparable to those obtained in the standard shear-box. These pilot tests showed that shearing had to progress to very high strains before critical state was reached for the Hauxton sand. Leighton Buzzard sand, a more round and uniform size and shape sand, was tested in hopes that the strains needed to reach critical state would be much less. Because the design of the device limited the ultimate shear strains that could be achieve, very few tests on sand were actually conducted by Wroth. This in turn, inspired the testing

of smooth spherical glass beads and steel ball bearings which are discussed below. It was shown that the sands and glass beads behaved similarly with the exception in the displacement required to reach critical state. Fig. 2.28 shows a representative curve for the shear stress-displacement behavior of Leighton Buzzard sand under a vertical effective stress of 261.3 kPa (37.9 psi). A void ratio versus displacement curve is shown for three of the tests (Fig. 2.29). The sand samples tended to have greater scatter in void ratio compared to the glass beads. Overall, this scatter seemed to increase with the irregularity of the particle size and shape.

Stroud (1971) presents tests on Leighton Buzzard sand ($<$ No.14 and $>$ No.25 B.S. sieve) using the SSA Mk 7, a further developed and improved version of the Cambridge device used in Wroth (1958). Major changes in the mechanical design helped overcome a weak contact causing slippage between the sand grains and the top sample boundary. The addition of more precise load cells and improvements to the system boundary conditions also corrected the large non-uniformities developing within the sample and the underestimates of stress and strain measured at the boundaries as described by Cole (1967). Initial tests and comparisons with results from Cole (1967) show that the adjustments corrected the non-uniformity and boundary issues (Fig. 2.30).

After running several pilot tests to assess the ability of the newly modified device to apply uniform stress and strain conditions on a sample, Stroud conducted a study on the behavior of Leighton Buzzard sand subjected to low stress level simple shear conditions. Fig. 2.31 shows a series of constant vertical stress tests. These samples all began at similar void ratios of 0.530, very close to the densest state; however, they were tested under different vertical effective stress values, σ_{yy}. As clearly seen in Figure 2.31a, the tests conducted at lower σ_{yy} values are stiffer at low

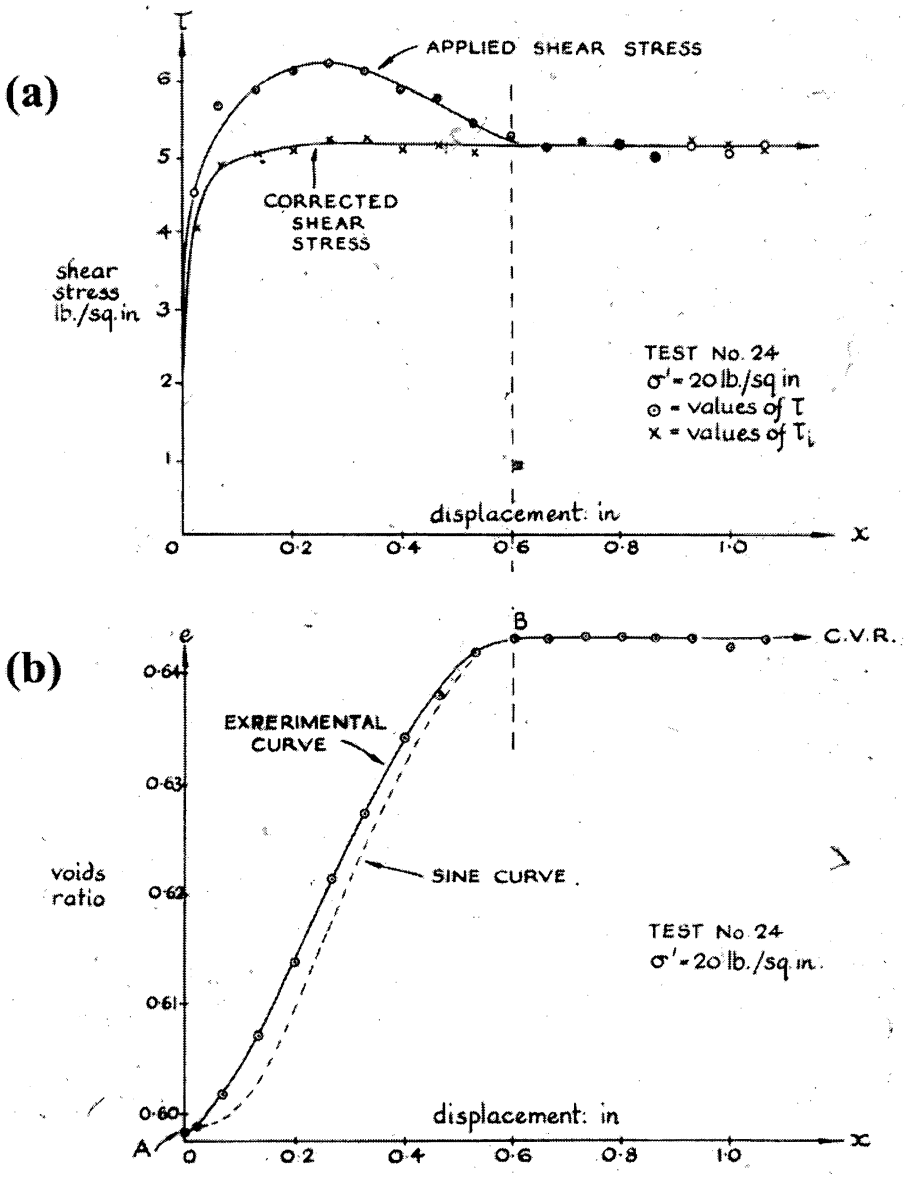

Fig. 2.28. Representative results from simple shear tests on Leighton Buzzard sand (Wroth, 1958)

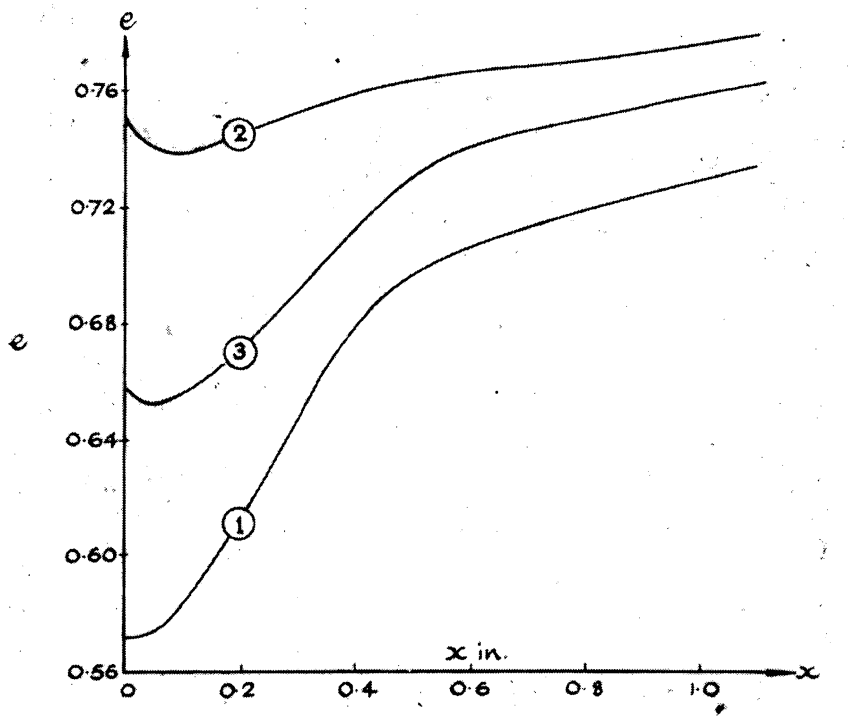

Fig. 2.29. Void ratio relationships during shearing for simple shear tests on Leighton Buzzard sand (Wroth, 1958)

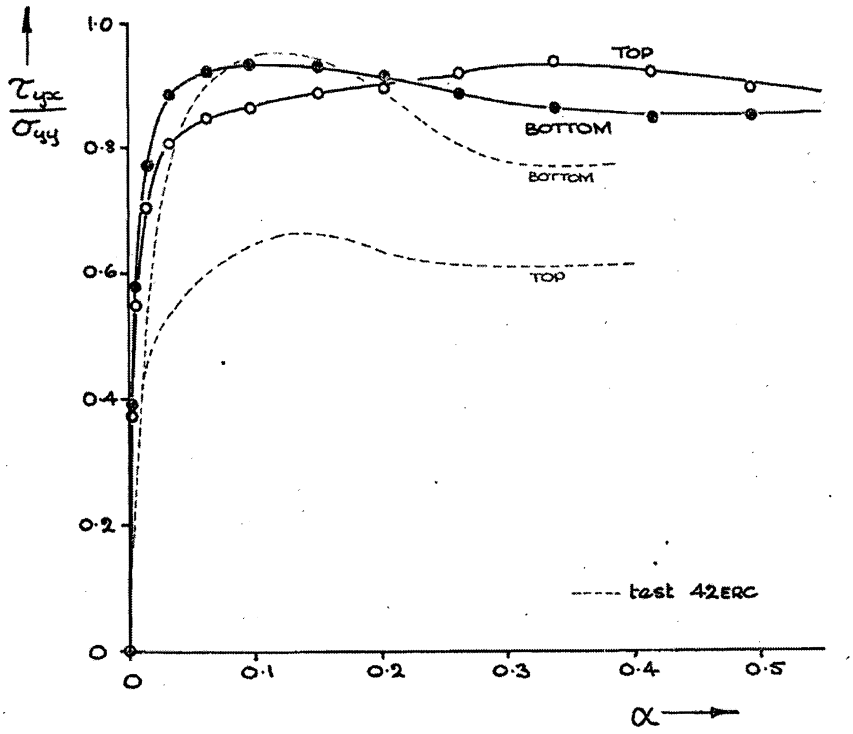

Fig. 2.30. Comparison of stress ratios at the top and bottom of the central third of the sample for simple shear tests on Leighton Buzzard sand (Stroud, 1971)

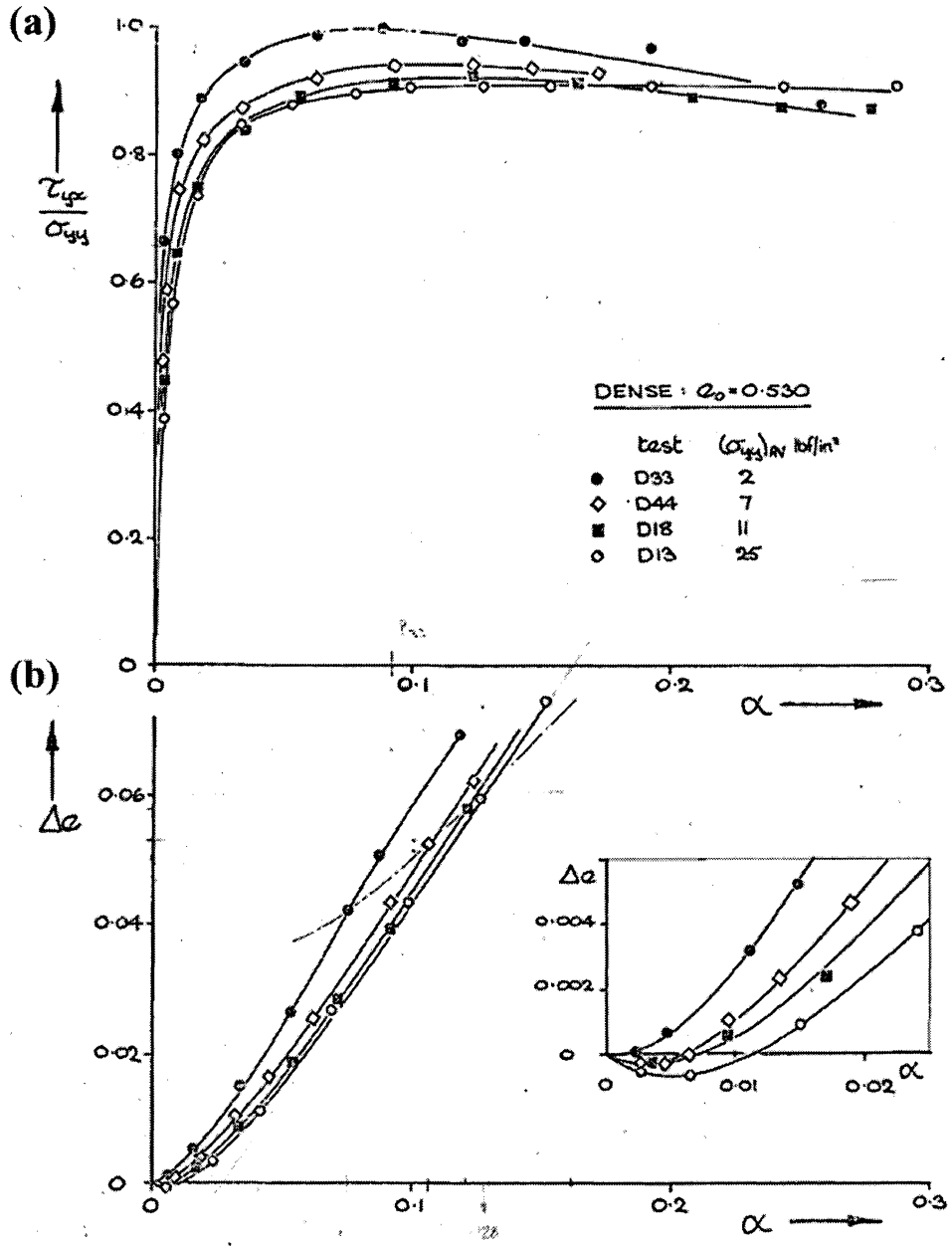

Fig. 2.31. Results from simple shear tests on dense Leighton Buzzard sand (Stroud, 1971)

strain values (i.e. the curve is steeper during the early stages of the test when σ_{yy} is low). Lower values of σ_{yy} also lead to higher peak values of shear stress ratio, τ_{yx}/σ_{yy}, and this peak tends to occur at lower shear strain values. Figure 2.31b shows the volumetric response of the samples. All samples initially contract and then dilate as shear straining progresses. The initial contraction for all of the samples is very small due to the fact that the samples are prepared at void ratios near the minimum void ratio of Leighton Buzzard sand, reported as 0.510 by Kolbuszewski (1965). The higher values of σ_{yy} tend to lead to greater contraction of the sample, while lower vertical stresses tend to allow dilation much more quickly and at lower values of shear strain. It should be noted that although the dilation rates have slowed towards the end of the tests, volumetric changes are still occurring (i.e. the samples are not at critical state at the final shear strain). As shown by Wroth (1958), straining must to continue to very large values before this condition is reached.

Stroud also conducted similar tests on loose samples of Leighton Buzzard sand (Fig. 2.32). As expected, the initial system is much less stiff, the shear stresses develop slower initially, and the peak is a lower value than that observed in the dense tests. The tests carried out at lower vertical stress values tend to reach their peak strength earlier than those at higher σ_{yy} values; however, the peak is not necessarily always higher as observed in the dense tests. Stroud comments that this could be due to slight underestimation of the measured stress ratio caused by non-uniformities experienced within the sample. In terms of volumetric response, the samples initially contract much more than the dense samples and the subsequent dilation rates are much lower. As with the dense tests, although the dilation rates are slowing near the end of the tests, volume change is still occurring. Therefore, the loose samples are also not at critical state at the final shear strain values.

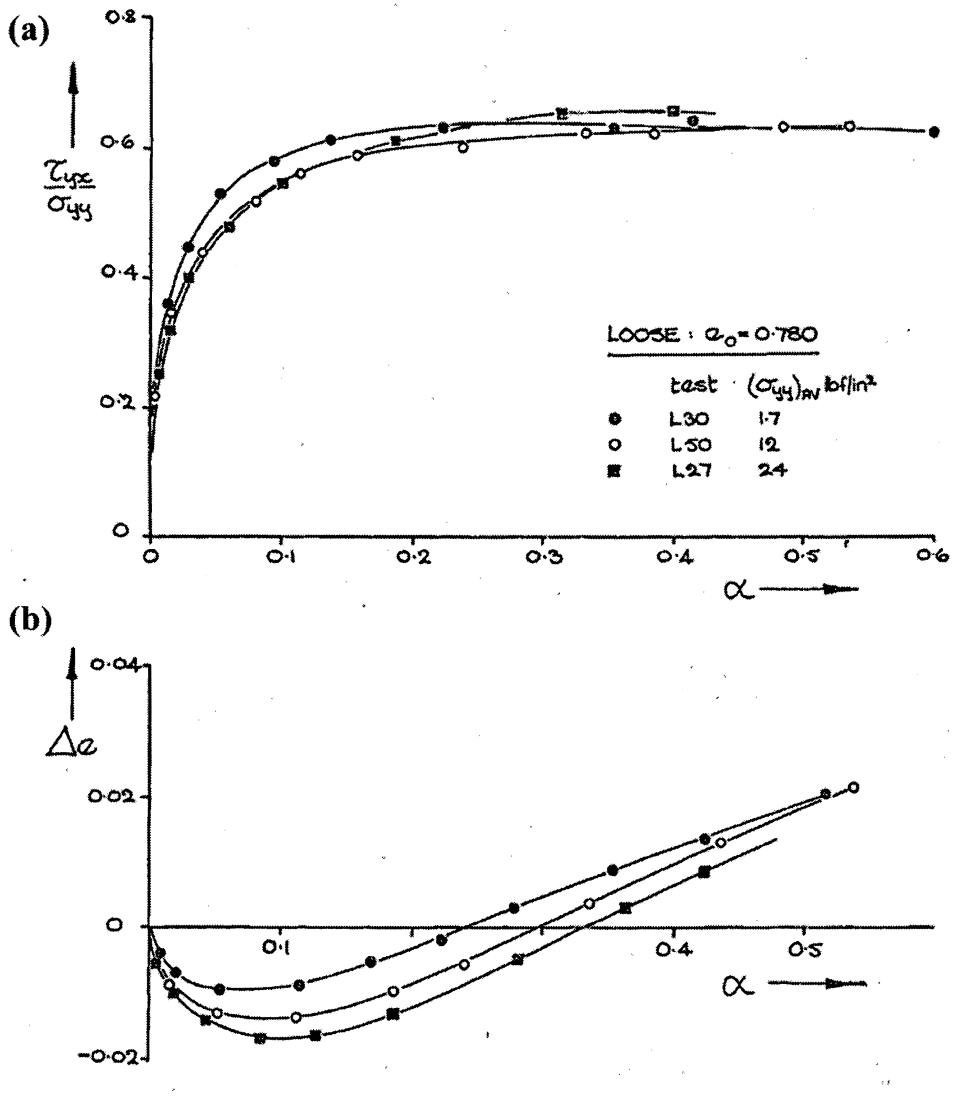

Fig. 2.32. Results from simple shear tests on loose Leighton Buzzard sand (Stroud, 1971)

The test data from the dense and loose tests was combined with results from Cole (1967) to explore the relationship of peak stress ratio, τ_{yx}/σ_{yy}, with vertical effective stress, σ_{yy} (Fig. 2.33). It can be seen from the plot that only the top boundary measurements were in error. The bottom sample boundary tended to

develop the expected frictional resistance. Plotted in log scale, the dense tests follow the expected linear trend quite well, but there are some differences observed in the loose tests at low vertical stress values. In stress space (Fig. 2.34), the tests proceed in a relatively straight path until they are very near the max τ_{yx}/σ_{yy} value, at which point they begin to become less steep and approach tangent to the failure surface.

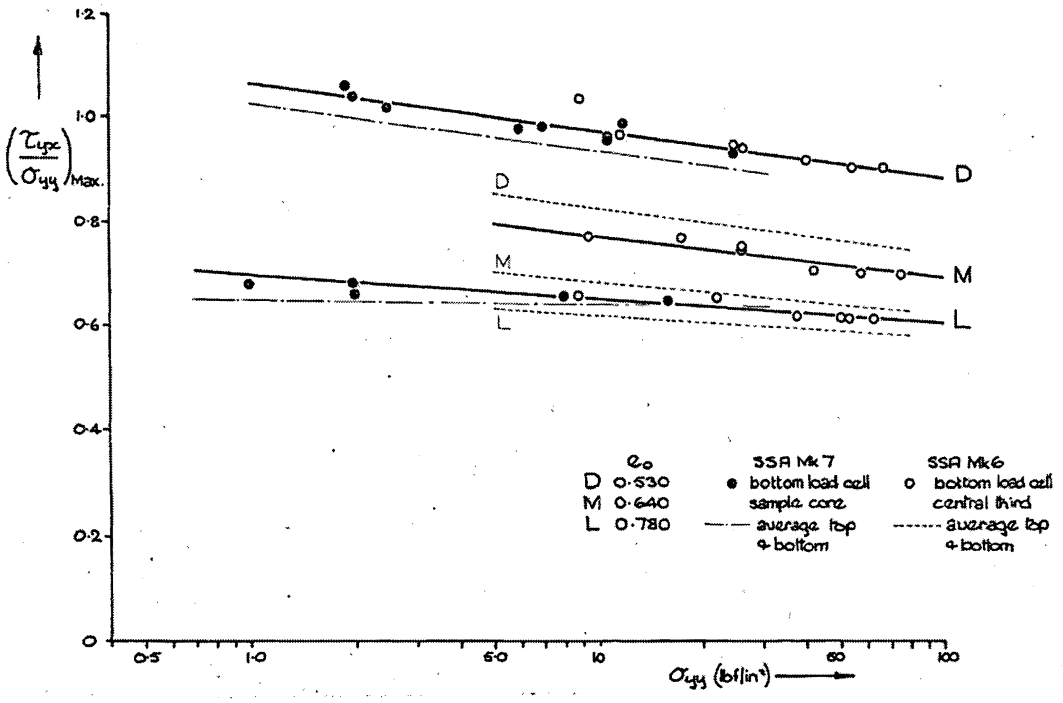

Fig. 2.33. Stress ratio versus vertical effective stress for simple shear tests on Leighton Buzzard sand (after Stroud, 1971)

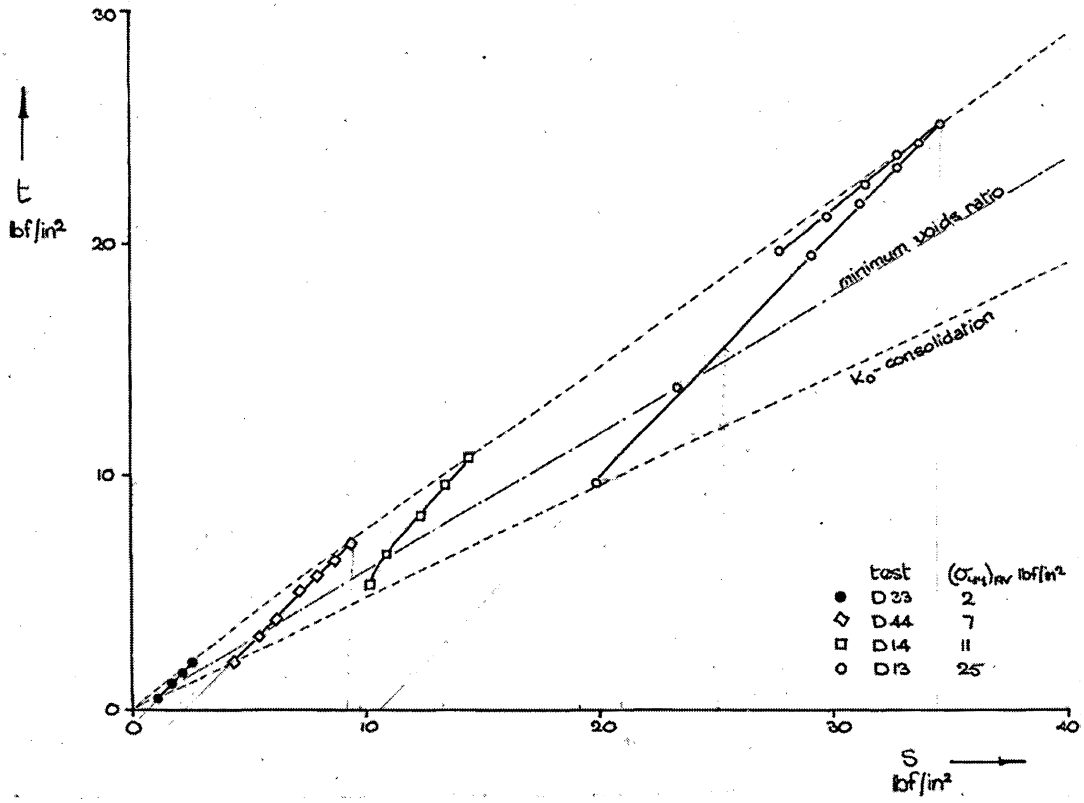

Fig. 2.34. Stress space (t,s) plot for simple shear tests on Leighton Buzzard sand (after Stroud, 1971)

Using X-radiographs (X-rays) taken during the testing, Stroud was able to compare internal and boundary strains. Samples of Leighton Buzzard sand were prepared with a placed grid of lead shot and internal strain measurements were deduced from the X-ray images (Fig. 2.35). For dense tests, Stroud found that the internal strains matched the boundary strains up to the point of peak stress ratio (Fig. 2.36).

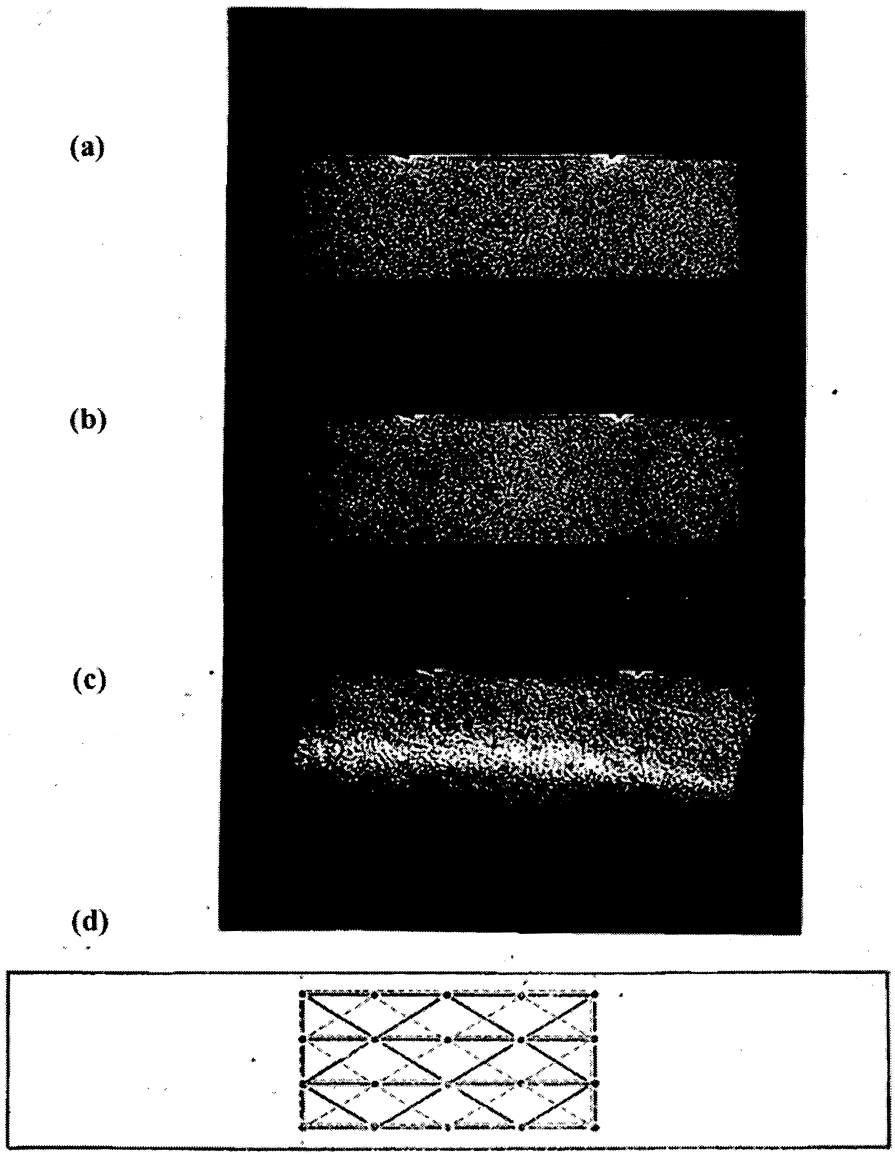

Fig. 2.35. X-ray images for simple shear tests on Leighton Buzzard (d) lead shot grid spacing and layout used for internal strain measurements (Stroud, 1971)

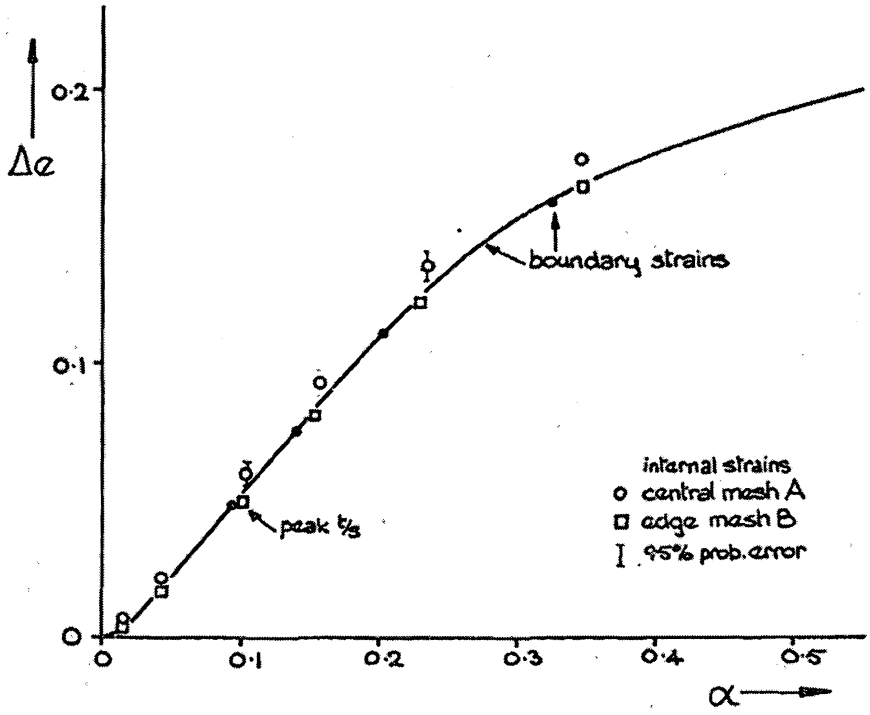

Fig. 2.36. Comparison of internal and boundary strain measurements for dense simple shear tests on Leighton Buzzard sand (Stroud, 1971)

After the peak shear stress ratio is reached, the internal volumetric and shear strains are slightly higher than those measured at the boundary, indicating a zone of higher displacement or rupture through the sample. Similar procedures were conducted for loose samples. It was found that the internal and boundary strains agreed up to the point when the sample began to dilate, at which point the localized zone developed in the center of the sample (Fig. 2.37). Also, the increased scatter in the data is most likely due to the sensitive structure of loose sand and the difficulty in preparing a truly uniform loose sample.

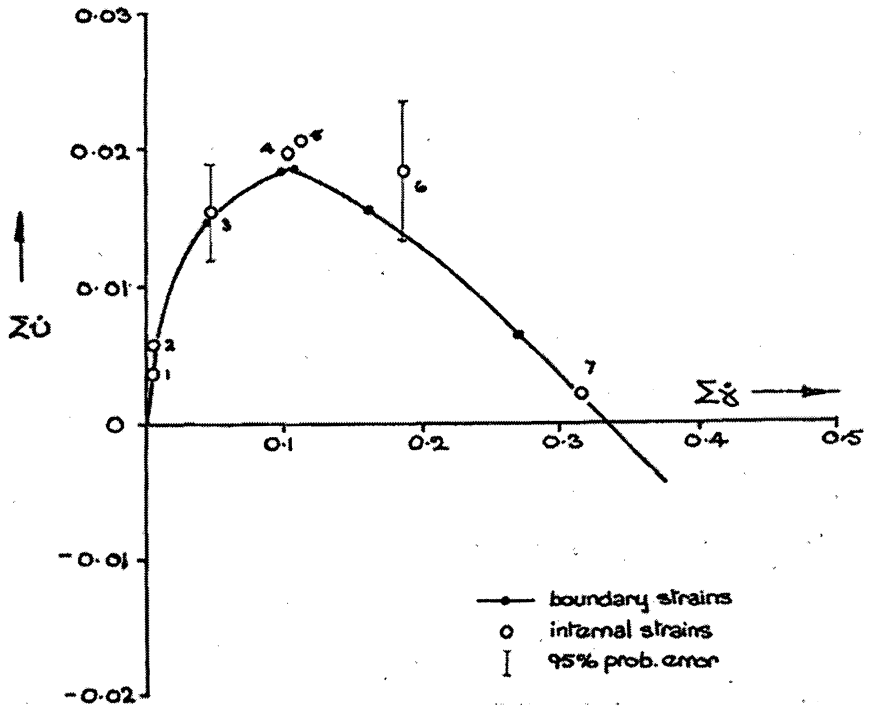

Fig. 2.37. Comparison of internal and boundary strain measurements for loose simple shear tests on Leighton Buzzard sand (Stroud, 1971)

Budhu (1979) presents further testing on sands using a modified version of the Cambridge device, designated the SSA Mk 7R. The author also developed a cylindrical sample device (CSSA Mk1) similar to the NGI-type device for comparisons of the two apparatuses. Refer to Budhu (1979) for the design specifications and review of the actual device. Both devices impart different stress and strain conditions on the sample. Fig. 2.38 shows the distribution of normal stress across the sample boundaries for the two devices.

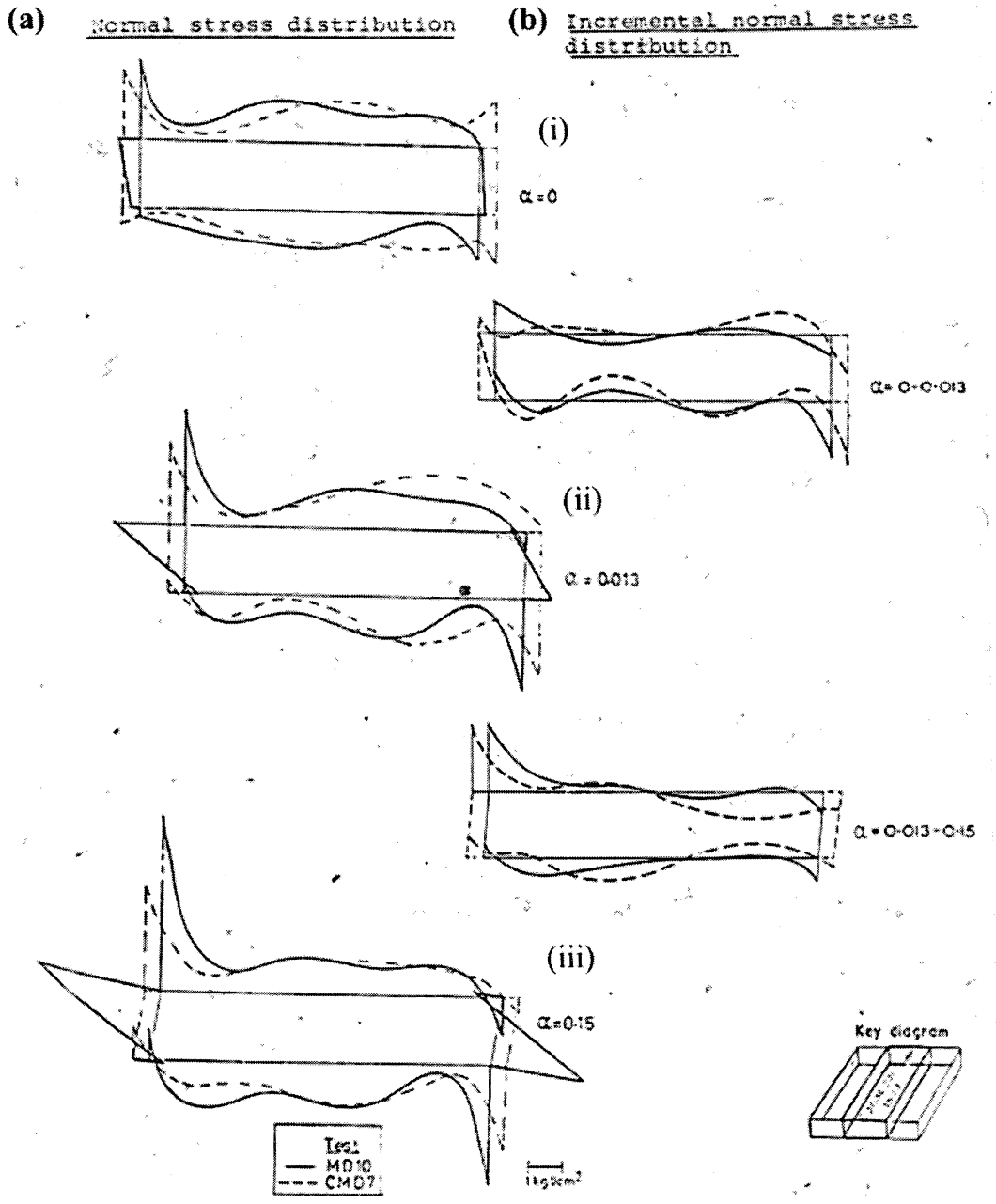

Fig. 2.38. Comparison of boundary normal stress measurements for simple shear tests on Leighton Buzzard sand (Budhu, 1979)

It is clear from the diagrams that the stresses across the bottom cap agree more closely than those across the top cap. While there are differences at the sample edges, both devices tend to subject the sample to similar normal stresses at the sample core (iii). Plots of normal stress and shear stress versus strain were generated for dense tests of the various sample types (Fig. 2.39).

Test designations starting with C represent the cylindrical sample, M represents monotonic tests in the Cambridge device, and STR-D13 is a test from Stroud (1971). Both CMD8 and STR-D13 were carried out under similar conditions with a vertical effective stress of 171.62 kPa (1.75 kgf/cm^2). Similarly, CMD7 and MD10 were conducted under the same vertical effective stress of 98 kPa (1 kgf/cm^2). For both paired cases, the normal and shear stresses on the bottom boundary tend to be higher for tests conducted in the Cambridge device. On the top boundary, however, the opposite was true for both cases until a shear strain value of approximately 15%, at which point the MD10 developed higher stresses than CMD7. Fig. 2.40 displays the respective test results in terms of stress ratio.

It is clear from the plot that STR-D13 is initially more stiff than the cylindrical sample. Tests CMD7 and MD10 are very similar in response. The only real difference is in the bottom cap measurements for CMD7 at low shear strain ranges. This difference is also the greatest in the other pair of tests. The peak values for each pair of tests are comparable; however, the samples tested in the Cambridge device tend to reach the peak value at lower strains when compared to the cylindrical device. In a comparison of stresses within various regions throughout the sample, Budhu showed that the central third of the sample closely resembles the measurements in the sample core for the Cambridge device (Fig. 2.41). Also, sample core measurements for the two device types are comparable. The sample core in both devices is not affected by any boundary or geometrical differences and most closely represents the true simple

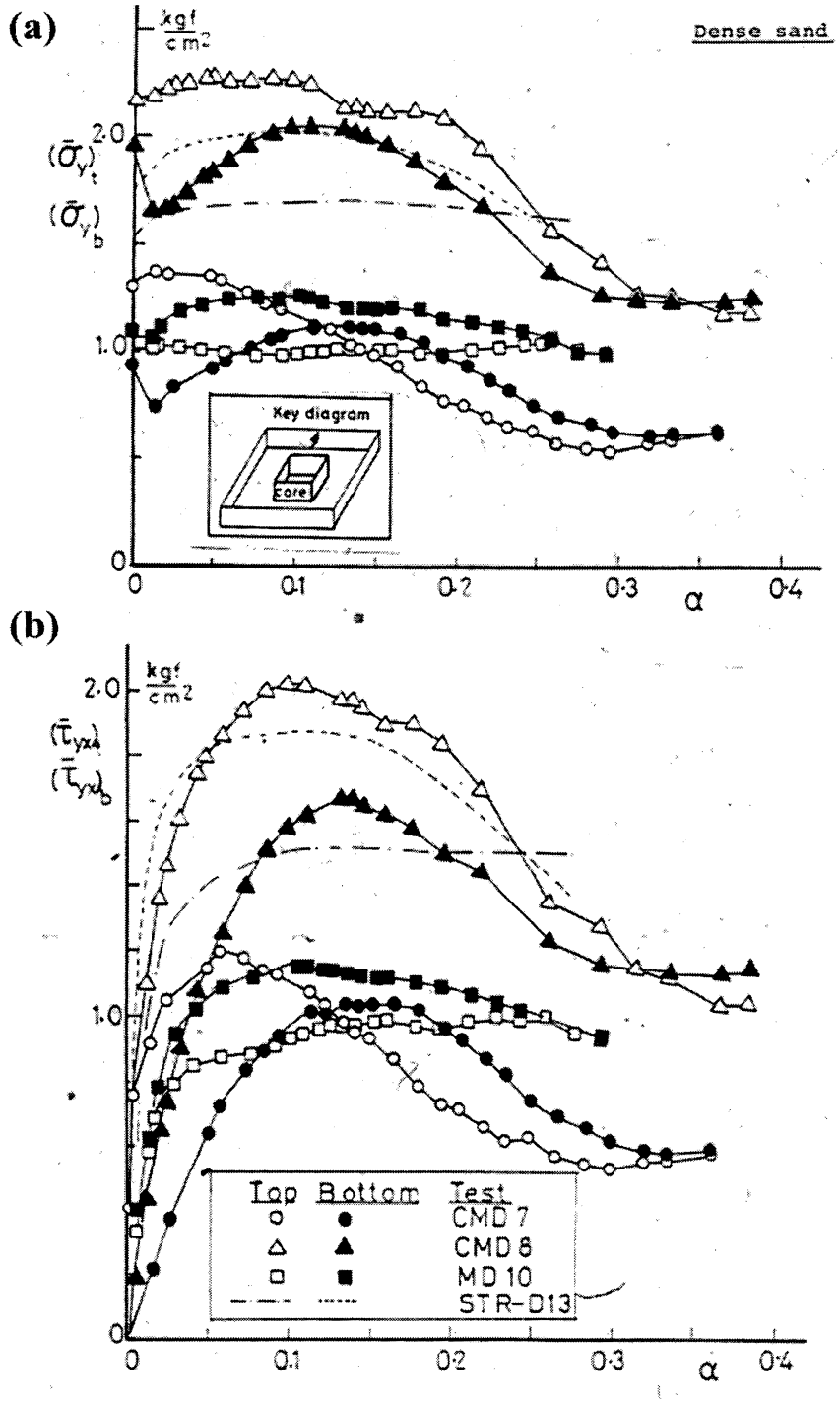

Fig. 2.39. Comparison of vertical and shear stress measurements on the top and bottom boundaries of the sample core (Budhu, 1979)

shear conditions in terms of stress and strain. One issue that should be addressed is the fact that the average stress ratio measured on the boundary (principal third) is likely at least 12% less than the value measured in the sample core, meaning the strength of a sample is generally underestimated when boundary measurements are used.

Both Stroud and Budhu agree that tests on loose sand are much more difficult than the dense cases. Sands tend to have a sensitive structure when they are in a loose state and it is very difficult to create samples under uniform stresses and strains. It is also very difficult to measure these values in a consistent and reliable

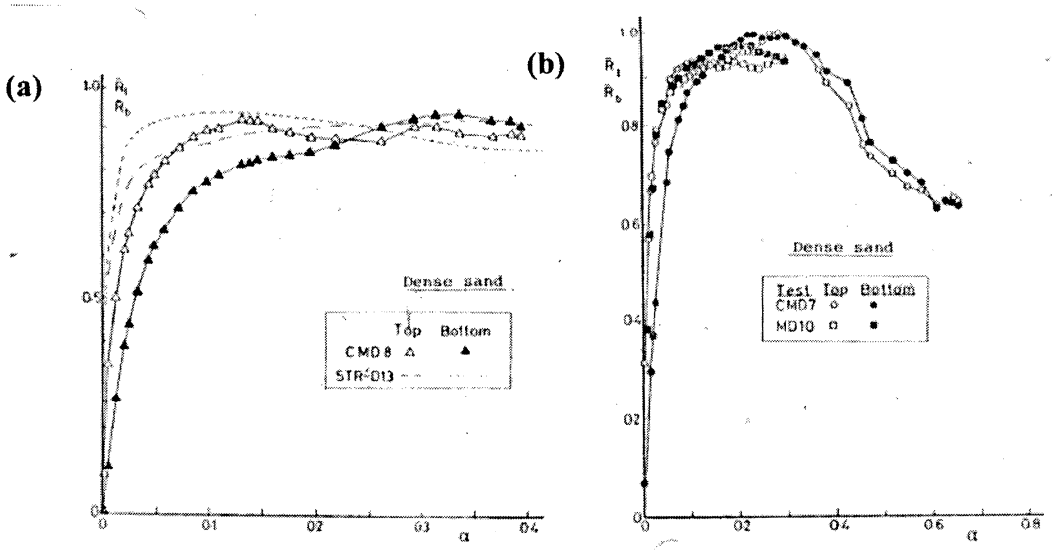

Fig. 2.40. Comparison of stress ratio measurements on the top and bottom boundaries of the sample core (Budhu, 1979)

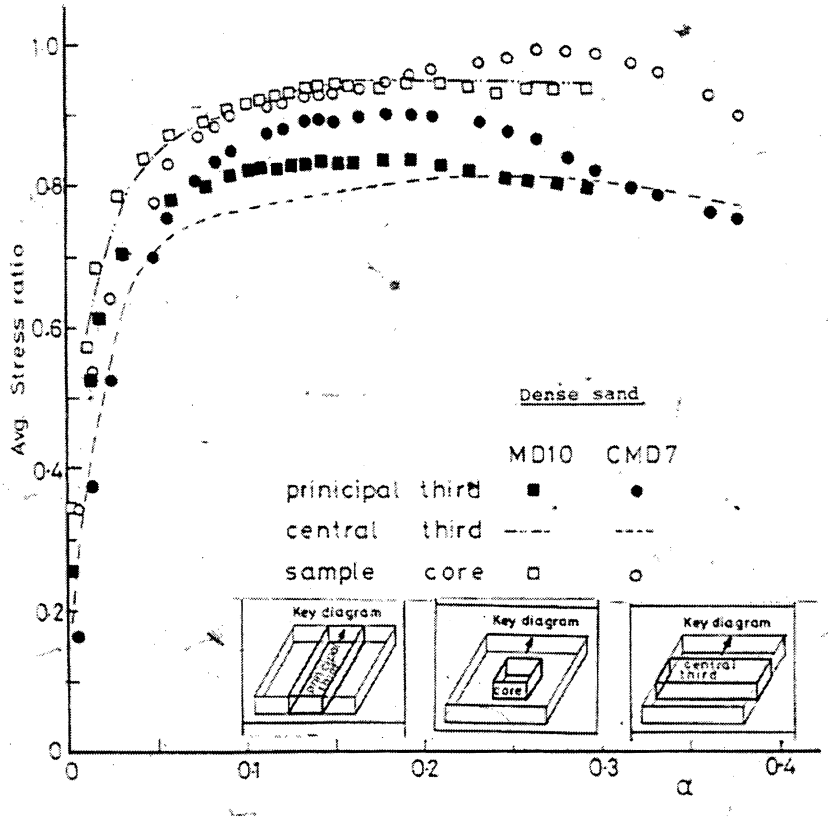

Fig. 2.41. Comparison of stress ratio measurements for various regions within the sample, dense tests (Budhu, 1979)

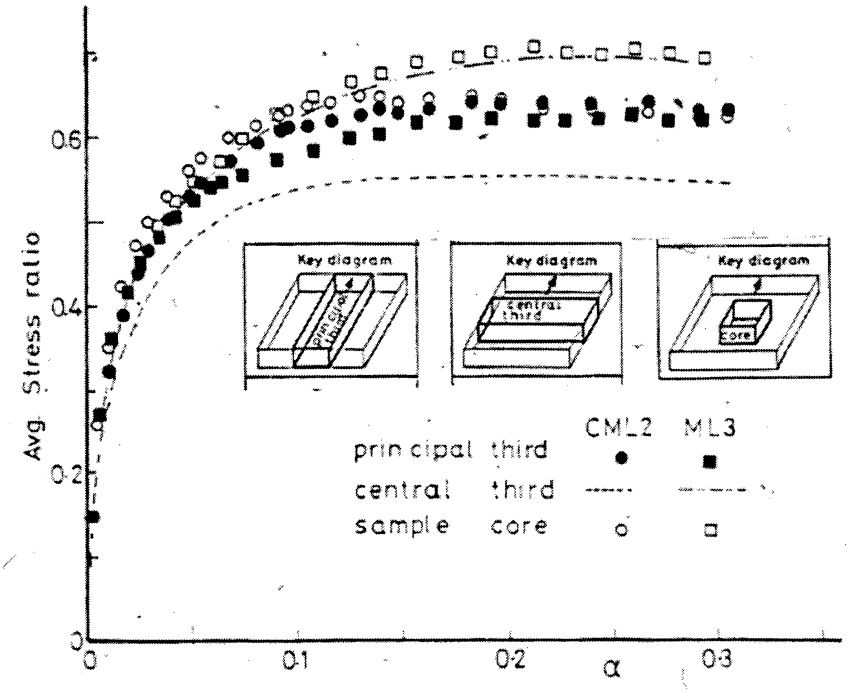

Fig. 2.42. Comparison of stress ratio measurements for various regions within the sample, loose tests (Budhu, 1979)

way during shearing and the results tend to be more scattered than for the dense tests. It is difficult to develop definite conclusions that hold for every loose case presented. What does seem to be true, however, is that the sample core is likely a good indicator of shear stress-strain behavior for both devices up to approximately 15% shear strain (Fig. 2.42).

In considering the strain measurements observed by Stroud, Budhu (1979) discusses the fact that the rupture zone is approximately horizontal through the middle of the sample, following the idea that rupture layers occur along the lines of zero extension and confirming rotating wall studies by Roscoe (1970) and James and Bransby (1970). Other researchers, however, have observed differently. Rowe and

Peaker (1965), de Josselin de Jong (1968), and Vesic (1973) showed the rupture planes to be oriented at an angle of $(\pi/4-\theta/2)$ degrees from the major principal stress, while Arthur et al. (1977a) showed the rupture planes oriented at $(\pi/4-1/4(\nu+\theta))$ degrees, where ν is the angle of dilation. Budhu (1979) found that for tests on fine Delft sand ($d_50 = 200\mu$m), the initial rupture zone was at an angle of about 11.5° inclined from the horizontal. The zone was approximately 10% of the sample height and continued to grow as shearing progressed. Two other zones also developed within the sample. Bassett (1967) observed the similar development of multiple rupture zones for 4 cm high samples tested in the Cambridge device. In fact, the choice of the standard height of 2 cm for all subsequent versions of the Cambridge device was specifically chosen to limit the formation of only one rupture zone within the sample. It is apparent from these two observations that particle size plays a role in how rupture planes develop in the sample.

Through similar X-ray imaging of dense cylindrical NGI-type samples, Budhu determined that the cylindrical samples develop rupture surfaces extending from the top left corner diagonally to the bottom right corner. Both of these regions correspond with locations where the normal stresses are higher from the non-uniform boundary conditions and suggests the possibility that the apparatus influences the development of the rupture zones within the sample. It should be noted that lateral strains were not properly controlled in these tests and some distortion was observed. Even when lateral distortion was essentially eliminated, differences in strain development were observed for the two different sample configurations. Based on the boundary measurements from an additional cylindrical test, the orientation of the rupture surface with respect to the major principal stress was found to be essentially the average of the methods proposed by Assadi (1975) and Arthur et al. (1977a). If the internal measurements of strain are taken, however, the value proposed by

Arthur et al. is a better prediction. It should be noted that these statements are made under the assumption that the principal axes and the principal strain increments are coincident, which is not necessarily true for granular soils at all strain ranges. Budhu goes on to comment further that the SSA Mk 7 actually has stiffer boundary conditions, causing the ruptures to most likely occur in the zero-extension direction as originally determined by Roscoe (1970) and James and Bransby (1970).

Additional conclusions from Budhu (1979) for simple shear tests on dense Leighton Buzzard sand include, but are not limited to the following:

1. Uniform strain conditions are maintained in the cylindrical NGI-type device for shear strain values less than 10%. The Cambridge device can maintain these uniform conditions up to 15% shear strain.

2. The development of rupture planes within a sample seems to be influenced by the stiffness of the device/sample boundaries, sample height to grain size ratio, boundary stresses, and the sample preparation methods.

3. For the Cambridge device, rupture zones tend to follow the direction of zero-extension; however, they are approximately at an angle of $\pi/4 - 1/4(\nu + \theta)$ from the major principal stress orientation for the NGI-type device.

4. The dilation of the cylindrical samples is highly underestimated by the boundary measurements for large strain values when compared to that of the Cambridge device measurements.

5. The constant cross-section of the cylindrical sample is not guaranteed by the wire-reinforced membranes.

Similar testing has been conducted for a number of other sand types. Drained simple shear tests on Ottawa sand by Vaid et al. (1981) agreed well with the afore-

mentioned trends for granular soils. Using a NGI-type device, Kim (2009) carried out simple shear testing on clean Nak-dong River sand. The findings are similar to those discussed above for Leighton Buzzard sand (Fig. 2.43).

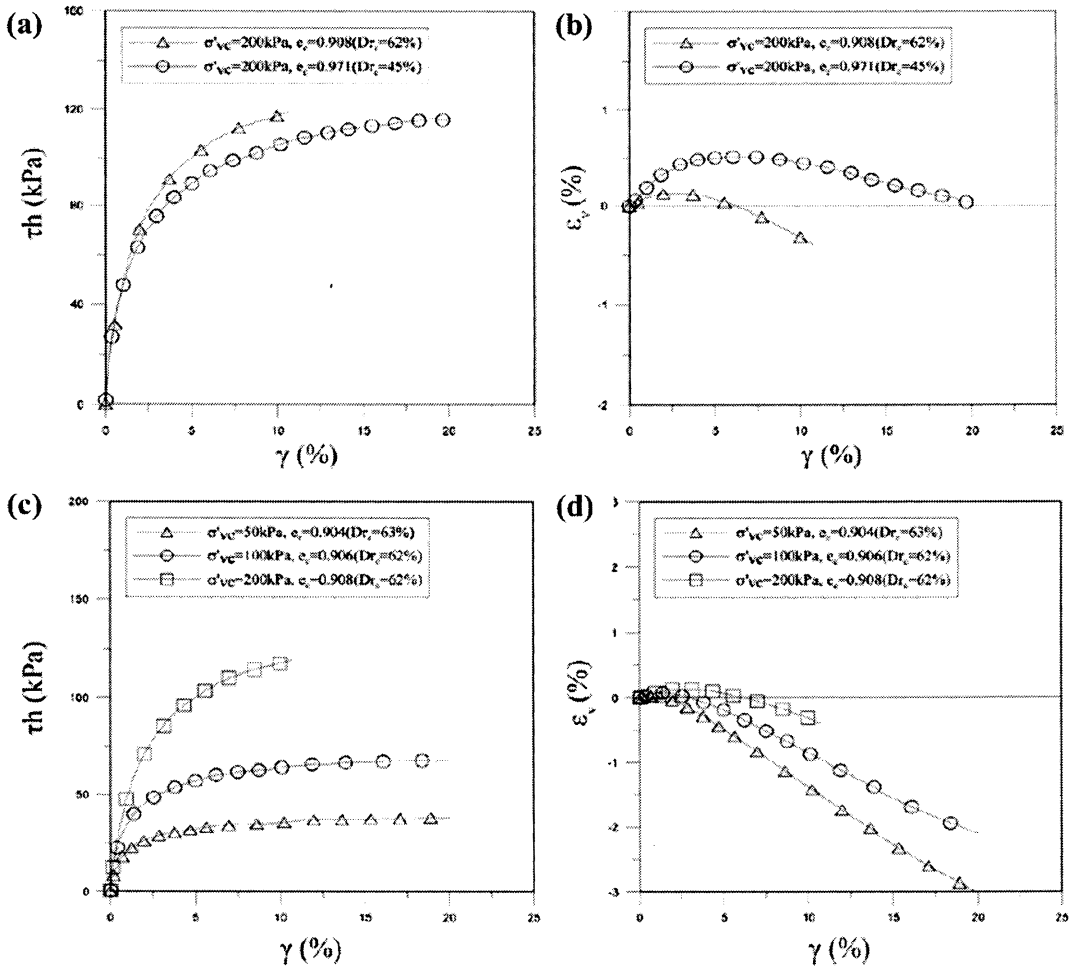

Fig. 2.43. Results for drained simple shear tests on Nak-dong River sand (Kim, 2009)

Higher shear strengths are exhibited for soils at higher initial density (a) and

for samples tested at higher confining stresses (c). Also, decreasing void ratios tend to lead to less contractive and more dilative behavior (b), while higher confining stresses tend to lead to a more contractive sample response (d). Results for undrained tests on Nak-dong River sand is given in the following section.

2.5.1.2 Undrained or constant volume testing

Although extensive testing has been conducted on sands in undrained loading, this particular research is limited to dry samples and drained testing. Only a short description is given for the undrained behavior of sands in simple shear.

Vaid and Sivathayalan (1996) conducted a study on the undrained simple shear behavior of Fraser river sand using a NGI-type apparatus. Samples prepared at various densities were tested under a common vertical effective stress of 200 kPa (Fig. 2.44a). It is clear from the figure that, similar to drained testing, higher initial densities result in higher strengths. Additionally, the presence of a phase transformation is evident for all samples except for the sample prepared at the highest initial density (lowest initial void ratio of 0.836). This phase transformation occurs at the location where the response changes from contractive to dilative, and causes the sample to, again, gain strength.Samples at higher densities gain strength faster. Samples at very low initial void ratios (high densities) are already initially dilative and begin to gain strength very early in the test (e.g. sample at e=0.836). For samples prepared at the same void ratio, peak shear stress increases with increasing vertical effective stress (Fig. 2.44b). In a discussion on data presented in Vaid and Sivathayalan, Idriss and Boulanger (2007) point out that the stress ratio at the phase transformation location appears to be independent of vertical stress and increases rather with increasing density and shear strain (Fig. 2.45). They also show that similar results were obtained for undrained testing of Toyoura sand in Yoshimine

et al. (1999) (Fig. 2.46).

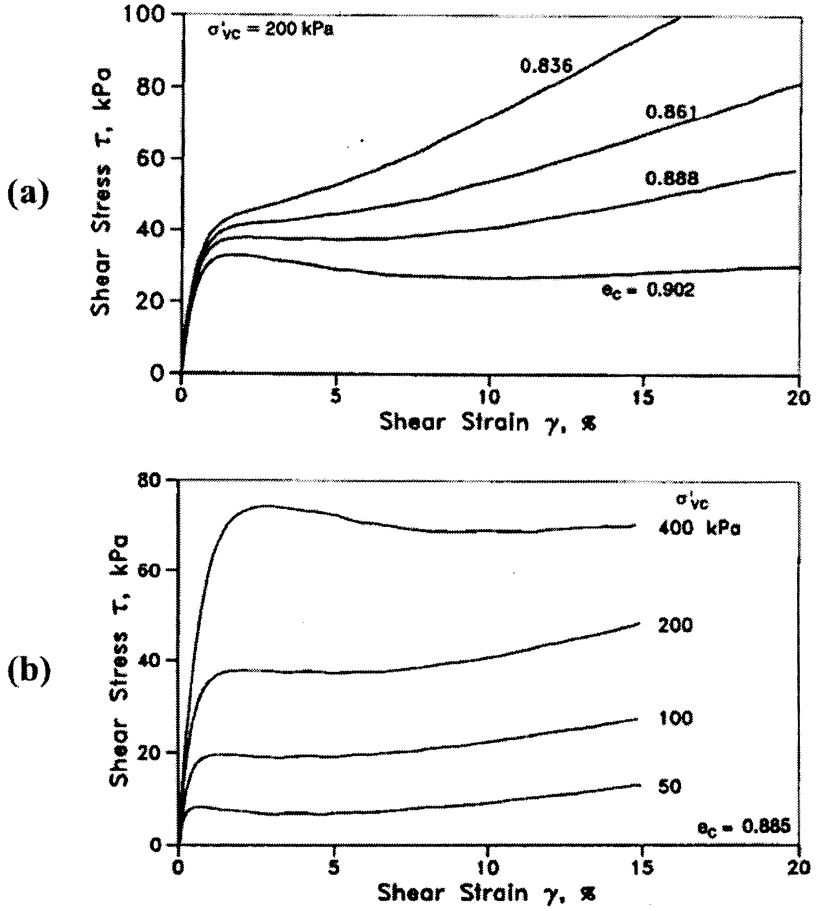

Fig. 2.44. Results for undrained simple shear tests on Fraser river sand (a) varying density (b) varying vertical effective stress (Vaid and Sivathayalan, 1996)

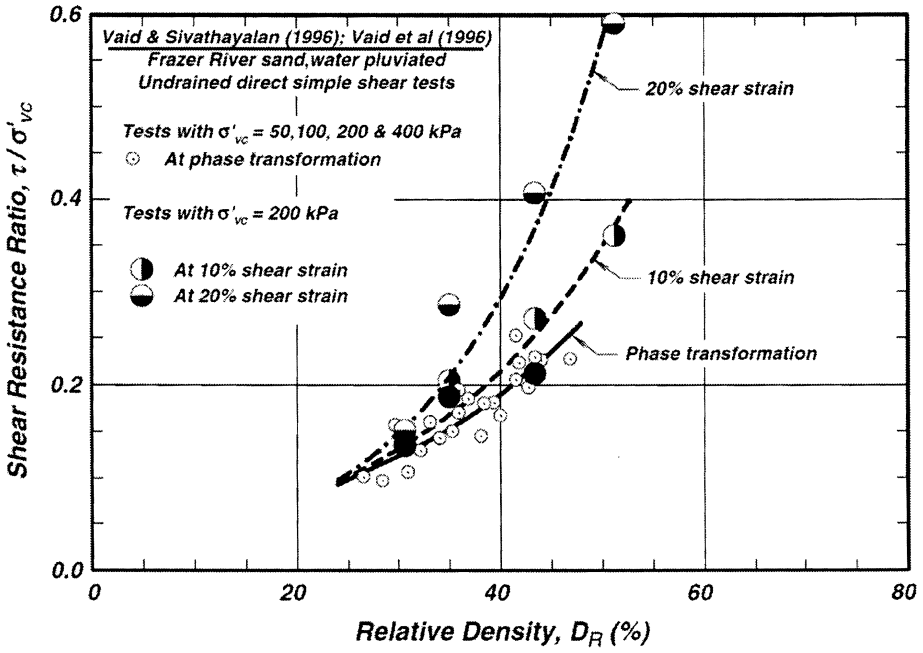

Fig. 2.45. Stress ratio versus relative density for undrained simple shear tests on Fraser river sand (Idriss and Boulanger, 2007) (after Vaid and Sivathayalan, 1996)

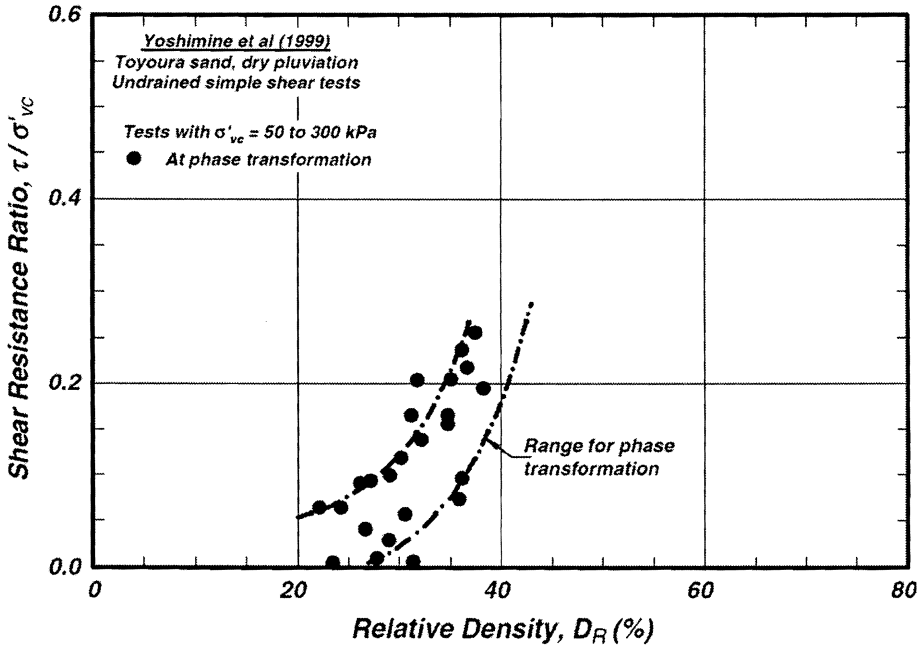

Fig. 2.46. Stress ratio versus relative density for undrained simple shear tests on Toyoura sand (Idriss and Boulanger, 2007) (after Yoshimine et al., 1999)

Undrained testing of Nak-dong River sand was conducted under various initial densities and confining stresses by Kim (2009) (Figures 2.47 and 2.48). The loose samples of Fraser river sand are contractive, showing a peak response followed by strain-softening, while all of the loose Nak-dong River samples tend to be completely dilative without really exhibiting a phase transformation zone (Fig. 2.47a). It is also clear from the plots that vertical confining stresses influence the pore pressures generated (Fig. 2.47b). Lower density samples tend to have lower strength (Fig 2.48a), but generate higher pore pressures (Fig. 2.48b). Fig. 2.49 shows that sample preparation method also affects the soil response in undrained loading.

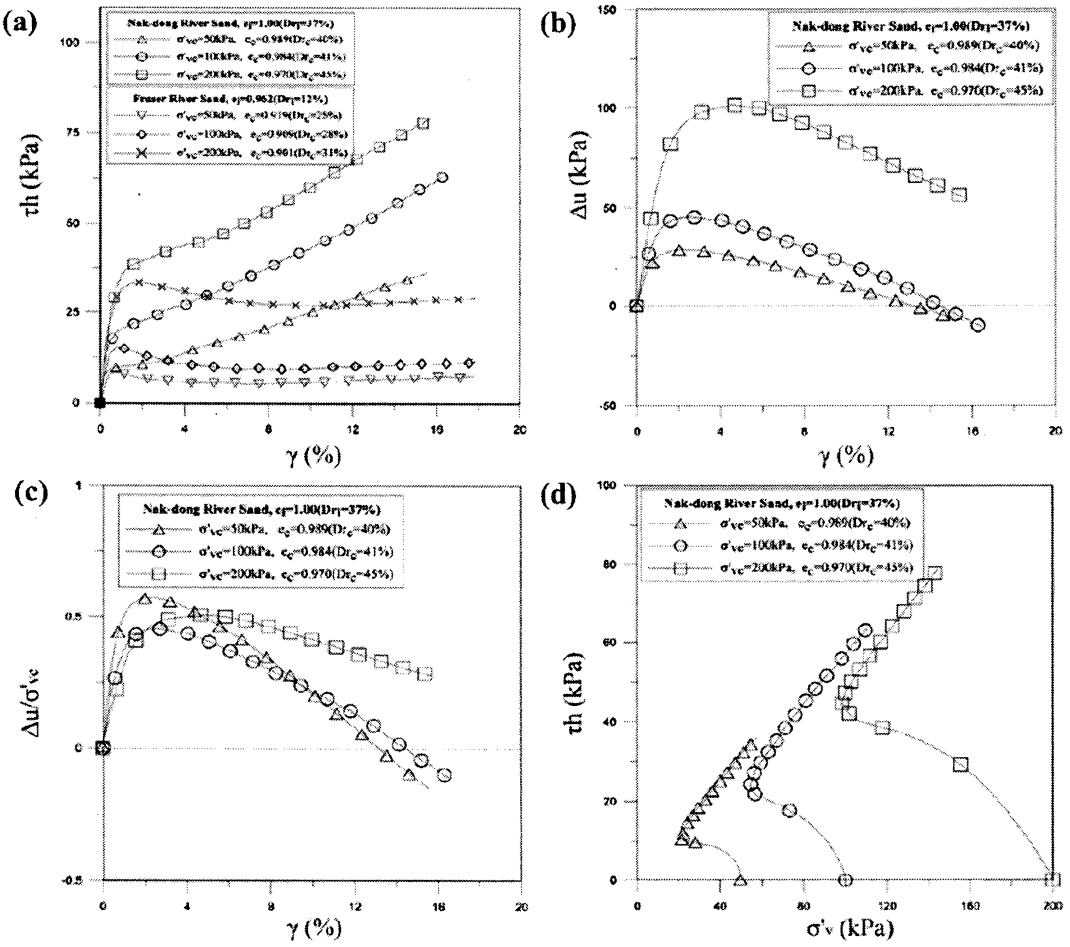

Fig. 2.47. Results for undrained simple shear tests on loose Nak-dong River sand (Kim, 2009)

Although they are at slightly different densities, it is still apparent that water pluviation creates a sample that is slightly contractive, while air pluviation generates a sample that is mostly dilative. Pore pressures are also higher in the water pluviated sample which follows the trends based on the density differences. It is also possible that water pluviation allows for the preparation of samples at lower densities, which may be on the other side of the threshold for contractive/dilative behavior. It would

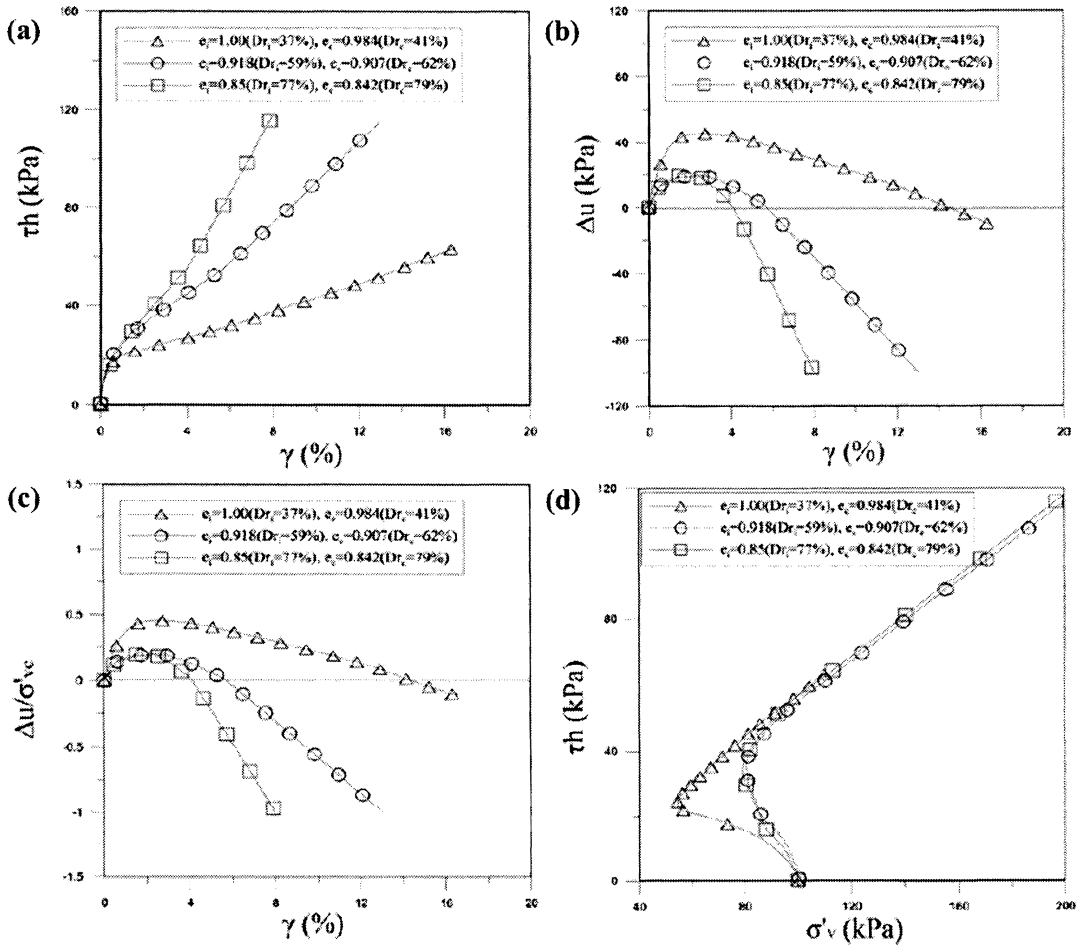

Fig. 2.48. Results for undrained simple shear tests on loose Nak-dong River sand at a vertical effective stress of 100 kPa (Kim, 2009)

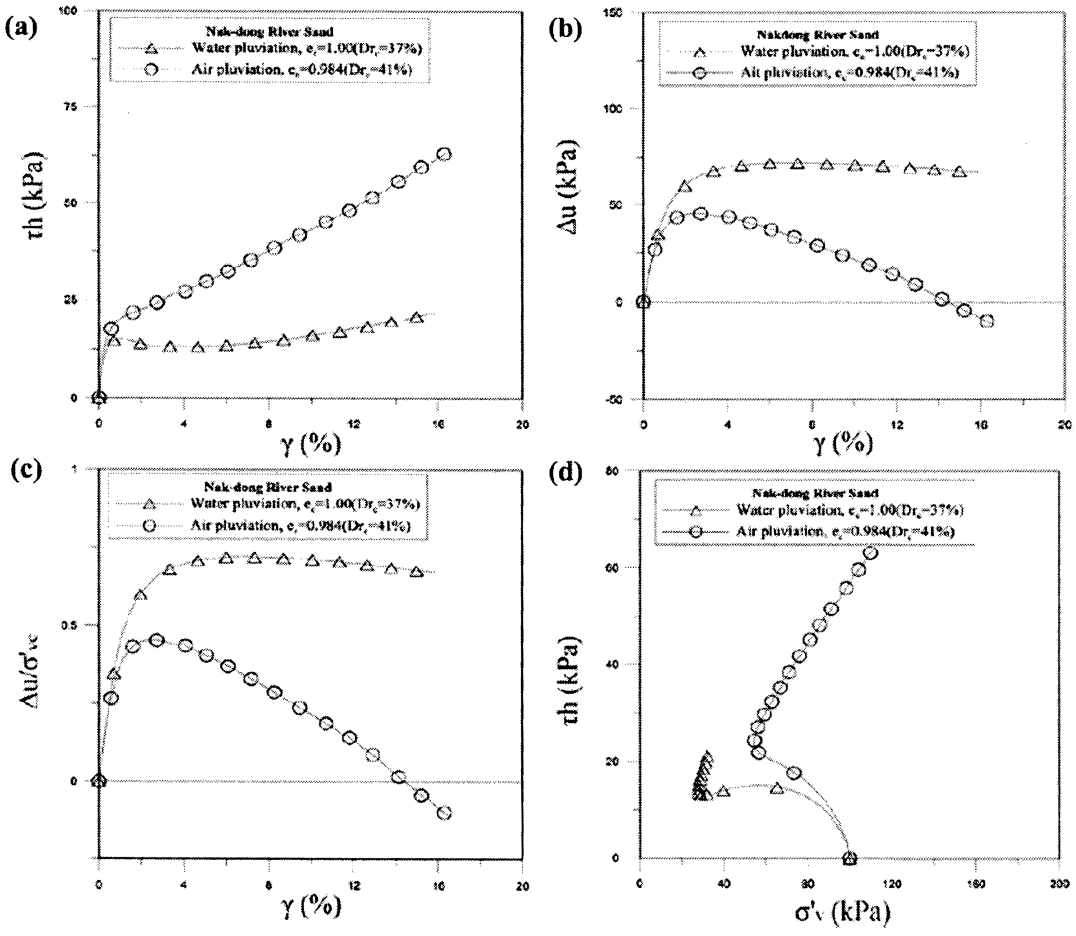

Fig. 2.49. Comparison of sample preparation techniques for undrained simple shear tests on loose Nak-dong River sand (Kim, 2009)

be much more comparable if the samples were at the exact same relative density; however, this is very difficult to do in a laboratory setting.

2.5.2 Monotonic Direct Simple Shear Testing on Glass Spheres

In an effort to reduce the strain necessary to reach critical state, Wroth (1958) conducted simple shear tests on granular materials that were more spherical in shape and uniform in size than typical sand. Although there was some crushing and breaking, the initially loose glass bead samples reached a critical state condition just before the maximum shearing capabilities of the device. The beads tested had a range of diameters between 0.75 and 0.80 mm and a specific gravity of 2.89. Fig. 2.50 shows a representative curve for the shear stress-displacement behavior under a vertical effective stress of 384.0 kPa (55.7 psi). A void ratio versus displacement curve is shown for three of the tests (Fig. 2.51).

It is clear from the plot that only two of the tests (numbers 3 and 5) were at critical state when the maximum shear displacement of the device was reached. Test number 8 was still dilating at the end of the test and would most likely approach the other two sample void ratios. No samples were produced with a void ratio higher than that of critical state because of difficulties with preparing a loose sample and the samples immediate densification with the application of the normal load. In an effort to obtain samples that would reach critical state under the displacement capabilities of the device, metal ball bearings were also tested. The results of these tests are summarized in the following section.

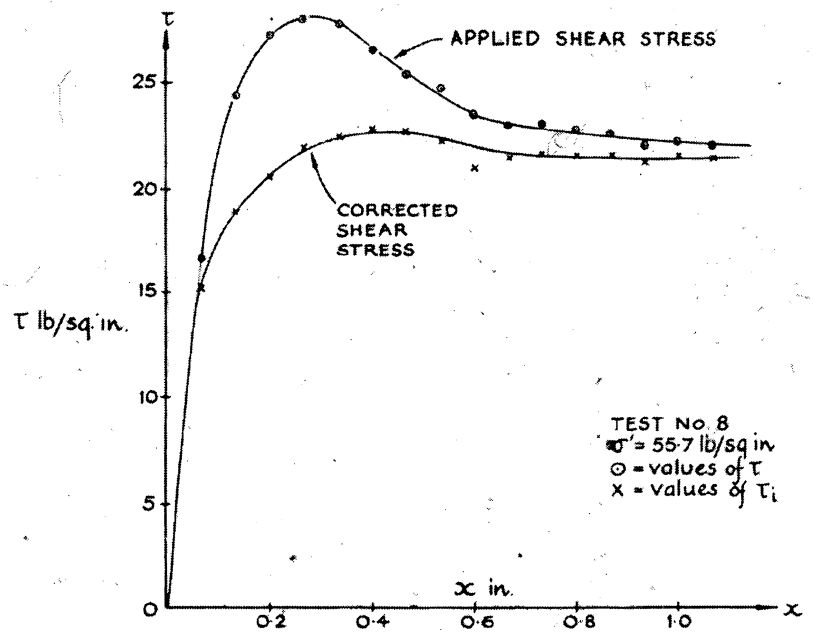

Fig. 2.50. Representative results from simple shear tests on glass beads (Wroth, 1958)

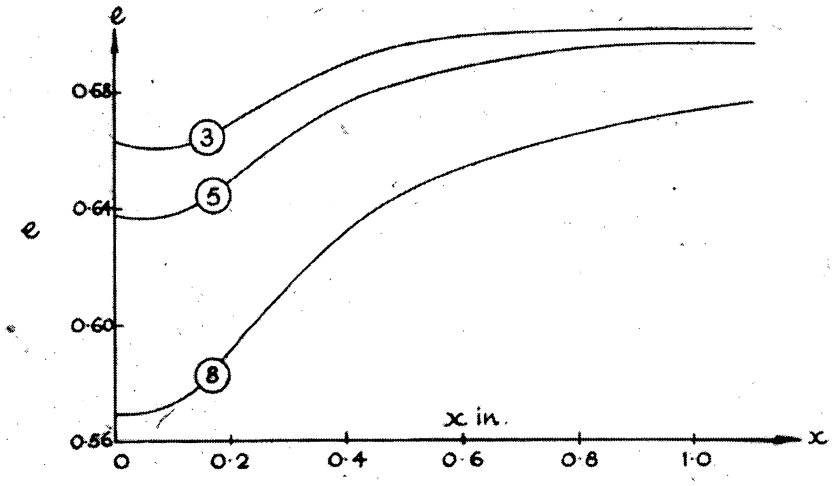

Fig. 2.51. Void ratio relationships during shearing for simple shear tests on glass beads (Wroth, 1958)

Table 2.1. Summary of results from simple shear tests on glass beads (after Wroth, 1958)

Normal Stress σ' kPa (psi)	Number of Tests	Mean Critical Voids Ratio e_u	Shear Stress τ. kPa (psi)
26.9 (3.9)	2	0.6658	11.31 (1.64)
137.9 (20.0)	9	0.6454	53.43 (7.75)
261.3 (37.9)	5	0.6368	100.7 (14.6)
384.0 (55.7)	4	0.6306	148.2 (21.5)
507.5 (73.6)	7	0.6279	198.6 (28.8)
630.9 (91.5)	3	0.6261	265.4 (38.5)

Table 2.1 summarizes the glass bead test results. Tests conducted at different vertical effective stresses ultimately reach different critical void ratios and define different final conditions on the critical void ratio line (Figs. 2.52 and 2.53).

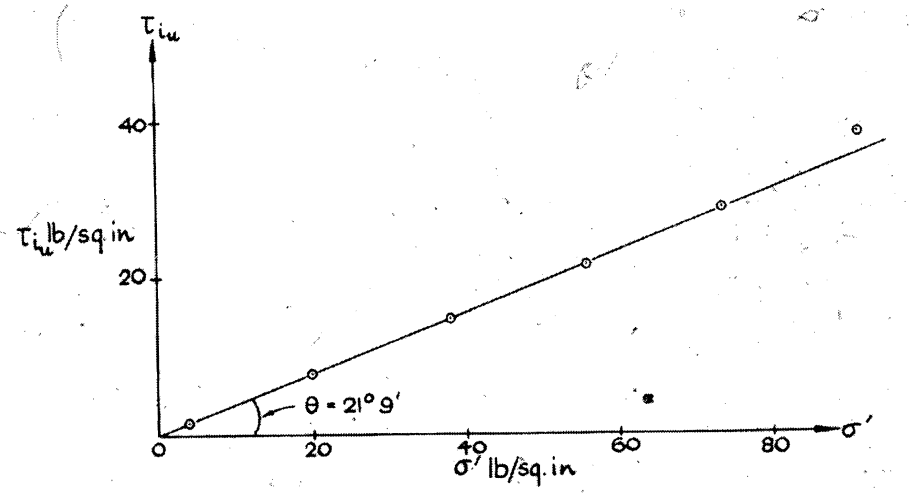

Fig. 2.52. Ultimate shear stress values for various σ'_v values, gives elevation view of critical void ratio line for glass beads (Wroth, 1958)

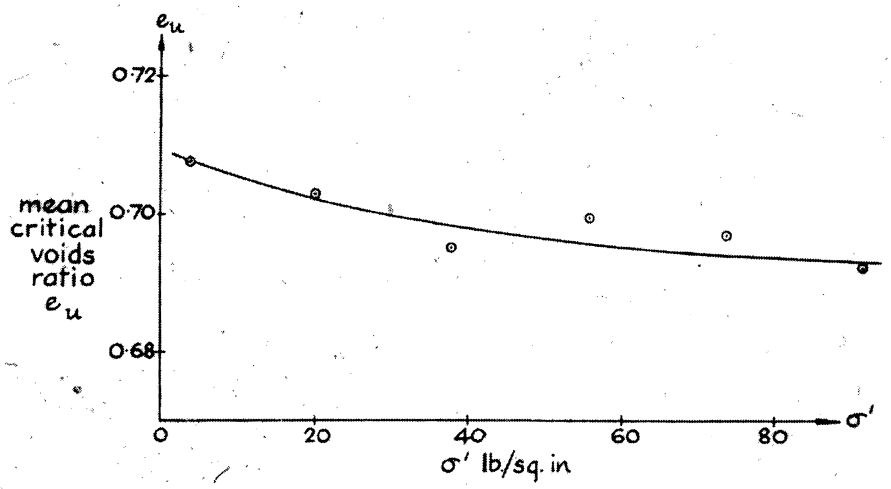

Fig. 2.53. Void ratio relationship for various σ'_v values, gives plan view of critical void ratio line for glass beads (Wroth, 1958)

These curves represent the elevation view and plan view of the critical void ratio line. The drained yield surface is then essentially a plane passing through the e-axis and inclined at an angle of θ from the horizontal. This angle was found to be 21.15° for the glass beads. The value for τ_i is defined as

$$\tau_i = \sigma' \tan_\Theta = M\sigma' \tag{2.19}$$

The mean critical void ratio appears to be only slightly influenced by the vertical stress value. It should also be noted that the scatter about the critical void ratio line was less for the glass beads than for the sand; however, the scatter was greater than that of the steel balls. The overall behavior of the glass beads looks similar to the sand samples with the exception of the increased amount of shearing required to reach critical state.

If instead the peak applied shear stress is considered, $\tau_f = \tau_i + \tau_{e_f}$, an elevation

view of the Hvorslev surface can be plotted for the glass beads. While the void ratio curves do not follow the sinusoidal trend seen in the metal sphere results, the general pattern and similar predictions for the shape of the Hvorslev surfaces still holds. Fig. 2.54 shows τ_f plotted versus e_f where each straight line represents the section of the Hvorslev surface for a given σ'. Although the scatter is slightly higher for the glass bead data, both the glass beads and the steel spheres behave similarly in simple shear.

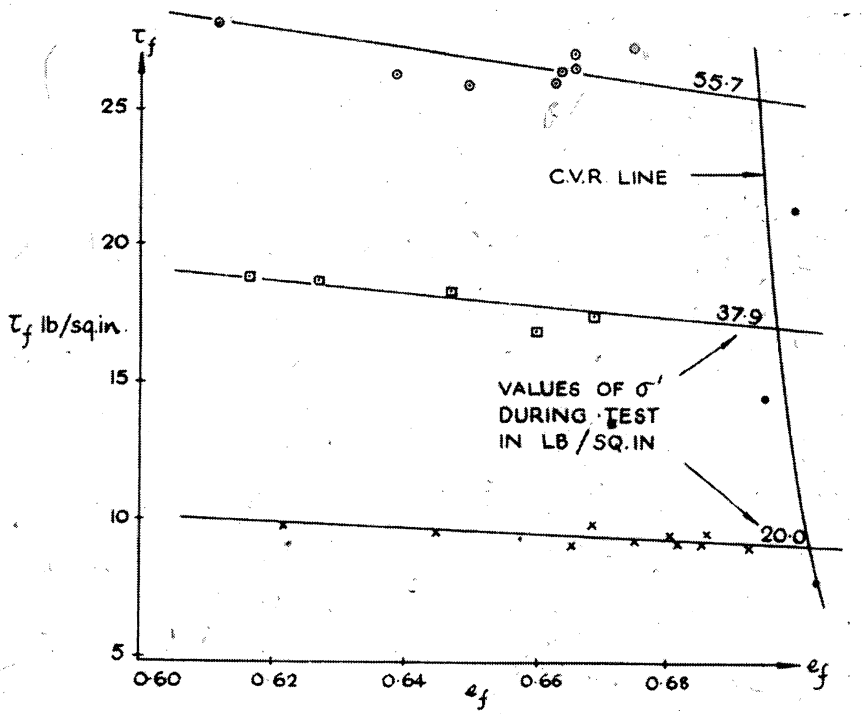

Fig. 2.54. Hvorslev surface for glass beads (Wroth, 1958)

Recently, researchers at the University of British Columbia have conducted dry/drained simple shear tests on glass beads to be used as validation data for numerical DEM models (Dabeet et al., 2011). Several different vertical stress values

Table 2.2. Summary of test parameters for simple shear tests on glass beads (after Dabeet et al., 2011)

Lab test ID	e_c	σ'_{zz} (kPa)
GLS-2mm-100-D-M	0.6	100.7
GLS-2mm-100-D-M-R	0.606	100.6
GLS-2mm-150-D-M	0.598	151
GLS-2mm-200-D-M	0.593	200.4

were tested for the 2 mm diameter glass bead samples. The samples were created at similar densities by air-pluviation and tested in a NGI-type device. Table 2.2 summarizes the test parameters and Figs. 2.55 and 2.56 show the results.

The two samples tested under similar void ratio show good agreement and verify repeatability of the sample preparation and testing methods. The relationship for the samples tested under different vertical stresses (a) is as expected (i.e. higher vertical stresses result in higher overall shear stresses). The authors state that the three stress ratio curves plot essentially on top of one another, which is what is typically observed in Fraser river sand tests. According to the trends shown by Roscoe et al. (1958), Stroud (1971), and Budhu (1979), the peak shear stress tends to increase for increasing vertical stress and the peak stress ratio tends to decrease (e.g. Fig. 2.57).

This trend does seem to be present in the glass bead data, although it is less pronounced than in some of the previously discussed cases on sand. It should be pointed out that these tests were only carried out to 5% shear strain. At this strain, the strength is continuing to increase and it is very difficult to determine if this trend would continue and hold true for the peak value. The difference in vertical stresses is actually quite small and for most previous results, the initial low strain responses are similar. This may play some factor in why the data is overlaid on each other.

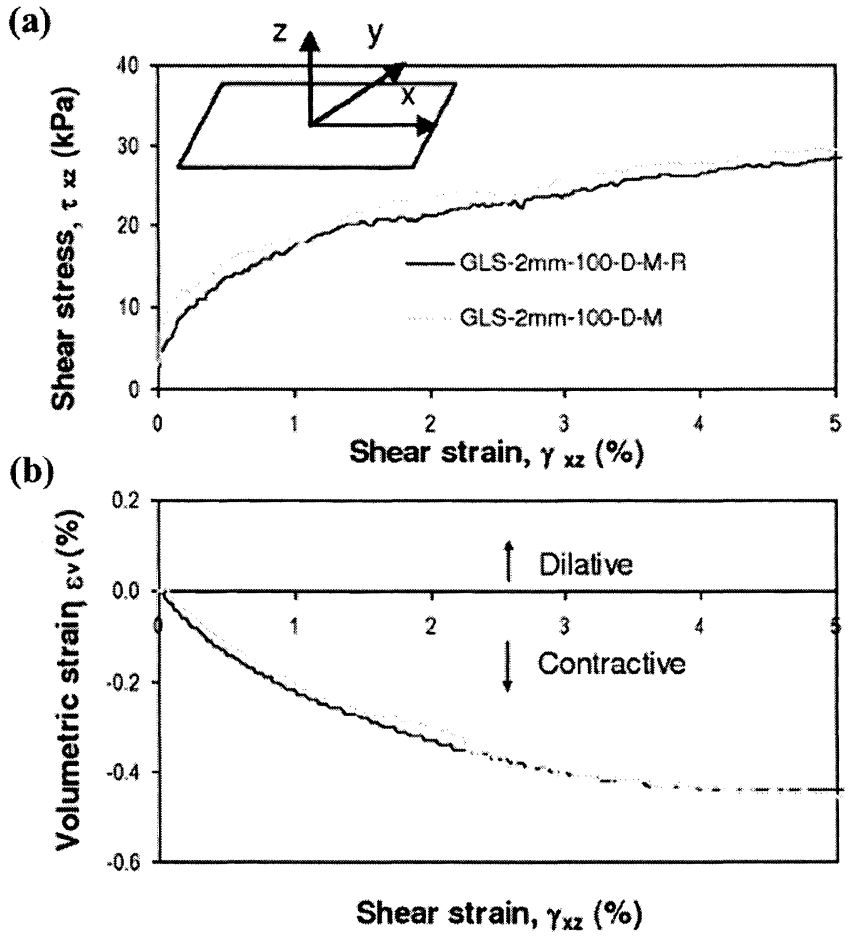

Fig. 2.55. Results of monotonic simple shear testing on glass beads to show repeatability (Dabeet et al., 2011)

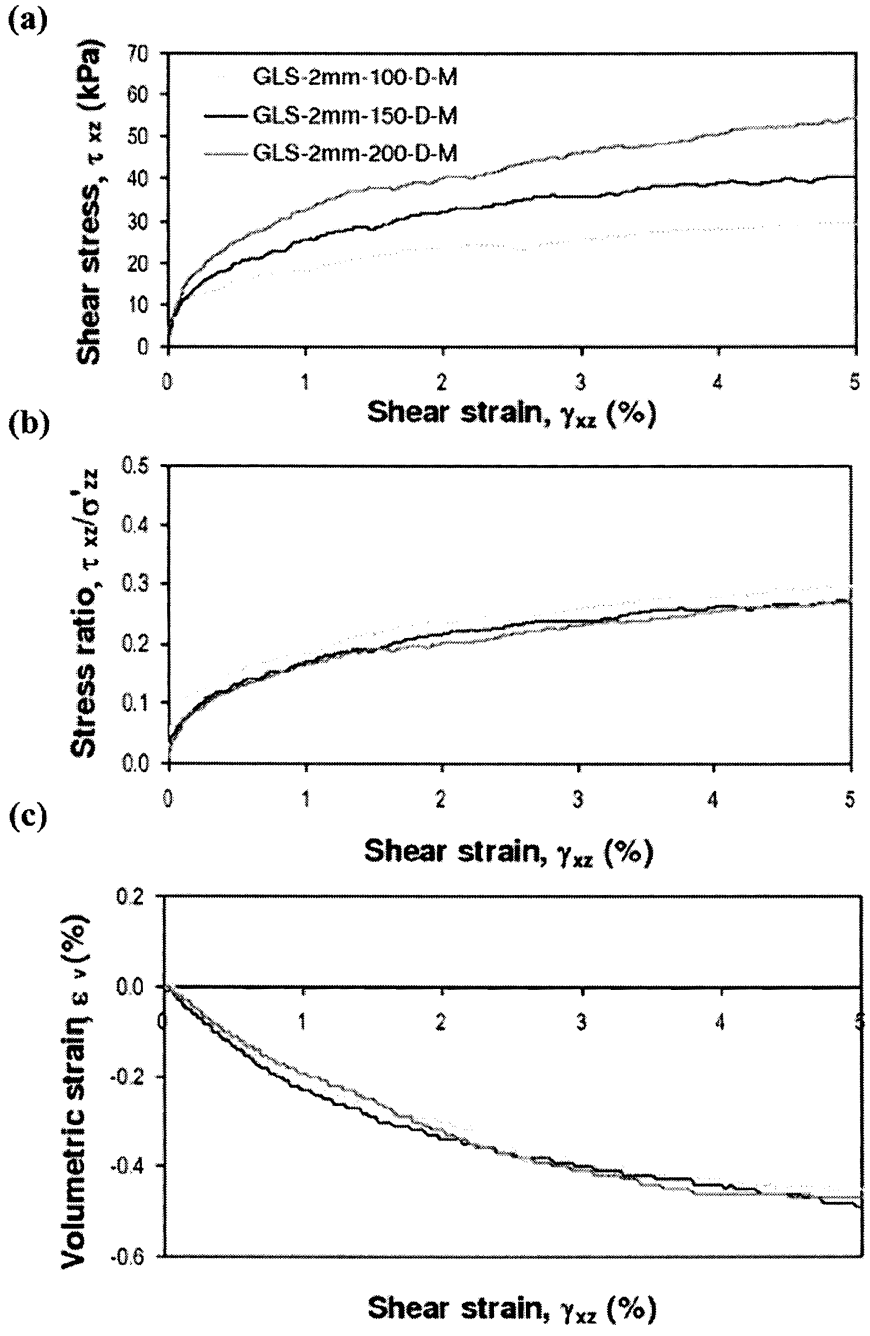

Fig. 2.56. Results of monotonic simple shear testing on glass beads at different vertical stresses (Dabeet et al., 2011)

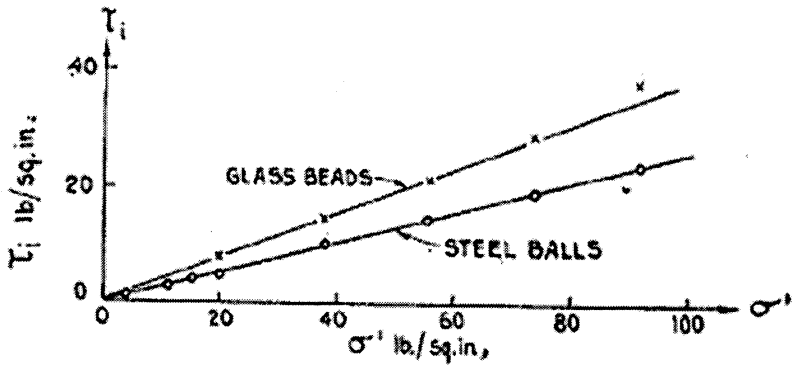

Fig. 2.57. Trend of peak shear stress with varying vertical stress (Roscoe et al., 1958)

In terms of volumetric strain, the response is contractive and very similar for the various confining stresses. Typically, one would expect the contractiveness of a soil to decrease with decreasing confining stress. This is not the case for the glass bead tests presented. The authors comment that an increased density caused by the higher stress levels may offset this trend and that similar observations have been made for Fraser River sand tests by Wijewickreme et al. (2005). Essentially, within the range of vertical stresses tested, it appears that volumetric strain is insensitive to confining stress for tests on glass beads. It should be noted that these tests were only conducted to 5% shear strain and it is difficult to judge what may occur at higher strain levels. The use of this data to validate DEM models is discussed below.

2.5.3 Monotonic Direct Simple Shear Testing on Metal Spheres

As a result of successful tests on glass beads, Wroth (1958) also tested steel balls with a nominal diameter of 1 mm and an allowed ball diameter variation of 0.015 mm. An additional discussion of this testing can also be found in Roscoe et al. (1958).

These particles reached critical state conditions at much lower strain values, allowing for a study of the critical void ratio to be carried out for the material. Drained tests were conducted under a number of different conditions. A representative stress-displacement curve is shown in Fig. 2.58a for a sample initially at the densest possible state and under a vertical effective stress of 137.9 kPa (20 psi).

As shown in the void ratio versus displacement curve in Fig. 2.58b, the sample dilates until a displacement of 0.6 in (80% shear strain), at which point it reaches critical state and no further volume change is observed. Wroth also showed that the shape of the curve in the early stages of the test is very close to sinusoidal. This condition was observed in all tests where the sample began at a void ratio below the critical void ratio. Fig. 2.59 shows the results for five of the nine tests performed on steel balls at various initial void ratios and with a constant vertical effective stress of 137.9 kPa (20 psi).

The samples all reach critical void ratio values that lie within a vary narrow range with a total scatter of less than 0.006. Plots of void ratio versus shear stress show that samples with different initial void ratios will all end at essentially the same point on the critical void ratio line when sheared under the same applied vertical stress (Fig. 2.60).

For tests conducted a different vertical effective stresses, the samples will again follow a similar trend ultimately reaching a different final condition on the critical void ratio line. Table 2.3 summarizes the test results.

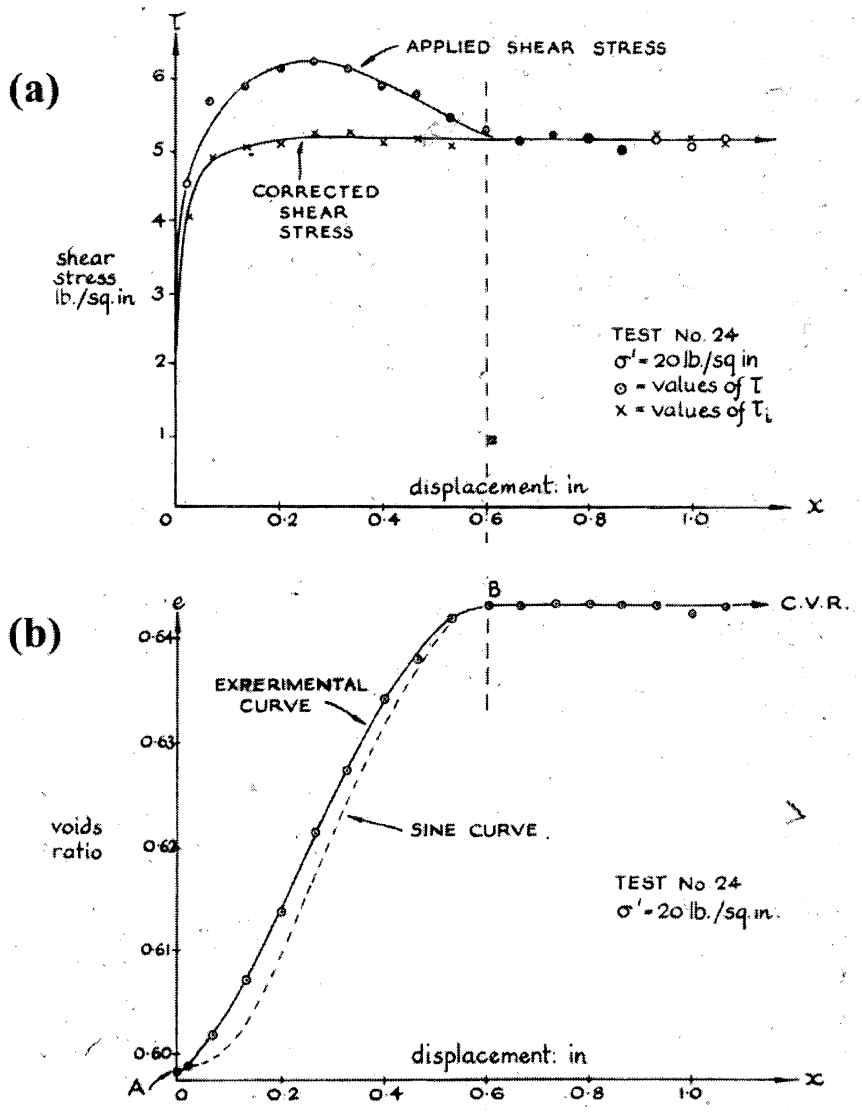

Fig. 2.58. Representative results from simple shear tests on steel balls (after Wroth, 1958)

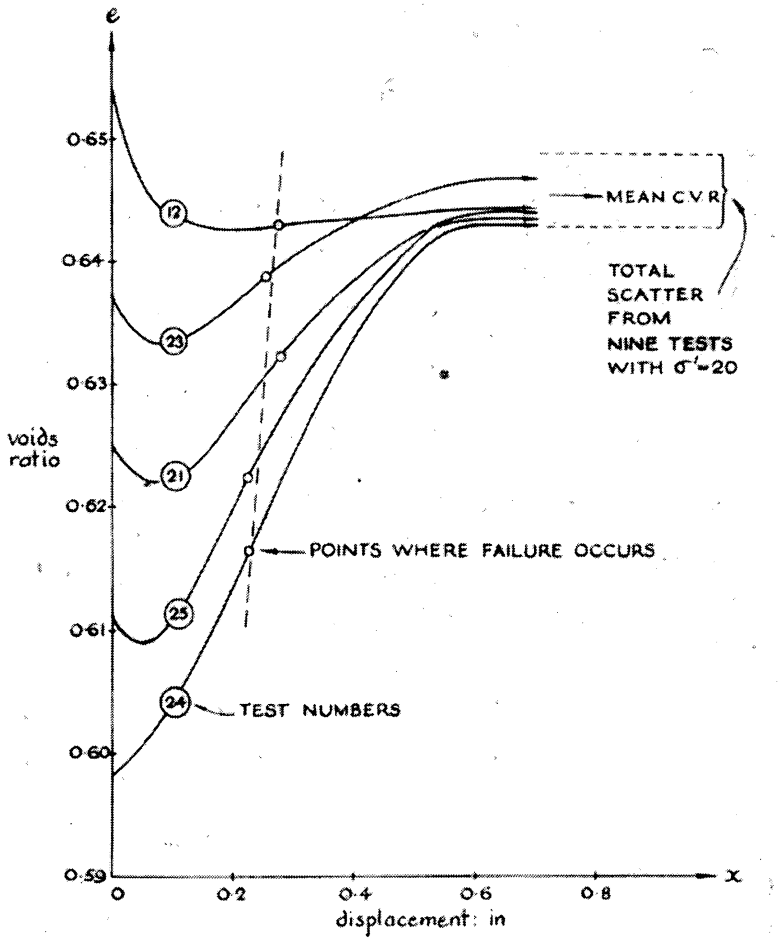

Fig. 2.59. Void ratio relationships during shearing for simple shear tests on steel balls (Wroth, 1958)

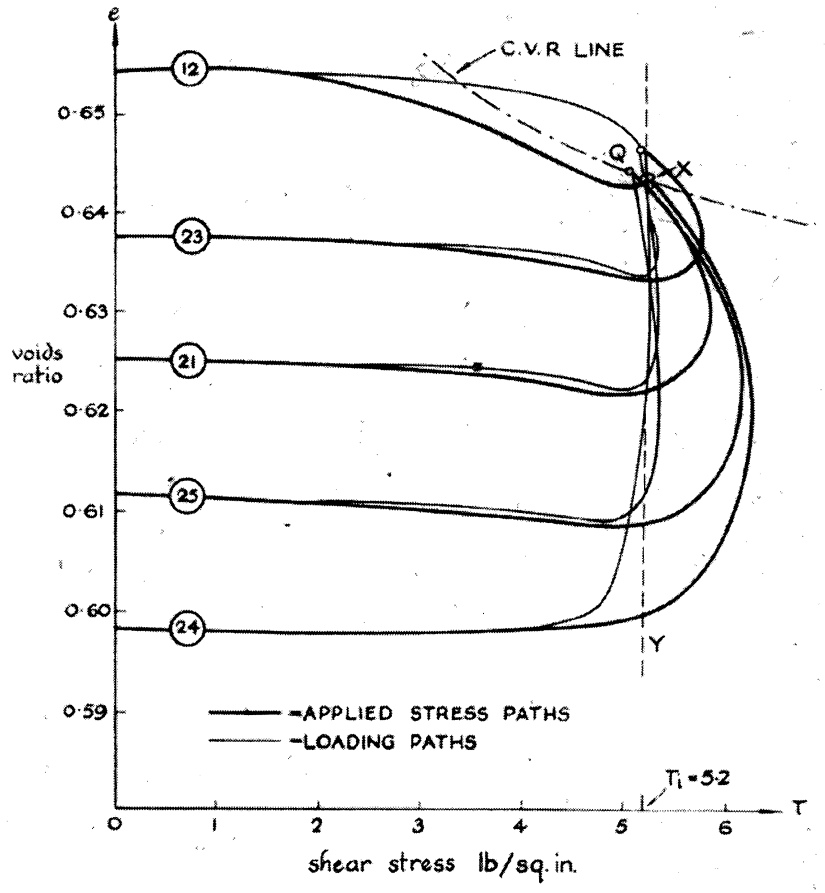

Fig. 2.60. Applied test paths for simple shear tests on steel balls (Wroth, 1958)

Table 2.3. Summary of results from simple shear tests on steel balls (after Wroth, 1958)

Normal Stress σ' kPa (psi)	Number of Tests	Mean Critical Voids Ratio e_u	Mean Ultimate Shear Stress τ kPa (psi)
26.9 (3.9)	2	0.6658	8.76 (1.27)
76.5 (11.1)	2	0.6544	21.72 (3.15)
107.6 (15.6)	1	0.6473	27.99 (4.06)
137.9 (20.0)	9	0.6454	35.71 (5.18)
261.3 (37.9)	5	0.6368	67.57 (9.80)
384.0 (55.7)	4	0.6306	99.3 (14.4)
507.5 (73.6)	7	0.6279	129.6 (18.8)
630.9 (91.5)	3	0.6261	164.8 (23.9)

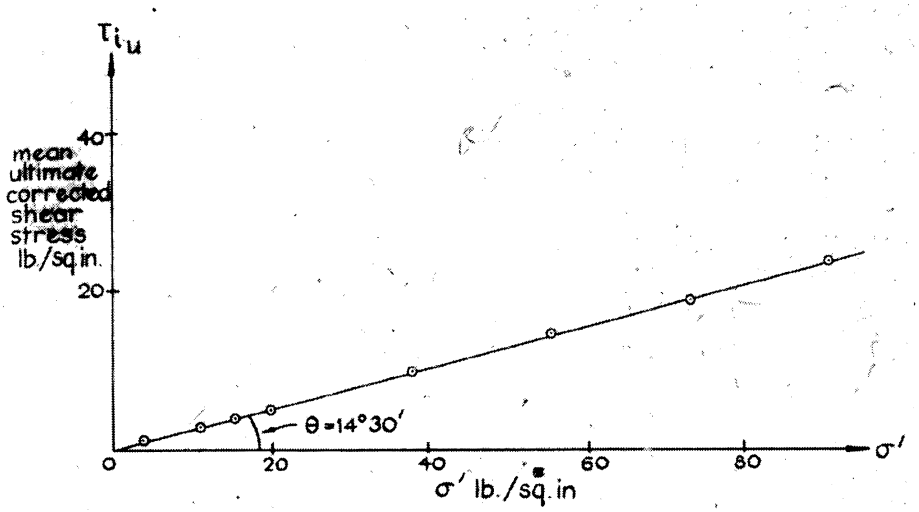

Fig. 2.61. Ultimate shear stress values for various σ'_v values, gives elevation view of critical void ratio line for steel balls (Wroth, 1958)

Similar to the glass bead data analysis, Wroth also developed a plot of the drained yield surface and critical void ratio line for the steel balls (Figs. 2.61 and 2.62). The scatter in void ratio across the critical void ratio line was less for the steel balls than for the glass beads. The inclination angle of the yield surface, θ, was

found to be 14.5° which is much lower than the value found for glass beads. Figs. 2.63, 2.64, and 2.65 show the various projections of the yield surface.

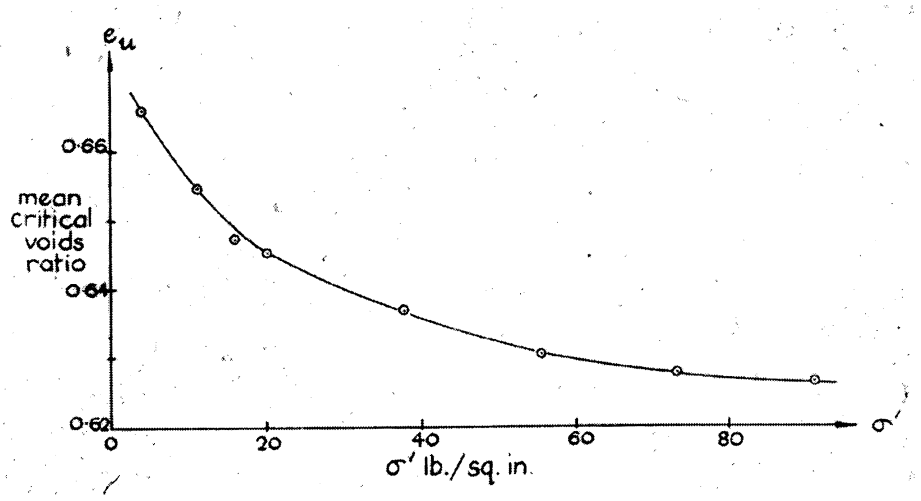

Fig. 2.62. Void ratio relationship for various σ'_v values, gives plan view of critical void ratio line for steel balls (Wroth, 1958)

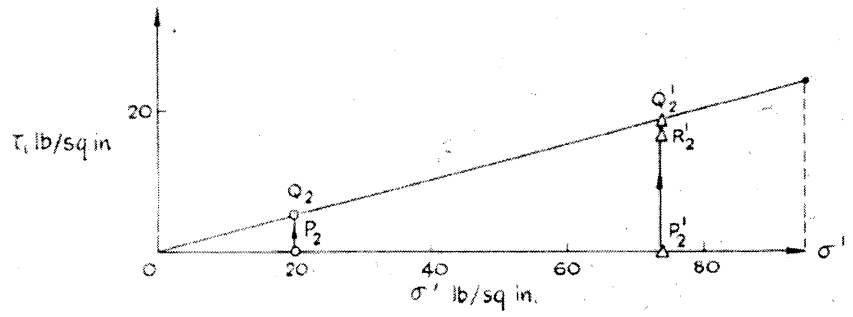

Fig. 2.63. Projection of drained yield surface for steel balls, τ versus σ'_v (Wroth, 1958)

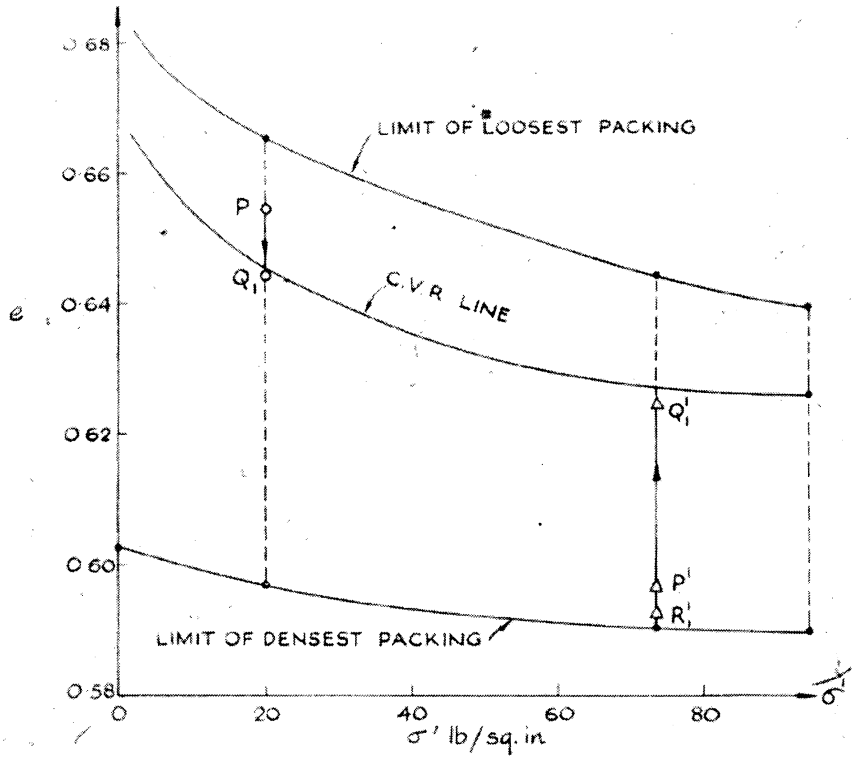

Fig. 2.64. Projection of drained yield surface for steel balls, e versus σ'_v (Wroth, 1958)

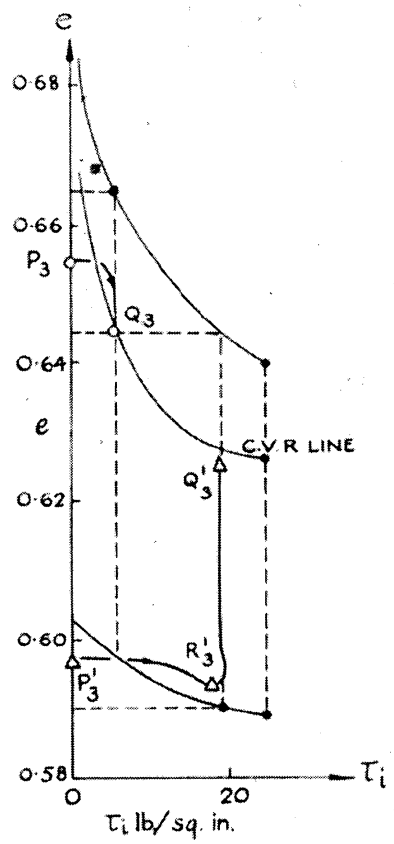

Fig. 2.65. Projection of drained yield surface for steel balls, e versus τ (Wroth, 1958)

Two paths are shown on each figure starting at P for the loose case and P′ for the dense case. In each case, the paths move directly towards the yield surface and then move along the yield surface approaching the critical void ratio line. The isometric view of this surface is then shown by combining the three elevation views (Fig. 2.66).

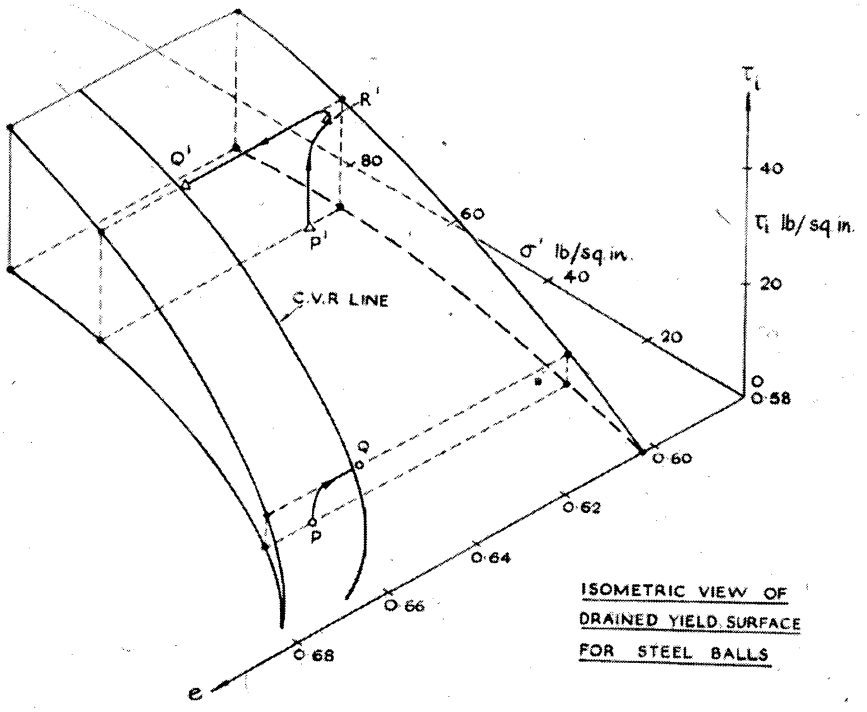

Fig. 2.66. Isometric view of drained yield surface for steel balls (Wroth, 1958)

Similar to the glass bead data, a prediction of the Hvorslev surface can be made for the steel balls. Fig. 2.67 shows τ_f plotted versus e_f where each straight line represents the section of the Hvorslev surface for a given σ'.

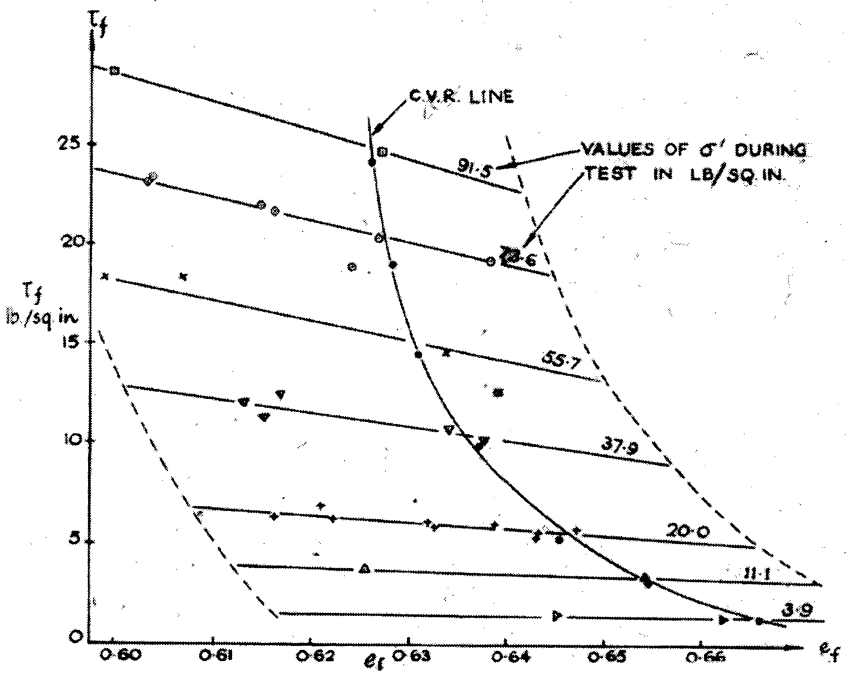

Fig. 2.67. Hvorslev surface for steel balls (Wroth, 1958)

It should be noted that the straight lines are not parallel, but rather their gradients increase linearly with increasing normal stress. The results for the steel spheres is very similar to that of the glass beads. Wroth states, "Since the behavior of glass beads has been shown to be similar to that of silt and sand by the triaxial tests...the steel ball results can be assumed to be representative of all granular material, so long as their packing remains random."

The random packing of particles is a very important feature when using idealized granular media to simulate the behavior of sand. For spheres of equal size, Graton and Fraser (1935) showed that random packings tend to become regular as the assembly undergoes shearing or is disturbed. This regular packing influences the behavior and ultimate strength of these samples and causes them to deviate from

what would be expected in natural samples where the particle sizes are varied. This is especially true for cyclic tests, or tests with any type of stress/strain reversal. This was also observed in the steel ball reversal tests conducted by Wroth (1958). The data exhibit differences in behavior due to the locking mechanism created by the regular packing of the particles. This interlocking or regular packing will be referred to as crystallization in later discussions.

2.6 Discrete Element Method (DEM) Modeling

Particulate discrete element method modeling, or distinct element method (DEM) modeling, has the advantage from a geotechnical perspective to be able to simulate large strain problems, as well as be used in laboratory element test simulations to examine particle-to-particle interactions. DEM models are used to simulate particulate assemblies of disks (2D) or spheres (3D) representing idealized granular material. The system is modeled as individual or discrete particles allowed to make and break contacts. When simulating laboratory element tests, loads and deformations can be applied to virtual samples and the underlying particle-scale mechanisms governing the overall response can be monitored and analyzed. Changing contact forces, contact orientations, particle rotations, localized stress and strain, and other quantities can be measured. The DEM data also allows for statistical analysis of soil fabric, rather than merely describing it qualitatively. Research and field practice in the past have relied largely on empirical observation of the macro-scale response of materials. Because DEM models are highly indeterminate systems, they require this type of data for validation. Not only do these validated DEM simulations have the potential to provide information about the testing device and conditions the soil element is subjected to, they also provide a means to "look inside" the material and better understand the fundamental particle interactions driving this response, thus

advancing our understanding of soil response in general.

2.6.1 Theory and Background

Originally proposed by Cundall (1971) for use in studying rock mechanics, and later applied in the area of Geotechnical Engineering by Cundall and Strack (1979), the distinct element method is a numerical method capable of modeling the mechanical behavior of assemblies of rigid disks or spheres. As outlined in O'Sullivan (2002), the distinct element method incorporates a "soft sphere" approach in which rigid particles are allowed to overlap slightly at the contact points. In this soft sphere approach, multiple simultaneous contacts are allowed and the linear and angular dynamic equilibrium of the contacting particles are solved over discrete time increments. In other words, DEM models treat particle interactions as a dynamic or transient process in which equilibrium occurs when the net forces acting on the particles are zero (Cundall and Strack, 1979). The contact forces and displacements of the particles are calculated as the simulation progresses using the Verlet algorithm, an explicit timestepping algorithm identical to the explicit algorithm used in finite-difference continuum based methods. The timestep is chosen to be sufficiently small, so that velocities and accelerations are assumed to be constant and disturbances are propagated only to the adjacent contacting particles. The resultant forces on any disk or sphere are, therefore, only dependent on the interactions with the disks or spheres in contact. It is this feature which allows DEM to be used for large assemblies of particles without large memory requirements or time-costly iterative processes. A detailed overview of the theory and background of particulate DEM and its applications within geomechanics is given in O'Sullivan (2011).

DEM simulations begin with an initial user defined geometry and loading or deformation schedule for the system. The calculation cycle begins with a search for

contacting particles. Once the contacts are detected, a force-displacement law is used to calculate the forces at each contact and a net force for each particle is determined. This force-displacement relationship is based on the corresponding particle overlap and the normal and shear stiffness defined for the material. Newton's second law is then used to calculate the acceleration of the particle based on the net force acting on it. The acceleration is integrated twice to obtain particle displacements and rotations and the particle positions are updated according to these displacements. The contact overlaps are then re-detected and the cycle continues until some user-defined ending condition is reached (Fig. 2.68).

The advantage of this method over continuum based methods is the ability to model the system as individual or discrete particles allowed to make and break contacts. Information such as particle positions, rotations, and contact forces is available for each individual particle within the assembly. As noted in Cundall (2001) and Potyondy and Cundall (2004), DEM works well for granular assemblies and is able to capture granular material behavior, while only requiring very simple particle geometries, simple contact laws, and only a few material parameters as inputs. Beyond the contact model, no material constitutive model is needed for DEM simulation, as is required in the traditional sense for continuum based models. In other words, the material behavior emerges during the simulation as a function of the system itself.

Although DEM models do not require many user defined inputs, they are computationally more intensive than continuum based models. DEM requires cycles to be carried out in the sample generation and preparation phases, whereas continuum methods allow for the initial geometry and stress state to be directly specified. Also, the non-linearity of granular systems and the fact that an explicit time integration approach is used requires DEM codes to implement small time increments. In ad-

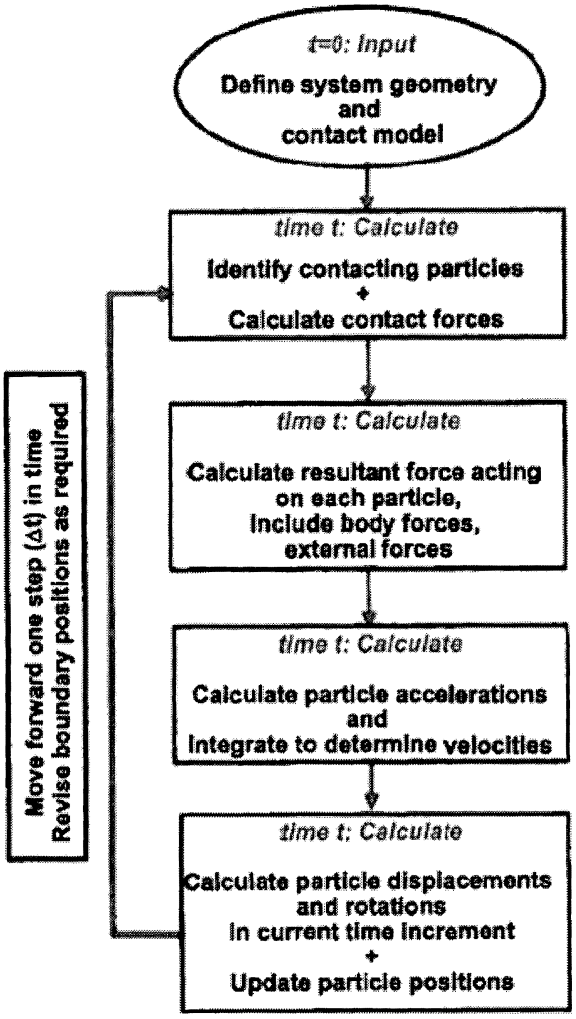

Fig. 2.68. Schematic diagram of sequence of calculations in DEM (O'Sullivan, 2011)

dition to these requirements, modeling a large number of particles is necessary to solve interesting problems, further increasing the computational costs. As computers continue to increase in speed, so will the capabilities of using DEM to study soil response. It is unlikely, however, that DEM would ever replace its continuum based counterparts, but instead be used to study the laboratory element and microscopic scale response of granular materials in order to supplement and further develop continuum models.

2.6.2 DEM Codes and PFC3D

The original DEM code, BALL, developed by Peter Cundall and described in Cundall and Strack (1978) models two-dimensional assemblies of disks. BALL requires two groups of input parameters: geometrical data and physical properties data. The geometrical data consists of defining the positions and orientations of the rigid wall boundaries, as well as the locations and radii of the disk particles. The wall boundaries are strain controlled by setting a velocity and cycling a number of times until the intended displacement is reached. The physical property inputs include: density, cohesion, inter-particle friction coefficient, shear stiffness, and normal stiffness. Contact and global damping can also be defined. A later development and extension to BALL, TRUBAL, is a three-dimensional code which defines spheres as the base particle shape.

Many of the subsequent developed/addapted codes use these two programs as the basic framework (CONBAL (Ng, 1989) and DISC (Ting et al., 1989)). Some researchers have also developed their own DEM codes (DIBS (Walton, 1982), GLUE (Bathurst and Rothenburg, 1989), and YADE (Kozicki and Donze, 2008)). Commercial programs, PFC2D and PFC3D, are also available (Itasca, 2004; 2008). These programs were developed by Itasca Consulting Group Inc., Minneapolis, Minnesota,

U.S. and are based on the original description of the distinct element method provided in Cundall and Strack (1979). An overview of some of the other available discrete method based codes, including methods which range outside of the particulate based method types, can be found in O'Sullivan (2011).

This research was conducted using Particle Flow Code in three dimensions (PFC3D) produced by Itasca Consulting Group, Inc. (Itasca, 2008). PFC3D can be used to model the behavior of an assembly of spheres, or it can be used to model arbitrary shapes and solids by clumping or bonding spheres together, as described in Potyondy and Cundall (2004). The spheres are treated as rigid bodies and the process and assumptions typical of particulate DEM simulations are followed (Kishino, 1999; Potyondy and Cundall, 2004). The force-displacement behavior is defined by a contact model and the possible addition of parallel bonds and viscous dashpots. PFC3D has the built-in options of either a linear contact model or a simplified Hertz-Mindlin contact model. The linear contact model linearly relates contact forces and displacements by constant contact stiffness values. The simplified Hertz-Mindlin contact model, instead relates forces and displacements non-linearly through non-constant stiffness values. The stiffness values for this model are based on the user defined material properties (shear modulus and Poisson's ratio), as well as the current normal force. For most simulations, the linear contact model should be sufficient. This model is generally more appropriate for use in cases where particles are bonded together. The Hertz-Mindlin model should be used for simulations in which capturing accurate behavior at small-strains is important and for assemblies without bonds and consisting of mostly compressive stresses. Several other contact models are provided in the manual and company website and can be easily implemented. There is also a method for inputting a user defined contact model if a more complex model is needed or is applicable.

PFC has several benefits making it a widely used DEM software code. Relatively large numbers of particles and complex problems can be run on any standard computer with a Windows operating system. Only small amounts of RAM are required and the simulation runtimes are mainly processor speed dependent. Creating system boundaries and generating particles are straightforward processes using a basic set of pre-defined functions and commands. PFC also automatically adjusts the timestep during the simulation to account for the number of contacts present and any changes in contact stiffness. While much of the "background" coding already exists, users are required to develop their own functions and algorithms for more complex simulation control and monitoring. These user-defined variables and functions are written in the FISH programming language embedded within PFC. Additionally, both existing and user-defined variables can be set as history variables and can be recorded and monitored through the duration of the simulation. The program also offers a plotting option where the history information and the simulation geometry can be visualized and monitored, as well as the ability to output the recorded histories to a file for post-processing in another program. More information related to the features present in PFC3D and its capabilities can be found in Itasca (2008).

2.6.3 Previous Studies on Granular Material Behavior using DEM Element Tests

Numerous DEM studies have been conducted in an effort to better understand granular material behavior. Due to the computationally intense nature of DEM, most of these studies have consisted of element tests rather than full-scale or field-scale boundary value problems. Early work in DEM has shown verification in the methods (Cundall and Strack, 1979) and has included studies on material fabric and its affect on stress-strain response (Cundall et al., 1982; Bathurst and Rothenburg, 1989), the effects of principal stress directions on granular response (Arthur et al., 1986), as

well as many other studies on the key factors that influence granular soil behavior. Several relatively recent studies have shown that DEM can be used with confidence to study the micromechanical response and overall macro-scale behavior of idealized granular material. For example, Bolton et al. (2008), Cui and O'Sullivan (2006), and Potyondy and Cundall (2004) verified that DEM could capture the "frictional" strength response observed in granular soils (i.e. peak shear stress increases with increasing confining stress). Researchers have also shown the sensitivity of granular response and peak stress to initial void ratio (Thornton, 2000; Rothenburg and Kruyt, 2004; Powrie et al., 2005), as well as the presence of a critical void ratio and unique stress pertaining to samples reaching critical state at large strains (Thornton, 2000; Rothenburg and Kruyt, 2004; Salot et al., 2009). Colin Thornton and colleagues (Thornton, 1997; Thornton and Antony, 1998; Thornton, 2000; Thornton and Antony, 2000; Thornton, 2010) have performed numerous studies on granular soil behavior using assemblies of spherical particles in axisymmetric triaxial and true triaxial simulations. Simulating axisymmetric compression tests using an assembly of spheres, Thornton and Antony (1998) and Thornton (2000) showed that DEM was able to capture the response expected for loose and dense sands tested at a constant mean stress (Fig. 2.69).

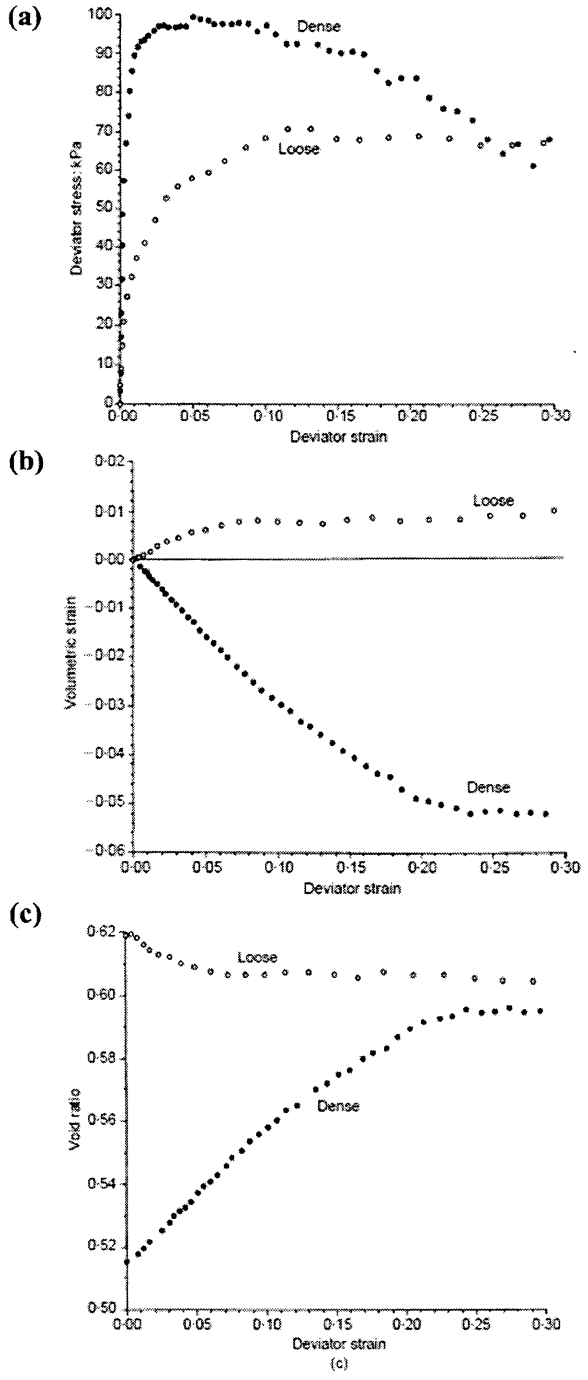

Fig. 2.69. Results of an axisymmetric compression simulation (a) deviator stress (b) volumetric strain (c) void ratio (Thornton, 2000)

The dense assembly gained strength quickly until a peak deviatoric stress was reached, at which point it began to decrease showing strain softening behavior. The loose assembly continued to gain strength as shearing progressed exhibiting strain hardening behavior. Similar responses are seen in equivalent physical triaxial compression tests on loose and dense sand. In terms of volumetric response, the loose sample contracted and the dense sample dilated, both reaching a constant volume condition at high strains and following trends seen in experimental tests on sand.

Granular soils are known to have two components which contribute to their strength: contact friction and "interlocking" due to angular particle shapes. DEM allows these features to be examined separately. Thornton and Sun (1993) used numerical simulations of true triaxial axisymmetric compression tests to single out the effects of interparticle friction. The results showed that increased interparticle friction values increased the shear modulus, shear strength, and dilation rate of both loose and dense assemblies. Increased friction also lead to increased structural anisotropy. Thornton (2000) used additional axisymmetric compression tests to further study the influence of interparticle friction on the mobilized friction angle and void ratio (Fig. 2.70).

Both the mobilized internal friction angle and the critical void ratio increase with increasing interparticle friction. Micromechanical observations showed that the ratio of sliding contacts and the average number of contacts per particle decrease with increasing friction. In turn, friction is said to be primarily a kinematic constraint. By separating the normal and tangential force contributions, Thornton was also able to show that the tangential contributions to the deviator stress are quite small in relation to the normal force contributions (Fig. 2.71).

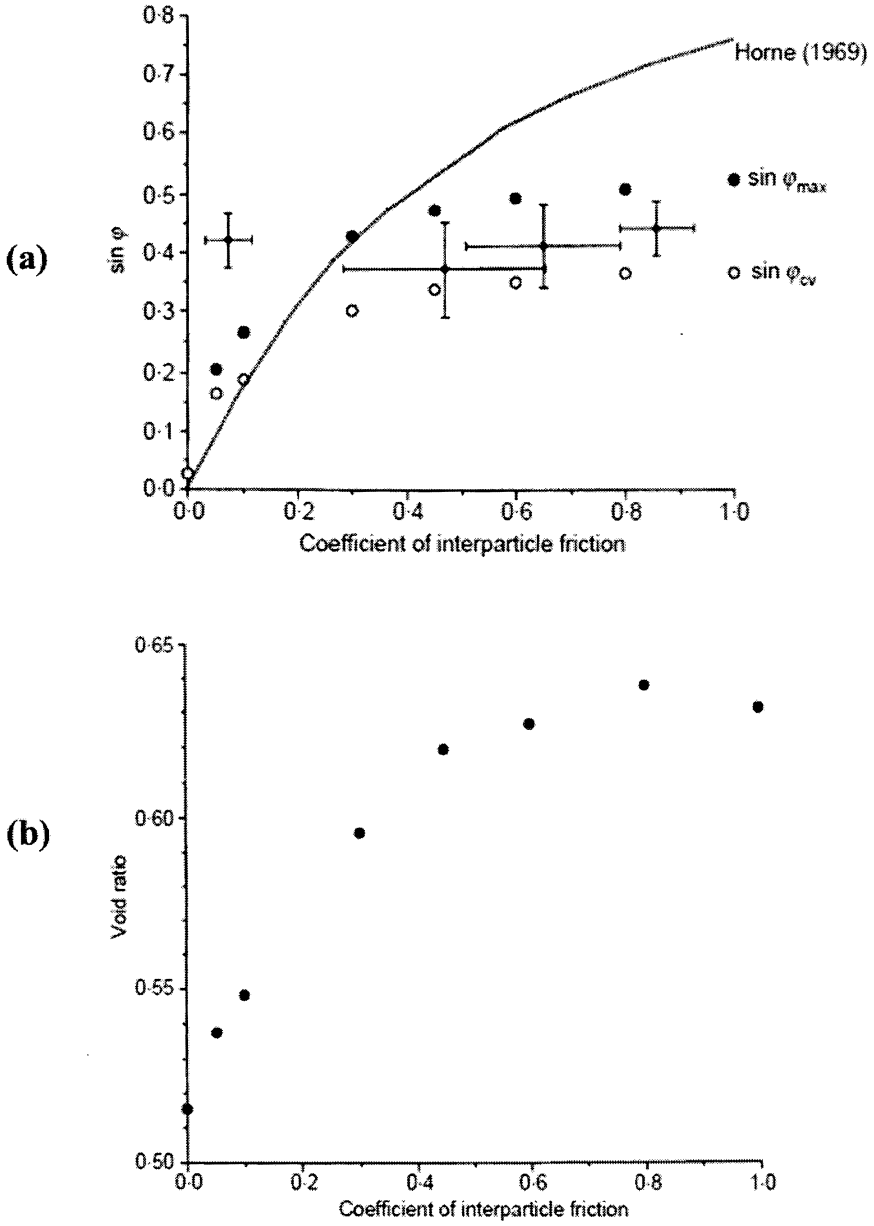

Fig. 2.70. Effects of interparticle friction on (a) mobilized friction angle ϕ (b) critical void ratio (Thornton, 2000)

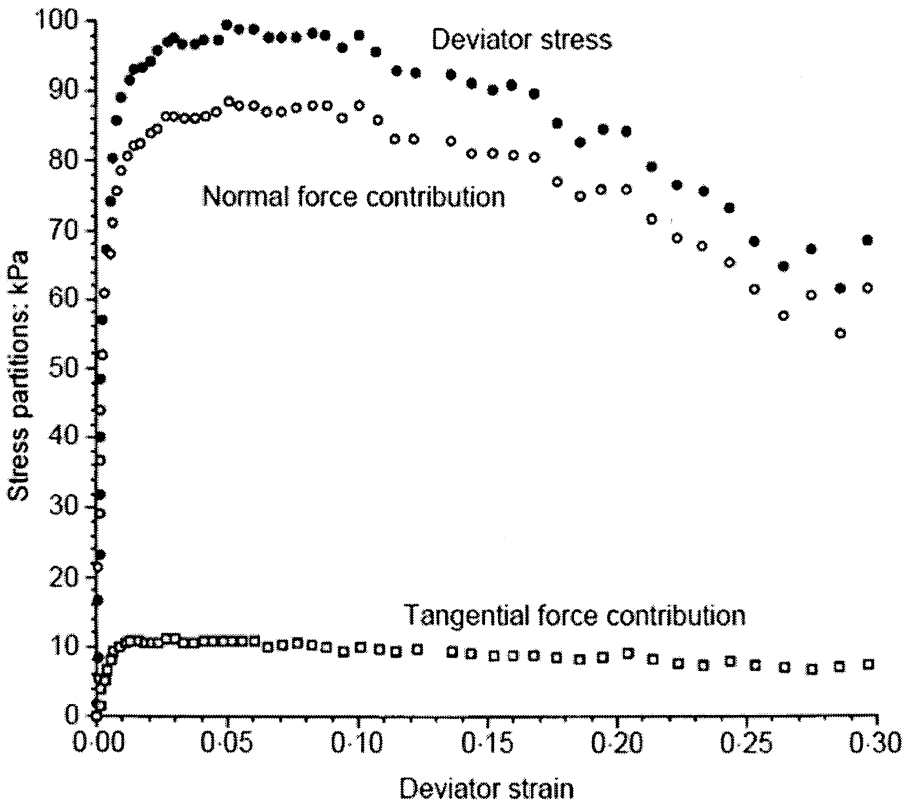

Fig. 2.71. Comparison of normal and tangential contact force contributions with deviator stress (Thornton, 2000)

Ng (2004) instead studied the effects of particle shape on shear strength, as well as the influence of anisotropy and the intermediate principal stress. As mentioned previously, researchers have shown experimentally that the intermediate principal stress influences the shear response and that the strength of a granular soil is dependent on all three principal stresses. Ng (2004) numerically verified this using DEM simulations of true triaxial tests under various stress paths. The results showed that dilation rate is insensitive to particle shape, but varies for differing stress paths. For triaxial compression tests ($b = 0$), the stress-strain response appears to be insen-

sitive to both particle shape and stress path. This was not, however, the case for the triaxial extension tests ($b = 0$), where it appears that anisotropy due to particle shape has an influence on the overall stress-strain response.

Masson and Martinez (2001) and Thornton and Zhang (2001) performed DEM analyses of the direct shear test using 2-dimensional disk elements. For the loose and dense samples tested in Masson and Martinez (2001), the results qualitatively agree with the expected behavior for sands tested in direct shear. The dense sample shows a higher strength and dilative behavior, while the loose sample is contractive and exhibits lower overall strength. Plots of instantaneous velocity show a clear distinction in shear flow behavior between the loose and dense samples (Fig. 2.72).

The bottom half of both specimen have a sort of block-like movement guided by the imposed shearing. The top half and middle zone, however, are different. The top half of the dense sample dilates and a sudden change in shear flow is noticed through only a very small slice of the mid-section. The loose sample, on the other hand, displays very little movement of the top particles and a much wider and more erratic shear zone through the central portion. The particle displacements and rotations are also very different for the two samples (Figs. 2.73 and 2.74).

The particle displacement and rotation values for the dense sample further confirms this thin shear band, which has also been observed in previous experimental studies on idealized materials. The loose sample displays a more scattered distribution of displacements and rotations. From plots of contact orientations, changes in fabric are clear for the dense sample, whereas the loose sample displayed only slight differences.

Additionally, very recent studies have demonstrated DEM's ability to capture effects of anisotropy and the non-coaxial behavior of granular soils (Wang et al., 2008; Li and Yu, 2009; 2010; Yimsiri and Soga, 2010). Arthur et al. (1986) began the early

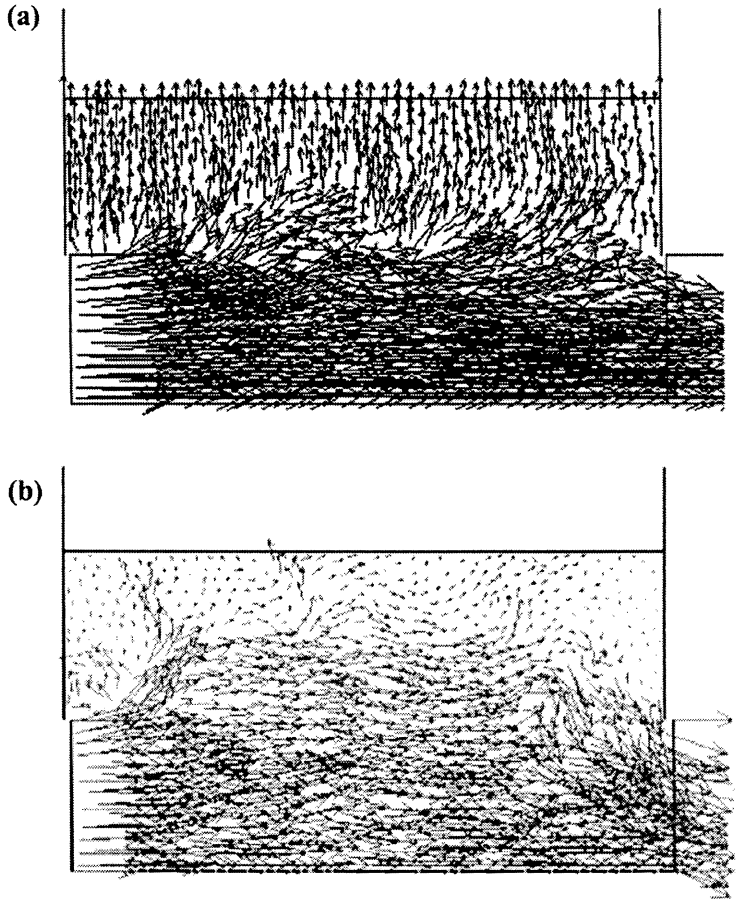

Fig. 2.72. Instantaneous velocity of particles (a) dense sample (b) loose sample (after Masson and Martinez, 2001)

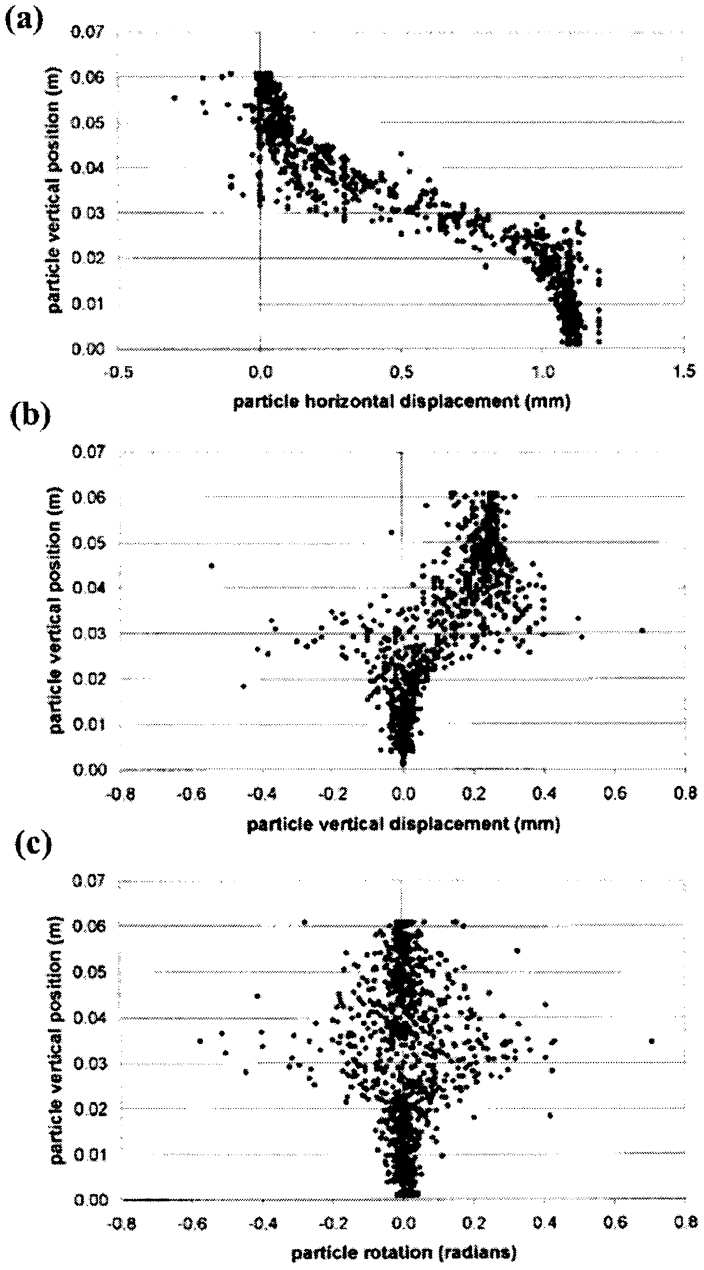

Fig. 2.73. Vertical profiles of particle displacement for the dense sample (Masson and Martinez, 2001)

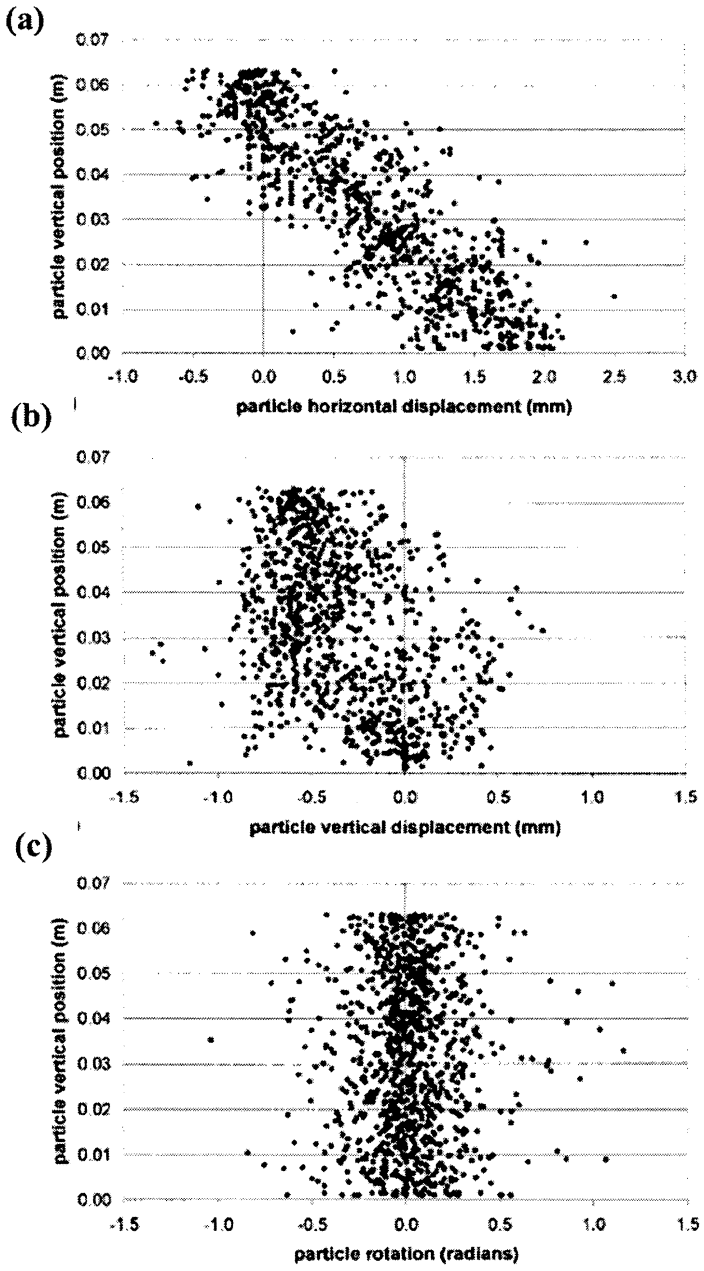

Fig. 2.74. Vertical profiles of particle displacement for the loose sample (Masson and Martinez, 2001)

work in this area by showing the non-coaxial behavior of soil in two-dimensional assemblies subjected to a change in principal stress direction. The numerically produced cures qualitatively resemble the experimental curves obtained in the Directional Shear Cell (DSC). More recent studies by Li and Yu (2009) have used PFC2D to study the non-coaxiality of granular soils under a smooth rotation of the principal stress direction as seen in simple shear testing and most field conditions. Particles were generated within a hexagonal boundary and then isotropically consolidated to a high confining pressure of 1000 kPa. Deviatoric shearing was then applied in the vertical direction while the mean normal stress was maintained constant. The rotational shearing was applied with the major principal stress direction being rotated at a constant value while the strain components were recorded. As with other similar work, the principal stress and strain directions were shown to be non-coincident (Fig. 2.75).

As described in Yu (2008), Wang et al. (2008) showed similar results in three-dimensions while simulating simple shear tests (Fig. 2.76). For both samples starting at two different stress ratios, it is clear that the principal stress and principal strain increment directions are not coincident. They do, however, become aligned at higher shear strains, which is also observed in experimental tests in simple shear.

The examples given above, as well as in the next section, represent only a small number of the relevant studies. A more in depth overview of some of the key features of granular soil behavior and the corresponding DEM studies is given in O'Sullivan (2011).

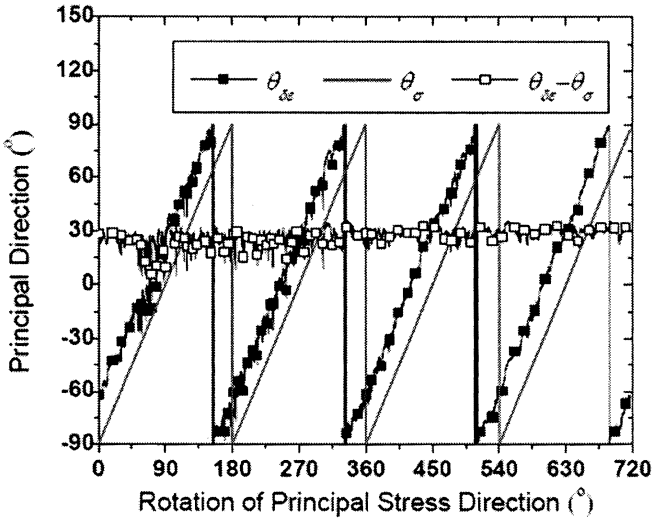

Fig. 2.75. Directions of the major principal stress and major principal strain increments (Li and Yu, 2009)

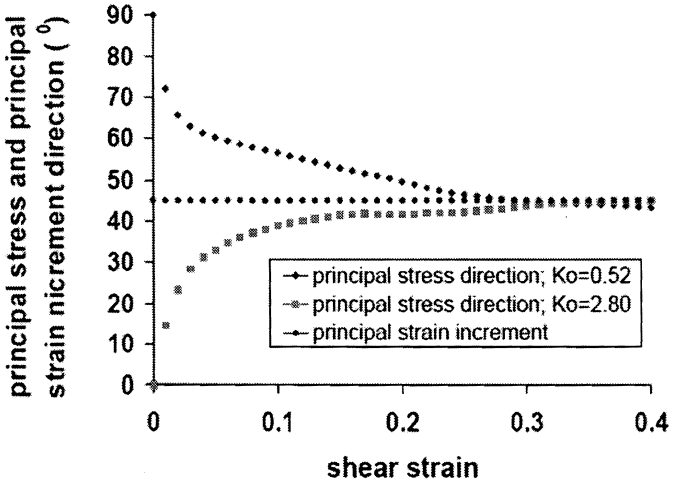

Fig. 2.76. Comparison of principal stress and principal strain rate increment direction for two samples at different K_o (Wang et al., 2008)

2.6.4 Previous Experimentally Validated DEM Element Tests

Because assemblies of particles are highly indeterminate systems, only a few analytical solutions exist for regular packing of uniform sized particles (Cundall and Strack, 1979; Thornton, 1979). For random packings of polydisperse (i.e. multiple particle size) assemblies, it is useful and even necessary to validate them with experimental results if they are to be compared to and used for further analysis of physical element tests. Validation studies consist of developing DEM models which replicate the physical conditions as accurately as possible. The size, number, and material properties of the particles are accurately modeled, along with the geometry, boundary conditions, and loading conditions of the system. Once the DEM simulation sufficiently resembles the macro-scale physical test results, the data recorded from the DEM simulation can be used to gain further information about the micromechanical behavior and particle-scale response.

Early two-dimensional studies of assemblies of disks were experimentally verified by rods and photoelastic disks. Cundall and Strack (1978) and Cundall and Strack (1979) compared simulation results from the BALL program to the experimental results on photoelastic disks by Oda and Konishi (1974) and de Josselin de Jong and Verrujit (1969), respectively. Thomas (1997) carried out a similar verification for the discontinuous deformation analysis code, DDAD, using stiffer borosilicate rods tested and simulated in biaxial compression. The response of the rod assemblies was much different than the typical response expected for sand. Also, several issues with modeling actual rod geometries and an error in the shear spring formulation lead to less than ideal results. Rod tests conducted at the University of Amherst were used to validate DEM simulations of a loaded foundation and biaxial shear tests in a directional shear box (Acheampong, 1996). The results for the loaded foundation

were found to be sensitive due to the small number of particles used. The response was highly sensitive to the linear spring stiffness used and showed no sensitivity to the use of a non-linear formulation of the contact model. It is not apparent that the value of interparticle friction used in the simulations was the measured value for the physical rods. The initial stiffness of the numerical response was higher than that of the physical tests and the peak stress was observed at lower strain levels in the physical tests. The results for the biaxial tests agreed well with the experimental response; however, it should be noted that boundary conditions were not accurately modeled for either case.

Also using experimental validation as a method of verification for a DEM code, O'Sullivan et al. (2002) studied the influence of particle shape and surface friction on the macro-scale response of rods in biaxial compression. For regular packings, it was found necessary to use precision manufactured rods due to the sensitivity of the experimental response to small differences in geometry. Fig. 2.77 shows the results for biaxial compression of hexagonally packed rods and disks.

For random packings of polydisperse rods, it was found that the number of particles must be sufficiently large to reduce sensitivity to small perturbations. Biaxial test simulations for two sample sizes (224 and 896 disks) showed that the smaller sample was much more sensitive to the distribution of radii, meaning the response was more sensitive to the change of only a few contact points (Fig. 2.78). The results for similar tests using 5,728 and 12,512 disks showed essentially the same response for both particle numbers (Fig. 2.79). While this may seem to indicate DEM results can be upscaled, care should be taken for comparisons with systems of different boundary and loading conditions, or particle geometries (O'Sullivan, 2011).

In three-dimensional tests, assemblies of spheres are experimentally validated by idealized spherical materials commonly consisting of steel ball bearings or glass

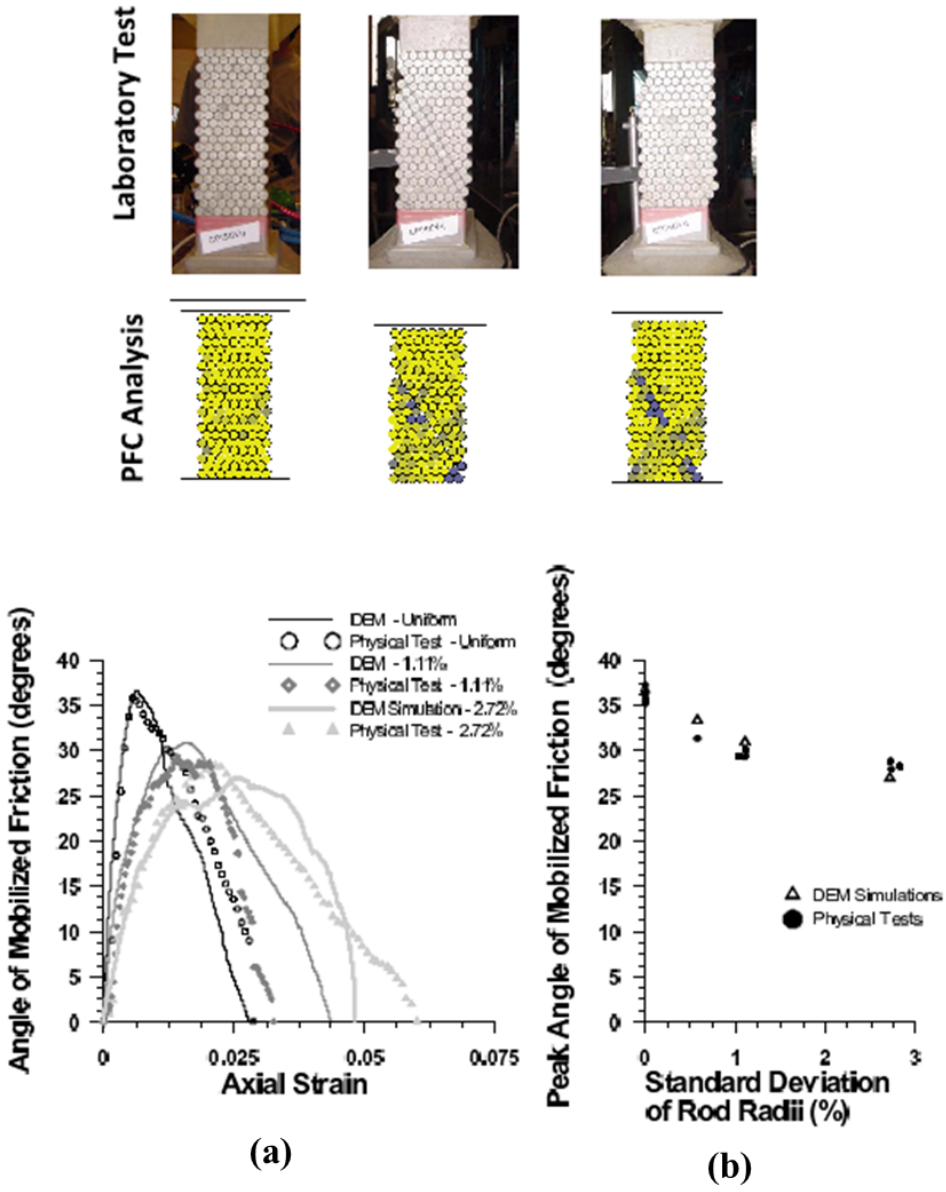

Fig. 2.77. Results of code validation study using a system of hexagonally packed rods in biaxial compression and an equivalent disk two-dimensional DEM simulation (O'Sullivan, 2002)

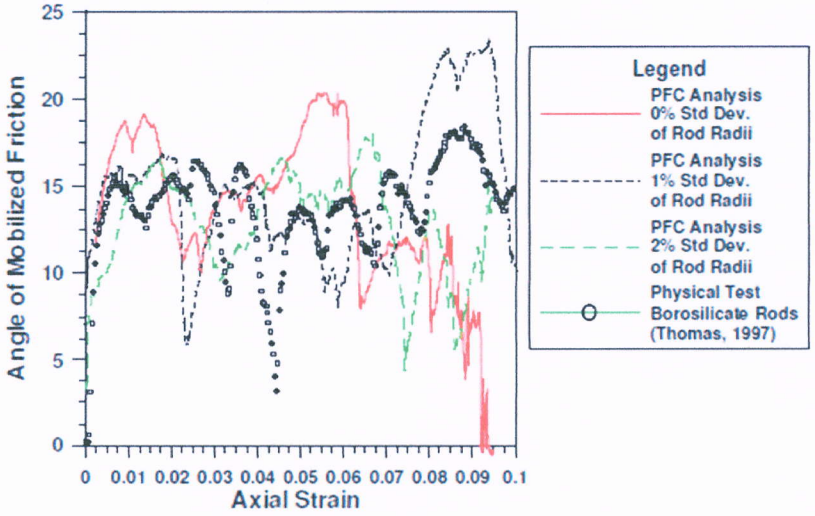

(a) Stress strain response of samples with 224 disks

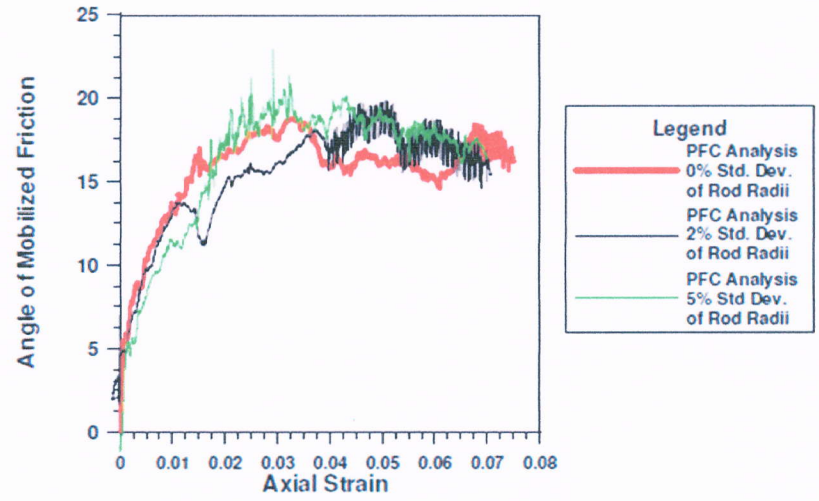

(b) Stress strain response of samples with 896 disks

Fig. 2.78. Illustration of sensitivity of systems to number of particles (O'Sullivan, 2011)

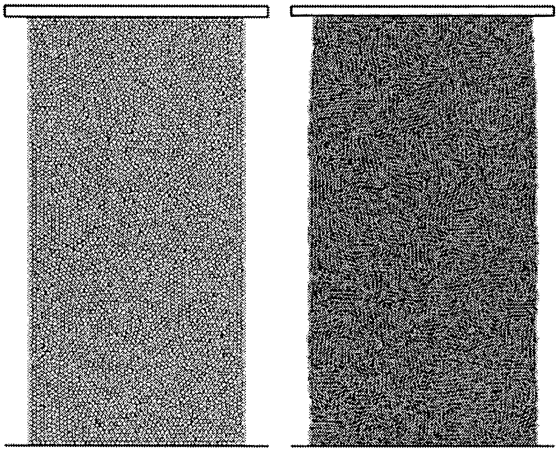

(a) Initial disk configuration for biaxial test with 5,728 disks (Specimen A)

(b) Initial disk configuration for biaxial test with 12,512 disks (Specimen B)

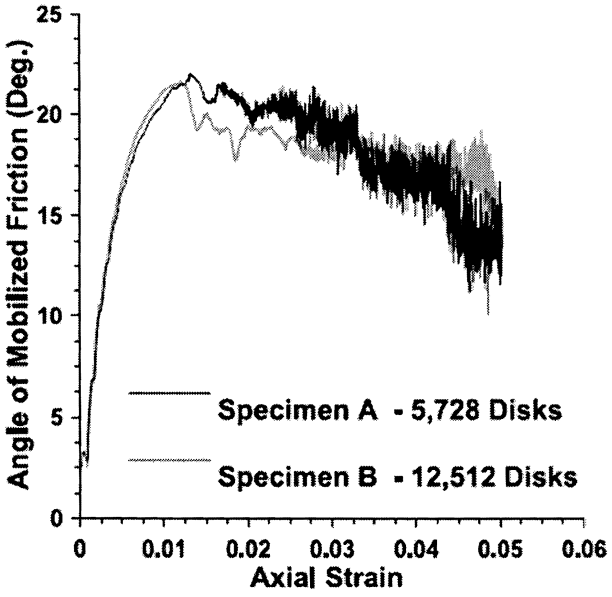

(c) Specimen response for large random biaxial simulations, indicating location of strain measurement points

Fig. 2.79. Response for two large, dense, two-dimensional disk samples in biaxial compression (O'Sullivan, 2011)

beads. Early verification of the program TRUBAL (Cundall and Strack, 1979) compared the numerical DEM results with the earlier experimental results by Rowe (1962) for a regular packed assembly of spheres. Rowe tested an assembly of 1672 polished steel spheres with a measured friction angle of 7°. The results from this study are also given in the PFC3D manual (Itasca, 2008).

Thornton and Sun (1993) conducted numerical simulations of axisymmetric compression tests on glass beads performed experimentally by Parikh (1967). The size of the spheres used in the DEM model differed from the actual physical diameters and gradation, and a value of interparticle friction was assumed rather than measured. Periodic boundaries were also used for the simulations rather than rigid boundaries. The DEM simulation obtained a slightly lower value of ϕ_{max} than what was found in the experimental results. Thornton and Sun attribute the error to a difference in boundary conditions and the fact that the physical glass beads are not perfectly spherical. No mention of differences due to particle friction is made. A more detailed discussion of these examples along with additional validation and verification studies are given in O'Sullivan (2002).

More recently, Cui and O'Sullivan (2006), and Wang and Gutierrez (2010) have studied the response of granular materials in simulations of direct shear element tests. These studies explored the heterogeneity of the contact forces and strains present in the direct shear apparatus, giving a better understanding of the limitations of the physical testing apparatus and possible improved design capabilities as shown in Zhang and Thornton (2007) and Wang and Gutierrez (2010). Cui and O'Sullivan (2006) tested grade 25 precision steel spheres with uniform radii of 0.992 mm. The properties of these spheres were satisfactory in O'Sullivan et al. (2004) and the interparticle friction coefficient was determined to be 0.096 (5.5°). The friction coefficient for the ball-boundary interface was determined to be 0.175 using 25 tilt tests. The

authors tested assemblies of approximately 11,700 spheres in a 60mm wide square cross-section direct shear box. Samples were prepared by air pluviation followed by tamping. Two series of tests were performed at a range of normal stresses. One set was conducted at void ratios ranging from 0.574 to 0.591 and a second set was initially preloaded giving slightly lower void ratios of 0.539 to 0.574 (Figs. 2.80 and 2.81).

Three different DEM samples were prepared, two of which used a form of radius expansion, and a third which used settling under gravity (e=0.518-0.577). The DEM results are similar to the experimental results with no major differences noted for the differently prepared numerical samples (Fig. 2.82).

The experimental tests had an average ϕ' of 25.0°, while the numerical results had an average ϕ' of 23.8°. The authors expected the numerical results to have a higher value because the samples were more dense. A study of the influence of interparticle friction showed that the peak ϕ' increases with increasing interparticle friction values. The authors state that as shearing occurs the particles' surfaces are roughened, increasing the friction value. This is, therefore, a likely contributor to the difference in peak response.

The microscopic information for a selected representative simulation shows large non-uniformities in stresses and strains in the direct shear tests (Fig. 2.83).

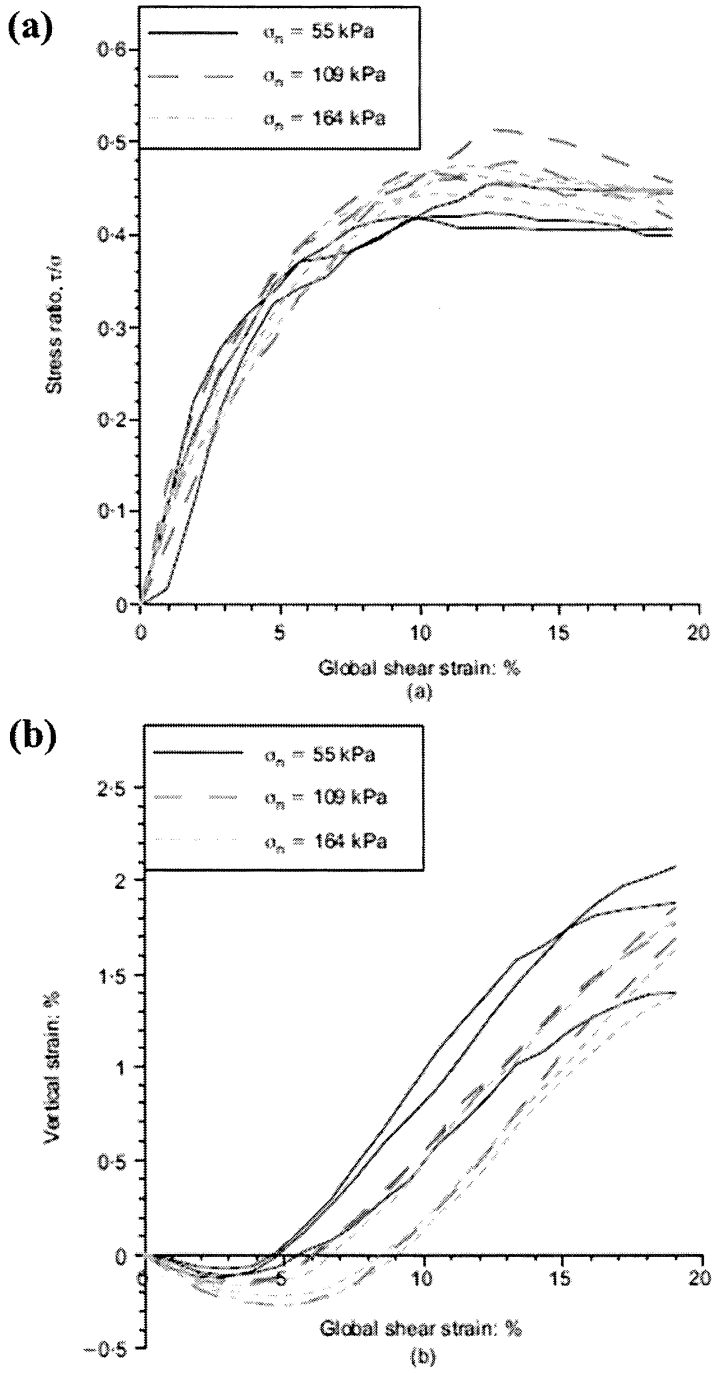

Fig. 2.80. Response for laboratory direct shear tests on steel spheres without preloading (Cui and O'Sullivan, 2006)

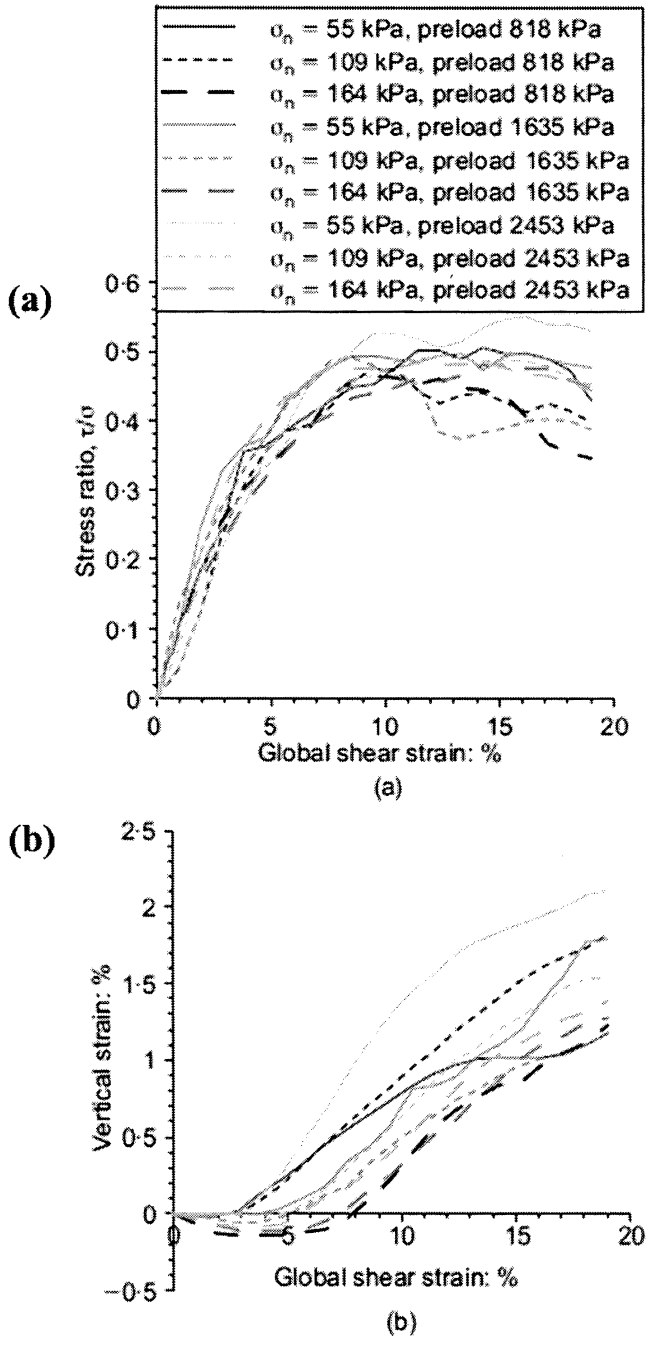

Fig. 2.81. Response for laboratory direct shear tests on steel spheres with preloading (Cui and O'Sullivan, 2006)

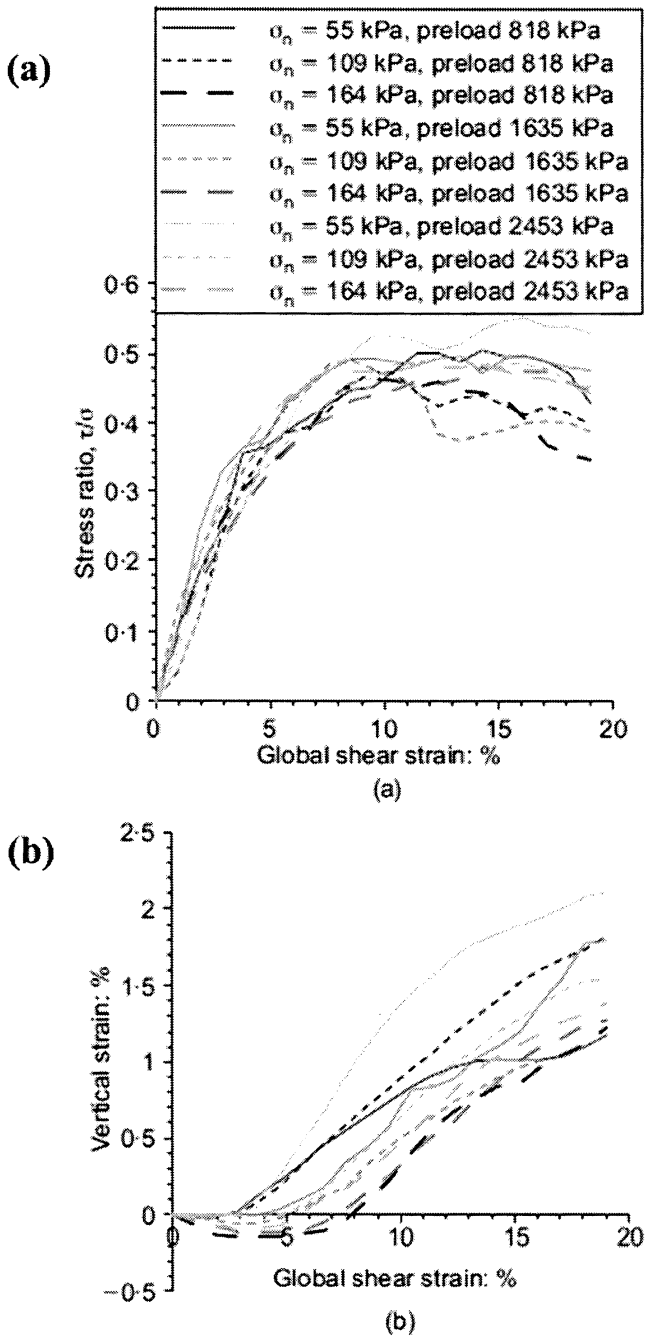

Fig. 2.82. Response for numerical direct shear tests on spheres (Cui and O'Sullivan, 2006)

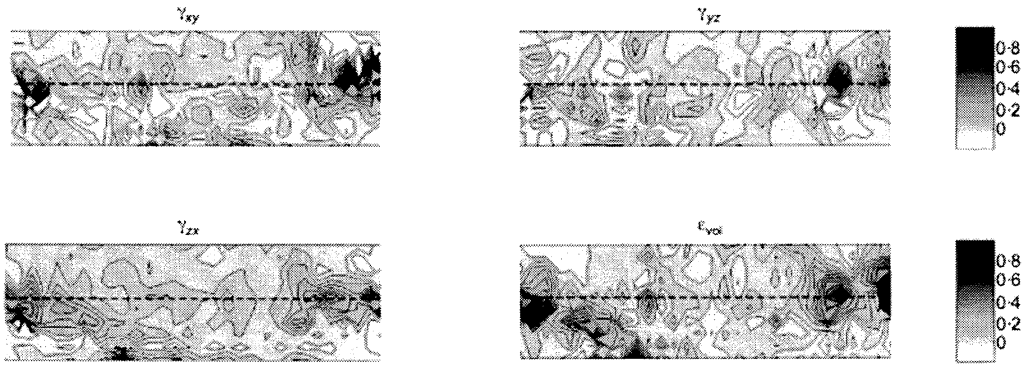

Fig. 2.83. Strain contours for global values of shear strain from 0 to 15.3% (Cui and O'Sullivan, 2006)

The shear stresses calculated at the boundary are much lower than those calculated through the mid-height of the sample. Additionally, plots of the deviator fabric also seem to give a better indication of the peak response behavior than do plots of coordination number (Fig. 2.84). A detailed account of this study can be found in Cui (2002).

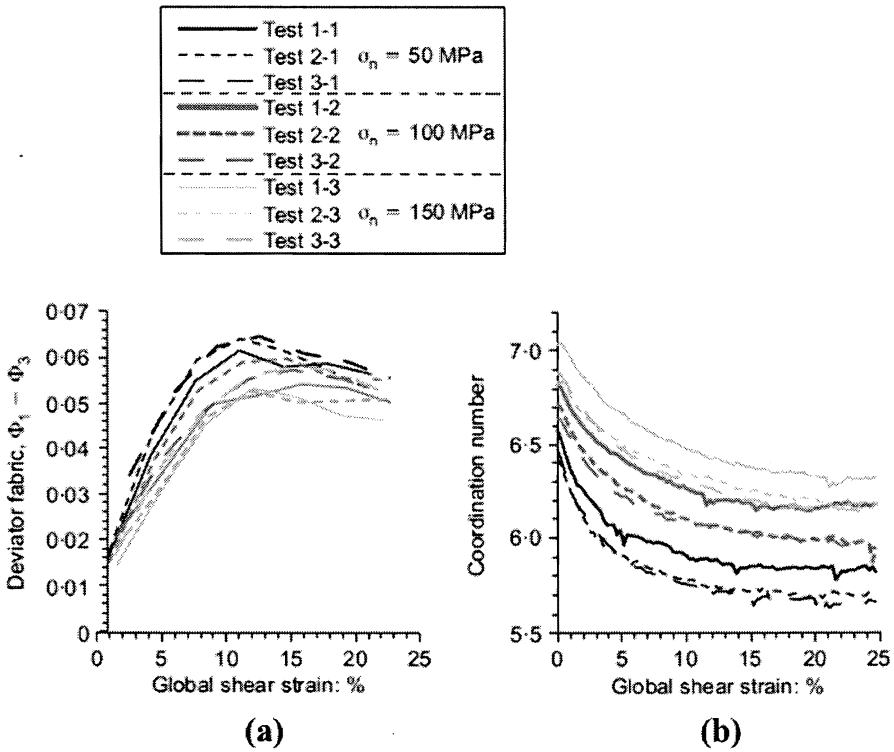

Fig. 2.84. Response for laboratory direct shear tests on steel spheres (Cui and O'Sullivan, 2006)

2.6.5 Previous Studies of Simple Shear using DEM

Bashir and Goddard (1991), as well as Zhuang (1993) performed numerical simulations of two-dimensional simple shear tests. These tests were limited to very small particle numbers (56 and 132 disks); however, the micromechanical responses observed were as expected. Force chains built up during shearing until they reached a limit and buckled/collapsed, at which point the forces were either transferred to another particle or the sample densified and new force chains were formed. Zhuang (1993) used the results to relate the coordination number to percolation theory to develop the geometric percolation threshold and the elastic bond percolation threshold.

For coordination numbers that are larger than the geometric critical coordination number, at least one force chain will span the specimen boundaries. While both of these studies provided valuable qualitative information, the few number of particles tested limits their usefulness quantitatively.

Shen et al. (2010) presents a study of the use of two-dimensional DEM models to simulate simple shear testing. Two configurations were used in the study to simulate the various boundary conditions present in existing simple shear apparatuses: hinged rigid lateral walls (Cambridge device), and laminar sidewalls (SGI-type device) (Fig. 2.85). While the overall responses are similar (Fig. 2.86), several differences are shown in the internal material response. Both the contact force network and distribution of strains within the samples are very different (Fig. 2.87). Similar to results shown previously, the internal stresses differed from the boundary stresses (Fig. 2.88).

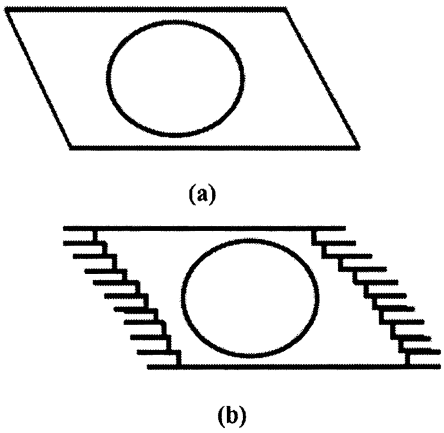

Fig. 2.85. Schematic plot of testing boundary conditions (a) Cambridge hinged rigid lateral walls type apparatus (b) Laminar type apparatus (Shen et al., 2010)

In physical tests using the SGI or NGI-type device, only boundary stresses and strains are available, meaning the recorded data underestimates the actual internal stress subjected to the sample. Shen also observed non-coaxial behavior. The angle of non-coaxiality began at approximately 20° for all simulations and then decreased to 10° near 1% shear strain. As shearing progressed, the angle further reduced becoming approximately 0° at 9% shear strain.

Shen (2013) presents a more detailed account of the study in which a total of four different simple shear boundary configurations were simulated using two-dimensional DEM models. Because of its relevance to this research, only the laminar type device configuration results are discussed. Shen generated two initial samples using a radius expansion algorithm: a 5,000 particle prototype samples and a 20,000 particle sample for which the results are shown. Table 2.4 gives the particle material properties used.

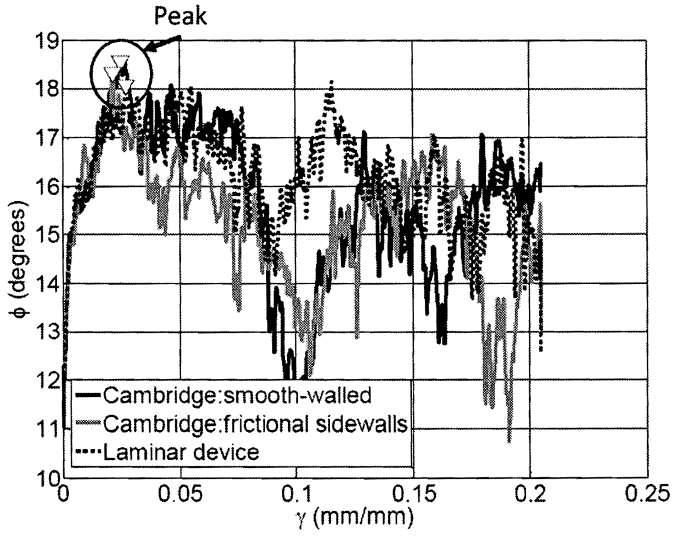

Fig. 2.86. Comparison of angle of shearing resistance for the three sample conditions (Shen et al., 2010)

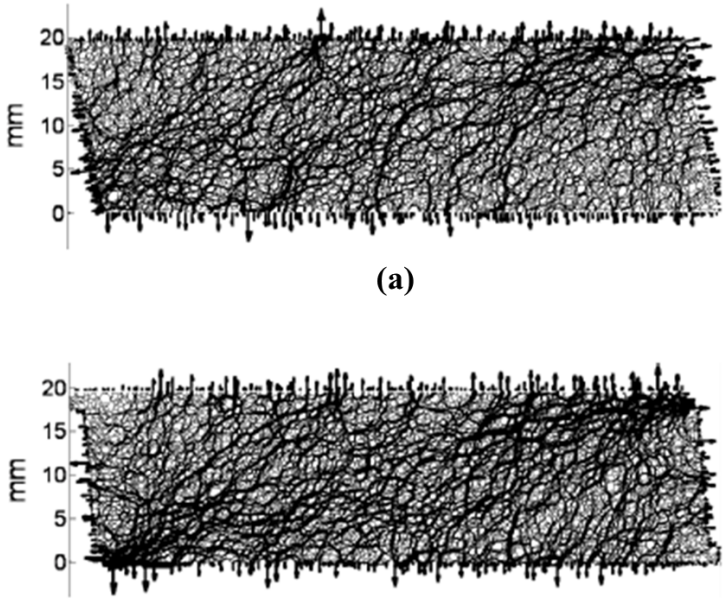

Fig. 2.87. Contact normal force diagrams (a) Frictional Cambridge-type apparatus (b) Laminar-type apparatus (Shen et al., 2010)

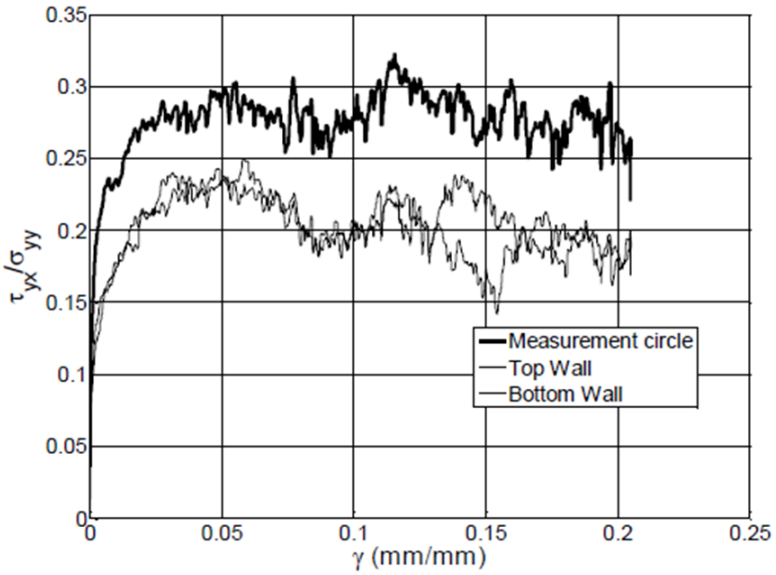

Fig. 2.88. Comparison of shear stress ratios measured at various locations for the laminar-type sample (Shen et al., 2010)

Table 2.4. Material properties used in simple shear 2D simulations (after Shen, 2013)

Model parameter	**Value**
Number of particles	5,000 and 20,000
Particle density	2650 kg/m$\hat{3}$
Normal and shear stiffness (linear)	1x10$\hat{4}$ N/mm
Particle damping coefficient	0.01
Interparticle friction coefficient, μ_s^p	0.5
Friction coefficient between particles and walls, μ_s^w	0.5 (top & bottom) 0.0 (sidewall)
Particle size for 20,000 particle specimen	0.13-0.38 mm

A range of interparticle friction values were used to generate samples at various densities. Although several different methods were tried, only a small range of void ratios was attainable. Samples were then compressed to obtain several different initial stress states.

To create the laminar boundary walls, 10 wall segments were placed on each side of the assembly. These wall segments were controlled by a user-defined servo control algorithm, so that the net force on the corresponding horizontal wall segments (representing rings in 3D) at any given time was approximately zero. The bottom cap moved horizontally at a constant strain rate chosen to maintain quasi-static conditions. The top cap was only allowed to move vertically, with its motion governed by a servo stress controlled algorithm which maintained constant vertical stress. An initial comparison of the 5,000 and 20,000 particle sample tested at a vertical effective stress of 0.2 MPa, showed clear differences in internal measurements of shear stress ratio for the two sample sizes (Fig. 2.89). The boundary stress ratio measurements for the two samples were similar up to 6% shear strain, after which point the samples exhibited different responses (Fig. 2.90).

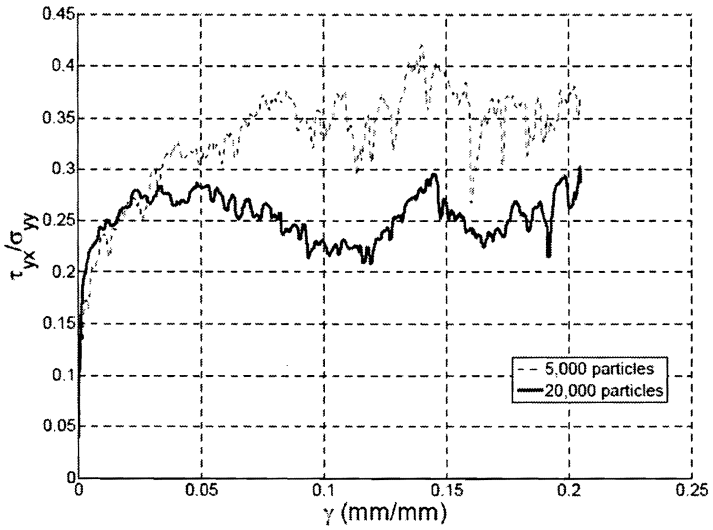

Fig. 2.89. Comparison of shear stress ratios measured in the measurement circle (Shen, 2013)

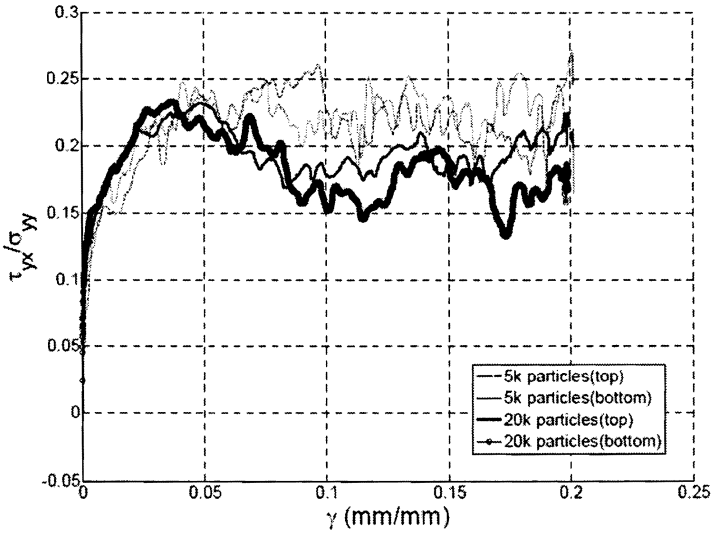

Fig. 2.90. Comparison of shear stress ratios measured at the top and bottom boundaries (Shen, 2013)

The 20,000 particle sample reached a peak stress ratio of 0.24 at approximately 5% shear strain and then softened, while the 5,000 particle sample continued to fluctuate across a stress ratio value of 0.23. It is also clearly evident from the two plots that the stress response measured at the boundaries is different than the response measured within the sample. Shen also noted differences in the angle of shearing resistance and the volumetric strain response, as well as slight differences in the orientation of the major principal stress.

Shen simulated three different boundary conditions in order to investigate the influence of slippage at the boundaries and the effects of measurement location for the servo control. Simulations A and B used flat frictional boundaries, while simulation C used fixed disk boundaries where the boundary disks were virtually "glued" by fixing their rotation to zero and their velocity equal to the top and bottom caps. Tests A and C used the measurement circle values to control the vertical stress conditions. Test B used the top boundary measurements. It is clear from Figs. 2.91 and 2.92 that the fixed boundary response is different from the other two tests.

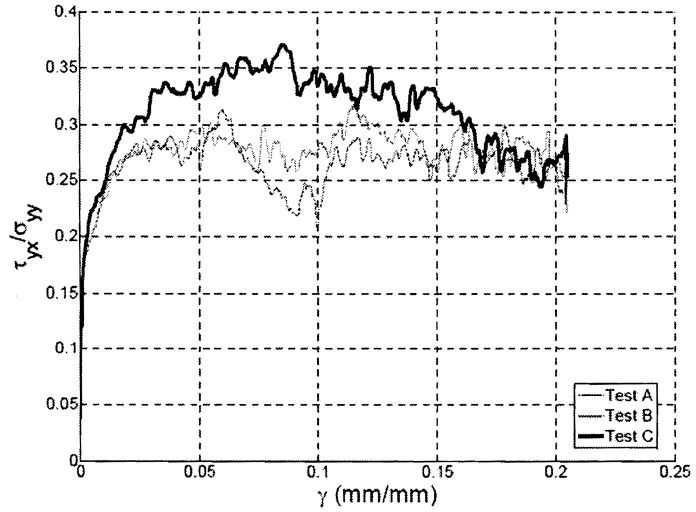

Fig. 2.91. Comparison of shear stress ratios for the laminar-type sample with different boundary conditions (Shen, 2013)

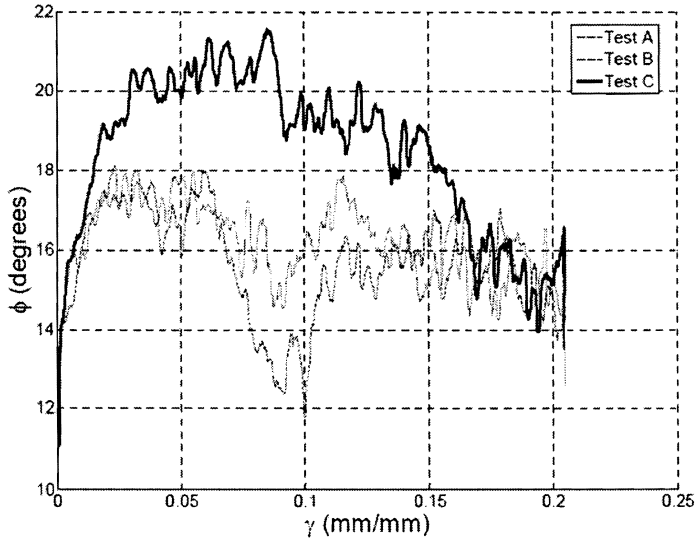

Fig. 2.92. Comparison of the angle of shearing resistance measured for the laminar-type sample with different boundary conditions (Shen, 2013)

The peak response is also higher for this type of boundary condition. No major differences were observed for the orientation of principal stress for the three tests and strain plots showed little or no slippage at the boundaries for the fixed-disk boundary simulation.

The initial simulations conducted by Shen, used 10 vertically stacked rings. To achieve uniform shear deformation, ASTM-D6528 (2007) recommends that the thickness of each ring should be less than 1/10 of the total specimen thickness. Shen performed an additional simulation with 20 rings, in order to test the sensitivity of the response to this condition. The two simulations showed only slight differences in stress ratio (Fig. 2.93), angle of shearing resistance, orientation of the principal stress, and volumetric response.

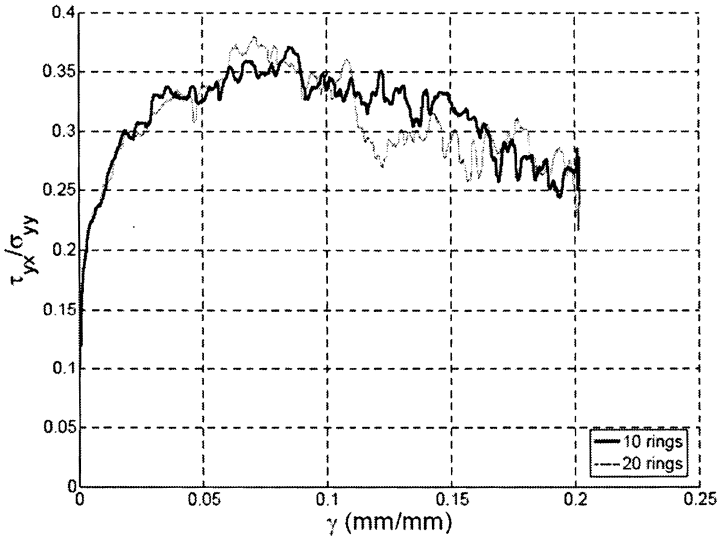

Fig. 2.93. Comparison of shear stress ratio for the 10 and 20 ring simulations (Shen, 2013)

Shen conducted all further testing with the 20,000 particle sample with 10 rings and fixed disk boundary conditions.

Shen performed three simulations keeping initial void ratio constant and varying vertical stress. No significant differences were observed in any of the recorded responses (Fig. 2.94).

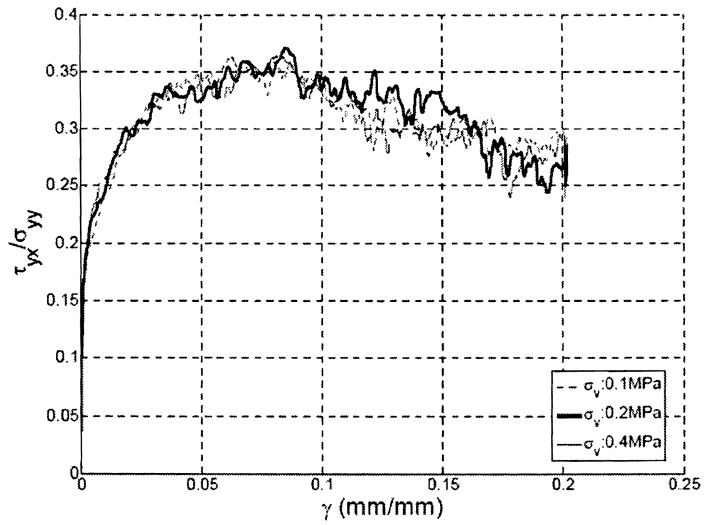

Fig. 2.94. Comparison of shear stress ratio for 10 ring simulations at different constant vertical stresses (Shen, 2013)

As mentioned previously, Roscoe et al. (1958) and Stroud (1971) showed that higher vertical stresses tend to give lower peak stress ratio values. The data presented by Shen for both the laminar and Cambridge devices contradicts this statement. The range of vertical stress values tested by Shen (2013)is relatively small compared to the range of those previously tested for sand. Additional simulations are needed to better understand this observed difference. It should also be noted that these

simulations are two-dimensional disks, and it is difficult to project the relationship to a similar three-dimensional simulation.

In terms of micromechanical response, Shen found that, although differences existed in the boundary and internal stresses, the distribution across the sample was generally uniform. Contact force rose diagrams show that the initial conditions reflect a somewhat homogeneous sample at K_0 conditions (i.e the majority of contacts are oriented vertically). At the peak shear strain, the contacts shift and are oriented mostly between 0 and 90°, with the largest concentration between 30 and 50° to the horizontal. Fig. 2.95 shows the rose diagrams for the initial and peak conditions.

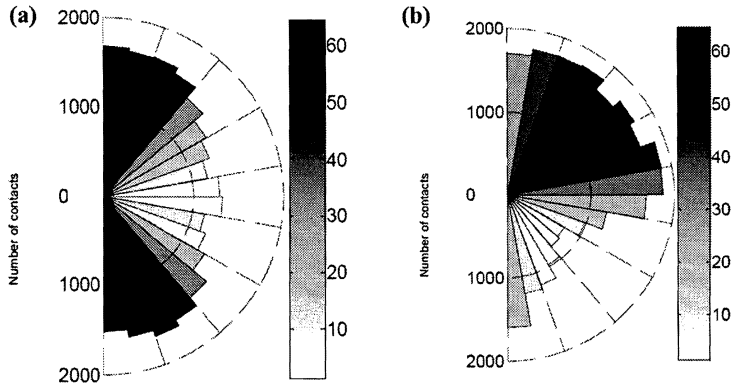

Fig. 2.95. Contact force rose diagram at (a) initial state 0% shear strain (b) peak 8.5% shear strain (Shen, 2013)

The major principal stress orientation at 8.5% shear strain was approximately 44° to the horizontal, matching this contact orientation zone. Using the central measurement sphere data, Shen was able to plot the angle of principal stress and principal strain rate orientation. Similar to previously discussed findings for granular soils, Shen observed non-coaxial behavior (Figs. 2.96 and 2.97).

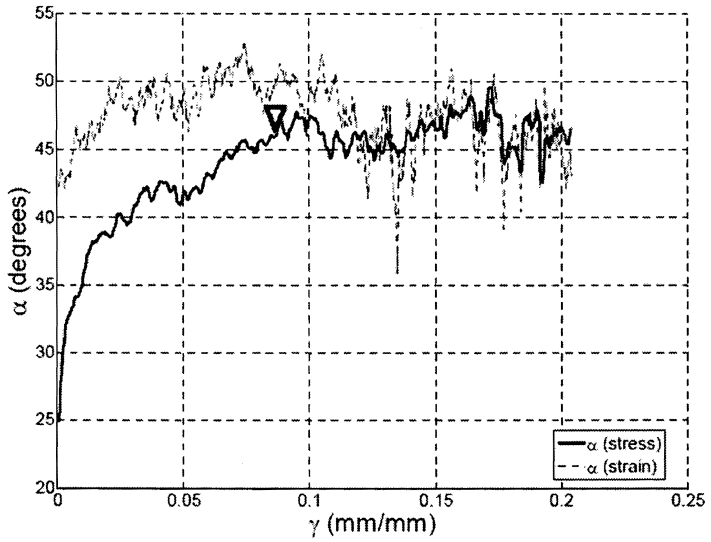

Fig. 2.96. Comparison of major principal stress orientation and major principal strain rate orientation during shearing (Shen, 2013)

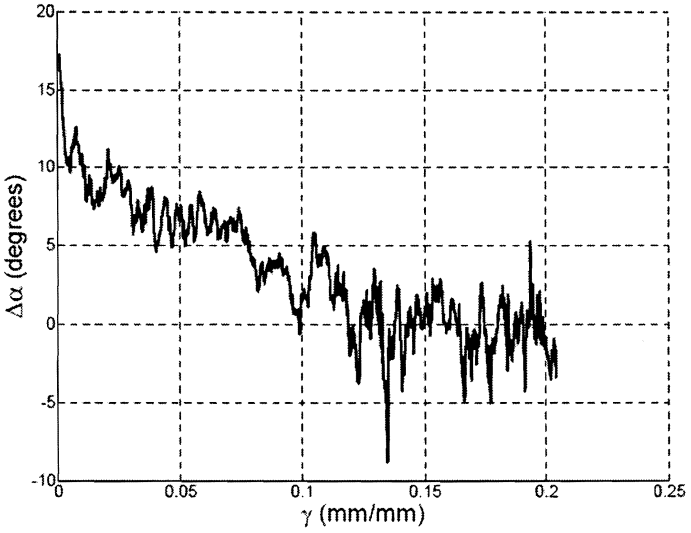

Fig. 2.97. Angle of non-coaxiality during shearing (Shen, 2013)

Initially at low strains, the principal strain rate and principal stress axes are not coincident. The strain rate orientation lags behind the principal stress until a shear strain of approximately 0.12. These results show that two-dimensional DEM simulations can successfully capture the expected granular soil behavior in simple shear. The findings from Shen's work are extremely valuable and provide an excellent platform to build this current three-dimensional research upon.

A recent study by Dabeet et al. (2011), using validated DEM model simulations of glass beads, examines the response of idealized granular soils to monotonic direct simple shear loading. PFC3D was used to model spheres representing the glass beads tested in the laboratory. The laboratory findings were discussed in a previous section. The geometry of the DEM assembly was chosen to match that of the laboratory device sample (approximately 70 mm in diameter by 20-25 mm high). Approximately 10,000 particles were generated using the radius expansion technique to a final diameter of 2 mm (similar to the physical laboratory particle sizes). The sample was compressed vertically by the top and bottom rigid boundary walls until the desired initial stress state was reached. A measurement sphere was used to monitor the stresses and void ratio of the sample during compression, as well as during the shearing phase. Measurement spheres are essentially virtual volumes over which PFC calculates average quantities such as stress, strain rate, porosity, etc. In this study, a measurement sphere with a radius of 8 mm is located within the central specimen core. One main issue arises with this method for validation studies using an NGI-type device. Many researchers have shown that sample core measurements differ from the boundary measurements for both stresses and strains (Cole, 1967; Stroud, 1971; Budhu, 1979; Dounias and Potts, 1993; Shen, 2013). These DEM simulations are validated by NGI-type device experimental data and no modifications to the device or the instrumentation are explained. Therefore, it is assumed that

boundary measurements were used in the laboratory and comparing the DEM sample core data directly could be misleading. It should also be noted that because measurement spheres calculate average quantities over the volume, the values obtained are extremely dependent on the size of the sphere used in relation to the particle size, further complicating their use for direct comparison to boundary measurements.

The simulations used a linear contact model requiring values for equivalent normal and shear stiffness. Two different values were tested to determine the most accurate in comparison with the laboratory data. The same value was used for both the normal and the shear stiffness. Figs. 2.98 and 2.99 show the results for the PFC simulations for K=500 and 50 kN/m, respectively.

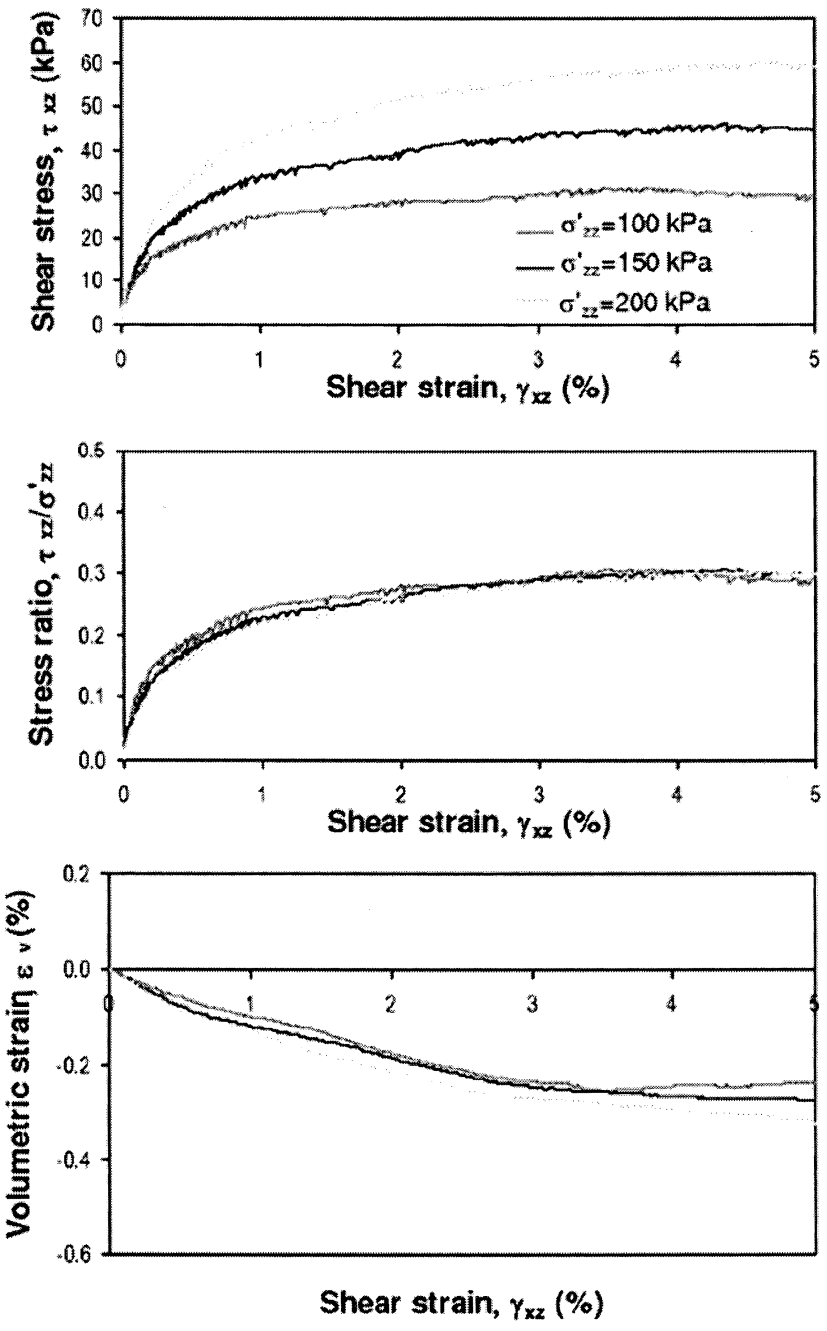

Fig. 2.98. Results for DEM simple shear simulations at different constant vertical stresses with K = 500 kN/m (Dabeet et al., 2011)

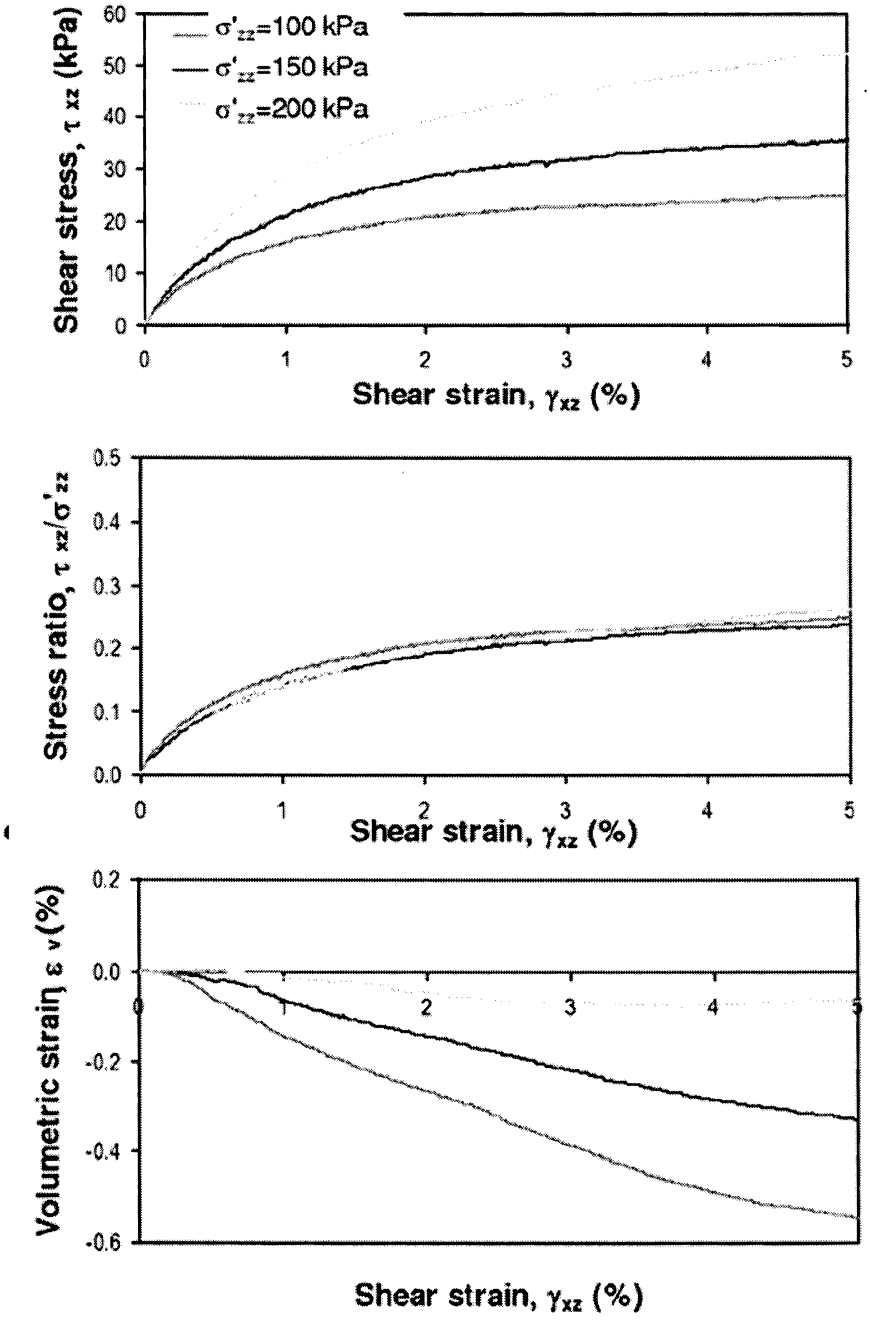

Fig. 2.99. Results for DEM simple shear simulations at different constant vertical stresses with K = 50 kN/m (Dabeet et al., 2011)

Although the laboratory and simulation data are not plotted together, it appears that the stiffness of 500 kN/m gives the most replicative curve shape. An investigation on the effect of the interparticle friction was conducted for the sample at lower stiffness. The highest friction value of 0.3 showed only slight increases in peak shear stress response. The value of 0.2 was used for the simulations presented. It is unclear if this value is physically reasonable for glass or if any attempts were made to measure interparticle friction in the laboratory.

While the curves presented seem to match the general trend of the laboratory data, several differences should be noted. The peak stress values, as well as the shear ratios are different for the DEM and laboratory data. Also, the laboratory sample appears to be continuing to increase in shear stress at 5%, while the DEM simulation for 500 kN/m has flattened out. The volumetric response is also different for the two samples with the laboratory sample contracting much more than the DEM samples even though it begins at a denser state. The trend in volumetric response, however, is similar for the laboratory and more dense DEM sample. Overall, this work shows that DEM can capture the three-dimensional behavior of granular material in simple shear and that laboratory validation of DEM simulations is a useful, but in no way an easy practice. While the inputs into a PFC simulation are very few, there is still much needed exploration into the sensitivity of the results to the various parameters. Wijewickreme et al. (2013) expanded upon these results in order to study the stress state in the DSS device. Both constant stress and constant height simulations were performed. The results show that the planes of maximum stress obliquity rotate during strain progression. Therefore, it appears that there is not simply one failure mode assumption that accurately calculates the friction angle for all values of strain.

2.7 Conclusions

The work presented above represents only a small number of the documented cases in which DEM simulations have been used to study granular soil behavior. What is apparent, however, is that a large number of questions still remain to be answered. The micro-scale information gained from simulating this type of physical element test can not only increase the understanding of the underlying mechanisms driving the drained response, it can also give insight into the actual testing conditions the samples experience in the device.

3. EXPERIMENTAL TESTING

Simple shear testing has been used extensively to study the behavior of granular soils, but due to the test constraints and difficult data interpretation there are still many questions left unanswered. The experimental testing program covers a number of different monotonic simple shear test conditions. The experimental results are then used as a means to validate the discrete element method (DEM) simulations presented in Chapter 4.

3.1 Sample Specifications

As mentioned previously, modeling sand is very difficult because of the large number of particles, and the interlocking behavior that arises from its angular particle shape. A cubic inch of Ottawa sand can contain over 250,000 individual particles. The computational time required for modeling even this small sample is unreasonable given current single-threaded DEM programs and computer capabilities. Additionally, PFC3D restricts modeled particle shapes to either spheres or clumps of spheres. Modeling easily analytically described spheres simplifies the contact detection, contact model requirements, and the overall calculations, greatly reducing the computational time required for a simulation. In order to satisfy PFC requirements and to provide a means to directly compare the experimental and numerical results, precision chrome steel ball bearings were used as the physical granular material.

Ballotini are available in many different materials, ranging from glass to titanium. Thornton and Sun (1993), Thornton and Lanier (1997), and Dabeet et al. (2011) used experimental data from physical glass ballotini tests to validate DEM models and showed success in qualitatively matching the responses. Similarly, Cundall and Strack (1979), O'Sullivan (2002), O'Sullivan et al. (2004), Cui and O'Sullivan

Table 3.1. Tolerances for grade 25 Thompson precision balls as specified by ABMA STD-10

ABMA Grade	Deviation from Spherical Form (mm)	Lot Diameter Variation (mm)	Allowable Ball Gage Variation (mm)	Maximum Surface Roughness (μm) "Ra"
25	0.00060	$\pm$ 0.000600	$\pm$ 0.0025	0.051

(2006), and Cui et al. (2007) used precision chrome steel ballotini for DEM validation and also found the qualitative response to be satisfactory. Wroth (1958) and several other researchers have commented on the tendency of glass beads to crush or compress. It is the author's opinion that precision metal spheres provide a more easily and accurately modeled material because they are not susceptible to particle crushing, they have more uniform shape and surface characteristics, and they are not likely to exhibit compressible behavior at the relatively low range of stresses tested. A number of metal sphere materials are available, the most common and inexpensive being a high-carbon chromium alloy steel, designated American Iron and Steel Institute (AISI) 52100. The current study used AISI 52100 Grade 25 precision chrome steel spheres manufactured by Thompson Precision Ball. This grade was selected because of the sufficiently accurate tolerances in size and sphericity maintained during manufacturing. The grade designation for sphericity is essentially the surface roughness and spherical form precision to which they are manufactured. Grade and gage designations for the particle size represent the amount of variation in the lot (actual) and nominal (specified) diameters. All spheres are tested to ensure they meet the industry standards set forth by the American Bearing Manufacturers Association (ABMA) STD-10. Table 3.1 gives the tolerances for Thompson Grade 25 precision spheres. Similar spheres were used in O'Sullivan et al. (2004), Cui and O'Sullivan (2006), and Cui et al. (2007) and have shown to provide the necessary accuracy for

Table 3.2. Sample size and particle diameters

	Number of Particles	Nominal Diameter (mm)	Nominal Diameter (in)
Sample 1	2,500	2.38	3/32
	2,500	3.18	1/8
	2,500	3.97	5/32
Sample 2	20,000	1.19	3/64
	20,000	1.59	1/16
	20,000	1.98	5/64

successful validation and comparison.

As shown in a theoretical study by Graton and Fraser (1935) and experimentally by Wroth (1958) in simple shear reversal tests on steel bearings, samples comprised of uniform spheres tend to adopt a regular packing array even when the initial packing is random. This crystallization, or locking, can give erroneous and inconsistent results. To avoid crystallization, three different diameter sizes are used in each of two samples: a 7,500 particle "prototype" sample and a 60,000 particle sample. Table 3.2 gives the corresponding number and size of particles for each sample. The number of particles and corresponding particle sizes satisfy several constraints. A target range for the number of particles per sample was chosen to be between 5,000 and 60,000 particles, based on computational limits for the modeling portion of the project. Shen (2013) showed that the sample dimension to particle size ratio has an influence on initial void ratio, as well as the subsequent shearing results. The sample containing smaller diameter sizes and hence a larger number of particles was less sensitive and likely gave a better estimate of the average shear strength. Similarly, two samples were used in this study: a sample with a small number of particles to be used as a prototype, and a sample with a larger number of particles to assess

the influence of the number of particles used on the main findings. Using a small number of particles for the prototype sample allowed for all of the initial simulations, sensitivity studies, and DEM model development to be preformed with a reasonable amount of computational efficiency. The results for the 60,000 particle sample were compared to the results of the 7,500 particle sample and used to generate additional findings. In order for the two samples to be more directly comparable, the ratio of the minimum to maximum particle diameter was kept constant for both samples. Also, the particle sizes used for the two samples were directly proportional (i.e. each diameter size in sample 1 is twice the diameter size of sample 2).

According to ASTM-D6528 (2007), the specimen height to diameter ratio should not exceed 0.4. Additionally, the specimen height to ball diameter ratio should be greater than 10. For a 101.6 mm (4 in) diameter specimen, this allows a height of up to 40.6 mm (1.6 in) and a ball diameter of 4.06 mm (0.16 in). Although this specimen height is allowed by ASTM, results by Franke et al. (1979) suggest a D/H ratio of 3.75 as the lower bound. This corresponds to a H/D ratio of 0.27 and a average ball diameter of 2.7 mm. The smallest diameter available from Thompson was 1.19 mm (3/64 in), which determined the limits for sample 2. Based on the other available particle sizes and the constraints presented, the above combination of sample conditions were chosen. Although sample 1 satisfies the ASTM requirements, it slightly violates the suggestions proposed by Franke et al. (1979). A comparison of the two sample sizes was performed for the experimental and numerical studies to assess the influence of the number of particles used on the response.

3.2 Equipment

3.2.1 TAMU-MDSS

This research study employs the use of the new multi-directional simple shear apparatus developed by Dr. Giovanna Biscontin and graduate research assistant Cassandra Rutherford at Texas A&M University (Fig. 3.1). A detailed description of this device and its features can be found in Rutherford (2012).

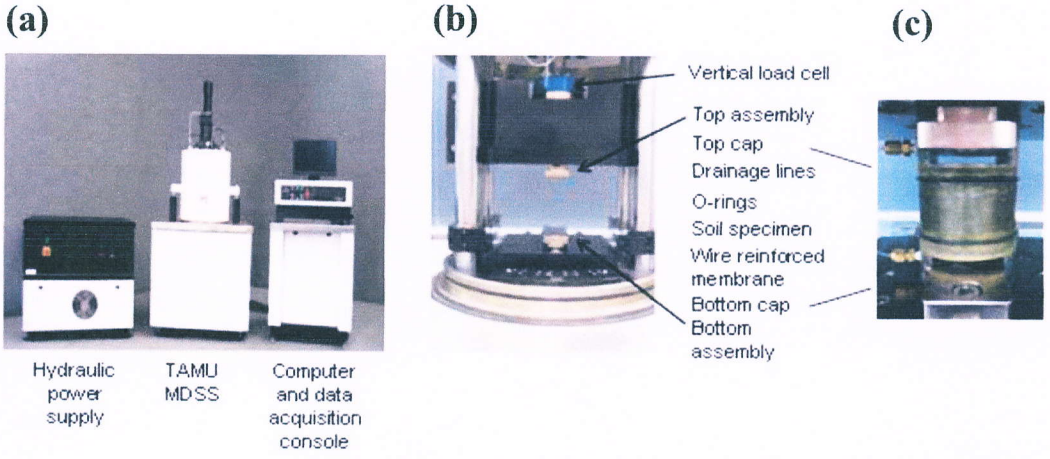

Fig. 3.1. TAMU-MDSS device (Rutherford, 2012)

This device is capable of loading along three independent axes allowing for application of vertical load and complex stress or strain paths in the horizontal plane. The servo-hydraulic controlled system allows testing at frequencies up to 20 Hz, as well as being able to test at displacement amplitudes up to $\pm$ 10 mm. This device also offers several improvements and additional features:

- A four column support was designed for the top assembly to minimize com-

pliance and increase the stiffness of the system, so that rocking motions are minimized.

- The TAMU-MDSS is equipped with a chamber allowing for back pressure saturation as well as additional lateral confinement during testing. Drainage lines are connected to both sample caps allowing for the independent measurement of both back-pressure and cell pressure. Two differential pressure transducers are also in place to measure the excess pore pressure and volume change during testing.

- Additionally, a multi-axis load cell located directly above the sample measures forces in three directions and torques about three axes allowing for extremely accurate data acquisition.

The device is controlled by Automated Testing Software (ATS), a closed feedback loop Proportional, Integral, and Derivative (PID) gain servo controller system. Values of P-gain are chosen based on the sample stiffness. Softer materials allow high P-gains, while stiff materials require low P values to keep the system stable. Because the metal ballotini create a very stiff sample, the system is extremely sensitive and the P-gain values were adjusted to smooth the control response. The correct values can only be determined by trial-and-error. The monotonic simple shear tests were conducted with a vertical P-gain of 30 and a horizontal P-gain of 10. The loose samples were more sensitive and required the vertical P-gain to be lowered to 15.

3.2.2 Parts and Accessories

The current configuration of the TAMU-MDSS, as described in Rutherford (2012), is capable of testing both clay and granular soil samples; however, changes in several of the sample components were required for the granular testing proposed.

The use of relatively large diameter chrome metal ballotini as the testing media required the need for a larger sample size and therefore, the machining of additional sample caps. Two options currently exist for lateral confinement to ensure k_0 conditions: NGI/Geonor wire-wrapped membranes and stacked thin metal confining rings. Because the stiffness of the steel ballotini is much higher than that of soils, metal confining rings were used to keep lateral strains to a minimum. A special split mold was also required so that the rings and interior membrane were in place before pluviating the sample. The following paragraphs describe the design and development of these components.

3.2.2.1 Caps

The caps previously developed for the TAMU-MDSS are 80 mm in diameter due to the restriction of the size of NGI wire-reinforced membranes available. As discussed previously, there are several restrictions for sample size based on the relatively large size of spheres available. An increased sample volume allows for the proper testing of the larger diameter chrome balls (i.e. 10 particles across the height of the sample); however, too large of a sample results in an unreasonable amount of particles for the modeling portion of the project. One of the main constraints in sample size for direct simple shear testing is the minimum diameter to height ratio. Larger diameter to height ratios (>3.75) limit the sample non-uniformities. Based on the work presented by Franke et al. (1979) and the size of particles available, 101.6 mm (4 in) diameter caps were designed and machined (Fig. 3.2). The top and bottom caps were both fitted with ports to accommodate the application of vacuum or any future testing where water is required.

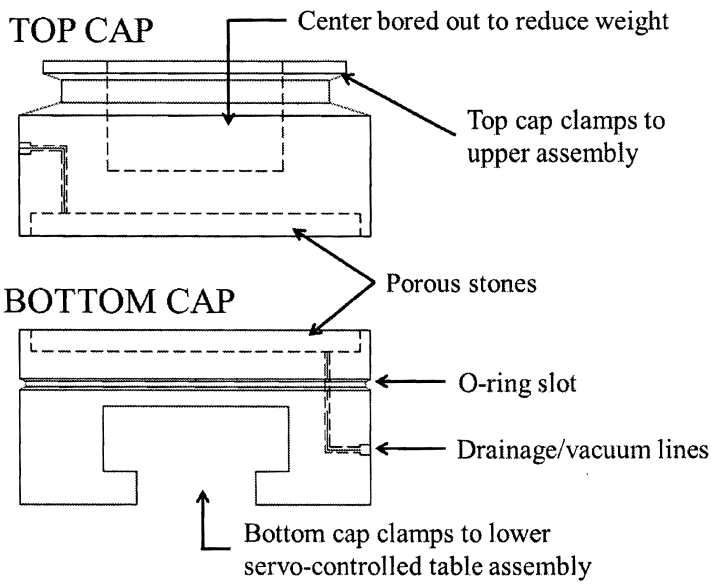

Fig. 3.2. Cross-sectional view of 4" diameter sample caps

3.2.2.2 Rings

To maintain the true simple shear plane strain conditions, the sample must maintain a perfectly circular sample cross-section (i.e. k_0 conditions) during the initial loading and shearing phases. ASTM D6528-07 and ASTM D2435-11 allow for either wire reinforced membranes or stacked rings to be used as lateral confinement methods for DSS testing. In a recent study comparing the two types of confinement, McGuire (2011) showed that the measured values of undrained strength for marine clays and low plasticity silts were very similar in both systems. The wire reinforced membrane samples exhibited more strain softening beyond the peak and higher vertical strains; however, the differences in the two systems were very small. The tests conducted in the TAMU-MDSS in Rutherford (2012), used NGI/Geonor wire-reinforced latex membranes and additional cell pressure around the sample to

minimize lateral expansion. The samples tested were soft Kaolin clay and shallow Gulf of Mexico marine clays and their stiffnesses are relatively small when compared to the strength of the wires. While some expansion is still probable between the wire reinforcement, the overall cross-section can be adequately maintained for these soft clay samples.

The chrome ballotini used in this study are virtually incompressible and their stiffness is much greater than the clay or sand samples normally tested using the wire-reinforced membranes. The metal ballotini would more than likely deform the wire-reinforced membrane and the k_0 condition would be forfeited. For these reasons, it was necessary to use a more stiff system, such as a stack of thin metal rings (Fig. 3.3). The steel ring dimensions are 4.4745" +- 0.0155" O.D., 4.0455" +- 0.0155" I.D., and 0.025" thick. The complete sample is confined by a stack of these individual rings with a thin latex membrane positioned between the spheres and the rings. This allows each ring to move as the sample boundary walls are sheared while still maintaining a close to perfect circular cross-section. To reduce any effects on the sample due to friction between the rings as they move, they are coated with a Perma-Slik G air dry MoS_2 spray application coating produced by Everlube Products. This coating has a coefficient of friction of 0.04 to 0.06 according to the ASTM D2714 test method. A correction factor was determined for the system to account for any effects of the membrane or rings on the measured shear stress. The methods and corresponding findings are presented in the experimental chapter below.

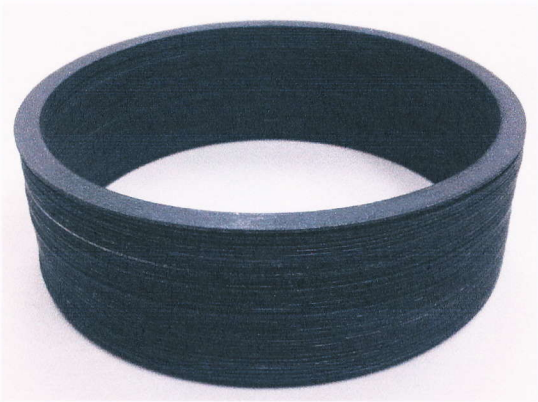

Fig. 3.3. Stack of coated rings used for lateral confinement

3.2.2.3 Split Mold

Because of the size of the sample, the use of the stacked rings, and the nature of preparing a granular sample, a special split mold was designed and machined (Fig. 3.4). This particular split mold allows for the sample to be prepared with the ring stack and membrane confinement already in place, minimizing changes in density. Similar to other commercially available molds, vacuum can be applied to the membrane for proper sample preparation and then to the prepared sample, allowing for the transfer of the assembled sample to the testing device with minimal disturbance. The top sections of the split mold are removed before shearing and the lower section is left in place to provide a base for the rings (Fig. 3.5). This base sits on top of a rubber o-ring placed within a machined grove to ensure the ring stack is level.

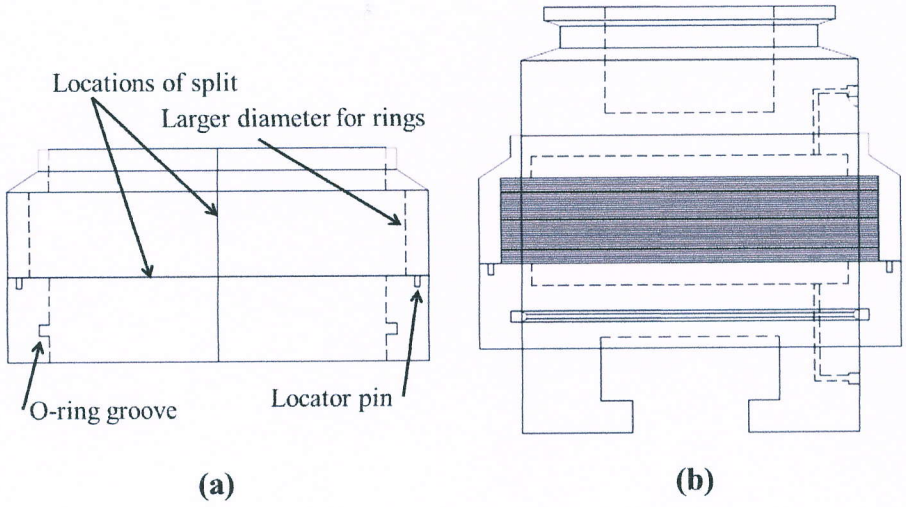

Fig. 3.4. Split mold (a) cross-sectional view (b) schematic of split mold and sample

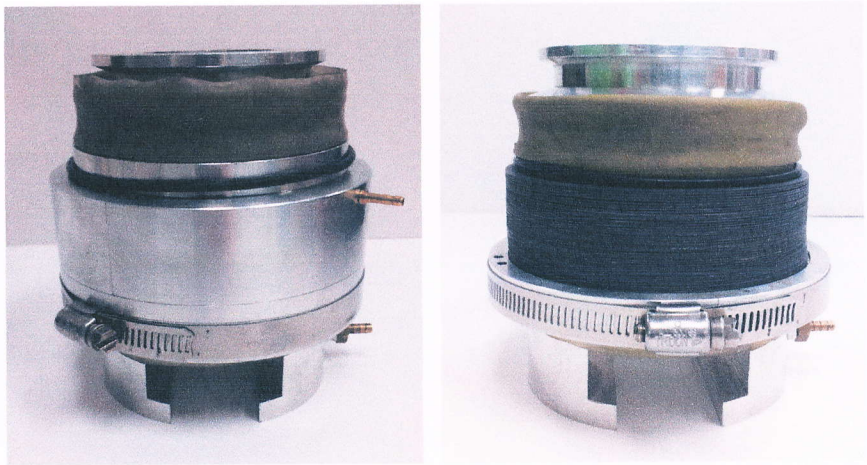

Fig. 3.5. (a) Prepared sample with split mold (b) sample with top sections of split mold removed and base section supporting ring stack

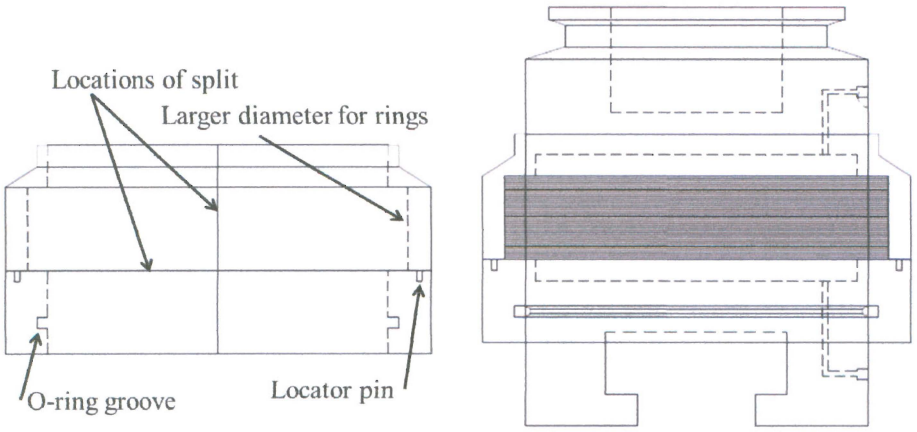

Fig. 3.4. Split mold (a) cross-sectional view (b) schematic of split mold and sample

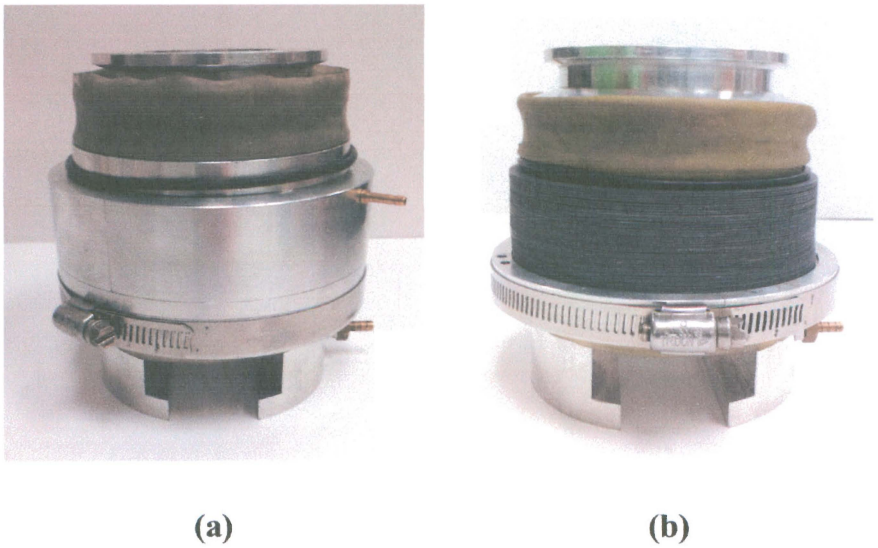

Fig. 3.5. (a) Prepared sample with split mold (b) sample with top sections of split mold removed and base section supporting ring stack

The split mold was also fitted with an additional extension ring allowing for testing of samples with various heights. Without the extension, a sample height of 25.4 mm (1 in) is targeted for the 101.6 mm (4 in) diameter sample. This ratio satisfies the previously discussed conditions for testing with sand and corresponds to similar H/D ratios commonly used. As mentioned above, sample 1 is comprised of particles which are slightly larger than the intended ratio of 10:1. For a sample height of 1 inch, the ratio of the sample height to average particle diameter is only 8. When all 7,500 particles are included, the sample height is increased and a ratio of 9 is reached. In turn, additional height is needed in the ring stack and the split mold. It should be noted that this additional height violates the findings of Franke et al. (1979), but is well within the requirements stated in the ASTM standard.

3.3 Experimental Testing Program

As mentioned previously, the overall goal of this study is to gain insight into the micromechanical mechanisms that drive granular behavior. The macro-scale information recorded during testing is used to study the overall response of the idealized granular material, and to validate the DEM models presented in the following chapters. For each of the test paths, the values measured include: vertical displacement and load, and horizontal displacements and loads independently for the x-axis and y-axis.

3.3.1 Initial Device Evaluation

3.3.1.1 Sample Boundary Conditions

Only a very limited number of studies on metal ballotini existed, so it was necessary to conduct several initial monotonic tests in order to obtain the preferred testing conditions. These tests gave an indication of the normal load and PID control

effects on sample response. One of the first adjustments made based on these tests was to the sample cap surfaces. It was determined that the porous stones did not create enough friction on the metal spheres at 50 and 100 kPa vertical effective stress to induce shearing throughout the sample. Several options are available to create a rough boundary. These include: caps with waffle-like depressions, caps with fin-like projections, and caps with particles fixed to the surface. The most practical option for both the experimental and modeling schemes is to use the caps with fixed particles. A similar approach was used in the DEM simulations by Shen (2013) and in the experimental investigation by Stroud (1971). Therefore, to reduce slippage at the boundaries and ensure simple shear conditions are transmitted through the sample, the metal spheres were physically glued using epoxy to the top and bottom porous stones. Figure 3.6 shows the rough sample boundaries created by gluing the spheres to the caps.

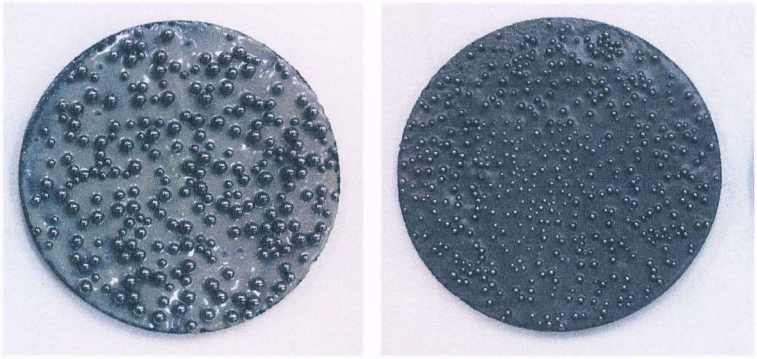

(a) **(b)**

Fig. 3.6. Top and bottom caps with epoxy fixed particles (a) sample 1 (b) sample 2

3.3.1.2 P-gain Evaluation

The TAMU-MDSS is a hydraulic servo Proportional Integral Derivative (PID) gain controlled system requiring various input values of P based on the stiffness of the sample. The P value can essentially be thought of as the accelerator controlling how fast the machine tries to reach a target load or displacement. A low P may be more stable, but will undershoot the targeted value. A high value will accelerate faster and more closely reach the target value, but it could be unstable. For certain systems, slight instability is not critical; however, for granular systems where the initial densities are trying to be maintained throughout initial loading and testing, oscillations should be minimized.

There is no set method or equation relating the P value with stiffness, therefore, a trial-and-error approach was used to determine the most appropriate value for P. For a monotonic strain-controlled test where the bottom plate is displaced along the x-axis, a P value is required for the vertical control (Pz), as well as the horizontal control (Px). Both values affect the sensitivity of the control and the machine's ability to hold a constant vertical stress. In other words, if a high P is chosen for the horizontal control, a sufficiently high P will also be required for the vertical control. If one is much faster than the other, instabilities will occur. It should also be noted that different values are generally required for displacement and stress control. Tests conducted in stress control tend to allow higher P-gain values than what is required for the same test in displacement control.

Initial P values for the strain controlled monotonic tests were set to Pz=150 and Px=250. These values correspond to gains used by Rutherford (2012), and provided a useful starting point to begin the analysis. The tests were performed at a shear strain rate of approximately 5% per hour. Note that tests at different

displacement rates would need different P values than those determined below. The target vertical load for the 50 kPa constant stress tests is 0.405 kN, shown by the horizontal line in the figures below. Figs. 3.7 through 3.11 show the progression of trials and corresponding vertical and shear control for the various P gains tested.

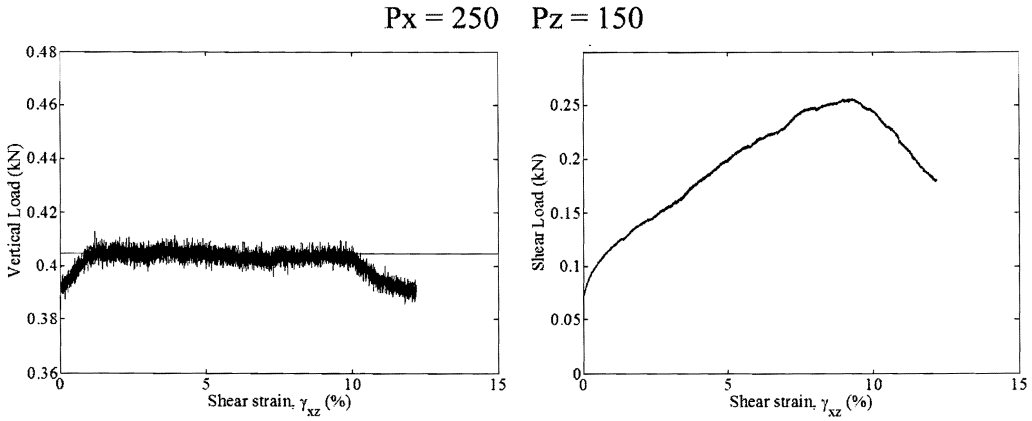

Fig. 3.7. Vertical and shear load control with Px=250 and Pz=150

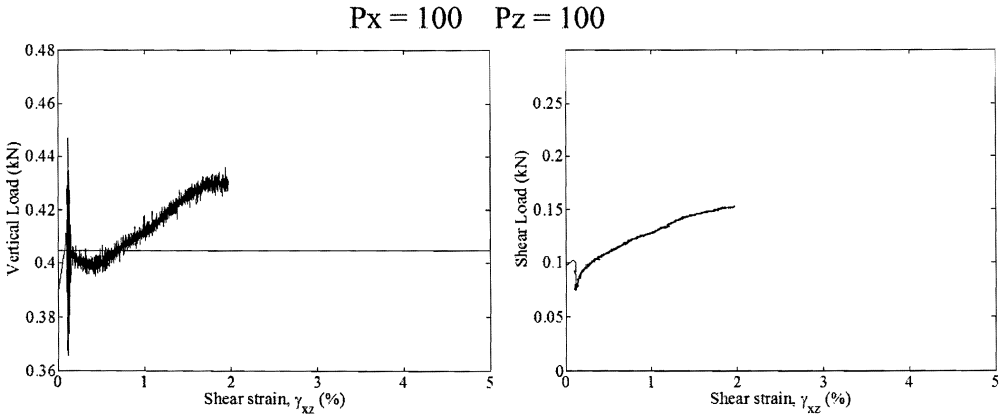

Fig. 3.8. Vertical and shear load control with Px=100 and Pz=100

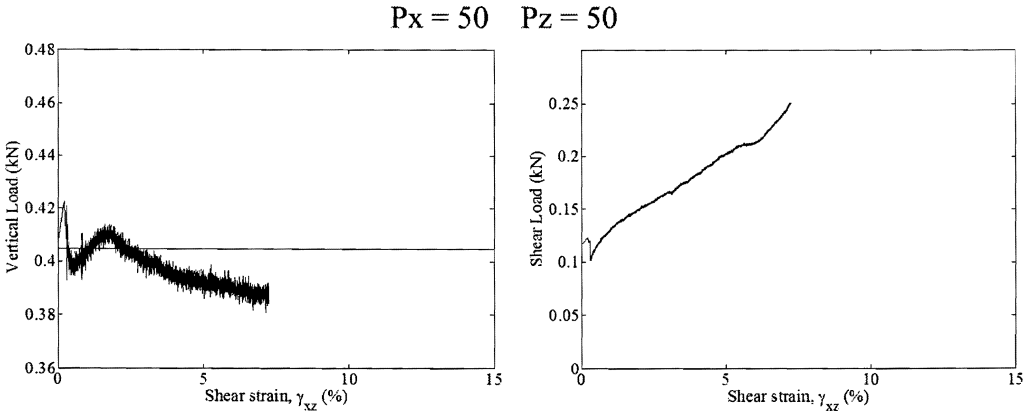

Fig. 3.9. Vertical and shear load control with Px=50 and Pz=50

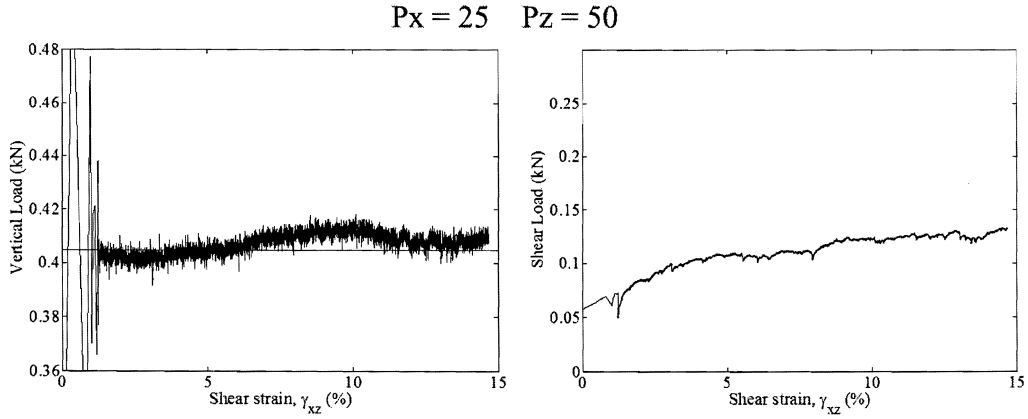

Fig. 3.10. Vertical and shear load control with Px=25 and Pz=50

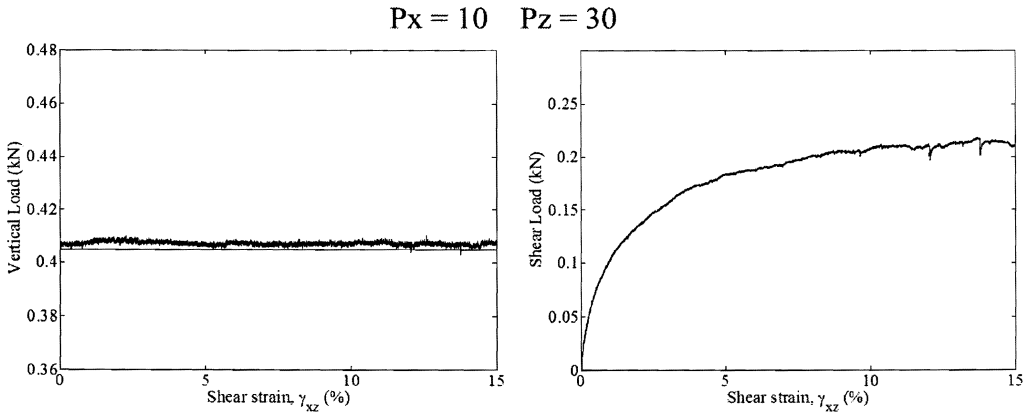

Fig. 3.11. Vertical and shear load control with Px=10 and Pz=30

The tests were each carried out to various shear strains based on the quality of the control at that particular P value. A number of other combinations of P values were tested between each interval presented, but are not shown because they provide no additional insight. As seen in the figures, several of the tests were initially unstable, but they were continued to assess the effects of the vertical control on the shear response. It is clear from the above plots that vertical stress control strongly influences the shear response, therefore, it is important for the constant vertical stress conditions to be properly maintained.

The initial settings allowed the load to slowly increase and then decrease after some time. It is clear from the plot that the vertical P value was too low to maintain the constant vertical load at the beginning of the test. A plot of the volumetric strain, representing the top cap vertical displacement, also supports this conclusion (Fig. 3.12).

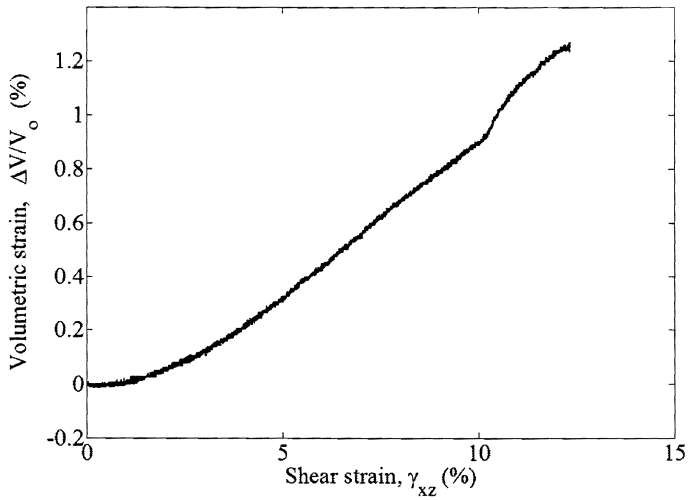

Fig. 3.12. Vertical displacement for Px=150 and Pz=250

The top cap position is initially held relatively constant, while the vertical stress decreases. The sample most likely contracts initially, slightly reducing the vertical load because the top cap cannot move down fast enough to maintain this value. Once the sample begins slowly dilating, the load is increased back to the intended value and the Pz gain is high enough to maintain these slowly changing conditions. The possible reasons for the load to decrease at approximately 10% shear strain is less clear. One explanation could be that the vertical P value was not high enough to quickly recover from a force chain collapse. In other words, if the load carried in a collapsed force chain is not immediately picked up by another force chain, the sample densifies until the contacts in a new force chain pick up the load. If the vertical control is not sufficiently fast in moving downward in this process, the load is decreased. It appears from the volumetric strain plot, however, that the top cap suddenly dilates around the same shear strain value where the vertical load decreases. This sudden dilation could also be caused by a response to force chain

disturbances and low vertical gain would not allow the device to recover quickly enough to correct the stress reduction. Overall, it is concluded that a higher value of Pz is needed for a Px of 250. The vertical control must be sufficiently fast to "keep up" with the horizontal displacements and changing vertical conditions due to force chain collapse.

Several attempts were made using equal values of Pz and Px, but this led to instabilities at the beginning of the test. It was initially believed that Pz was the major contributor to the unstable response, but after examination of the shear stress and shear displacement curves at the initial start of the test, it was determined that the plate initially "jumped" in the X-direction. This was true for all tests presented until the Px value was sufficiently low compared to the Pz value (Fig. 3.11). This combination of P gains gave good control for both loose and dense sands. In some cases, the Pz value was lowered during the initial loading phase to increase stability and limit oscillations. Some oscillations were unavoidable; however, and it was difficult to maintain the initial void ratio in the loose samples even at very low values of Pz.

3.3.1.3 Combined Data Correction

Two features of the device design and setup possibly affect the experimental results, but are not present in the DEM models. These are the table friction and additional resistance due to the membrane and frictional response of the confining rings. A separate study of each was conducted to determine the need for correcting the experimental data.

Rutherford (2012) showed that the measured load due to friction in the linear bearings was different in the X and Y horizontal directions. This is because the bottom assembly moves as one entire unit in the Y direction, while only the top half

moves in the X direction (i.e. less normal force equals less friction). Similar observations were made by the author during the initial device evaluation. Consequently, all tests were conducted along the X axis to minimize the effects of friction on the measured response. An initial assessment showed that the additional stress due to friction increased steadily, but remained less than o.6 kPa for all ranges of shear strain with zero vertical stress (Fig. 3.13).

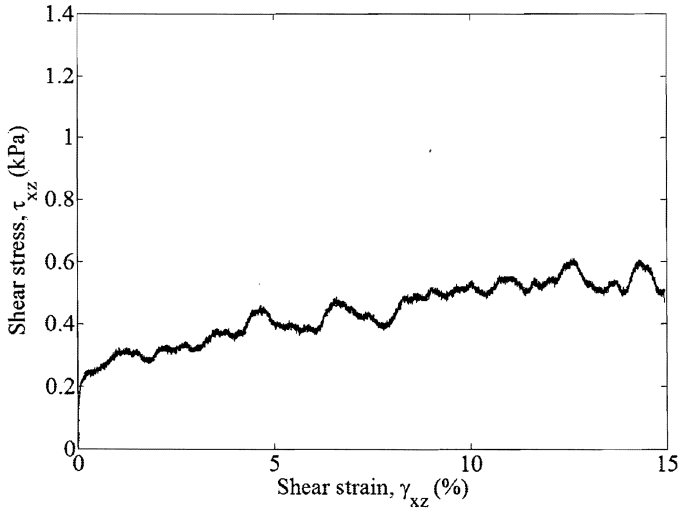

Fig. 3.13. Measured table friction for test with zero vertical stress

This test was conducted at strain rate of 1.5 mm/hr with no sample installed. A second test was performed to examine the response under a higher vertical stress. Free weights, equivalent to the load used for the 50 kPa tests, were stacked on the plate. The plate was then moved along the X axis at the same 1.5 mm/hr rate. The maximum stress due to friction was less than 0.7 kPa at all strain levels (Fig. 3.14). Therefore, the magnitude of normal force did not have a large impact on the measured table friction.

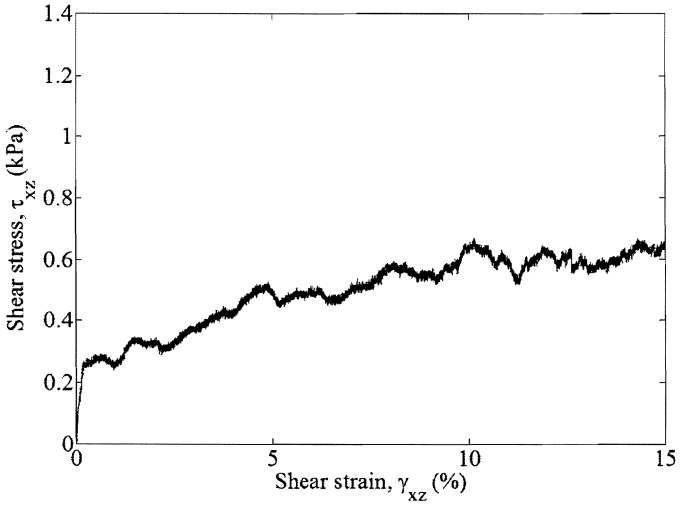

Fig. 3.14. Measured table friction for test with 50 kPa equivalent vertical stress

The system also allows for the linear bearings to be oiled, which reduces the friction. Fig. 3.15 shows the response for a test conducted directly after oiling and a test conducted after approximately 10-12 tests were conducted without oiling. The non-oiled test response reaches a higher peak table friction value of approximately 1.2 kPa at 11% shear strain. This finding showed the importance of routinely oiling the system. For the remainder of the testing, the system was oiled every third test.

In a study on the additional resistance caused by confinement systems, McGuire (2011) showed that the additional stress caused by the ring confinement system was slightly higher than that caused by the wire reinforced membrane. Both confining systems were tested with the membranes filled with water, following the idea that water does not carry shear stress and that any measured stress is due to the confining system alone. The rings used in McGuire's study were much wider than those used in this study (Fig. 3.16).

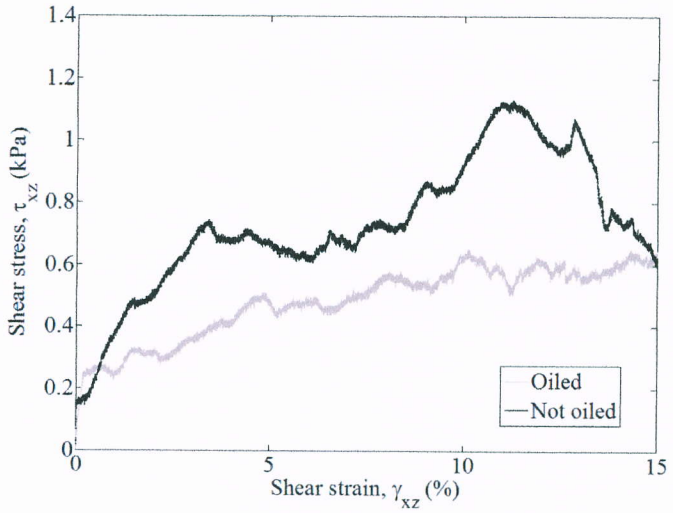

Fig. 3.15. Measured table friction for oiled and non-oiled tests with zero vertical stress

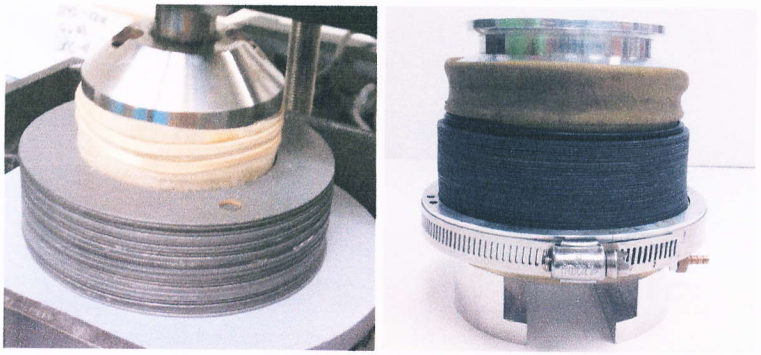

Fig. 3.16. Stacked rings (a) Geocomp Teflon rings (from McGuire, 2011) (b) rings used in this study

The thinner rings, in turn, have less surface area touching and should result in a lower stress. A similar study was conducted in this research to determine whether

a correction was needed to account for the ring confining system. Fig. 3.17 shows the measured response for a test with an empty attached sample. No water was used in this particular test.

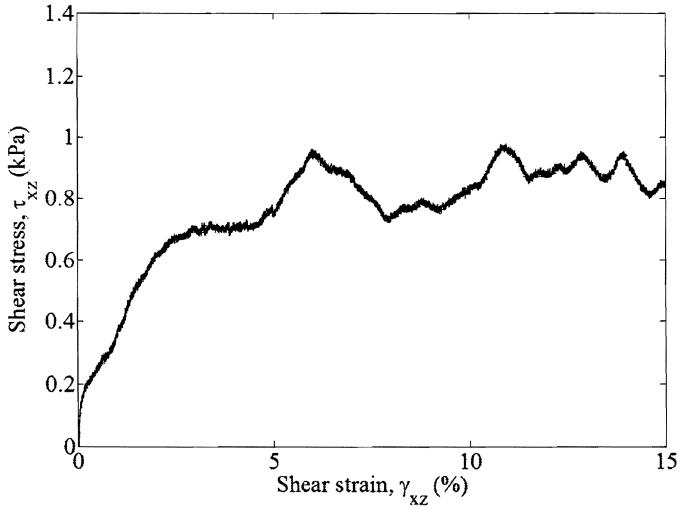

Fig. 3.17. Measured resistance for test with empty sample attached

An additional test was conducted with the sample filled with water at 13.8 kPa (2 psi). McGuire showed that the correction was not strongly influenced by the amount of backpressure present. For this reason, only one backpressure value was considered. Fig. 3.18 gives the response for the empty test and for the test conducted with water.

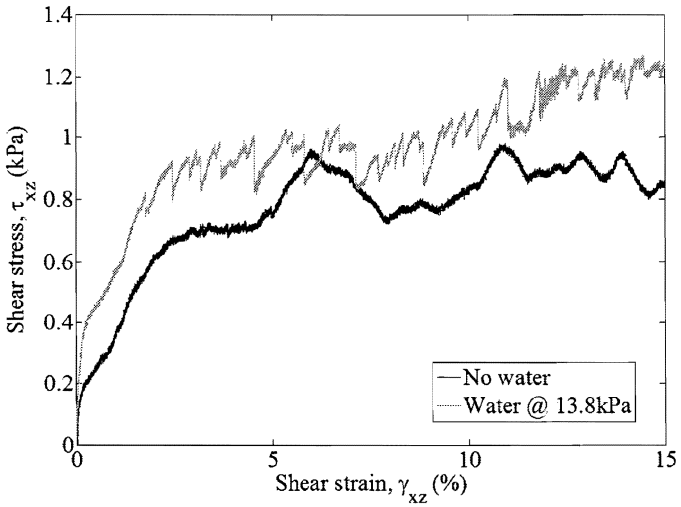

Fig. 3.18. Measured resistance for membrane ring confinement system

A combined correction was determined by adding together the response for the 50 kPa equivalent test and the ring confinement test and subtracting out the friction test at zero load to account for the already included frictional component in the ring correction data. Fig. 3.19 shows an example of a corrected and uncorrected test. Although the magnitude is small, the confinement system and table bearing friction do influence the measured shear stress response, most notably at higher strain values. Because the experimental results are used for validation of DEM samples where the effects of table friction and membrane and ring resistance are removed, all of the experimental results presented henceforth are corrected.

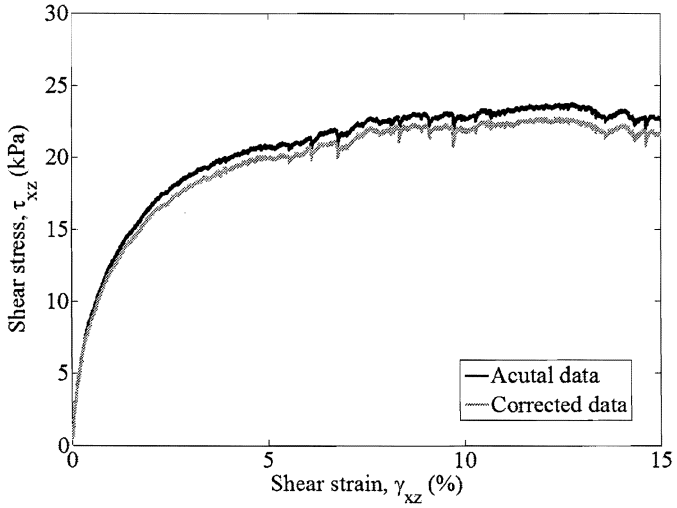

Fig. 3.19. Example of corrected and uncorrected data

3.3.2 Laboratory Sample Preparation

3.3.2.1 Background

Previous laboratory studies have shown that sample preparation methods affect the sample fabric and hence the mechanical response observed. Differences in soil response during the later stages of testing have been attributed to variations in the initial fabric of the sample even when the samples are created at the same densities (Oda, 1972; Ladd, 1974; Mulilis et al., 1977; Nemat-Nasser and Tobita, 1982; Wood and Yamamuro, 1999; Vaid et al., 1999; Vaid and Sivathayalan, 2000; Jefferies and Been, 2006). Early studies consisted of exploring the effects of specimen preparation on the shearing behavior of clean sands both in monotonic and even cyclic triaxial testing. Mulilis et al. (1977) showed that the preparation method also greatly affected the liquefaction potential of reconstituted sand samples. The majority of these studies were conducted using triaxial and cyclic triaxial undrained

tests and considered only relatively low strain ranges. Recently, Sadrekarimi and Olson (2012) showed, however, that critical state behavior was independent of the specimen preparation method. Ring shear tests performed on three different clean sands showed that the critical void ratio values plotted on the same critical state line, irrespective of sample preparation method. It should be noted that the simple shear tests were only carried out to 15% shear strain in the current study. Critical state is generally obtained at much higher strains.

Laboratory sample preparation methods for sands generally consist of some form of deposition (wet or dry), often followed by tamping or vibrating to obtain denser samples. Dry or air pluviation is the most common method used to create dry samples at different densities. This method replicates the depositional process for natural alluvial and marine deposits. Specimen are prepared by "raining" sand from a hopper of various forms, often through a dispersing screen. Different drop heights and aperture diameters are used to generate samples of various densities. The hopper is moved vertically as the sample is deposited in order to keep the drop height constant and create a uniform sample. The previously discussed experimental testing by Stroud (1971) followed this air pluviation method using a set of hoppers developed by Cole (1967). Stroud lists four basic requirements that should be met when preparing samples:

1. The air voids should be uniform throughout

2. A full frictional contact should be developed between the top surface of the sand and the face of the top sample cap

3. The surface of the sand should mirror the surface of the sample cap, so that the load is distributed to the sample uniformly

4. The sample should be the least disturbed as possible and care should be taken during preparation and loading to avoid local disturbances and overloading

Vaid and Negussey (1984) and Wijewickreme et al. (2005) used air pluviation techniques and showed that density increases with increasing fall height and decreasing mass flow rate for Ottawa and Fraser River sands, respectively. Wijewickreme et al. (2005) generated a characteristic curve relating density with flow rate and average fall height for Fraser River sand (Fig. 3.20).

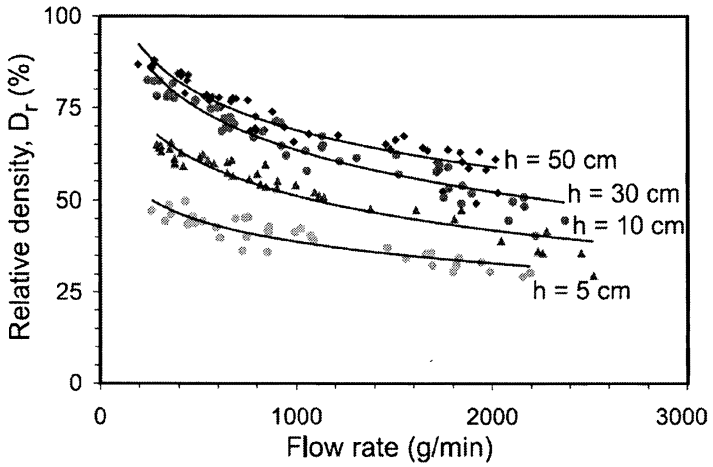

Fig. 3.20. Characteristic curve relating sample density to flow rate and drop height (Wijewickreme et al., 2005)

Two adaptations of the dry pluviation method are used in order to create looser samples. Dry funnel deposition is often used to reduce the drop height, thereby, reducing the density of the sample. Sadrekarimi and Olson (2012) created samples at the loosest possible fabric by using a funnel with a tube attached. Dry sand was poured into the tunnel with the tube initially touching the bottom of the specimen

mold. The funnel and tube were then slowly raised vertically to deposit the sample with a near zero drop height. A second method uses a mesh sieve to generate a loose sample. The sand is deposited with the mesh in place at the bottom of the sample mold. Once the particles have settled, the mesh is slowly raised through the sample generating a more loose and uniform sample than what was initially pluviated.

Wet pluviation is similar to air pluviation except that the particles are deposited through water. This process replicates the soil fabric formed by natural alluvial deposition. Some studies have rained dry sand through water; however, depositing pre-saturated sand is preferred (Wood and Yamamuro, 1999). Wood and Yamamuro describe a method in which the sand is initially placed in water in a volumetric flask and de-aired. The sample mold and attached lines are filled with water and the flask is inverted lowered to the bottom of the split mold. The sand is deposited by slowly raising the flask vertically keeping a zero drop height. Similar techniques have been used by a number of other researchers (e.g. Mulilis et al., 1977 and Vaid and Negussey, 1984). Kammerer (2002), in a study on liquefaction potential of sands, used wet pluviation followed by either pulling a screen up through the sample to create a looser sample, or vibrating the base to create a denser sample.

An additional method, moist tamping, is used to replicate field cases in which sand is deposited as hydraulic fill and then submerged. Dry sand is mixed with water to obtain a specific water content and then is poured and gently tamped into the sample mold in a number of layers. Similar to standard compaction procedures, each layer is scarified before the next is placed. This method produces samples that are very resistant to densification and tend to exhibit a contractive, strain-softening behavior. The main advantage of the method is that it allows for precise control over a range of void ratios. As noted in studies by Sadrekarimi and Olson (2012), tamping at a low water content (5%) produced a stable sand fabric over a large range of void

Table 3.3. Maximum and minimum void ratio following ASTM standards

	Sample 1 e_{min}	**Sample 1** e_{max}	**Sample 2** e_{min}	**Sample 2** e_{max}
Average void ratio	0.594	0.719	0.583	0.684
Standard Deviation	0.002	0.020	0.002	0.011

ratios that were maintained well after the split mold was removed. In a study on liquefaction potential of sands under various conditions, Boulanger et al. (1993) used moist tamping procedures because of the added ability to control sample density very precisely. Kammerer (2002) notes, however, that the method does not produce sample fabrics which are well representative of true field conditions.

Several variations of the methods presented above have also been proposed by researchers for various applications and relevant situations. Note that more dense samples can be generated for any of these methods by simply vibrating or tamping the sample. This is often carried out in lifts in order to create a more uniform sample.

3.3.3 Laboratory Sample Preparation used in This Study

As an initial assessment of the possible range of void ratios, the maximum and minimum densities were determined according to ASTM D-4253 Method 2A and D-4254 Method A, respectively. Table 3.3 gives the resulting void ratios. These values were determined using an 80 mm diameter metal container. The range obtained was extremely small compared to the normal range for sands, but they fell in line with previous finding for metal ballotini. The inability to create a larger range of void ratios is most likely due to the very low inter-particle friction and spherical shape of the metal ballotini.

Once the maximum and minimum void ratios were determined, several options

Table 3.4. Void ratios for various sample preparation methods

Method	1	2	3	4	5	6
Average void ratio	0.630	0.722	0.706	0.738	0.711	0.687
Standard Deviation	0.005	0.016	0.020	0.007	0.008	0.019

were considered to create various intermediate void ratios. Because no water was used in this testing, air pluviation was the preferred sample preparation method. A method similar to that used by Stroud (1971), Vaid and Negussey (1984), and Wijewickreme et al. (2005) was initially employed to create samples at a range of densities. Hoppers with a number of different aperture sizes, mesh sizes, and drop heights were tested; however, the range of densities created was small and very inconsistent. Several other methods were also performed in a effort to create more uniform and repeatable results. Table 3.4 summarizes the various methods and corresponding average void ratios and standard deviations. Note that these studies were carried out only for sample 1.

Method 1 consisted of vibrating and tamping the sample in three separate lifts. This was intended to create the densest sample. Method 2 used a 5.5 mm square opening mesh, which was kept at a constant distance from the sample height as the metal spheres were poured through. Method 3 was a similar technique using a 7.7 mm square opening mesh. Methods 4 and 5 consisted of placing the 5.5 mm and 7.7 mm mesh, respectively, at the bottom of the sample and then raising the mesh vertically through the sample after pluviation. This was intended to give a loose and uniform sample. Method 6 was simply air pluviation with no mesh in which the bottom of the hopper was removed quickly and the particles were allowed to free-fall. As with previously tested methods, the range of void ratios was quite small

and several of the methods were inconsistent.

These trials were conducted using the split mold rather than the metal container. It was determined that for a 101.6 mm (4 in) diameter sample, the void ratio measured was very sensitive to sample height. In other words, because the diameter was significantly large, only slight changes in height had a significant impact on the void ratio. These differences were due to not only the experimental variability in the density, but also to the instrument precision and the accuracy of the volume of solids used for the calculations. For example, the calipers used measured to the 0.005 mm. A difference of only 0.005 mm in height gave a difference in void ratio of 0.007. This difference due to measurement precision only is approximately 7% of the total range of the void ratios obtained. The number of particles and volume of solids used was estimated based on the weight of each particular size used and the corresponding density. The number of particles actually present in the samples could have varied from the number used in the void ratio calculations. Considering the 4.0 mm particles used in sample 1, a difference of only 5 particles makes a difference of 0.002 in void ratio (2% compared to the total range). These possible measurement errors were more severe for sample 1 because of the increased particle size to volume ratio. A comparison of the densest void ratios from various containers and calibration methods was made to ensure that the measurements were accurate for samples in the split mold. The densest case was used because it was the most repeatable for all containers. To control the possible variability in the split mold measurements, a number of very careful height measurements were taken at various locations across the sample and averaged for each trial. Ultimately, the sample was vibrated following the same procedure used to determine minimum void ration for sample 1. The e_{min} calculated for the split mold was 0.602 compared to 0.594 as determined originally in the 80 mm diameter container. This difference is well within the variation expected

for measurement error and showed the techniques to be satisfactory.

Because of the narrow range attainable, only the loosest and densest states were of interest for the subsequent laboratory testing. Two methods were finally determined to be the most repeatable and create the most uniform samples for the densest and loosest states. The method used to create the dense sample had a low standard deviation showing it was repeatable. This method is also similar to the methods outlined in the ASTM standard for determining the maximum density of a granular material. Method 4 gave the highest void ratios for samples 1 and 2 and was repeatable. It also likely created a uniform sample. The void ratio determined using this method was higher than that obtained following the ASTM procedure for sample 1. For sample 2, the two values were very close. Method 4 also had a smaller standard deviation and was therefore more repeatable for both samples than the funnel procedure used in the ASTM method. Method 5 gave similar results, although, the sieve openings were slightly too large and resulted in a lower void ratio. Table 3.5 gives the resulting void ratios for the 7,500 and 60,000 particle samples at the densest and loosest states. Note that sample 2 uses a 3.2 mm (1/8 in) mesh sieve. The sample preparation steps using the split mold are described below for the loose and dense cases.

Prior to pluviation of the sample, the split mold, rings, membrane, and bottom sample cap were assembled with vacuum attached to pull the membrane close to the sides of the split mold and rings (Figure 3.21).

Table 3.5. Dense and loose void ratios for sample 1 and sample 2

Sample	1	2
Dense void ratio	0.630	0.607
Standard deviation	0.005	0.006
Loose void ratio	0.738	0.672
Standard deviation	0.007	0.012

Fig. 3.21. Split mold assembly prior to pluviation

To achieve a dense sample, the metal spheres were poured directly into the split mold in three lifts. Each lift was vibrated by tapping the exterior face of the split mold and then tamped to further densify the sample before adding the next lift. Once the last particles were vibrated, the sample top was lowered into place and tamped to ensure a full frictional contact between the sample and the top cap. Vacuum was applied to the sample through the bottom port and height measurements were taken.

To achieve a loose and homogeneous sample, the sieve was placed into the split mold. The sample was then poured into the cylindrical sieve and the sieve was slowly pulled up through the sample (Fig. 3.22)

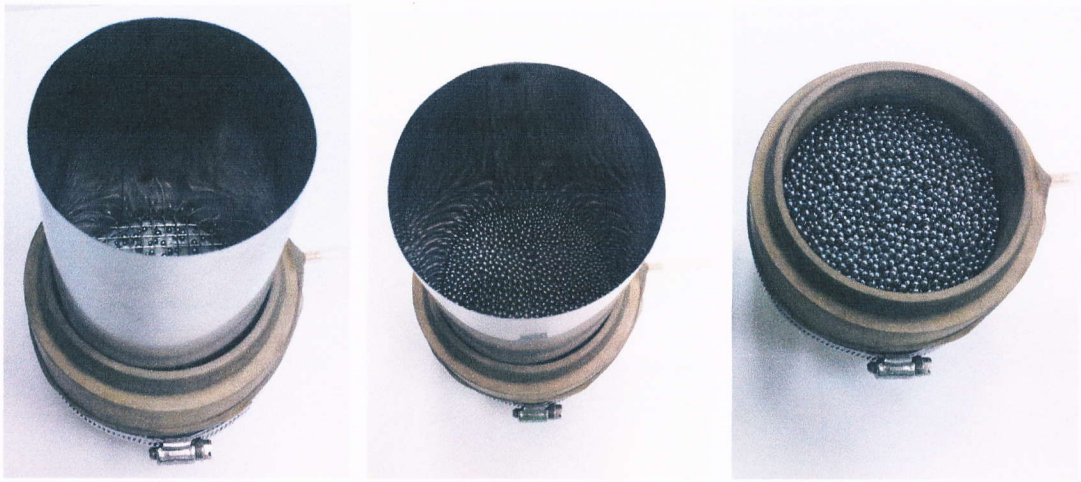

Fig. 3.22. Sample preparation process for loose samples

The sample top cap was lowered into place and gently positioned to ensure a full frictional contact with the top cap. The vacuum hose was moved to the bottom port to apply vacuum to the sample, and height measurements were taken. The sample was then transferred to the device and prepared for testing (Fig. 3.23).

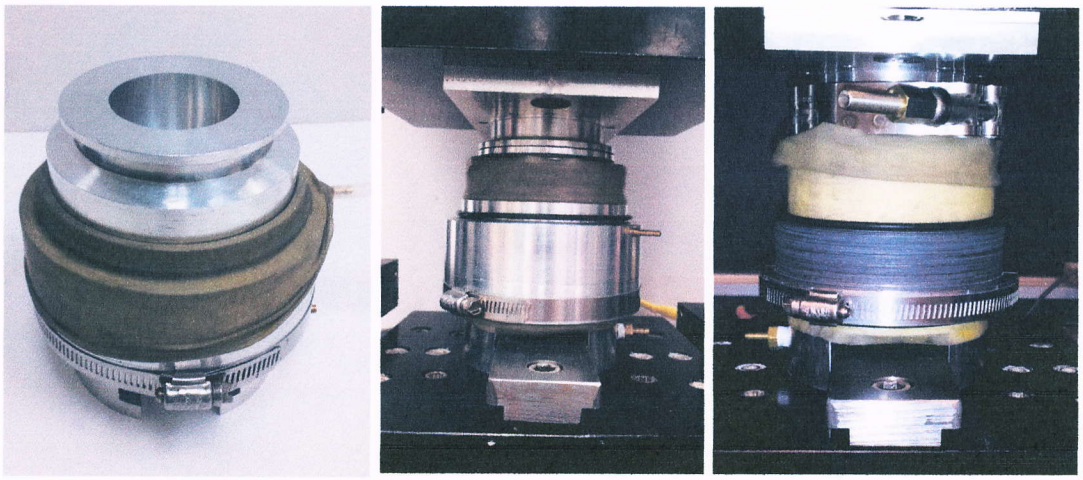

Fig. 3.23. Prepared sample and placement in device

One issue that was also addressed was the possible effects the top glued particles had on the overall measured void ratio. It was noticed that, even for the dense samples where the internal void ratio was most likely very similar, the measured overall void ratio values were different for the flat and fixed particle boundaries. A slight difference in the height, caused by the different boundaries, led to a relatively large difference in void ratio when compared to the total range generated. All of the initial void ratio determinations were conducted using flat boundaries. Once the fixed particle caps were used, the measured sample height did not correspond to the correct void ratio. This is likely due to the thickness of the epoxy and the fact that particles are not able to fill all of the voids at the glued boundary. To correct for this influence, the maximum and minimum void ratios determined using the flat boundaries were also set as the void ratios for the fixed particle boundary and the sample height was adjusted to correspond to these values. In other words, for a void ratio of 0.63, the sample height for flat and fixed particle boundaries would be 24.41 mm and 28.11 mm, respectively. Careful measurements and repeated trials were performed to ensure the correct void ratio was maintained in both cases.

3.3.4 Experimental Procedure and Testing Program

The testing procedure consists of six steps.

1. Assemble split mold, rings, membrane, and bottom cap. Apply vacuum to split mold port to pull membrane taught to the mold.

2. Prepare sample as described above for a loose or dense sample. Vacuum is placed onto sample port before taking height measurements and is maintained during installation and initial loading.

3. Place sample into MDSS device, align, and tighten bottom T-bar to clamp the

sample bottom cap. Zero the load cells and then lower vertical assembly to the desired seating load. The device is currently in displacement control.

4. Clamp top cap to top assembly using V-clamp. Change from displacement control to load control. Slowly remove the vacuum.

5. Lower vertical assembly to desired vertical effective stress and carefully remove split mold.

6. Shear sample under desired simple shear conditions.

These represent the basic steps used in similar types of testing; however, several additional studies were conducted to ensure repeatable results. For example, the vertical assembly is initially lowered in stroke/displacement control. The sample can then be clamped to the device under either stroke or load control. Either way, in order to run a constant stress test, the vertical control must be switched to load control. Slight oscillations occur when this switch is made. It was determined that the least amount of disturbance occurred when the sample is clamped down in stroke control and then switched over under a low seating load of approximately 0.13 kN (30 lbs) or less. A vacuum is applied to the sample throughout these steps to further minimize disturbances. Once the sample is in load control, the vacuum is slowly removed and the sample is loaded to the desired vertical stress. The split mold is then removed and the sample is sheared. The vacuum and split mold removal were also tested at various phases. The least amount of disturbance occurred when the vacuum was removed at the seating load. The removal of the split mold was less dependent on the conditions. In several cases, the control became unstable during loading and the P-gain was lowered until the system was stable. The loading process caused only negligible changes in the void ratio of the dense sample, but it often

Table 3.6. Testing program

Test Designation	σ'_v **kPa**	**Sample Number**	**Number of Tests**
MD-50-1	50	1	8
MD-50-2	50	2	3
MM-50-1	50	1	1
MM-50-2	50	2	1
ML-50-1	50	1	2
ML-50-2	50	2	2
MD-100-1	100	1	1
MD-100-2	100	2	2
ML-100-1	100	1	2
ML-100-2	100	2	2
MD-200-1	200	1	1

resulted in significant changes in void ratio of the loose samples.

The testing program was chosen based on the need to experimentally validate DEM models, but also based on the need to better understand the differences in uni-directional simple shear soil response for various testing conditions. Table 3.6 gives the experimental testing program for this research. Tests labeled M represent monotonic tests and the designations D and L represent dense and loose samples, respectively. The designation MM represents tests that were conducted at an intermediate or medium density. The test designation also contains the vertical effective stress value and the sample number. Sample 1 contains 7,500 particles and sample 2 contains 60,000 particles. The particle sizes are specified above for the two samples.

3.4 Results and Discussion

3.4.1 Monotonic Testing

Monotonic tests were conducted at a rate of 1.5 mm/hr which is approximately five percent per hour based on the average sample heights for the loose and dense sample. As shown in Table 3.6, a number of different testing conditions were carried out to study the effects of varying vertical stress and density on the stress-strain response.

3.4.1.1 Repeatability

A number of tests were conducted initially for the dense case for samples 1 and 2 at 50 kPa to assess repeatability and determine the expected experimental scatter. The results are plotted below in Figs. 3.24 and 3.25. The void ratios for the sample 2 tests were between 0.590 and 0.600.

The results for both samples follow trends seen in previous tests on glass beads and steel spheres. At low strains, the responses are very similar. They then begin to spread out as shearing progresses. Plots of volumetric strain and void ratio show additional variability for the samples. The sample 1 tests had initial void ratios (at 50 kPa) within a range of 0.597 to 0.622. Although this range of densities would explain some differences in stress ratio response, the results do not follow the normal trends expected for the corresponding volumetric response, indicating that the scatter is due to experimental variability. For example, the curve labeled 1 in Fig. 3.24 shows a lower initial stress response and is more contractive than the other samples. One would expect this sample to be one of the loosest; however, the void ratio lies in the mid range throughout the test. Also, the curve labeled 2 is the densest and shows the most dilative response. This would generally also be the curve with the highest peak stress ratio; however, it is the lowest. Even with the slight scatter, the results

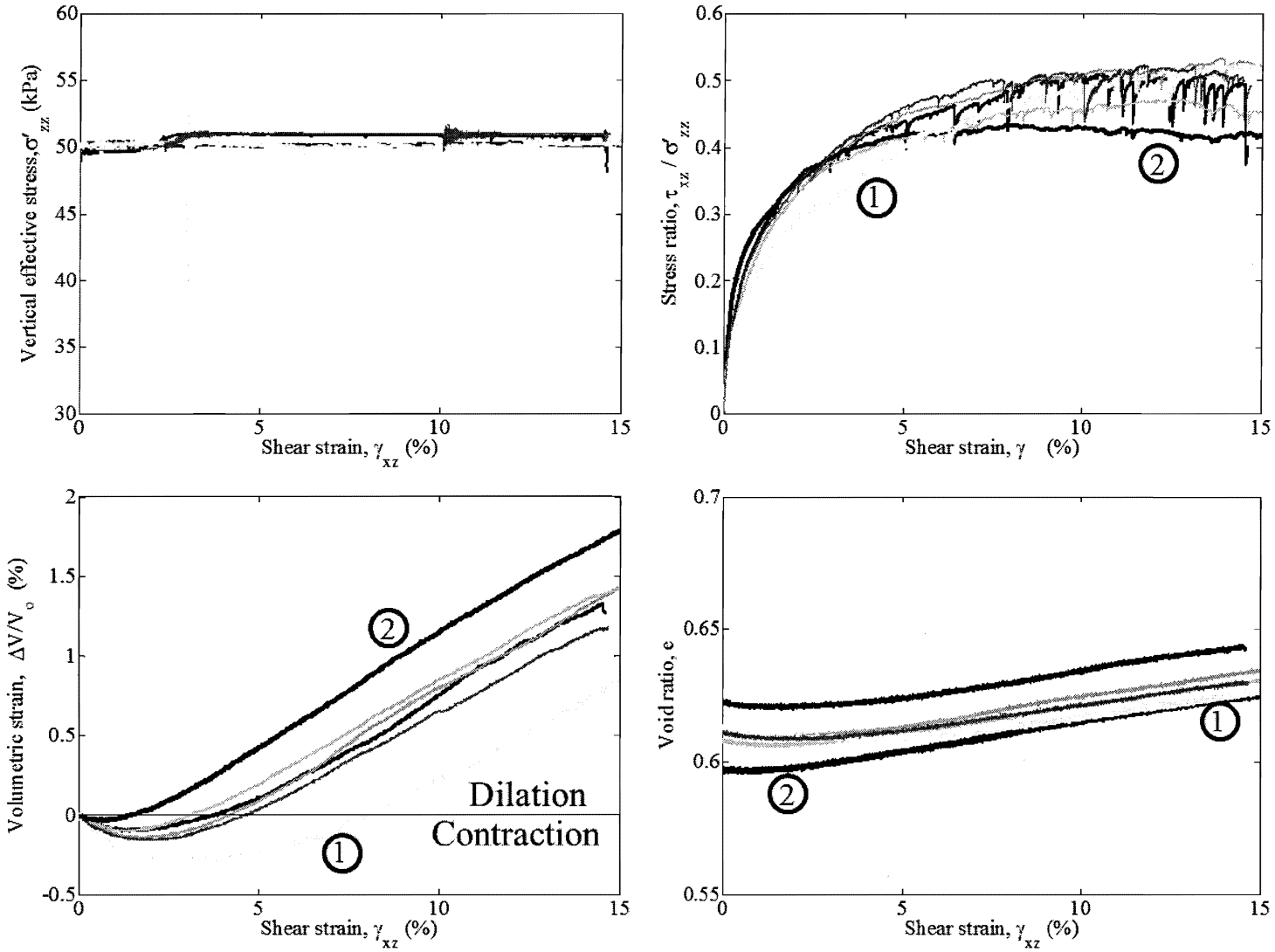

Fig. 3.24. Results for MD-50-1 showing experimental scatter

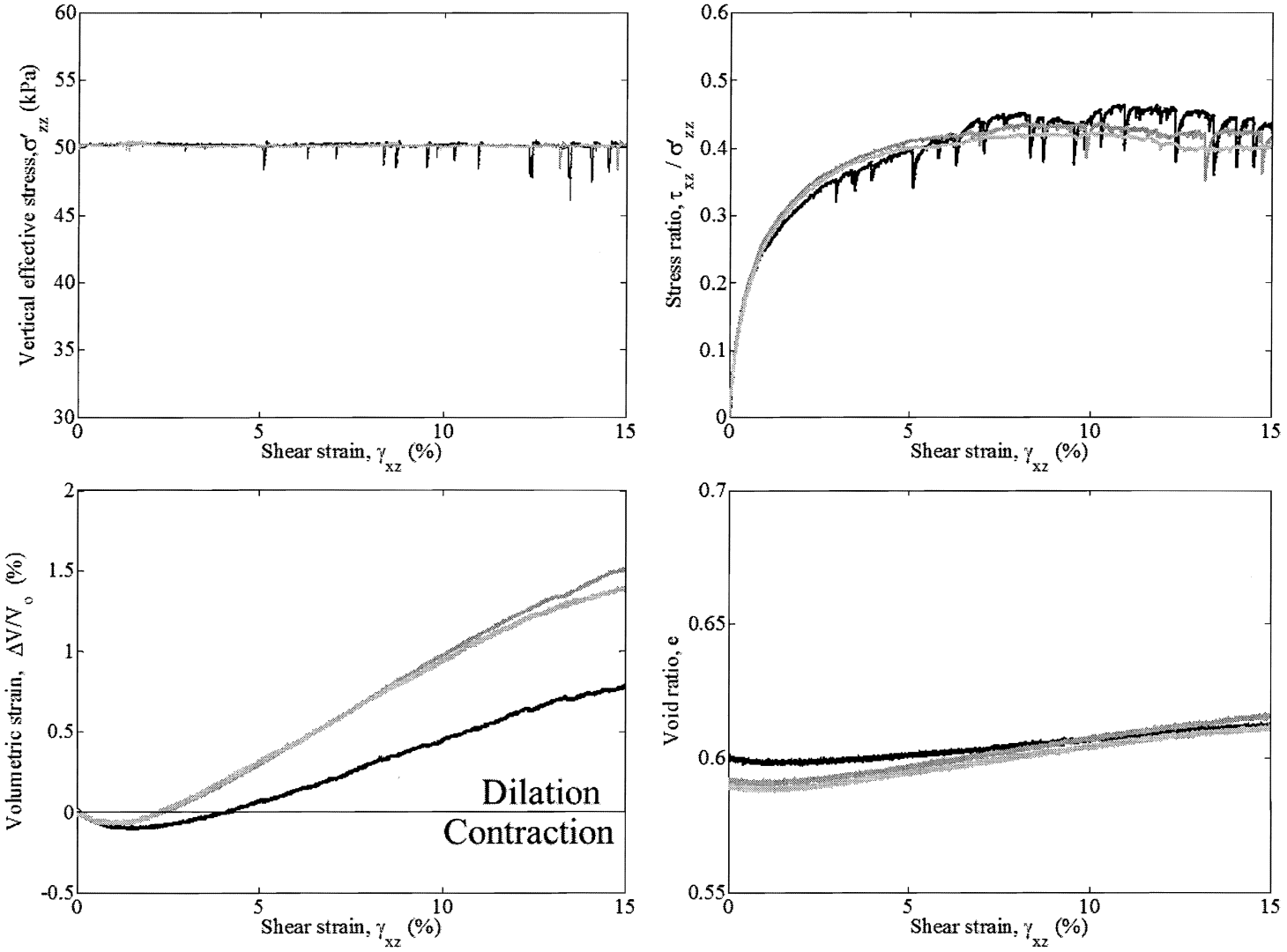

Fig. 3.25. Results for MD-50-2 showing experimental scatter

show that the methods are repeatable and they provide an "envelope" to compare the simulation data with.

The tests conducted on sample 2 show very similar responses with one another. Two of the samples are almost identical, while the third differs in volumetric response. This is most likely due to the instabilities experienced in the normal load during shearing, as well as the fact that the sample is slightly less dense initially. These instabilities are shown as "spikes" in the plot of vertical effective stress versus shear strain. The resulting influence on stress ratio can also be seen. At each of these spikes, the vertical load essentially vibrates the sample causing it to contract. This limits the dilation rate of the sample and most likely explains the different volumetric response. Overall, these tests are more uniform and repeatable than sample 1. The following paragraphs compare the two sample sizes and corresponding responses and present the selection of representative tests from each.

3.4.1.2 Effects of sample size on response

Several researchers have shown both experimentally and numerically that the particle size to specimen size ratio, or the number of particles within the sample influence the response. As shown above in Figs. 3.24 and 3.25, sample 1 exhibited more scatter than sample 2 which was expected. Slight disturbances have a greater influence in the overall response for samples with larger particle sizes. Also, the volumetric response was different for the two samples. The dilation rate is much less for sample 2 than for sample 1 at 15% shear strain. Sample 2 is beginning to approach zero volume change and would most likely reach critical state before sample 1 if shearing continued. In order to directly compare the two sample responses, the data was plotted together (Fig. 3.26).

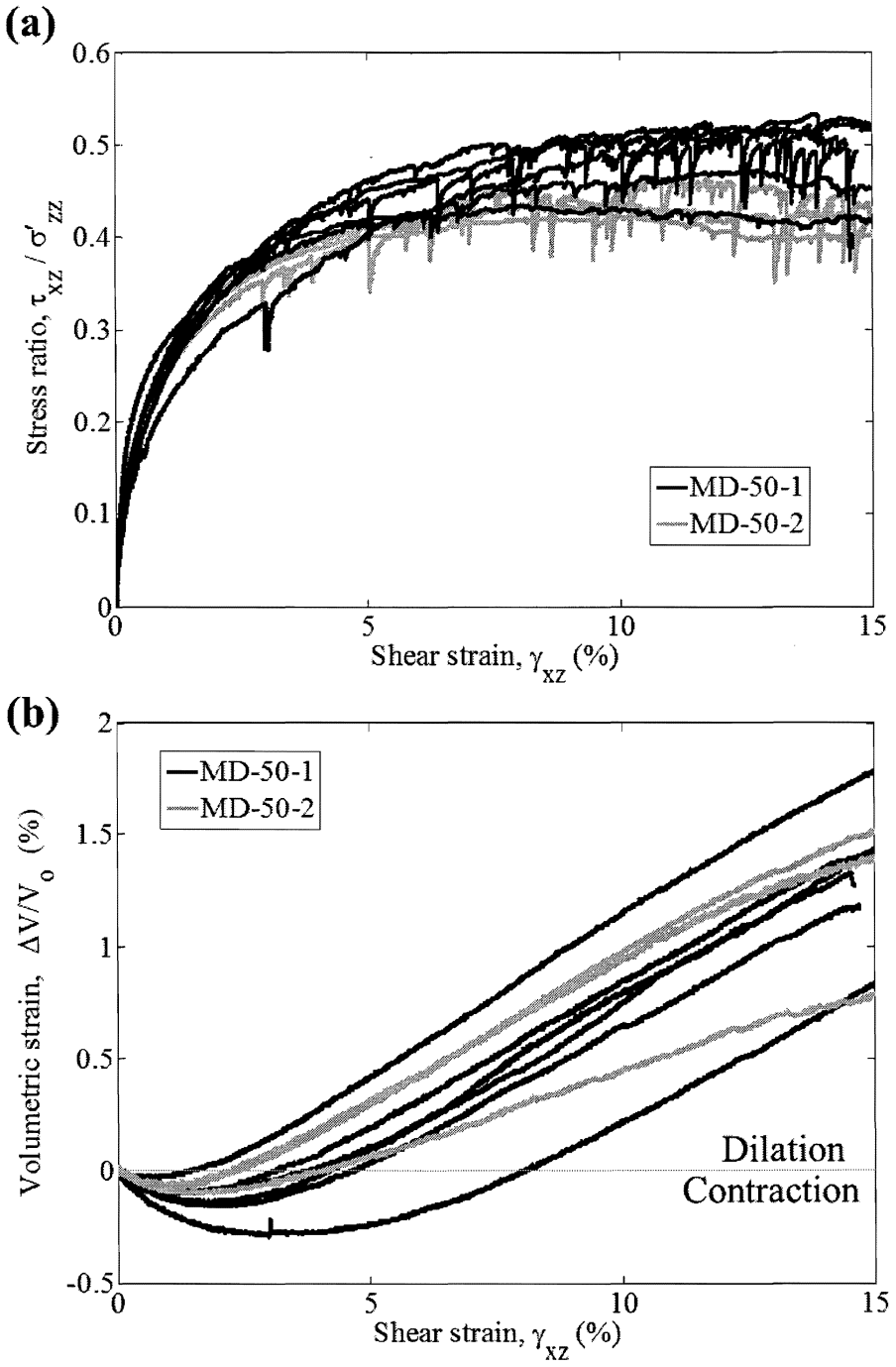

Fig. 3.26. Results for MD-50-1 and MD-50-2 samples

The results for sample 2 plot within the results for sample 1. These samples exhibit a lower peak stress ratio than sample 1 and it is clear from plot (b) that the volumetric change is slowing for sample 2. Overall, the results plot within a decently narrow range that can be later compared to the simulation data as a whole. Two representative curves were also chosen. One curve from sample 1 and one curve from sample 2 are shown in Fig. 3.27. These curves were chosen because they exhibit an average response in terms of stress ratio and volumetric behavior and the stress control was well maintained during testing.

The initial portion of the curves matches well. Only a slight difference is observed at shear strains above 7%. The sample 1 test continues to gain strength, while the sample 2 test exhibits a very small amount of strain softening. The volumetric response is also similar with the sample 1 test exhibiting a slightly more contractive behavior. The overall trend and dilation rates are similar. A comparison was also made for the samples at a vertical effective stress of 100 kPa (Fig. 3.28). The stress ratio response and volumetric response are very similar for the three samples. Representative samples from each were chosen for subsequent comparisons of the influence of density and vertical effective stress on granular behavior.

The medium dense samples also exhibited differences in response between the two sample sizes (Fig. 3.29). The stress ratio response was very similar up to a approximately 7-8% shear strain, at which point the sample 1 test continued to gain strength and the sample 2 test peaked slightly and then leveled off. The volumetric response for the samples was very different. The sample 1 test exhibited more contracting initial response compared to the sample 2 test. Once the samples were dilating, both exhibited similar dilation rates.

A similar comparison was also made for the loose samples tested at 50 kPa and 100 kPa vertical effective stresses. Figs. 3.30 and 3.31 show the results for the two

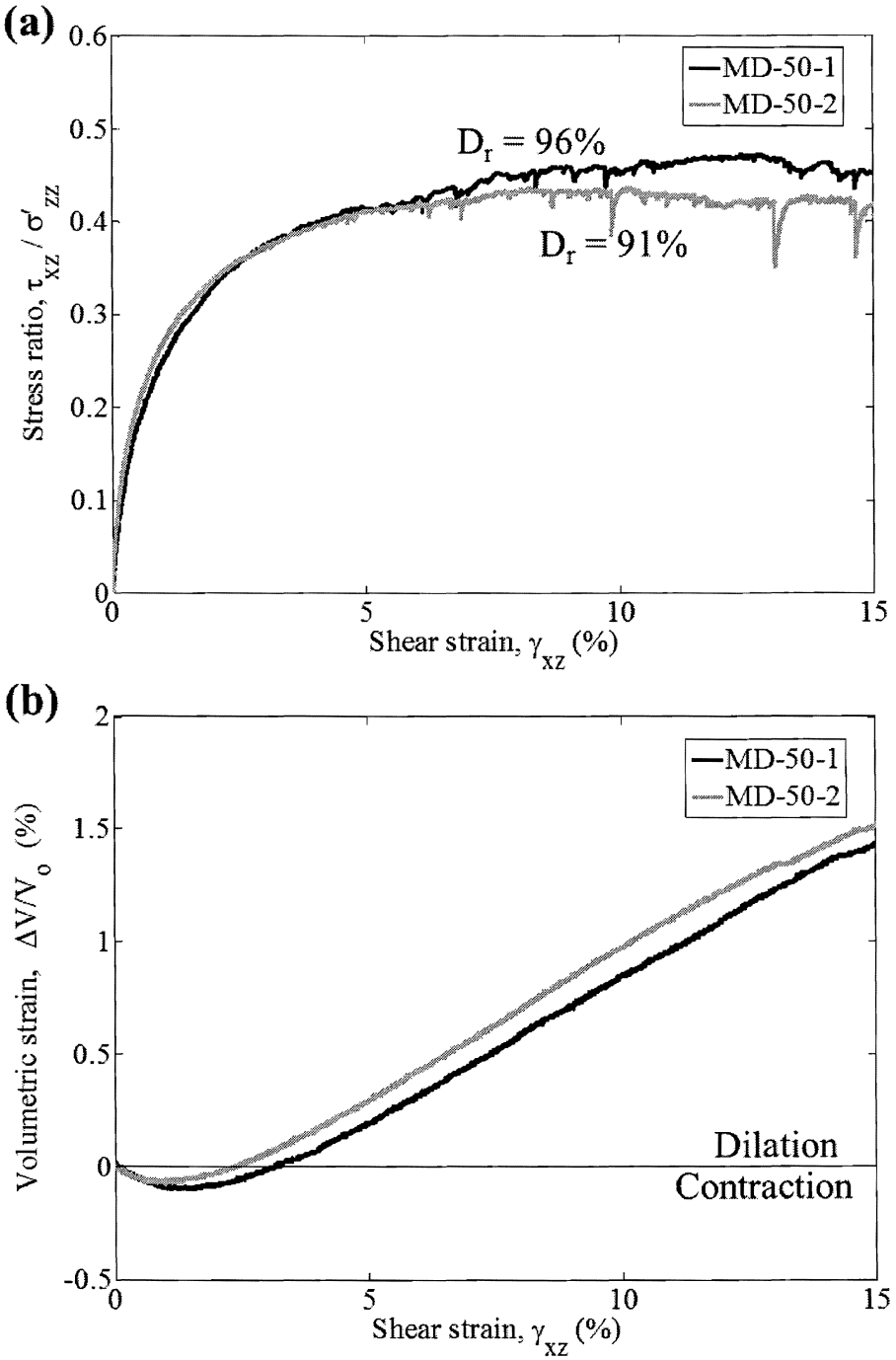

Fig. 3.27. Comparison of MD-50-1 and MD-50-2 responses (a) stress ratio (b) volumetric strain

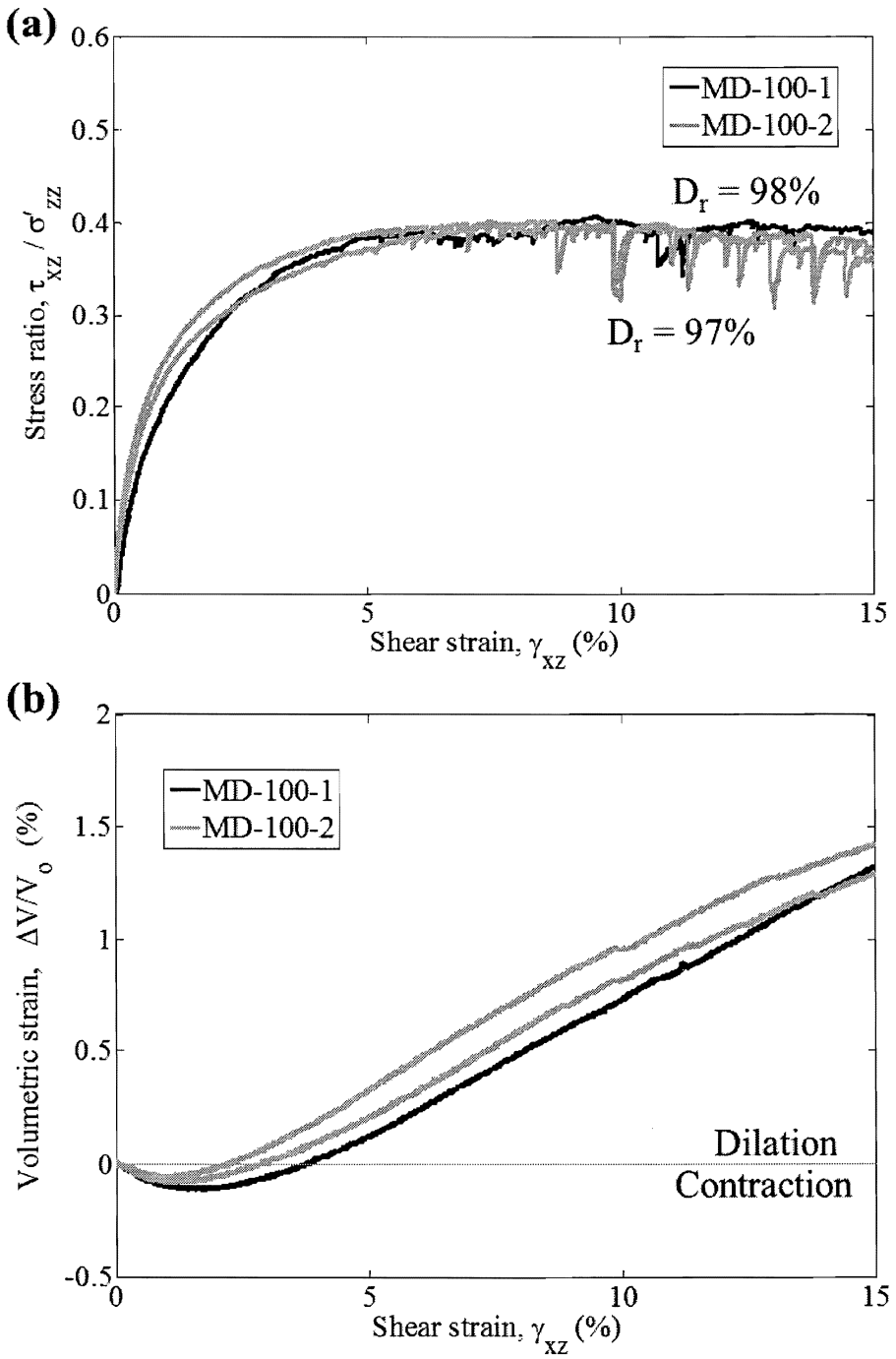

Fig. 3.28. Comparison of MD-100-1 and MD-100-2 responses (a) stress ratio (b) volumetric strain

samples. The response for samples 1 and 2 at 50 kPa are very similar.

One exception is the sample 1 test that begins at a higher initial void ratio, labeled 1 in the plots. This test had an uncharacteristic response in that it was a much more loose behaving sample, but it was closer to the stress ratio response exhibited by the sample 2 tests. This response does, however, make sense when relative densities are considered. The plot of void ratio versus shear strain is somewhat deceptive. Even though the samples appear at the same void ratio, they are not at the same relative density (Fig. 3.30d). The void ratio range for sample 2 is shifted slightly less than that of sample 1. The three samples exhibiting similar stress ratio responses are within a relatively narrow relative density range. The sample that begins with a similar void ratio is actually at a much higher relative density. Therefore, it is reasonable that it would exhibit a higher stress ratio peak. These differences were not experienced in the dense samples previously discussed because the samples are all prepared very close to the densest state and are all within a small range of relative densities.

The results for the tests on the loose samples conducted at 100 kPa showed very similar response and were within a small range of relative densities. The stress ratio response, as well as the volumetric response are as expected. The responses for the sample 1 and sample 2 tests appear to be more closely related at 100 kPa than at 50 kPa. A closer look at the effects of vertical effective stress on response is given in the following section.

3.4.1.3 Effects of vertical effective stress on response

For samples prepared at similar densities, the magnitude of vertical effective stress, σ'_{zz}, has been shown to influence granular soil response. Fig. 3.32 shows three samples tested at various values of vertical stress. Tests conducted at higher σ'_{zz}

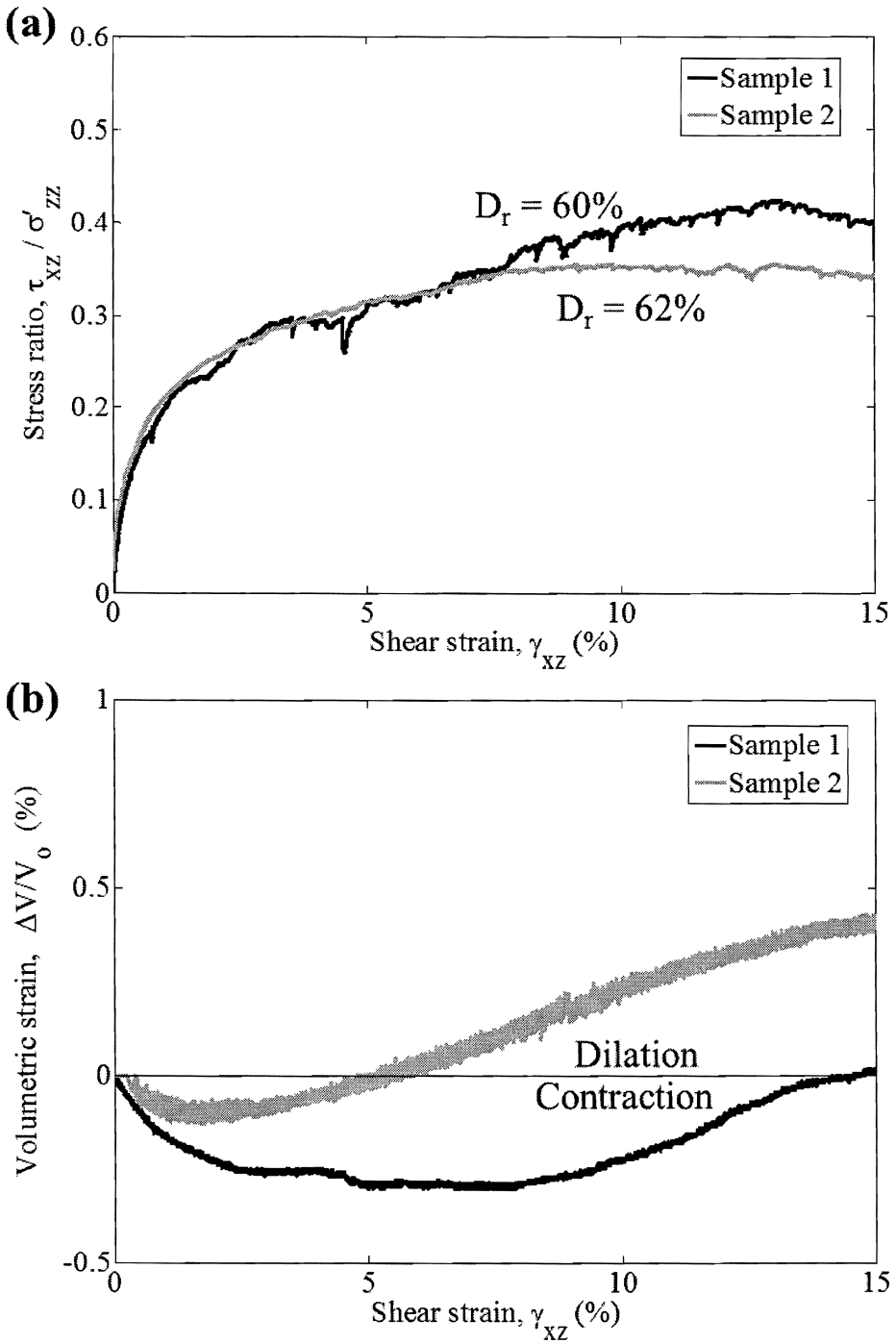

Fig. 3.29. Comparison of MM-50-1 and MM-50-2 responses (a) stress ratio (b) volumetric strain

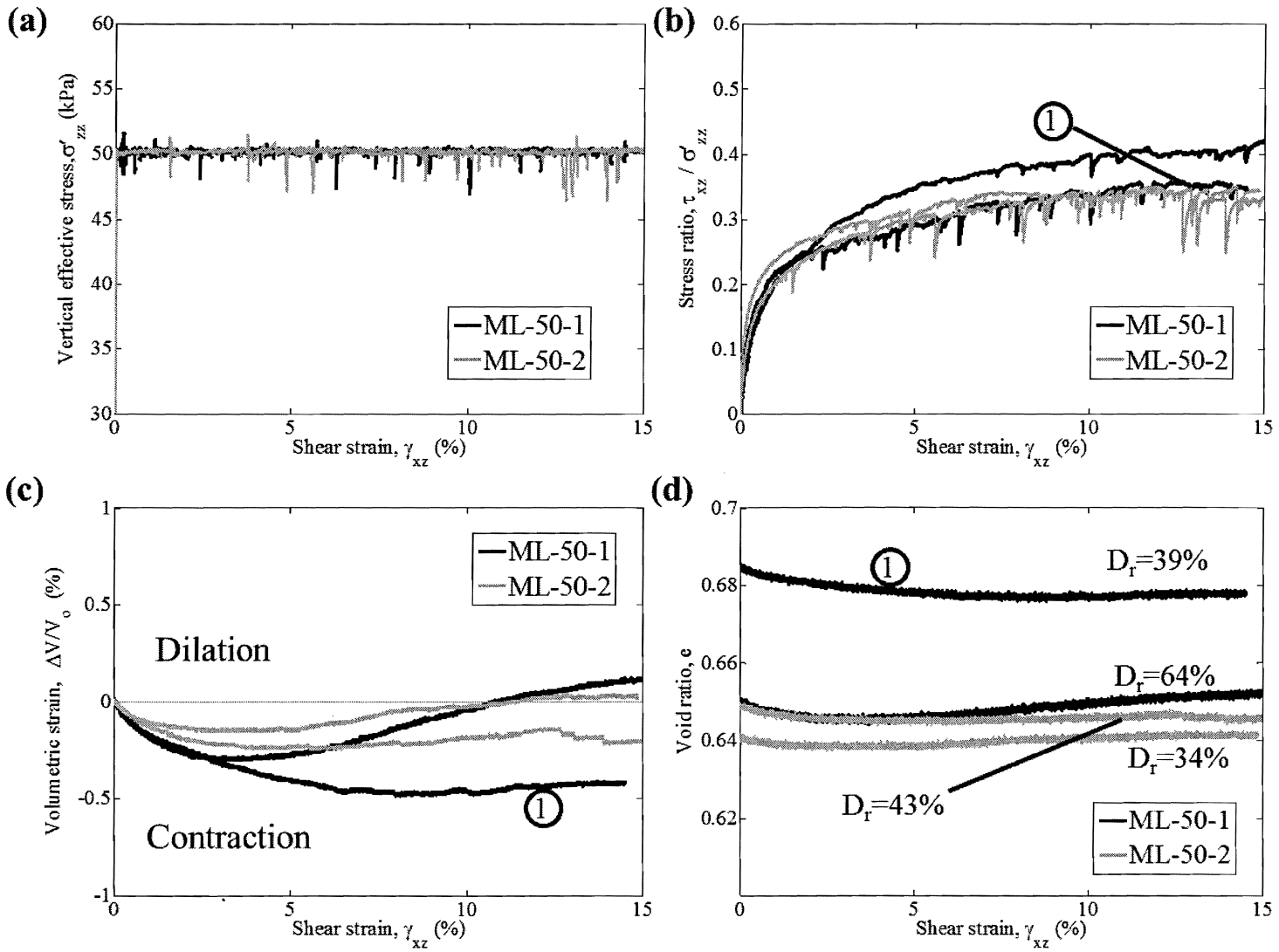

Fig. 3.30. Comparison of ML-50-1 and ML-50-2 responses (a) vertical stress (b) stress ratio (c) volumetric strain (d) void ratio

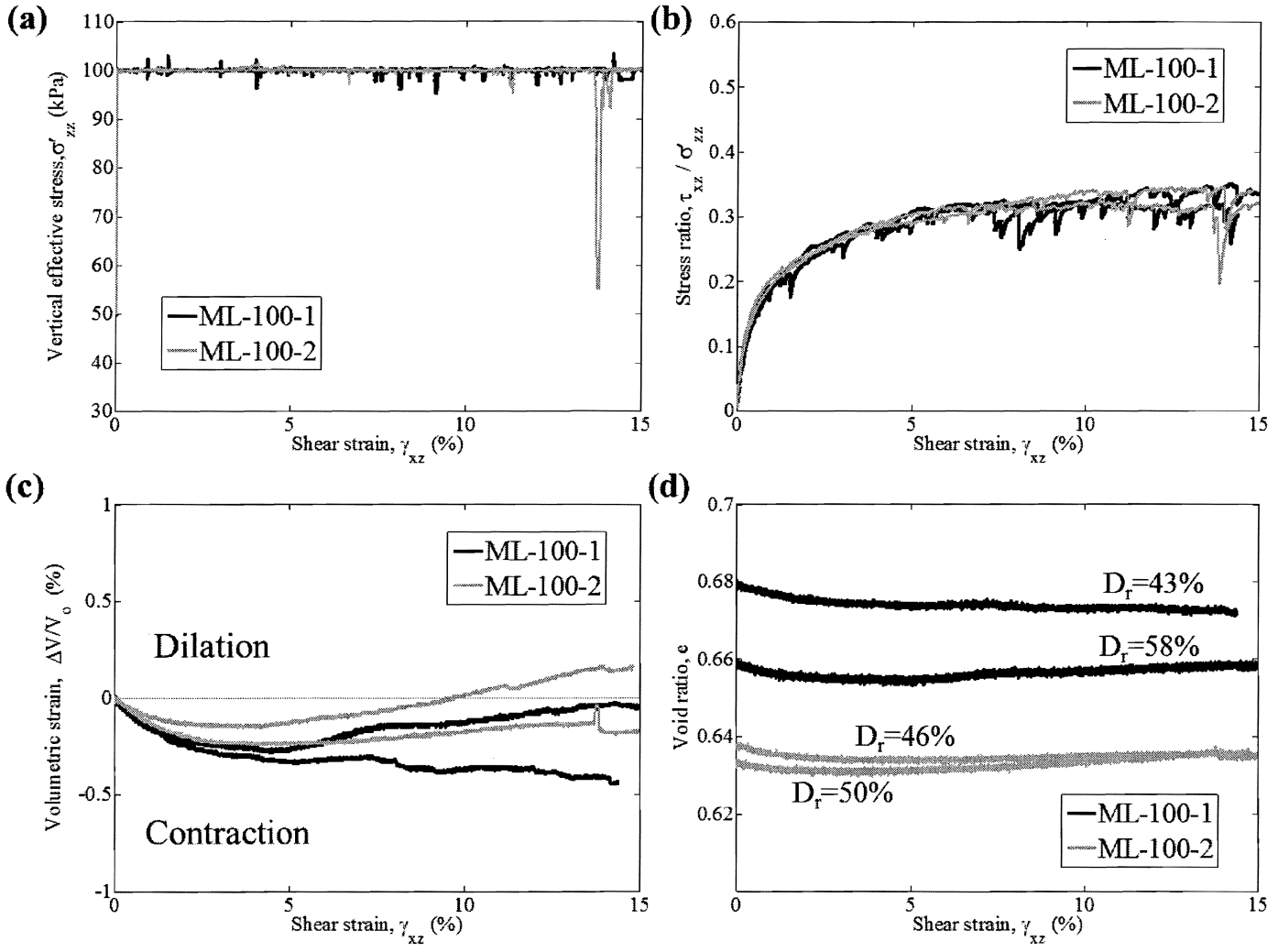

Fig. 3.31. Results for ML-100-1 and ML-100-2

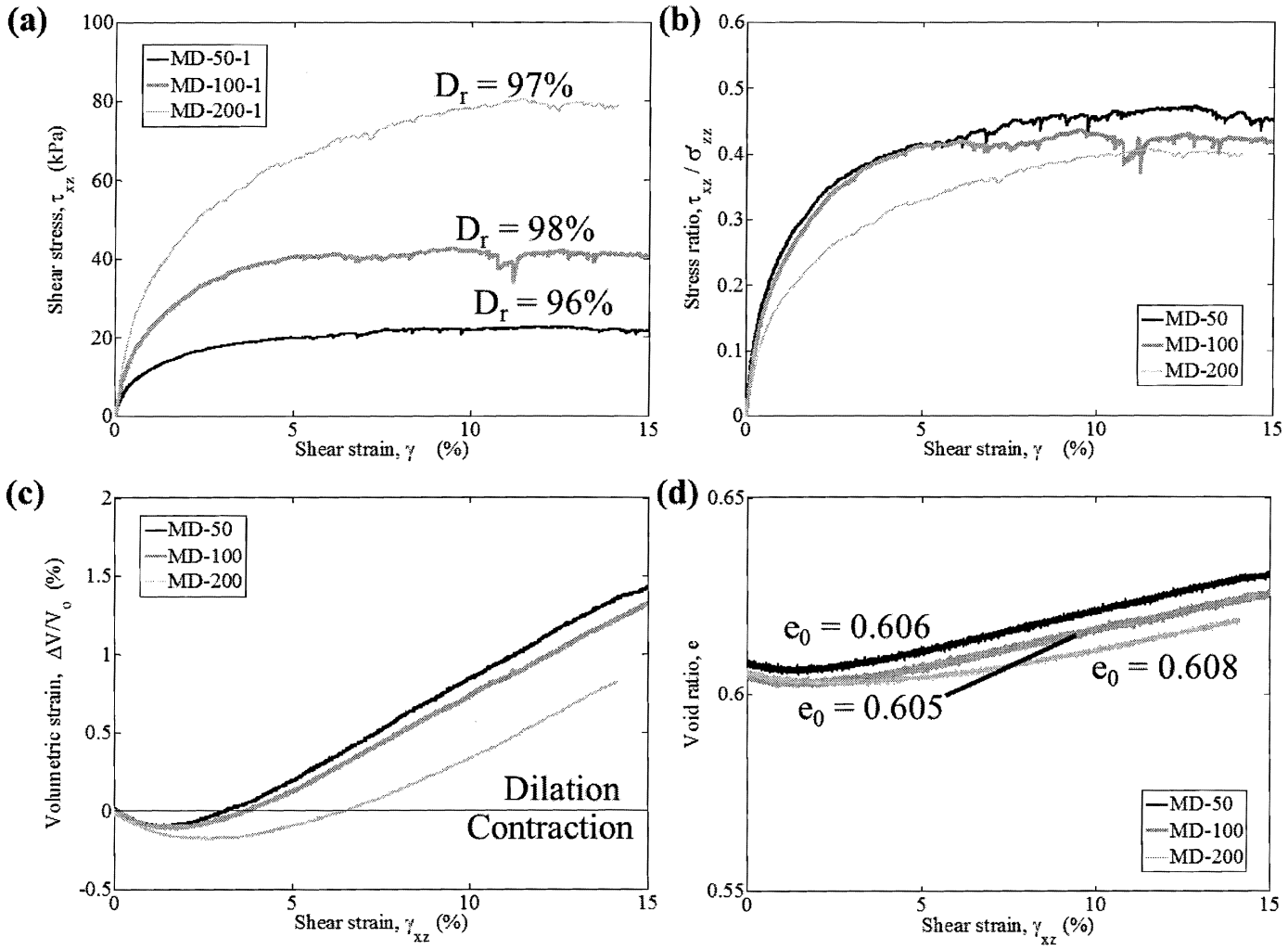

Fig. 3.32. Results for dense sample 1 tests at similar density and varying vertical effective stress

exhibit higher peak shear stresses. When normalized with vertical stress, however, the sample tested at lower σ'_{zz} should exhibit the highest peak stress ratio. These trends are observed in the plotted data (Figs. 3.32a and 3.32b). The volumetric response is also as expected. The sample tested at lowest confining stress has a more dilative response and tests at higher confining stresses exhibit more contractive responses. It should be noted that the range of stresses considered is relatively small compared to similar comparisons on sand. These comparisons usually consider peak stress ratio and the critical void ratio (Wroth, 1958), which is not obtained in the current study and is therefore, out of the scope of this project.

Only the dense case for sample 1 was tested at 200 kPa. The loose case for sample 1, as well as the loose and dense cases for sample 2 were tested at vertical stresses of 50 and 100 kPa and can be compared. Fig. 3.33 shows the results for the dense sample 2 tests. The trends are as expected. The sample tested at a lower vertical stress has a higher peak stress ratio and a more dilative response even though the other sample is at a higher relative density. The results for the loose samples also followed the same trends (Figs. 3.34 and 3.35).

3.4.1.4 Effects of density on response

Along with confining stress, another factor influencing granular soil response is relative density. A series of tests were conducted to study these effects. Fig. 3.36 shows the results for sample 1 tests at 50 kPa vertical effective stress. Only one intermediate density was prepared due to the low range of void ratios and the difficulty of maintaining a loose sample while clamping it to the machine. The results follow the expected trends. The tests with the highest density exhibit the highest peak shear strength and peak stress ratio (3.36a and 3.36b). One would also expect for the samples to eventually reach a common stress ratio and critical void ratio.

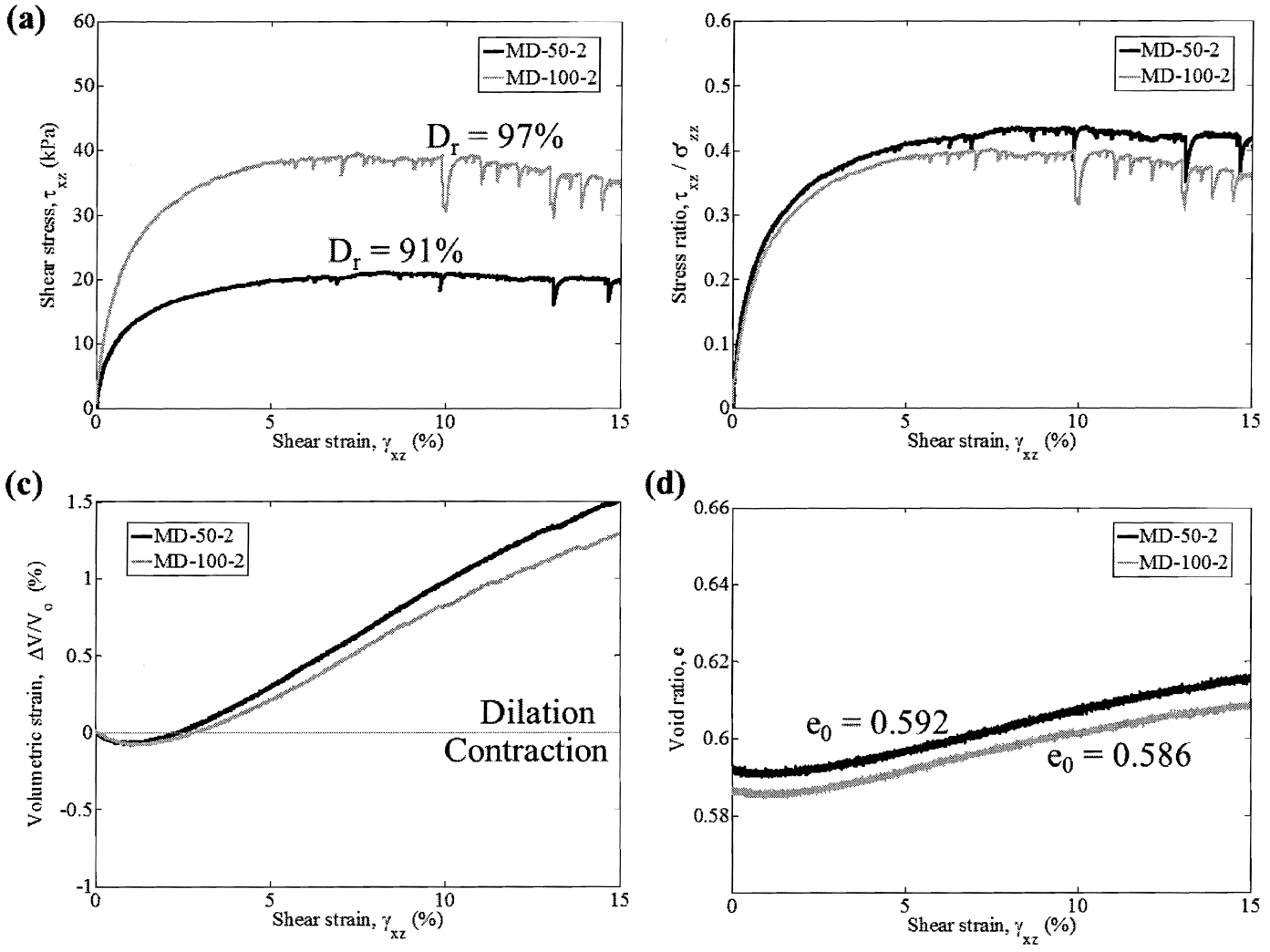

Fig. 3.33. Results for dense sample 2 tests at similar density and varying vertical effective stress

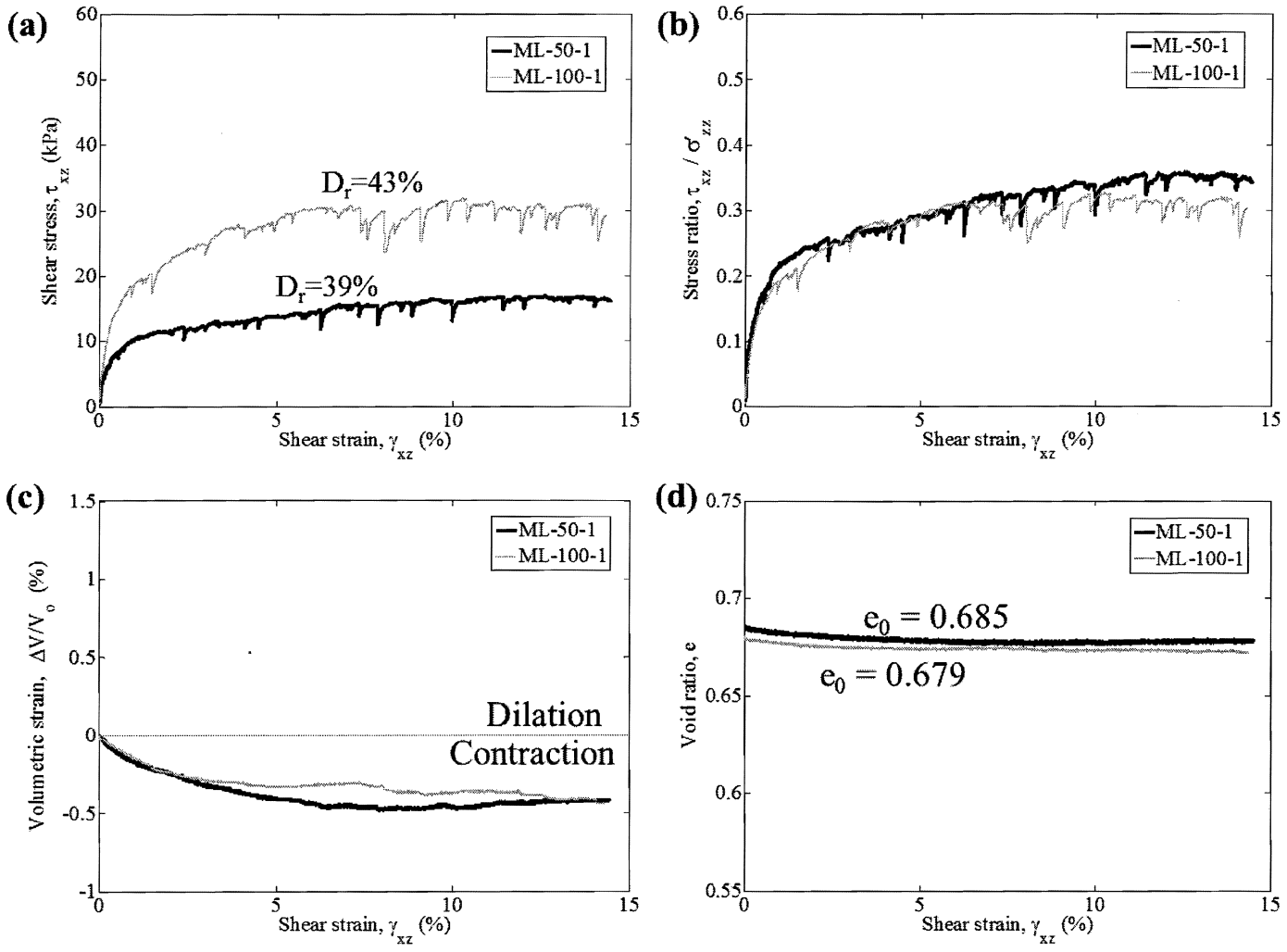

Fig. 3.34. Results for loose sample 1 tests at similar density and varying vertical effective stress

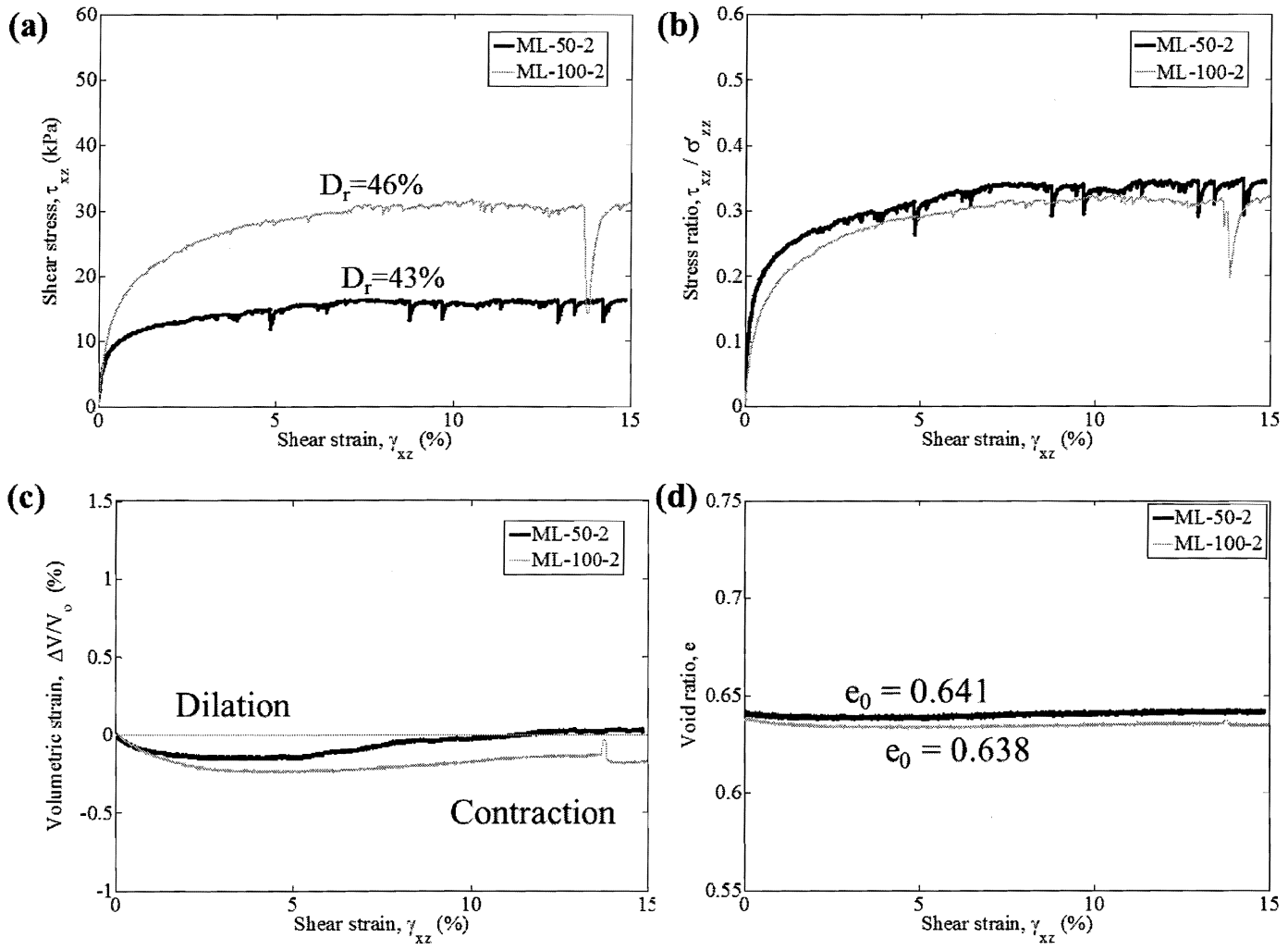

Fig. 3.35. Results for loose sample 2 tests at similar density and varying vertical effective stress

It is clear from Fig. 3.36 c that there is still volumetric change occurring at 15%. Therefore, these samples have not yet reached critical state. The volumetric response is also as expected. The loose sample contracts and the dense sample dilates. The mid-range density contracts initially and then begins to dilate at approximately 7% shear strain.

A similar comparison was made for the 60,000 particle samples. Again, only one intermediate density was tested due to the difficulty in preparing and maintaining the desired sample conditions (Fig. 3.37). The samples behave as expected, although the medium dense sample is closer to the loose sample strength than for the sample 1 tests. The dense sample exhibits a higher peak shear stress and peak stress ratio. The dense sample dilates, while the loose sample contracts until reaching a zero volume change condition. The medium dense sample initially contracts and then dilates until approximately 14% shear strain where it starts to have zero volume change. The void ratio is fairly constant for this sample throughout the shearing. Although the dense sample is not at critical state because volume change is still occurring, it is somewhat apparent from Fig. 3.37d that the samples are beginning to approach a common void ratio.

3.5 Conclusions

Overall these results show that tests on metal spheres follow the trends expected for sand and other granular media. These findings cover many different testing conditions and present useful validation data for the DEM simulation results. Direct comparisons of these two data sets are presented in Chapter 5.

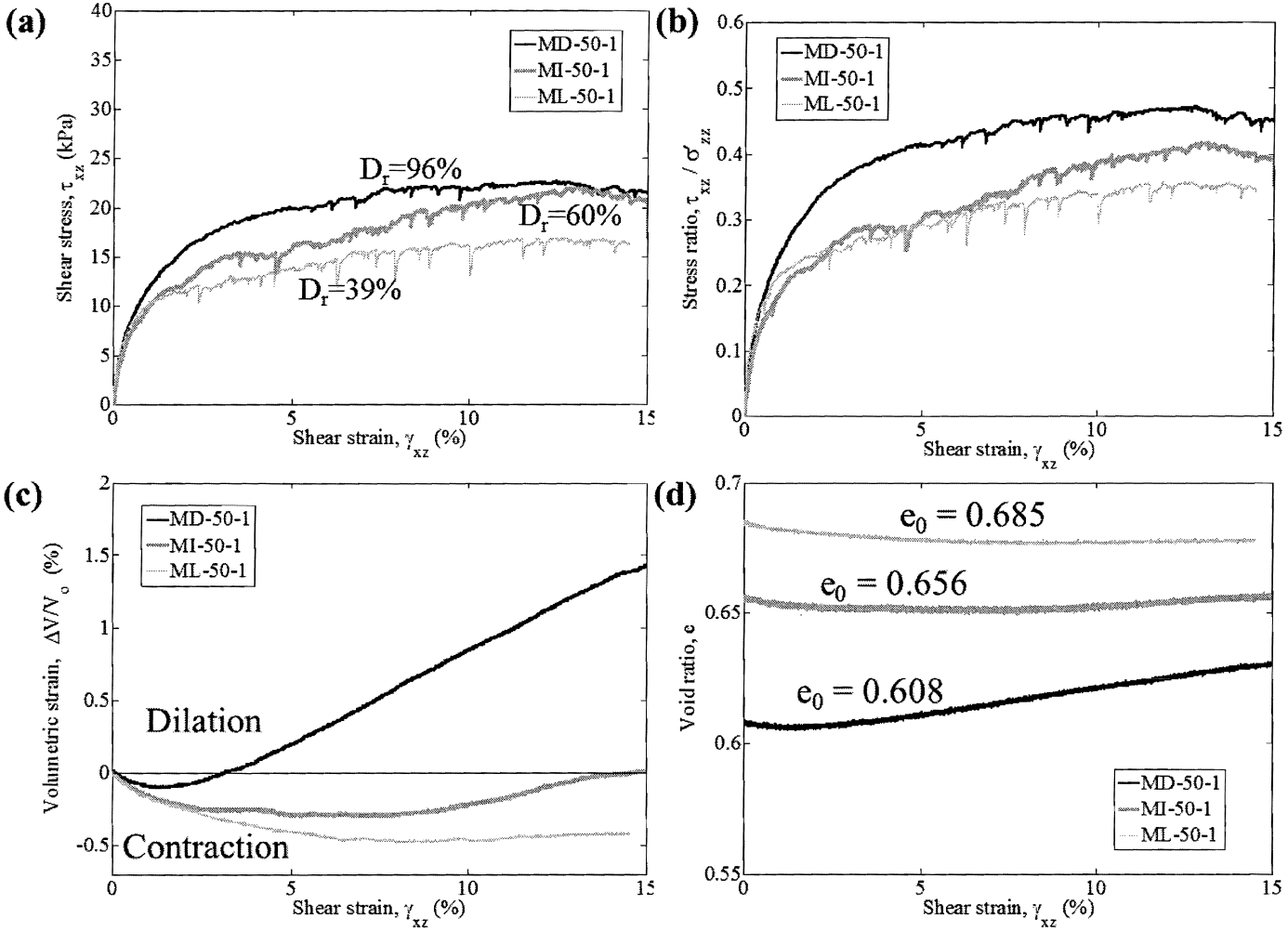

Fig. 3.36. Results for sample 1 tests at 50 kPa and varying density

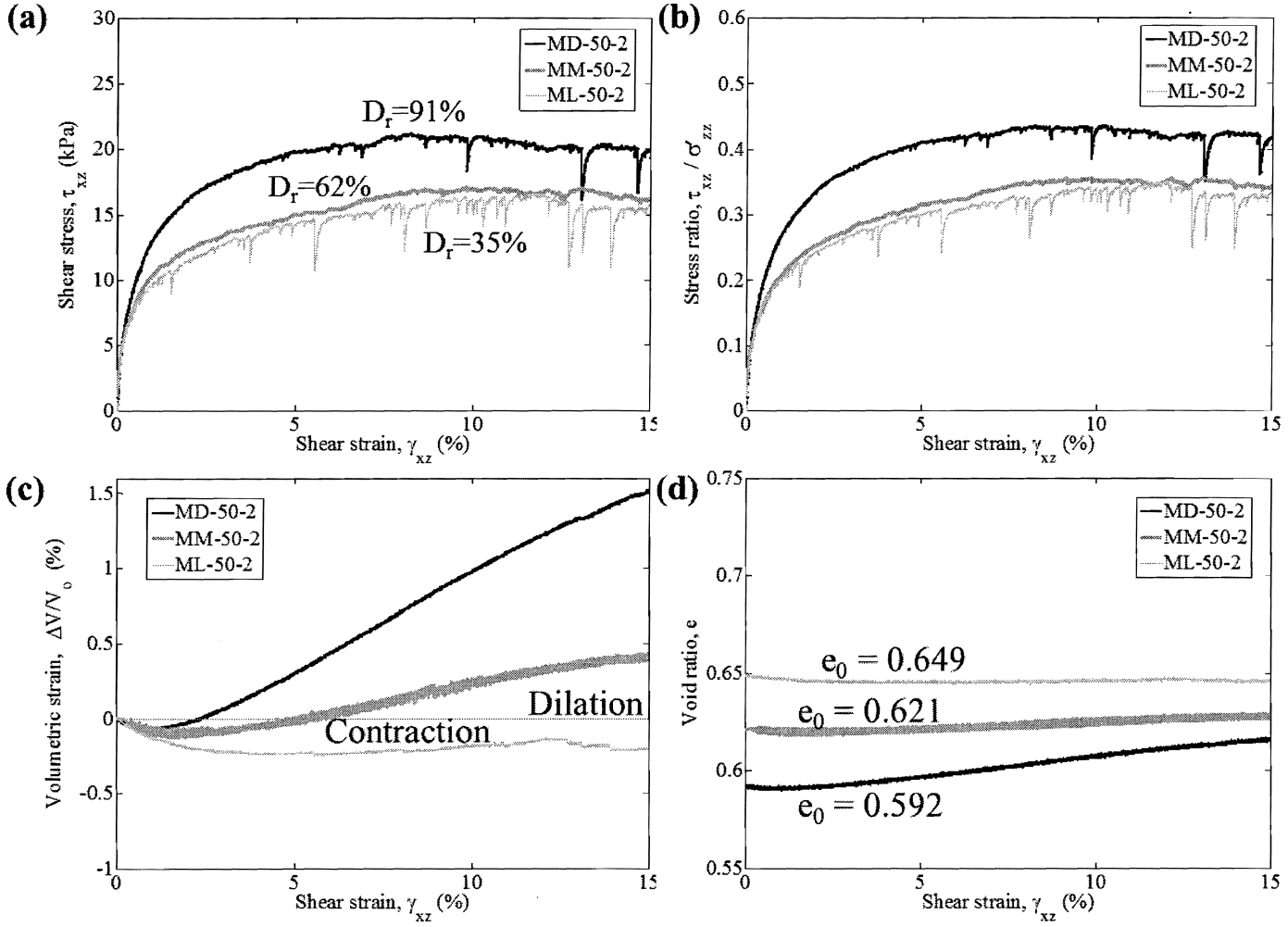

Fig. 3.37. Results for sample 2 tests at 50 kPa and varying density

4. DISCRETE ELEMENT METHOD SIMULATION DEVELOPMENT

4.1 DEM Model Development

The discrete element method (DEM) model simulations in this study were developed while keeping in mind two main objectives: their validation with the laboratory data presented in Chapter 5, and their intended use as an aid to gain a better understanding of the microscopic response of granular materials in simple shear. The DEM model development consists of four main parts: sample preparation, top cap servo stress control, confining ring servo control, and the shearing path control of the sample. Similar to the physical laboratory tests, samples in DEM must be prepared and brought to the initial stress state. The virtual samples are then sheared under similar boundary conditions as experienced in the laboratory device (i.e. constant vertical stress and minimal lateral strains maintained by the confining rings). The DEM simulation platform for this research is PFC3D.

4.1.1 Initial Sample Generation and Parameter Specification

As with any numerical method, an initial specimen generation process is required. This process includes the specification of the geometry and the material parameters used. The specification of the boundary geometry in PFC is straightforward. A 101.6 mm diameter cylinder is generated to replicate the laboratory sample and two flat boundary walls are generated to represent the top and bottom caps. A further discussion of the dimensions, placement, and control of the walls is given below.

Once the boundary geometries are defined, the physical particle geometry and material properties are then defined. Unlike finite element models, where the initial stress state, configuration, and constitutive model are defined, DEM models require

Table 4.1. Testing program

Input Parameter	Density (kg/m^3)	Shear Modulus (GPa)	Poisson's Ratio
AISI-52100	7700-8030	73.1-82.7	0.27-0.3
Used in PFC	7800	80	0.3

cycling to arrive at the initial specimen conditions. Also, rather than defining the material constitutive law directly, DEM simply uses a contact constitutive law. Depending on the contact model used, PFC requires several material parameters inputs. The modified Hertz-Mindlin contact model uses values of density, Poisson's ratio, and shear modulus. This contact model relates the forces and relative displacements non-linearly and, according to the PFC3D manual, is most appropriately used in cases where accurate small strain behavior is required. The linear contact model relates forces and relative displacements linearly and is used in most general cases. This particular study used the modified Hertz-Mindlin contact model. Each of the required input values is provided in the specifications for AISI 52100 steel alloy. Table 4.1 gives the specification ranges, as well as the values used in the PFC model. A sensitivity test was also performed during the validation stage to determine the influence of stiffness and contact model type on the response. The findings are discussed in Chapter 5.

The only other values entered into the DEM model are the values of interparticle friction and particle-wall friction. Previous studies have shown that chrome metal spheres of similar dimensions have interparticle friction angles between 4 and 7°. All of the initial prototype simulations were conducted with the interparticle friction angle set to 5.5°. This value was chosen based on average values in the literature and was also the value used by O'Sullivan (2002) and Cui et al. (2007).

To gain a better estimate of the actual physical values for the particles used in the laboratory, the inter-particle friction was measured for two of the steel bearing sizes by Ignacio Cavarretta at Imperial College London using an apparatus developed specifically for this purpose (Fig. 4.1).

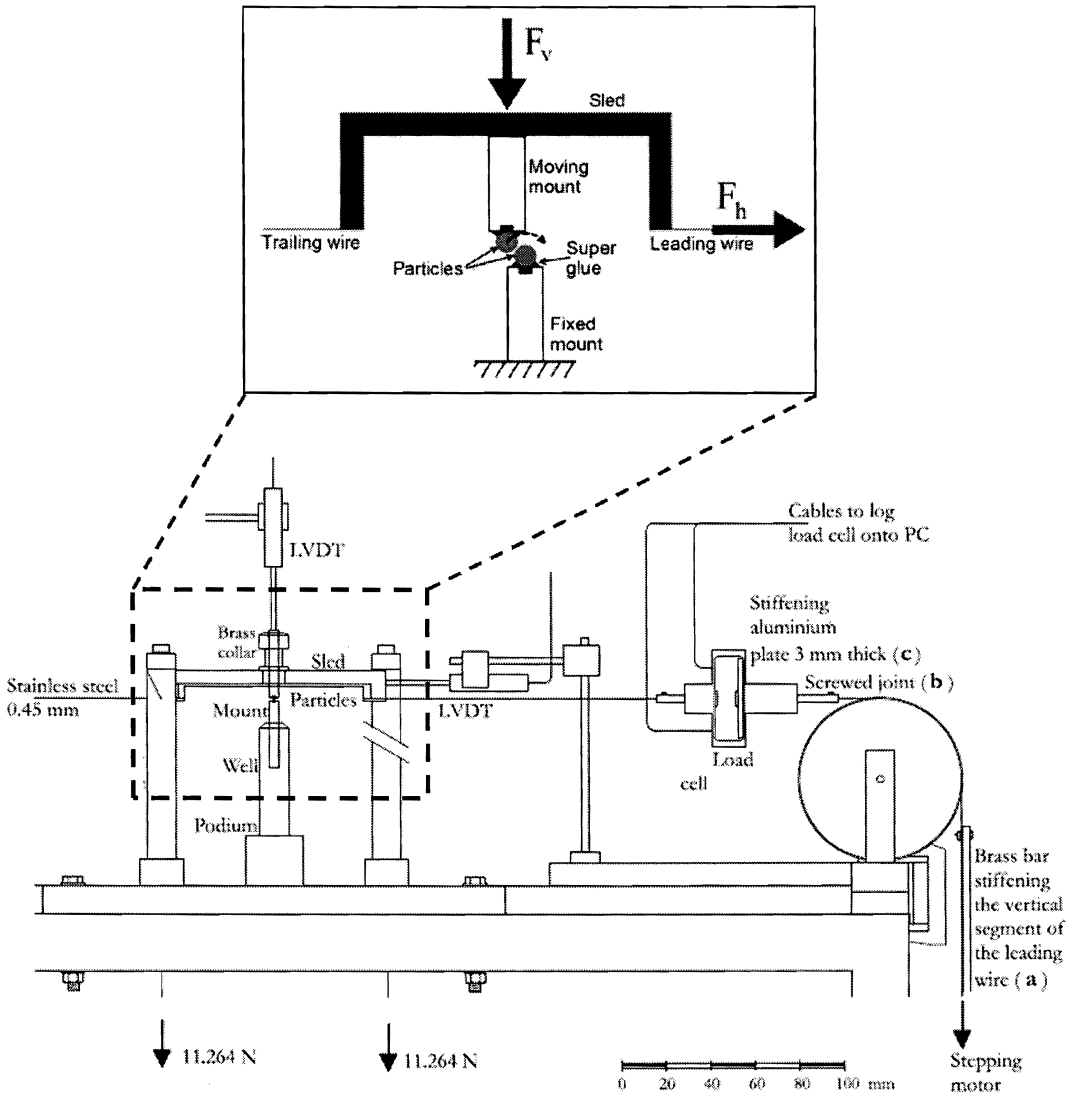

Fig. 4.1. Apparatus used by Cavarretta to determine interparticle friction (after Cavarretta et al., 2011)

Two particles are glued to the tips of small brass mounts and aligned vertically. The sled is moved horizontally by a lead wire connected to a stepper motor. A trailing wire with a hanging weight is also attached to the sled to provide a reaction force. Two additional guide wires ensure that the top assembly is only allowed to move vertically. The horizontal component of the frictional force is then given by the difference in the forces measured in the lead and trailing wires. The frictional force and interparticle friction is determined at the point when the two apexes of the spherical particles come into contact. The vertical force is also determined and the interparticle friction can be derived. The device and procedure are described in more detail in Cavarretta et al. (2011). Table 4.2 gives the values of interparticle friction angle at constant vertical displacement, the average inter-particle friction values, $\overline{\phi}_\mu$, and the corresponding standard deviation for the two sizes tested. The value ϕ_μ represents the interparticle friction angle at constant values of the vertical displacement using a normal force of 0.93 N and a shearing speed of 0.14 mm/hr. The value of $\overline{\phi}_\mu$ is taken as the arctan(μ) where μ is defined as the friction coefficient along the track of shearing defined as the ratio between the tangential and the normal force to the contact when the contact slope is given by $S_f x \triangle \delta_v / v_s$. Each set of particles were sheared twice, once in the initial direction and then again in an orthogonal direction.

The particle-wall friction was initially set to zero for the prototype simulations. As with the interparticle friction, the physical laboratory particle-wall friction was determined for use in the subsequent simulations. The friction interfaces were measured using a standard tilt-table method. Two groups of sample 1 size particles, a 20 particle clump and a 40 particle clump, were glued together to ensure no rolling and only pure sliding occurred. Both groups were tested against all of the relevant surfaces. For example, to determine the membrane-ball friction angle, the membrane

Table 4.2. Inter-particle friction angles

Particle Size	$\phi_{\mu,1}$ (°)	$\overline{\phi}_{\mu,1}$ (°)	$\phi_{\mu,1_{sd}}$ (°)	$\phi_{\mu,2}$ (°)	$\overline{\phi}_{\mu,2}$ (°)	$\phi_{\mu,2_{sd}}$ (°)
2.4 mm	4.2	3.7	1.8	4.5	3.9	1.4
2.4 mm	5.9	5.0	1.6	4.1	4.7	2.7
1.2 mm	9.4	8.5	4.4	15.5	11.8	4.9
1.2 mm	8.4	7.6	2.0	13.2	8.9	3.5

Table 4.3. Particle-wall friction angles

	Latex Membrane	**Porous Stone**	**Stainless Steel**
20 particles	18.1	22.2	8.9
40 particles	19.8	23.5	8.9

was attached to the tilting board (initially at zero degrees) and the 20 particle group was placed on the membrane. The board was tilted at an increasing angle until the particle group began to slide on the membrane. The angle at which sliding occurred was measured and recorded. The process was repeated for the 40 particle group and again for the other surface materials. Table 4.3 gives the resulting friction angles averaged over 10 trials for each of the material interfaces. Note that there is little variation for the 20 and 40 particle samples meaning that slight changes in normal stress are negligible. The 40 particle values were used in the DEM simulations.

As mentioned previously, the prototype simulations were begun before the interparticle and particle-wall friction values were determined. A sensitivity study was conducted in the sample preparation and shearing phases to asses the influence of these values on the void ratio and resulting response. These analyses and findings are discussed below.

4.1.2 DEM Sample Preparation

4.1.2.1 Background

A number of previous laboratory studies have shown that sample preparation methods can affect the mechanical behavior of granular materials. Even when samples are created at the same densities, initial variations in fabric can lead to differences in soil response during the later stages of testing (Jefferies and Been, 2006; Nemat-Nasser and Tobita, 1982; Mulilis et al., 1977; Vaid and Sivathayalan, 2000). The specimen preparation methods traditionally used in the laboratory were developed to recreate a given depositional pattern or in-situ soil fabric. These depositional patterns can not only create preferential contact orientation, but anisotropy can be introduced even for samples comprised of spherical particles (Oda, 1972). This inherent anisotropy has been shown to greatly influence stress-strain response, especially for cases involving principal stress rotation. Particulate DEM codes do not allow for a pre-specified initial packing of particles that is sufficiently dense to transmit stress or specification of a pre-defined stress state, i.e. the specimen preparation process itself must be simulated. If DEM simulations are to provide meaningful insight into soil response observed in element tests, it is important for the initial state (packing density and stress level) and fabric anisotropy of the computer generated sample to closely match the physical reality. This is particularly true for studies such as this, where element tests are used to validate DEM models. A key challenge is the lack of quantitative data on the fabric of real physical test specimens.

Several options exist for generating the specimens initial configuration and then transforming it into a percolating (stress transmitting) material. Bagi (2005) presents a comparison of several of the applied generation techniques and classifies each into one of two main categories: dynamic methods and constructive algorithms.

Constructive algorithms generate samples without the need for any periods of DEM calculations (i.e. the sample is created and directly input into the DEM model and the test simulation can proceed). Avoiding DEM calculation steps makes these methods effective and efficient; however, due to the complexity of the coding required, most of these algorithms have only been implemented in 2D. Examples include the advancing front approach proposed by Feng et al. (2003) and the inward packing method proposed by Bagi (2005).

Compression using rigid boundaries, radius expansion, and gravity settling techniques are all considered dynamic techniques meaning particles collide with one another and DEM cycles must be carried out. Most of these methods use a random generation approach for particle generation and placement. For 3D implementations, x, y, and z coordinates and a radius dimension are assigned using a random (or pseudo-random) number generation algorithm. If the particle overlaps an existing particle, it is randomly relocated until a position is found, or the number of tries reaches the maximum number set by the user. Samples with specified particle distributions can be created using this method. The result is always a diffuse (non-contacting) cloud of particles. The packing density can then be increased to create a percolating (i.e. stress-transmitting material) by isotropically compressing or K_0 consolidating the sample using the boundary walls. It is important that the compression is carried out at a sufficiently low speed so that the top and bottom boundary stresses remain sufficiently close in value, ensuring the sample reaches an equilibrium state properly. This requirement can cause the compression with boundary walls technique to be time intensive.

The radius expansion method is another option for densifying the diffuse cloud of non-contacting particles. In this case, particles are generated within the defined volume at a fraction of their target size. The particles radii are then expanded by

applying a multiplier or series of multipliers until the target is reached. Generally, the number of particles and the volume are set and the radii are adjusted until the target porosity is reached. Because this is a dynamic method and the expansions impart energy into the system, a series of DEM calculations must be run after each multiplier is applied. When the expansion is carried out in a step wise manner, the added DEM cycles can make this method very computationally expensive. Jiang et al. (2003) presented a dynamic method based on the experimental procedures proposed by Ladd (1978) that builds the sample up layer by layer and has the aim of producing loose samples.

In all of the methods described above, several issues arise when generating samples that will be used for experimental validation tests. Each of these methods is based on the idea that porosity is the target and the number and size of particles or the specimen geometry is adjusted accordingly. Most experimental devices require pre-defined geometries that make the isotropic boundary compression method less than ideal. Also, for experimental validation tests on metal ballotini, the number and size of particles is know while the porosity is often variable. The density/porosity is determined by the laboratory method used to create the sample. In terms of laboratory techniques, pluviation is most often used to create homogeneous granular samples at target densities. This makes the gravitational approaches a reasonable option for validation studies. The initial specimen can be created as a diffuse cloud and then a body gravitational force can be applied allowing the particles to settle into the specified geometry. Thomas (1997) used a random generator approach to place particles in a rectangular 2D mesh and then allowed them to settle under gravity. Marketos and Bolton (2010) used a similar approach to generate the particles and then moved the particles downwards until the particles contacted particles already at rest and slid into equilibrium.

4.1.2.2 DEM Sample Preparation Methods Investigated in this Study

Because these simulations are to be validated by laboratory data, it was important that the virtual samples matched the physical samples as closely as possible. As described previously, air pluviation is the most common laboratory method used for preparing dry sand samples and was the general laboratory method used in this study. This method, however, has been mostly abandoned by DEM modelers due to the costly time requirements. Radius expansion requires much less cycling and is the preferred method for most simulations, but as mentioned above, some general sense of the void ratio range is required, or flexibility in the size and number of particles is needed to make this process work properly. Compression with rigid boundaries is one method which may provide a compromise between these other two methods in that it allows for the number of particles to be generated at their actual size and it often requires less cycling than pluviation based techniques. With these factors aside, the main question is still, however, whether or not the sample preparation method used affects the initial fabric and subsequent response of the spherical assembly.

An initial investigation was conducted to determine the influence of these three methods on the initial fabric and shearing response. The sample preparation simulations were begun before the physical samples were tested and only an estimate of void ratio was known. The number of particles and sizes were also set for the physical sample and were not flexible in the virtual sample. For these reasons, the pluviation method was conducted first in order to provide an idea of the void ratio and the sample boundary dimensions needed for the radius expansion and compression with rigid walls techniques. The first step for any of these methods is the initial generation of the boundary geometry. A cylinder was generated with a 101.6 mm (4 in) diameter to match that of the physical sample. The height of the cylinder

was set at 152.4 mm (6 in) to match the cylindrical hopper height in the laboratory. Walls were placed at the top and bottom of the cylinder, as well as 50 mm from the top of the cylinder to create a zone for particle generation (Fig. 4.2a). The particles were then generated within the top 50 mm of the cylinder as a noncontacting cloud under no gravity load and with an interparticle friction angle of 5.5° (Fig. 4.2b). The wall friction values were set to zero. Note that all preliminary studies and prototype simulations were conducted on sample 1 only.

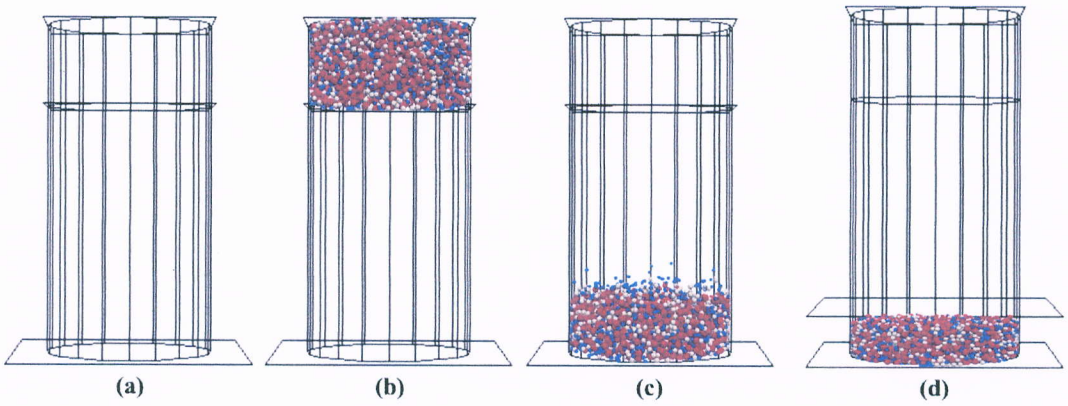

Fig. 4.2. Geometry and particle placement during sample generation and pluviation procedure

At this point, gravity was switched on and the particles were allowed to pluviate into the bottom of the cylinder until they reached a small unbalanced force representing dynamic equilibrium (Fig. 4.2c). In order to provide a consistent measure of void ratio, a wall representing the top cap was generated slightly above the highest particle and then a user-defined servo-stress control algorithm was used to lower the wall until the force was equal to the equivalent weight of the top cap in the laboratory (Fig. 4.2d). The velocity of the cap was set sufficiently slow so that the

process was quasi-static and the target force was reached monotonically. A further explanation of the top cap servo control is given below.

The second specimen was created using radius expansion. The pluviation method gave a good indication of the volume needed for the particle generation. The same diameter cylinder was created with a top and bottom wall, but the total sample height was only 30 mm. The height of the sample after the pluviation was actually 29.1 mm; however, when radius expansion was tried in three steps with this sample height, an error occurred and not all of the particles were generated. Also, the stresses on the top and bottom caps were extremely large. The boundary was moved to 30 mm at which point the radius expansion worked successfully. Particles were placed randomly within the volume at 0.512 times their actual size. The particles radii were multiplied by 1.25 three different times bringing them to their actual physical size. Each time the particles were expanded, an immediate buildup in energy occurred and was monitored by tracking the top and bottom cap stresses. Cycling was performed until the particles had reached equilibrium and the stresses were relaxed before the next expansion was initiated. Once the particles settled the final time, gravity was switched on and they were allowed to further settle into place. The resulting stresses on the top and bottom cap after equilibrium was reached were lower than that of the physical top cap weight. The top cap was then lowered as before using a user-defined stress control algorithm, so that a proper comparison could be made.

The third and final dynamic technique tested was compression using rigid boundaries. This method used the same cylinder diameter, but was instead at a height of 1.5 times the pluviation height (43.65 mm total height) with the top and bottom caps in place. The particles were generated using the same radius expansion technique as before, but because the volume was larger they were generated as a

Table 4.4. Void ratios for each of the dynamic sample preparation methods with the interparticle friction set to 5.5°

Method	Void ratio, e
Pluviation	0.6668
Radius Expansion	0.6815
Rigid Wall Compression	0.6703

noncontacting cloud. The same type of user-defined servo stress controlled algorithm was used to move both the top and bottom caps simultaneously toward the center of the sample. The stress on the top cap and bottom caps were monitored until both reached the target value. At this point, gravity was switched on and the particles were allowed to settle to equilibrium. This reduced the stress measured on the top cap, so it was moved downward again to re-obtain the target value.

Table 4.4 gives the resulting void ratios for each method. The void ratios determined using these methods were not the same. It was thought that any differences in shearing response would be more likely due to the differences in density and that any differences due to the actual fabric would be covered up. Therefore, the samples were again created with the interparticle friction lowered to 0.5°. A slightly different approach was taken in the pluviation method. Pluviating a sample at such a low ball friction value would take an unreasonable amount of time. Instead, the last file was used from the sample pluviated with the ball friction at 5.5°. The top cap was stopped and the friction angle was lowered to 0.5°. Cycling occurred until a small unbalanced force was reached and the top cap was lowered to again reach the target value. Table 4.5 gives the void ratios obtained for each method with the interparticle friction set to 0.5°. The pluviation and radius expansion void ratios are very close. The compression with rigid walls method created a slightly more dense sample, but the values are within a reasonable range to analyze and compare the sample fabrics.

Table 4.5. Void ratios for each of the dynamic sample preparation methods with the interparticle friction set to 0.5°

Method	Void ratio, e
Pluviation	0.6283
Radius Expansion	0.6299
Rigid Wall Compression	0.6213

The response of granular materials is known to be highly dependent on the initial packing density, as well as the initial stress level, the fabric anisotropy (based on the particle contact orientations), the stress anisotropy, and the principal stress orientations. The macro-scale properties of each sample are assessed, in this case, similar to the laboratory data by looking at the overall void ratios and measured stresses. It is clear that the macroscopic details of these samples are very similar. The void ratios and stresses have intentionally been brought to similar values. The advantage of DEM is in its ability to quantify more localized measurements of void ratio, stress, and strain and provide a microscopic look into the samples. Along with the overall measurement, the void ratio can be determined according to a height profile for different locations throughout the sample. Fig. 4.3 gives the corresponding void ratios for five vertical zones within the sample. Fig. 4.4 plots these values at the center height of the layer to provide a graphical view of the void ratio profiles.

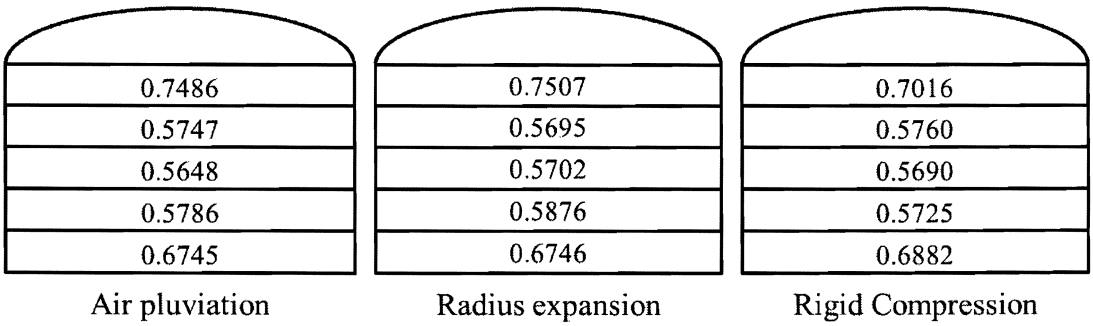

Fig. 4.3. Void ratios for five vertical zones within the samples

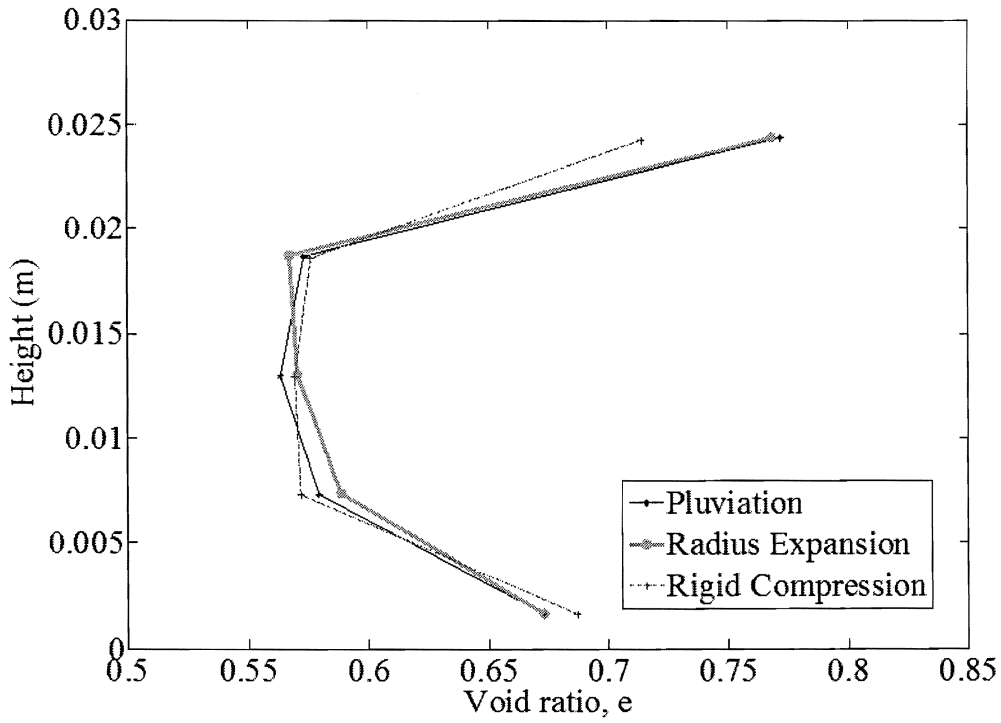

Fig. 4.4. Plot of void ratios within the five vertical zones

The volume contributions are correctly calculated to account for spheres that lie in two zones. It is clear that there are some boundary effects. In other words, the void ratios are higher where the spheres are bordered by a flat boundary, most notably the top boundary. Most of the zones are quite similar for the three methods. One exception is that the top boundary zone for the rigid compression sample has a lower void ratio than that of the other two samples. It is still difficult to conclude much in terms of differing sample fabric based on this information. A closer look at the microscopic information is needed in order to determine if any fabric differences are present.

As outlined in Potyondy and Cundall (2004), PFC3D allows for various parameter to be measured and recorded for defined measurement volumes, termed measurement spheres, located throughout the sample. Not only can quantities such as void ratio be averaged over the volume, these measurement spheres can also provide the average stress tensors. For each of the three prepared samples, five measurements spheres were placed in the locations shown in Fig. 4.5. Fig. 4.6 shows a comparison of void ratios for various measurement locations and Fig. 4.7 shows the void ratios for the five measurement spheres.

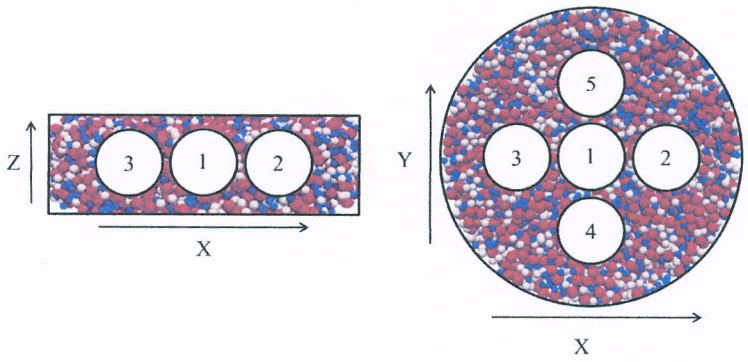

Fig. 4.5. Locations of measurement spheres within sample

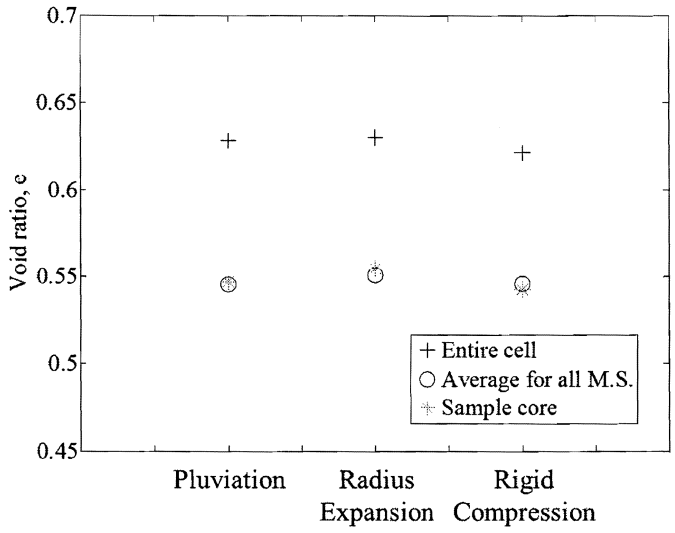

Fig. 4.6. Comparison of void ratio for various measurement locations

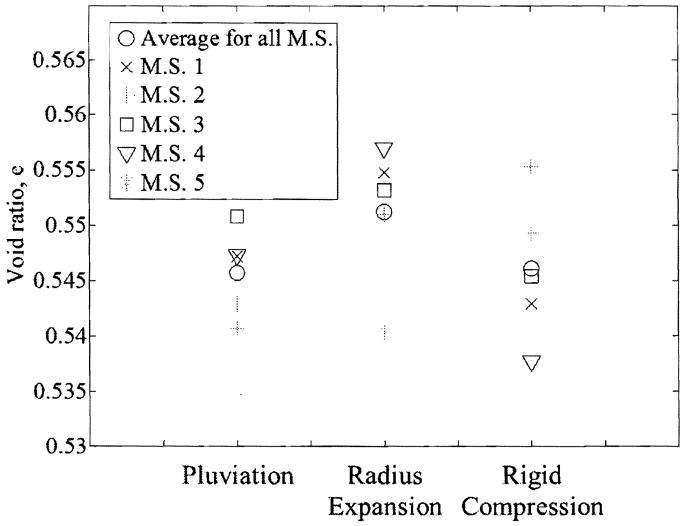

Fig. 4.7. Comparison of void ratios at five measurement sphere locations

For all three methods, it appears that the central zone of the sample is much more dense than than the void ratio measured for the entire cell. This agrees with the results from the layered approach above and shows that the boundary effects make the sample appear to be less dense than it actually is. In other words, using a measurement of the entire cell underestimates the actual density of the majority of the sample. The sample core is taken as M.S. 1 and is almost equal to the average for all of the measurement spheres for each method. The comparison of all measurement spheres shows that there is slight spatial variation in void ratio. The sample core (M.S. 1) and the average value obtained for all of the measurement spheres are closest for the pluviation method. This method also shows less overall spread in the void ratio range and is likely a more uniform and homogeneous sample in terms of void space. Additional considerations in stress distribution and fabric are needed to confirm this.

One method of quantifying the effects of the sample preparation method on sample fabric is to look at the coordination number. The coordination number is calculated as

$$Z = 2\frac{N^c}{N^p} \tag{4.1}$$

where N^c is the number of contacts and N^p is the number of particles. The coordination number quantifies the number of contacts per particle in the assembly and it gives a measure of packing density and contact intensity at the particle scale. It represents the most basic micro-scale measurement of the structure of a material. Figs. 4.8 and 4.9 show comparisons of the coordination number, Z, for various measurement quantities.

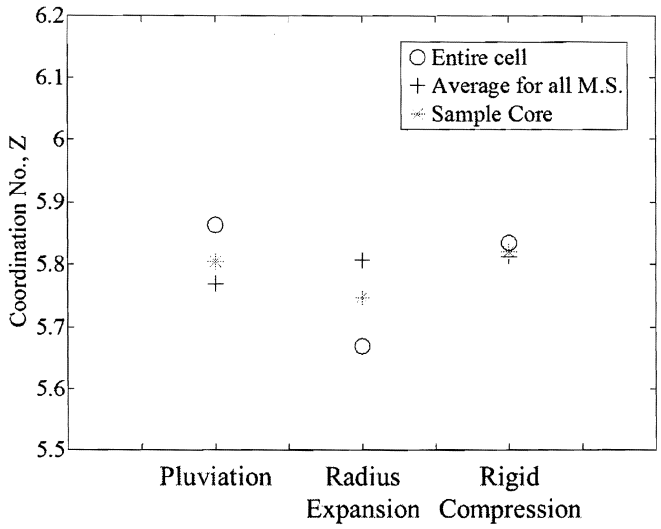

Fig. 4.8. Comparison of coordination number, Z, for various measurement locations

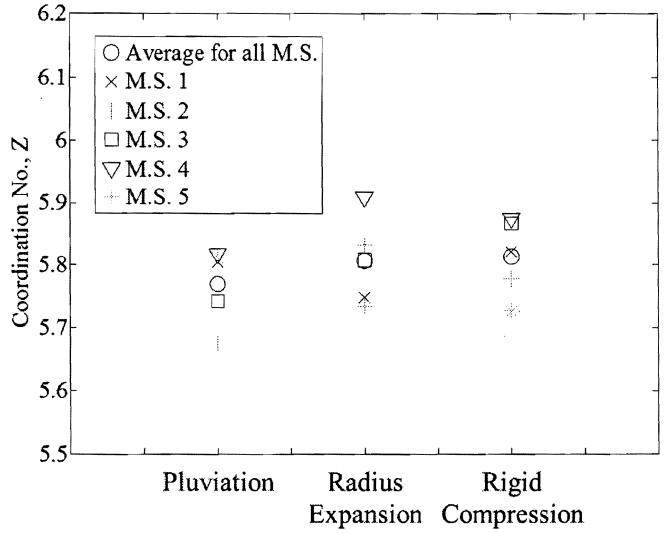

Fig. 4.9. Comparison of coordination number, Z, at five measurement sphere locations

The coordination number for the entire cell is also very representative of the sample core and average measurement sphere values for the method using rigid wall compression. The radius expansion method appears to generate the most varied distribution of coordination number and the measurement of the entire cell is not as representative of the sample core or average measurement sphere value. Although the rigid compression values are very similar on Fig. 4.8, it is the pluviation method that exhibits the least variable coordination values in terms of spatial distribution (Fig. 4.9). This again shows that the pluviation method produces a sample where the majority of the sample is uniform. The boundary effects, however, have a greater influence in the measured quantity for the entire cell.

An accurate measure of state must consider both the packing density and the stress level. While the vertical stresses originate from gravity, horizontal stresses can be induced during pluviation, giving a range of mean stress values. Such data is rarely obtainable in a physical pluviation; however, DEM data can be used to analyze the internal stresses. Following Potyondy and Cundall (2004), the representative average stress tensor for particle p ($\overline{\sigma^p}_{ij}$) is calculated as

$$\overline{\sigma^p}_{ij} = \frac{1}{V^p}\sum_{c=1}^{N^{c,p}} f_j^c x_i^c \tag{4.2}$$

where V^p is the volume of the particle, $N^{c,p}$ is the number of contacts involving particle p, f_j^c is the force transmitted via contact c, and x_i^c is the location of contact c. The average stress for the measurement sphere is then calculated as

$$\overline{\sigma^s}_{ij} = \frac{1-n}{\sum_{p=1}^{N^p}} V^p \sum_{p=1}^{N^p} \overline{\sigma_{ij}^p} \tag{4.3}$$

where N^p is the total number of particles and n is the porosity in the measurement

sphere. This porosity corrects for the fact that the stresses are zero in the void space. A comparison of the mean stresses $\overline{p}^p = \frac{1}{3}(\overline{\sigma^p}_{xx} + \overline{\sigma^p}_{yy} + \overline{\sigma^p}_{zz})$ for each method considered are presented in Figs. 4.10 and 4.11.

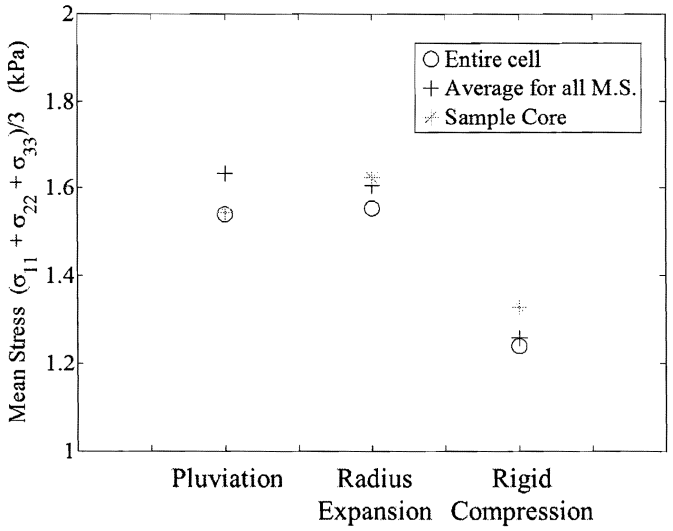

Fig. 4.10. Comparison of mean stress for various measurement locations

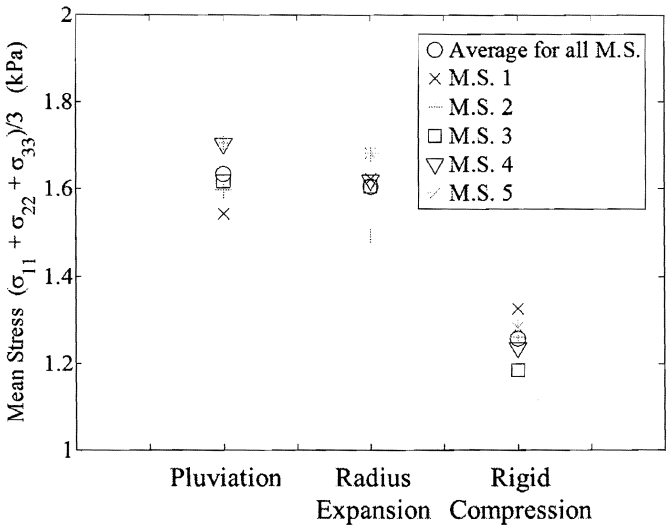

Fig. 4.11. Comparison of mean stress at five measurement sphere locations

From Fig. 4.10 it is clear that the mean stress measured for the entire cell is the same as that measured for the sample core. The average masured for all measurement spheres is slightly higher. For the other two methods, the entire cell measurement is closer to the average value for all the measurement spheres. It should also be noted that the rigid compression method results in a lower mean stress than the other two samples. Similar differences in magnitude are seen for all of the measurement sphere locations (Fig. 4.11). To get a better idea of why this is the case, the vertical stresses can be plotted in a similar manner (Figs. 4.12 and 4.13).

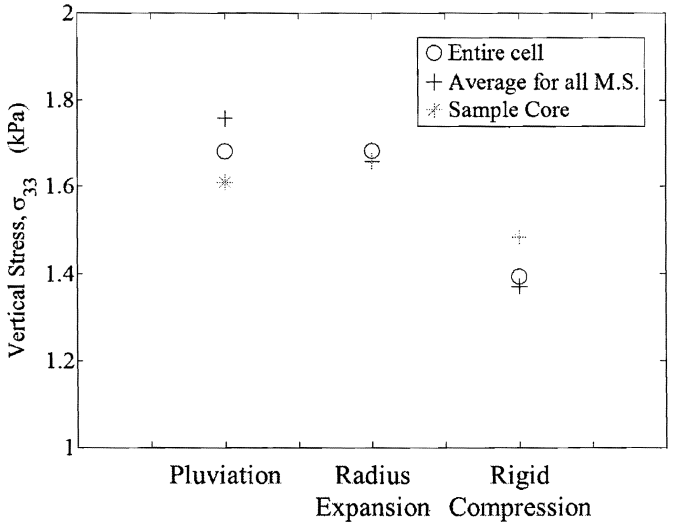

Fig. 4.12. Comparison of vertical stress for various measurement locations

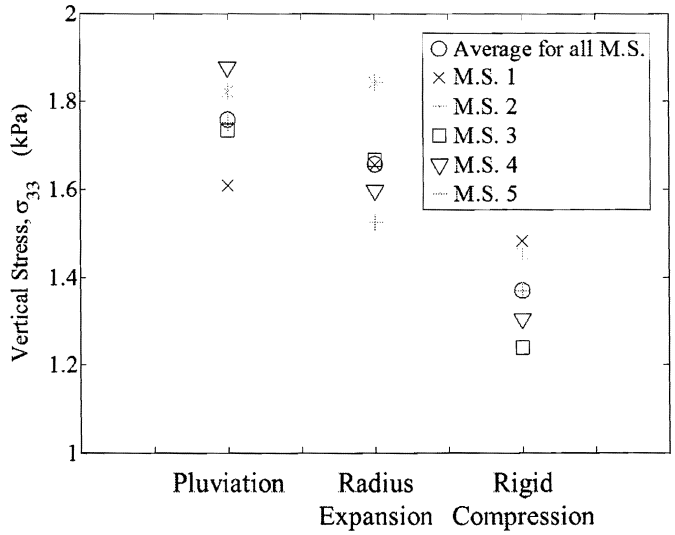

Fig. 4.13. Comparison of vertical stress at five measurement sphere locations

The target vertical stress for each of these simulations was approximately 1.02 kPa for the top cap stress. The values measured based on the average stress tensors from PFC are larger for each of these samples. If the additional stress due to the self weight of the particles (1.33 kPa) is considered, the bottom cap normal/vertical stress should be approximately 2.35 kPa and the middle of the sample should be at a vertical stress of approximately 1.69 kPa. This matches the values for the pluviation and radius expansion methods quite well. The rigid compression values are still less than expected. To examine whether this difference also held at higher vertical stresses, the normal load was increased to 50 kPa (Figs. 4.14 and 4.15).

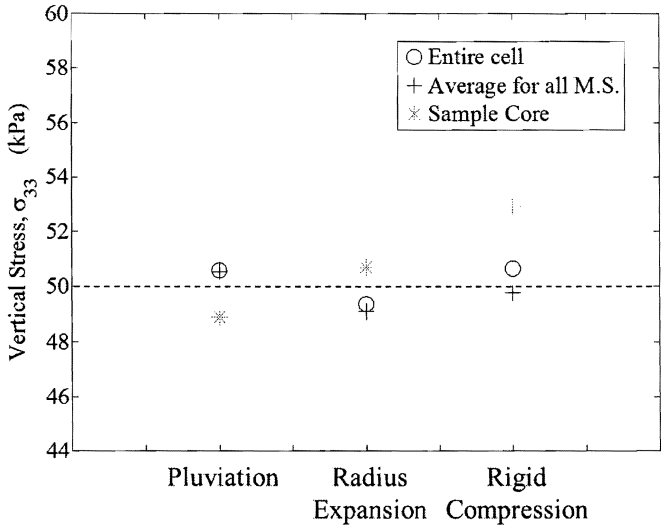

Fig. 4.14. Comparison of vertical stress for various measurement locations at a vertical effective stress of 50 kPa

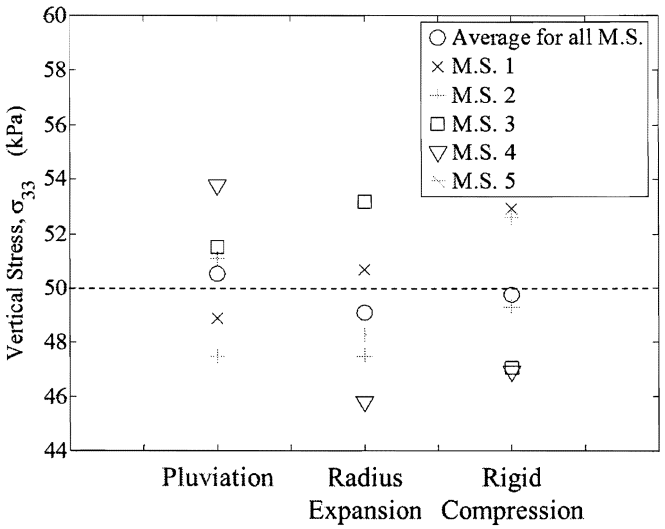

Fig. 4.15. Comparison of vertical stress at five measurement sphere locations at a vertical effective stress of 50 kPa

At 50 kPa vertical effective stress on the top boundary cap, the values measured for the entire cell and the average for all of the measurement spheres are close to the expected top boundary stress condition; however, the sample core values are varied. Several researchers have shown that internal stresses are different than the boundary stresses measured. This is also evident in these samples, most notably for the rigid compression sample.

The sample anisotropy can be quantified by considering the orientation of the contact normals. Following Satake (1982), the fabric tensor for a granular material is given by

$$\Phi_{ij} = \sum_{c=1}^{N^c} n_i^c n_j^c \tag{4.4}$$

where n_i^c is the unit normal vector describing the orientation of contact c and there are N^c contacts in the system. The eigenvalues of this fabric tensor give a measure

of the extent of clustering of the contact orientations around preferred, principal orientations. Fig. 4.16 shows the ratio of the major component of the fabric (Φ_1) divided by the minor component of fabric (Φ_3). Two separate calculations were made: one considering all contacts within the assembly and the second considering only the internal contacts and no boundary contacts. Larger values of fabric ratio signify more anisotropic samples.

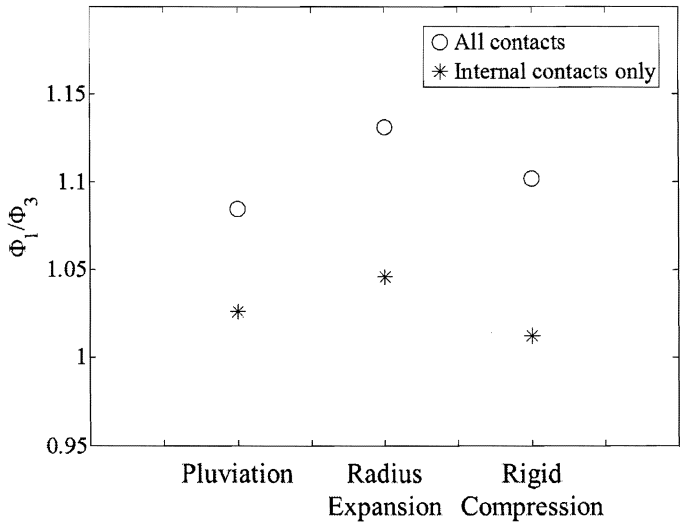

Fig. 4.16. Comparison of fabric with various contact conditions considered

These samples are all cross-anisotropic, which is expected from the K_o stress conditions imposed. When all contacts are considered, the pluviation method gives a more isotropic and uniform fabric. As seen in the figure, some difference in fabric ratio exist based on the contacts considered. The majority of the contacts are oriented vertically due to the imposed stress conditions. This, in turn, explains why the values become more isotropic (i.e. closer to one) when the boundary contacts are

removed. The internal sample is therefore more isotropic, most notably for the rigid compression sample. The radius expansion sample has the highest anisotropy ratio in both cases.

An additional method to examine the anisotropy of a sample is to examine the distribution of the orientations of the contact normals to the vertical. Fig. 4.17 presents the histograms for the contact orientations and compares them to a perfectly isotropic case.

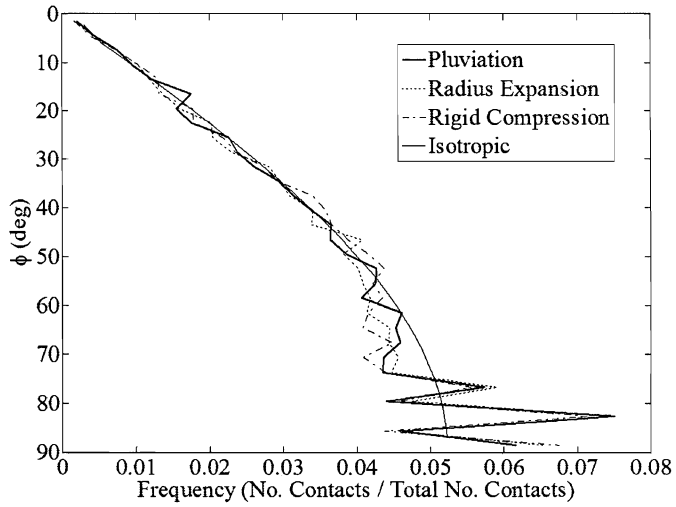

Fig. 4.17. Comparison of contact orientations with an isotropic case

These samples are all similar and it is difficult to make a strong determination of any differences. The pluviation method does appear to produce a sample that is more closely related to the isotropic case when compared to the other two. Note that all contacts were included in this analysis and that effects from the boundary conditions are most likely the cause of the large deviations from the isotropic case near 90° (i.e. close to the point where they are horizontally oriented).

The orientation of the contact normals can be further considered by plotting rose diagrams of the angles the unit normals make with the horizontal and the vertical planes. Fig. 4.18 gives the rose diagram for the direction/angles the unit normals make with respect to the x-axis (defined by 0°). Fig. 4.19 gives a similar diagram for the vertical orientation of the contact normals with respect to the z-axis (also defined by 0°). Note that these diagrams consider all contacts within the assembly.

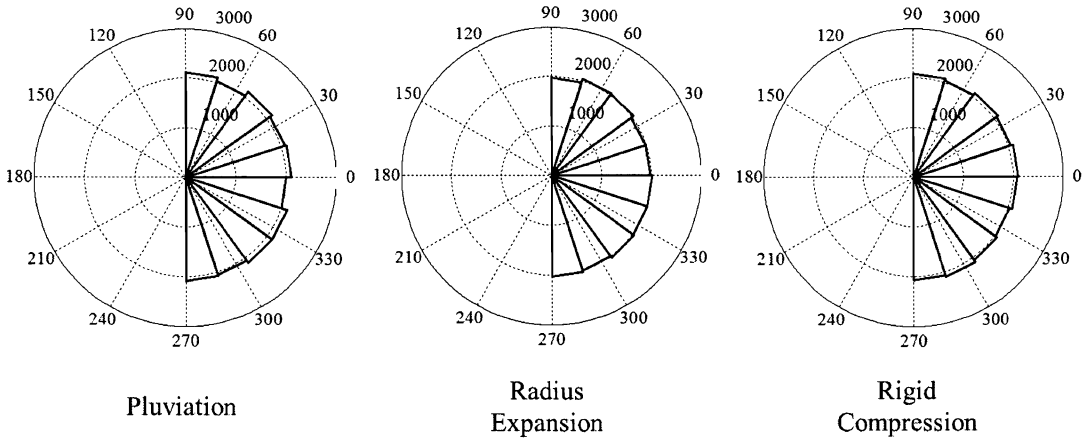

Fig. 4.18. Rose diagram of contact orientations with respect to the horizontal plane

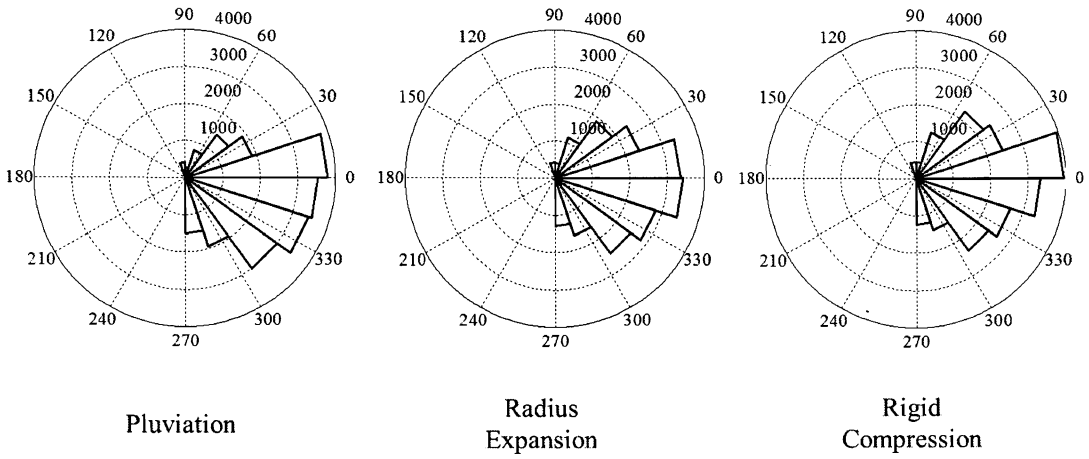

Fig. 4.19. Rose diagram of contact orientations with respect to the vertical plane

The horizontal rose diagrams look very similar for all of the methods and no real distinctions can be made besides the already determined cross-anisotropy of the samples. The rose diagrams for the orientation of the contact to the vertical, however, show several differences. The radius expansion method creates a sample with a somewhat symmetric distribution of contact angles about the vertical. The majority of the contacts are oriented between $\pm 18°$ from vertical. The rest of the contact orientations appear to be also symmetrically distributed at larger angles. The rigid compression method, on the other hand, produces a sample with the largest number of contacts oriented between 0 and 18° from vertical. The second preferred orientation is between 0 and -18° and the rest of the contacts are distributed symmetrically, similar to the rigid compression case. The pluviation procedure produces a sample like the rigid compression method, in that the largest number of contacts are oriented between 0 and 18°, but the rest of the contacts are heavily oriented in the negative angle range. In other words, while the majority of contacts are still oriented vertically, there are more horizontally oriented contacts in this sample compared to the

Table 4.6. Computational time for sample preparation phases with interparticle friction set to 0.5°

Preparation Method	**Time Required (hrs)**
Pluviation	102.11
Radius Expansion	134.72
Rigid Compression	16.48

other two samples. This agrees with the earlier discussion related to fabric ratio and fabric anisotropy.

While the overall macro-scale data suggests these samples are at similar initial states, the microscopic data shows slight differences. The pluviation sample overall tended to be more uniform in terms of packing density, stress distribution, and fabric. Based on the sample preparation phase only, no major findings warrant the use of one of these methods over the other. The decision, therefore, depends on how accurate one would like to replicate the laboratory samples, the possibility of differences in the subsequent shear response, and time constraints. Table 4.6 gives the computational time required for each of these methods with the interparticle friction set to 0.5°. This time includes the initial sample generation all the way through the placement of the top cap at 1.02 kPa. Note that the times are shorter for the other prototype simulations conducted at higher interparticle friction values. Also, the pluviation time includes the generation, pluviation, top cap placement at 5.5° interparticle friction, and then a second top cap placement after the interparticle friction angle was lowered to 0.5° and allowed to settle. The time would be approximately 48 hours less if only one top cap placement routine were conducted.

The pluviation samples take much longer to prepare than the rigid compression samples, but are actually faster than the radius expansion technique. Irrespective of

the computational time required, it was a top priority that the virtual PFC samples replicated the physical laboratory samples as closely as possible. Due to this constraint and the slight differences in findings discussed above, the pluviation method was chosen as the sample preparation method in this study. A further discussion of the procedure and the results from several sensitivity studies are given in the next paragraphs. For completeness of the above study, the three prepared samples were sheared to determine if any additional effects were observed. These findings are discussed following the pluviation study and the development of the simple shear control code and results.

4.1.2.3 Pluviation Method Investigation

Similar to pluviation methods in the laboratory, it was proposed that the pluviation methods used in the DEM simulations would affect void ratio, as well as other properties of the samples generated. Therefore, a preliminary study was conducted to assess the sensitivity of void ratio to various parameters and pluviation methods. The same methods used in the lab were simulated for the DEM samples (refer to Chapter 3). In each case, the noncontacting particle cloud was generated in the top portion of the 101.6 mm diameter cylindrical boundary, similar to the pluviation case described above. To expedite the study and reduce the time required for the particles to settle, a lower drop height was initially used. The particles were generated within the top 50.8 mm (2 in) of a 111.6 mm cylinder. A total of five different pluviation methods were tested, replicating the methods used in the laboratory. Table 4.7 summarizes the laboratory methods.

Although it was the last method described in the laboratory procedure, method 6 was the most simple simulation to set up and therefore, was conducted first in the DEM program. Once generated, the interparticle friction was changed to 5.5°, gravity

Table 4.7. Summary of pluviation methods tested in the laboratory and replicated in DEM

Method	Description
1	Pluviation with no mesh followed by vibration and tamping (3 lifts)
2	Pluviation through a 5.5 mm mesh
3	Pluviation through a 7.7 mm mesh
4	Pluviation followed by pulling a 5.5 mm mesh up through the sample
5	Pluviation followed by pulling a 7.7 mm mesh up through the sample
6	Pluviation with no mesh

was applied, and the bottom wall of the hopper was removed, allowing the particles to settle into the lower portion of the cylinder. No mesh was used for this method. This is the same pluviation method described above in the initial comparison of the sample preparation methods. By default, PFC applies local damping to the particles. Local damping is essentially used to damp accelerating particles and speed up the calculation time. For simulations where particles are in free-fall, little or no local damping should be applied. A sensitivity study was conducted to assess the effects of changing local damping. The method 6 type pluviation technique was repeated several times for various values of local damping: 0.7 (default), 0.5, 0.2, 0.05, and 0.01. The coordination number and kinetic energy were tracked for each simulation. Fig. 4.20 shows a plot of the kinetic energy and the coordination number for the assembly during the pluviation process.

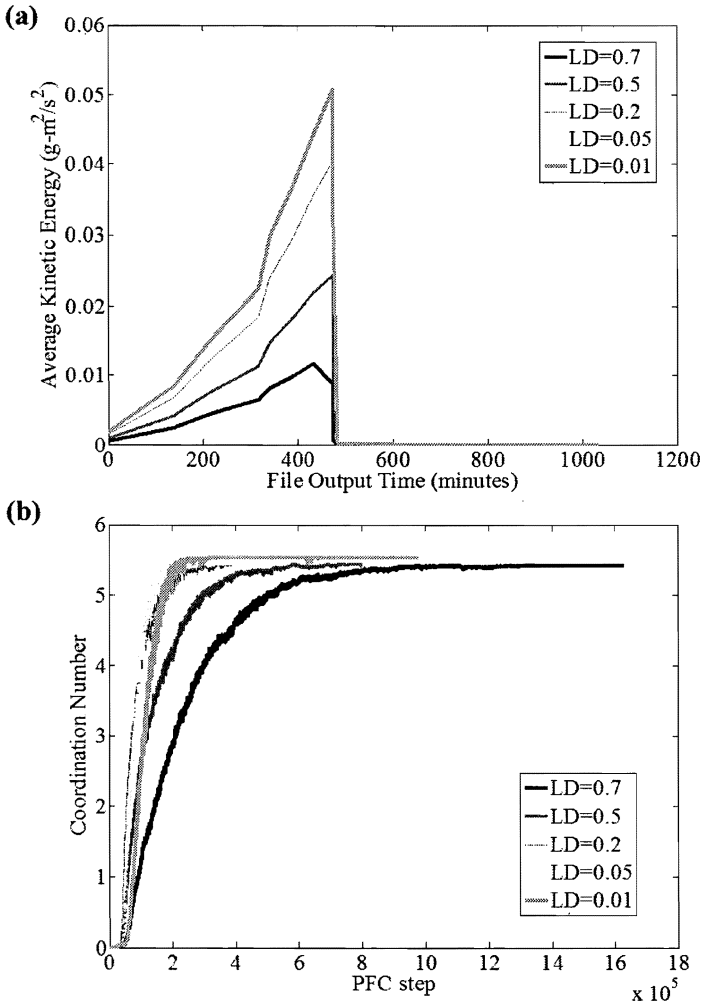

Fig. 4.20. Comparison of (a)kinetic energy and (b)coordination number for method 6 pluviation simulations for different local damping values

It is clear from the plot that lowering local damping increases the kinetic energy because the acceleration is not as damped, but all of the simulations appear to reach low kinetic energy values (settle) in approximately the same time. No major trends or differences were noticed for coordination number. The samples all reach a fairly consistent coordination number irrespective of local damping value. The local

damping value was set to 0.01 for all remaining simulations.

For methods 2 and 3, gravity was applied and the bottom hopper wall was removed, allowing the particles to pass through a stationary sieve and into the bottom of the cylinder. The mesh sieve in the laboratory was moved vertically to maintain a constant distance from the top of the sample; however, this was not implemented in the DEM simulations. The "virtual" sieve was located 35.4 mm above the bottom of the sample cylinder and was created by a series of line walls arranged in a square grid pattern. Two different mesh sieve opening sizes were simulated. Method 2 used a sieve with 5.5 mm square openings, while method 3 had 7.7 mm size openings. Methods 4 and 5 consisted of using the final file from method 6 and then "pulling" a mesh sieve up through the sample at a constant rate. Two mesh sieve sizes (5.5 mm and 7.7 mm openings) were used in the method 4 and 5 simulations, respectively. Due to the difficulty in modeling vibrating and tamping, method 1 was not simulated initially.

Each simulation was allowed to cycle to equilibrium while monitoring both the coordination number and the mean unbalanced force (i.e. resultant force causing acceleration). For each of the methods, the coefficient of friction of the particles was set to 0.0963 (5.5°), the wall-particle friction angle was set to 0°, and local damping was set to 0.01. Table 4.8 gives the void ratios resulting from each of these trials. Due to the time requirements, a top cap was not placed on all of these samples. The sample was divided as before into five vertical layers (Fig. 4.21). The average void ratios presented are the average of the 4 lower vertical layers of the sample.

Table 4.8. Summary of void ratios for the various pluviation methods tested in the laboratory and replicated in DEM

Method	e_{avg}	e_1	e_2	e_3	e_4	e_5
1	Not tested	–	–	–	–	–
2	0.594	3.731	0.588	0.577	0.562	0.650
3	0.606	2.624	0.594	0.587	0.578	0.663
4	0.629	2.996	0.573	0.577	0.627	0.629
5	0.624	2.228	0.566	0.580	0.609	0.740
6	0.618	2.941	0.596	0.590	0.596	0.692

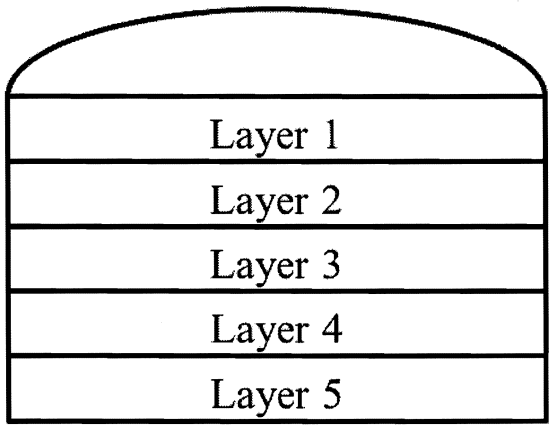

Fig. 4.21. Vertical layers used for void ratio distribution investigation

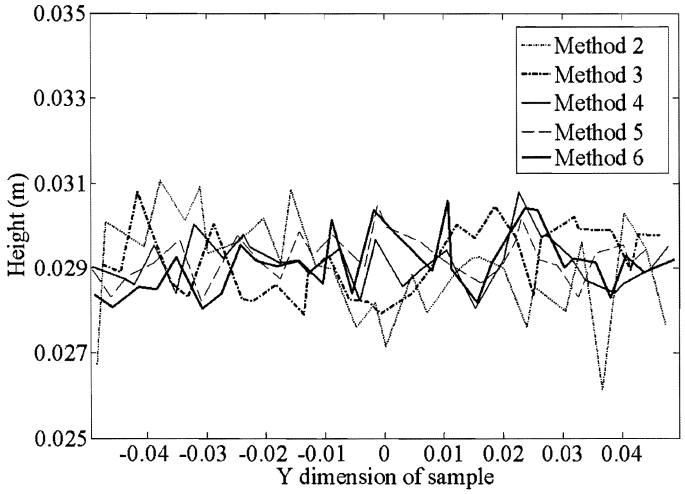

Fig. 4.22. Comparison of top particle profiles for pluviation methods

It is clear that the boundary effects at the top layer are extreme when no top cap is present. Fig. 4.22 shows a comparison of the top profiles of the samples. The lines plotted lie on the top boundary of each of the edge particles through the centerline of the sample. It is difficult to tell much from this plot except that the top boundary is very erratic. Considering the average void ratio for the four bottom layers, there is little variation in void ratios observed. Fig. 4.23 shows the void ratios versus with height for the bottom four layers.

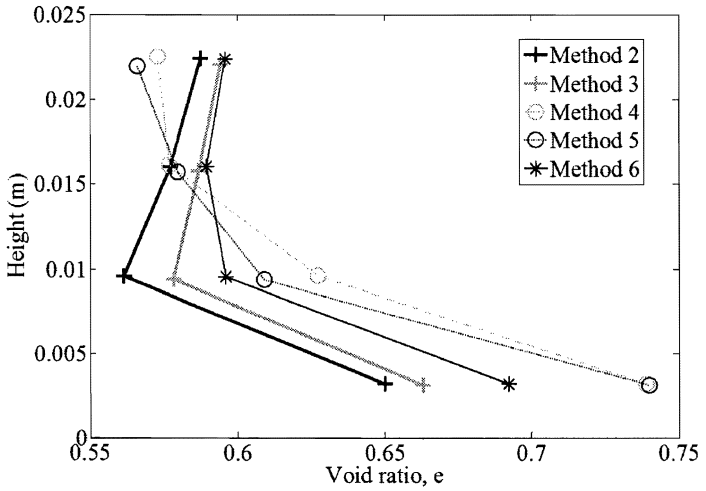

Fig. 4.23. Comparison of void ratio with sample height

The trends for the method 4 and 5 samples are similar, while the other three methods also have profiles similar to one another. A closer look at the microscopic information is needed to make any further conclusions regarding the methods. Similar to the analysis conducted for pluviation, radius expansion, and rigid compression, the results from five measurement spheres are plotted for void ratio, coordination number, and mean stress (Figs. 4.24, 4.25, and 4.26).

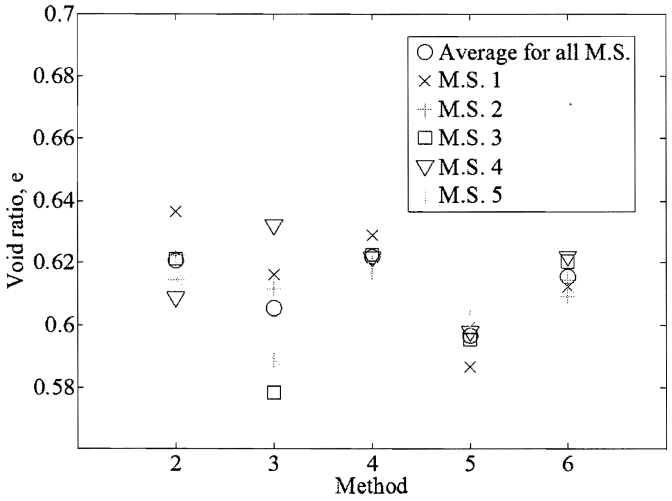

Fig. 4.24. Comparison of void ratio for five measurement spheres for the pluviation methods tested

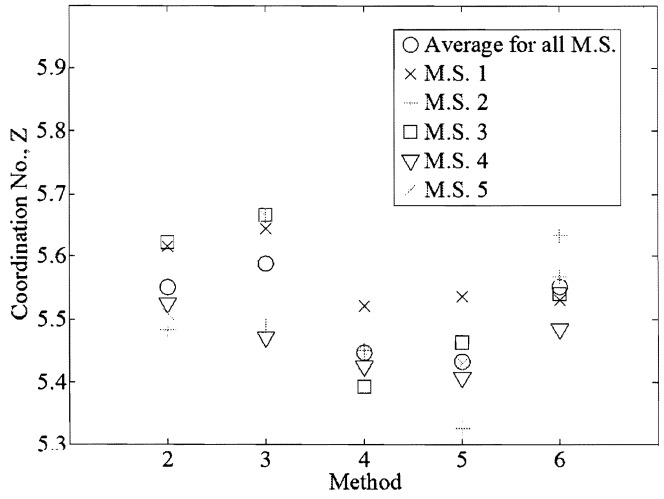

Fig. 4.25. Comparison of coordination number for five measurement spheres for the pluviation methods tested

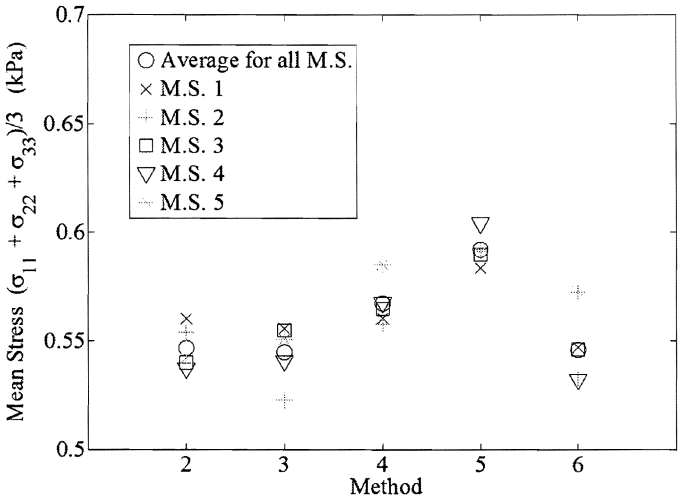

Fig. 4.26. Comparison of mean stress for five measurement spheres for the pluviation methods tested

Methods 4 and 5 create very uniform samples for all three values plotted. Method 4 tends to create the most uniform and homogenous overall. All five measurement spheres from method 4 fall among some of the highest void ratios observed. Method 6 also creates a uniform sample in terms of void ratio, but it is less consistent for coordination number and mean stress. The mean stress values are somewhat similar with the exception of M.S. 5. A plot of fabric ratio (Fig. 4.27) also shows that methods 4 and 5 produce samples which are uniform and more isotropic than the other samples. Similarly, a plot of the distributions of the contact normals to the vertical (Fig. 4.28) also shows that methods 4 and 5 produce the most isotropic samples. Overall, the different pluviation methods produce slight variations in the measured microscopic quantities. Method 4 produces the loosest and most uniform sample for the initial DEM simulations.

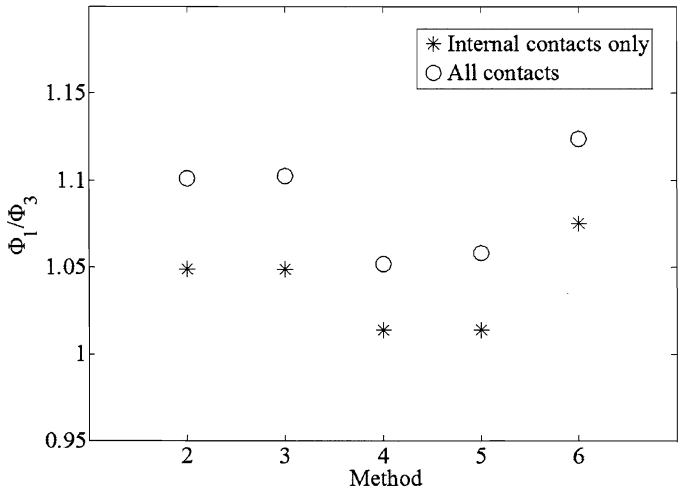

Fig. 4.27. Comparison of fabric anisotropy for the pluviation methods tested

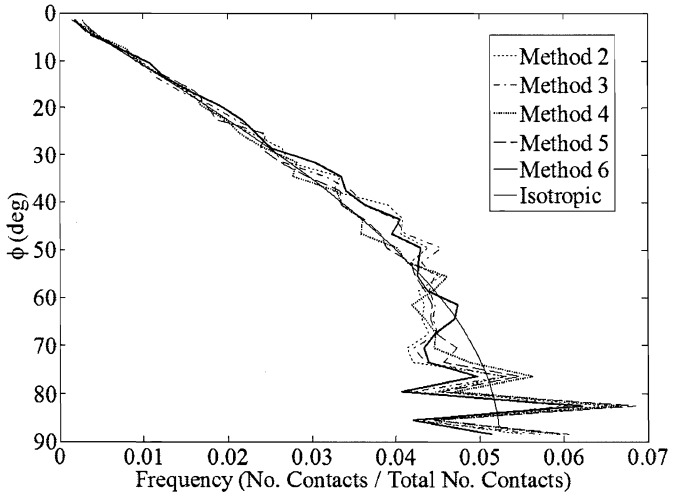

Fig. 4.28. Comparison of the distributions of the orientations of the contact normals to the vertical for the pluviation methods tested

Table 4.9. Summary of void ratios for method 6 with a sample top cap

Method	e_{avg}	e_{tot}	e_1	e_2	e_3	e_4	e_5
6	0.618	0.668	0.893	0.591	0.592	0.597	0.704

Method 4 is also the method that was used in the laboratory to produce the loosest samples. The DEM simulations resulted in a difference in void ratio of 0.035 from the loosest to the densest, while the laboratory range was 0.051. What is true for both the laboratory and the DEM simulations, however, is that method 4 results in the highest void ratio (loosest sample) in both cases. It is difficult to directly and quantitatively compare the results without the sample top cap. To better compare the laboratory and DEM samples, a top cap was added to the method 6. The updated void ratios for this sample are presented in Table 4.9. The average is calculated using all five layers. The void ratio was also determined using the entire cell volume, e_{tot}, rather than the average to check the difference in measurement methods. As presented in Table 3.4, the void ratio ratios for methods 4 and 6 in the laboratory were 0.738 and 0.687, respectively. Including the void ratio of the top layer which is more loose due to boundary effects raises the overall void ratio, but the DEM values are still lower than those obtained in the laboratory. This is not unreasonable based on the fact that the conditions in the DEM set up are not exactly like those of the laboratory. For example, the DEM sample currently has zero wall friction and a different drop height. Also, the speed of the mesh in method 4 could affect the resulting void ratio. Several additional sensitivity studies were conducted to assess the influence of these parameters on the overall void ratio.

The initial study consisted of varying the wall friction values and then the particle friction value to assess the sensitivity of void ratio to wall-particle friction. Table 4.10 presents the resulting average void ratios for method 4 and 6 using different

Table 4.10. Summary of void ratios for method 4 and method 6 with various values of wall and particle friction angles

Particle friction (°)	**Cap friction** (°)	**Side friction** (°)	**Sieve friction** (°)	**Method 4** e_{avg}	**Method 6** e_{avg}
5.5	0	0	0	0.629	0.618
5.5	30	30	10	0.640	0.625
5.5	23.5	19.8	8.9	0.623	0.629
6.5	0	0	0	0.631	0.624
6.5	30	30	10	0.647	0.629
10	30	30	10	0.668	0.653

wall friction angles and particle friction angles. The average void ratio is based on the four lower layers because no top cap was added to these samples. The wall friction angles of 23.5, 19.8, and 8.9° correspond to the friction values determined using tilt-table tests for each surface material in the laboratory. For particle-wall interactions, the largest of the two friction values was used. It is clear from the results that wall friction and interparticle friction affect the void ratio. Larger friction values result in higher void ratios and looser samples. Increasing wall friction tends to only slightly affect the void ratio, while interparticle friction values have a strong influence in the void ratio obtained. Again, it is difficult to directly compare these to the laboratory values because of the fact that only the bottom four layers are averaged. Even if the top layer void ratio were included by setting it equal to the previous determined value, the resulting void ratios would still be lower than the laboratory values. Therefore, even though friction values influence the void ratio, friction alone is not enough to account for the differences, even when unrealistically high values (10°) of interparticle friction are used.

The next set of simulations were carried out to assess the effects of free-fall conditions on void ratio. Three different drop heights were tested measured from the

Table 4.11. Summary of void ratios for method 4 and method 6 with various free-fall conditions

Drop height (mm)	**Drag force applied (Y/N)**	**Method 4** e_{avg}	**Method 6** e_{avg}
86.2	N	0.623	0.629
86.2 w/v_i	N	–	0.619
101.6	N	–	0.619
152.4	N	–	0.618
152.4	N	–	0.617
152.4	Y	0.616	0.618

highest particle drop distance. An additional sample was tested at the original drop height with an initial velocity applied to account for the additional free-fall acceleration of the particles if dropped from a higher drop height of 152.4. Also, the effects of drag force due to air resistance were also investigated. Table 4.11 presents the results. The interparticle friction was 5.5° for all simulations. The laboratory values of wall friction were used for this analysis (Cap=23.5°, Side=19.8°, and Sieve=8.9°). Drop height has very little influence on the void ratio for the DEM samples. The values are also much lower than what was determined in the laboratory for method 4. The loose samples are prepared in the laboratory by pluviating the sample from a 152.4 mm drop height and then pulling the sieve up through the sample. This was modeled as closely as possible in the DEM, yet the values are still much lower. The speed of the virtual mesh sieve was also thought to have some influence. Several trials were conducted for various velocities as well as various values of sieve friction value to try and gain a more loose sample. None were successful. Slowing the sieve down tended to lead to a more dense sample, which contradicts the expected relationship. The process of pulling the sieve through the sample was observed as the DEM simulations cycled by displaying the walls and particle geometries. This

showed several issues that could have caused the observed anomalies. Higher values of friction tended to cause the particles to "lock" and not fall through the sieve. This occurred on occasion in the laboratory procedure, but the particles were moved manually, so that they began to flow again through the sieve. This is very difficult and impractical to do in the DEM simulations.

Even with the large number of simulations conducted to study the influence of the various parameters, the DEM void ratios obtained were still much lower than those observed in the laboratory. Also, the densest sample had not been developed and due to the time required to place the top cap, it was not practical to model the tamping process. Many researchers have reported similar problems with creating a range of densities in DEM. It was important that the void ratios match the laboratory data in this study so that proper validation could be carried out. Two alternative methods were adopted in order to create a larger range of densities similar to the dense and loose cases in the laboratory. The densest sample was created by taking the final pluviated sample from method 6 and reducing the friction to 0.5°. The simulation was cycled until equilibrium was reached, at which point the top cap was controlled to bring the boundary stress back to 1.02 kPa. This produced a sample with a void ratio of 0.628 compared to a void ratio of 0.630 in the laboratory. The loose sample was created by setting the interparticle friction to a very high value (45°) and allowing the sample to pluviate as in method 6. This method created a sample with a void ratio of 0.709 compared to the laboratory value of 0.738. It should be noted that this is the void ratio of the prepared sample before placing it in the device. Due to vibrations and oscillations during installation, the laboratory samples were reduced to void ratios of approximately 0.70 at the start of the test, which is very similar to the DEM loose sample. Also, much of this additional work on void ratio was conducted after the development of the simple shear code and after

the prototype simulations were developed. The initial prototype samples used the sample generation files for method 6 with the interparticle friction value set to 5.5°.

4.1.3 Top Cap Servo Stress Control

A short introduction to servo stress control was given as a part of the sample preparation discussion. This required only a monotonic control algorithm and was a simpler version of the control needed to simulate the vertical control during simple shearing. The laboratory device used in this study is able to be either servo stress or strain controlled. For all of the testing conducted, the shearing occurred under constant vertical effective stress. Similar to the laboratory element test, the same type of servo control was developed for the DEM simulation. The first step in the control was to setup a user-defined servo stress control loop using the normal stress measured on the top cap boundary wall. Several researchers use the internal measurement sphere values to control the top wall; however, it was shown in the sample preparation section that the internal and boundary measurements are not always equal. Because the data is validated by laboratory data where the boundary stresses are measured, it was important that the same measurement type was used to control the DEM simulations. The algorithm considerers the difference in the measured and target boundary stress and multiplies it by a gain, α, (Eq.4.5).

$$v_{topcap} = -\alpha(\sigma_z^{target} - \sigma_z^{measured}) \tag{4.5}$$

The gain is set sufficiently low to ensure quasi-static conditions and limit oscillations. Based on the equations, if the stress measured is less than the target stress, the virtual cap velocity is negative and the cap moves down to increases the vertical pressure. If the force measured is more than the target force, the velocity is a positive value and the virtual cap raises to reduce the vertical pressure. This value was adjusted

every 10 cycles to ensure proper vertical control.

The cap was in place from the sample preparation phase, but a short period was given at the beginning of the simple shear file to ensure the vertical effective stress was at the correct value before shearing. Once the top cap control was steady, a search for all of the particles touching the top and bottom caps was conducted and the particles were flagged with a 1 or 2 for the top and bottom particles, respectively. The velocies in the x, y, and z-directions were then set equal to the respective velocities of the top cap and the rotations in all three directions were fixed for all of the flagged particles. These conditions essentially replicated the rough boundary physical element tests where the particles were glued to the caps. The top cap servo control is then carried out for the remainder of the simulation by monitoring the sum of the out of balance forces on the group of "glued" particles and the force on the wall. The out of balance forces on the particles must be summed and added to the force measured on the wall because the contact forces with the wall remain the same once the particles are glued. In other words, once those contacts are fixed, they cannot change even though the particles are transmitting additional forces. These additional forces show up in the out of balance forces of the individual particles. It should be noted that the control was switched from monitoring stresses to forces before the particles were glued in order to make the summation of the forces easier. The control of the combined forces is similar to the previous control scheme, if the force measured is greater than the target force, the top wall and "glued" particles are given a positive velocity. If the measured force is smaller, the top wall and glued particles are given a negative velocity moving the group downward, increasing the total force on the assembly. This control algorithm is continued for the shearing phase. The out of balance forces are summed every 10 cycles for the top glued particles and every 100 cycles for the bottom glued particles. Only the top glued particles are required to be updated and

controlled in the vertical direction.

4.1.4 Confining Ring Servo Control

Of the two main styles of simple shear devices available today, the NGI system accepts short cylindrical specimen laterally confined by either a stack of steel rings or a wire-reinforced membrane. Modeling these confining systems can be quite challenging and is often idealized or omitted. In Discrete Element Method (DEM) modeling, however, some type of lateral confinement/boundary wall is required creating the need for accurate modeling of the boundary conditions. Further discussion of these confining systems is given in Chapter 3.

The metal ballotini sample is much more stiff than clay and even sand specimen, therefore, it was necessary to use a stack of rings in order to provide enough lateral confinement. The laboratory sample has a thin latex membrane within the stack of rings. The laboratory data was corrected to account for any additional strength effects from the membrane and it was not necessary to simulate this part of the confining system. It was important, however, for the stack of rings to be replicated in the DEM simulations. The prototype sample consisted of 10 cylindrical rings controlled by a user-defined algorithm which was updated every 10 cycles. The rings were put in place before the samples were brought to the intended vertical effective stress during shearing. Only very slight changes in void ratio occurred from the addition of the rings and the removal of the original cylinder. It should be noted that the laboratory sample used approximately 35 rings each approximately 0.7 mm thick and weighing approximately 9.4 g each. Several DEM simulations were also conducted with 35 rings to assess the influence of the number and size of the rings compared to the particle size. These findings will be discussed below in the results section.

The algorithm for the ring control aimed at keeping the net force on the rings very close to zero. A loop was created to update each ring and track the corresponding velocities and net forces during shearing. First the wall was identified and the value of the net force was obtained using a PFC pre-defined variable. The acceleration was then calculated based on this force and the mass of the ring, which was taken as 10 g. This value is lower than what one ring of the corresponding thickness would weigh; however, it provided a starting point to develop the control algorithm. Also, it is essentially all relative and only affects the speed in which the ring moves to regain a zero net force. Once the acceleration is determined, it integrated to update the velocity. The wall velocity is set to the newly calculated value and the next wall in the loop is identified, repeating the process until all walls are updated. All of these calculations are made for both the X and Y directions. The net force on the rings is tracked throughout shearing to ensure the rings are being properly controlled and the forces are remaining close to zero. Fig. 4.29 shows and example of the top, middle, and bottom ring control histories. Every simulation was checked to make sure the normalized forces were less than 1% when normalized by the top cap force. If the normalized ring force ever went above that value, the simulation was canceled and restarted using a slower shearing rate.

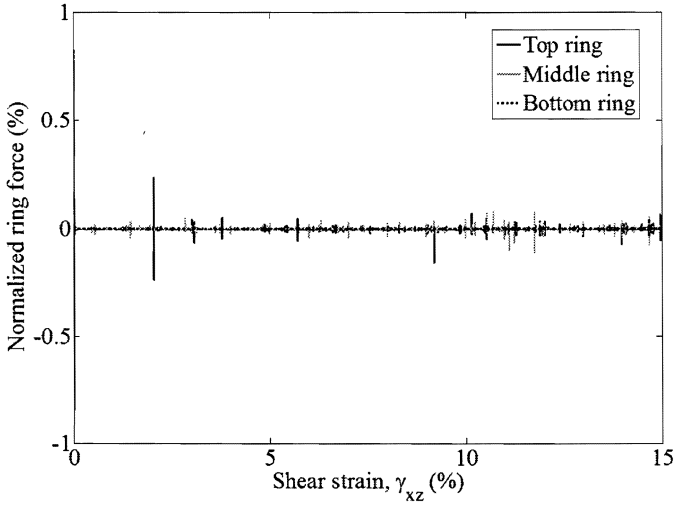

Fig. 4.29. Plot of the net forces on the top, middle, and bottom ring in an exmaple simulation

4.1.5 Shearing Path Control

Along with the vertical top cap and ring control algorithms, the bottom cap must also be controlled in order to subject the sample to simple shear conditions. The monotonic control algorithm consists of setting a constant velocity for the bottom wall and bottom glued particles and cycling to update the position until the desired displacement is reached. During the cycling, the other control algorithms are called and updated as scheduled. The velocity set in DEM simulations is not a physical or real-time value. The bottom cap velocity was determined by trial and error so that the simulation remained quasi-static and the ring control was able to perform as intended. Quasi-static conditions are monitored by comparing the top and bottom caps to ensure no dynamic effects are seen. In other words, the forces on the top and bottom cap should be similar and should increase and decrease together. If a larger value is suddenly observed on the bottom cap and not on the top cap, it is

most likely shearing at a speed too rapid for quasi-static conditions. This condition is described by the following equation (Eq. 4.6), where the difference in the two cap measurements is normalized by the top cap force.

$$Q\% = \frac{F_{bottom} - F_{weight} - F_{top}}{F_{top}} \tag{4.6}$$

where F_{bottom} is the force measured on the bottom cap, F_{weight} is the additional force on the bottom cap due to the self weight of the particles, and F_{top} is the force measured on the top cap. A value of less than 5% is desired for all simulations. If the value goes well above this limit the simulation is not used. Two possible adjustments can be made to correct the control: the alpha-gain for the top cap can be increased and/or the bottom cap can be sheared at a slower rate. If the alpha-gain is increased too much, the vertical control becomes unstable and oscillate. This requires the bottom cap to be slowed down in a trial-and-error approach until the value is less than 5%. Fig. 4.30 shows a plot of the quasi-static check parameter and a plot of the top and bottom cap boundary forces.

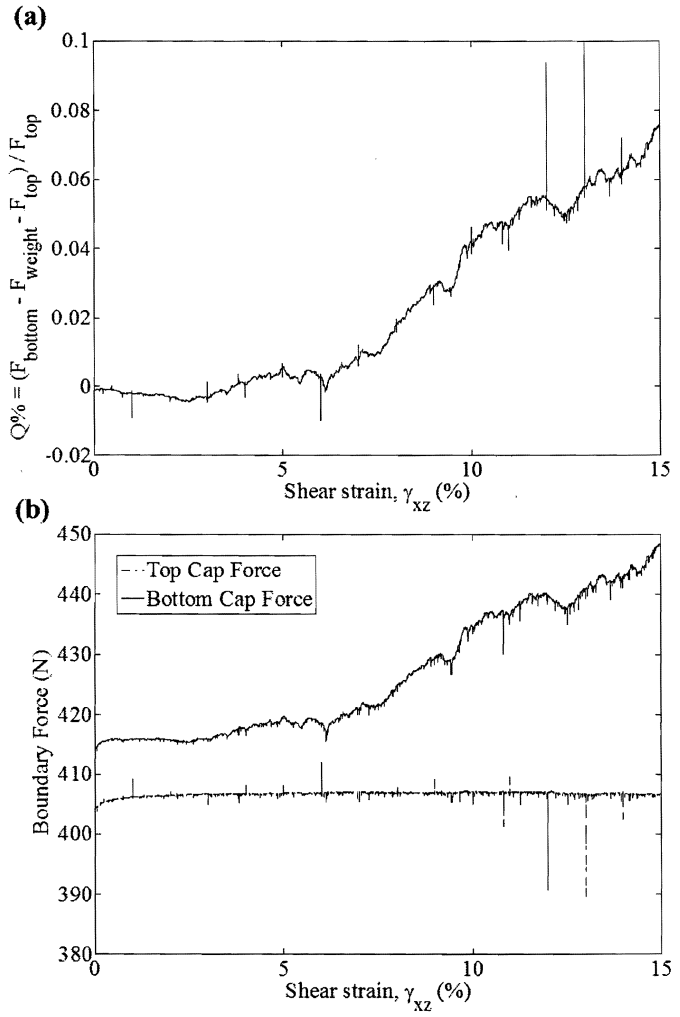

Fig. 4.30. Plot of the (a) quasi-static check and (b) top and bottom boundary forces for a sample not in quasi-static conditions

It is clear from Fig. 4.30a that the bottom cap was sheared too quickly and the normalized difference in the top and bottom caps is well above the 5% cutoff. Fig. 4.31 shows correct control and quasi-static conditions after adjusting the shearing rate. Similar comparisons were made for all simulations.

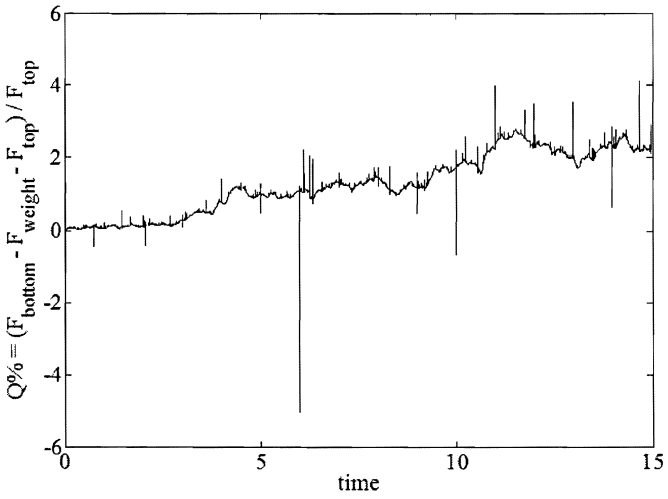

Fig. 4.31. Plot of the quasi-static check for the same sample as in Fig. 4.30 after the adjusting the shear rate and gain values

4.2 Simple Shear Simulation Results and Discussion

Several trials and adjustments of the control gains and shearing rate were needed to determine the proper values for quasi-static conditions for the prototype simulation. The original prototype sample was developed using the following conditions:

- Sample: Sample 1 prepared using method 6 with the interparticle friction angle equal to 5.5°
- Number of Rings: 10 confining rings with alpha equal to 0.1, no wall friction
- Vertical Effective Stress: 50 kPa with alpha equal to -6.0e-05 during shearing
- Shear Rate: 1.0e-04 m/s x-axis (not equivalent to physical time or speed)
- Final Shear Strain: 15%

Table 4.12. DEM prototype simulation testing program

Sample No.	σ'_v **(kPa)**	**Void Ratio** e_0
1	50	0.660
1	100	0.660
1	200	0.659
1	50	0625
1	50	0.690
1	100	0.689
2	50	0.620

Once the initial prototype was developed, a number of other testing conditions were simulated using the same basic code. Table 4.12 presents the initial prototype testing program for the DEM simulations. This program was aimed at providing information for the basic behavior of the simulated granular material. Along with the sample 1 prototype prepared using method 6, a more dense and a more loose sample were generated to assess the effects of varying density. These samples were prepared by varying interparticle friction as discussed previously. The loose sample was created by increasing the interparticle friction to 45° and pluviating the sample similar to method 6. The densest sample was created by using the above prototype files and lowering the interparticle friction to 0.5° and allowing the particles to settle into a denser state. The interparticle friction angle for both samples was returned to 5.5° prior to shearing. Also, one additional prototype simulation of sample 2 was generated. Similar sample preparation procedures and conditions, as listed above, were used to generate this sample. The only significant differences were the number of particles and the initial void ratio, although it is likely that the relative densities of the sample 1 and sample 2 prototypes were similar. All of these simulations were sheared with the same gains listed above, 10 confining rings, and an interparticle

friction of 5.5°; however, the sample 2 simulations were sheared at a velocity of 1 mm/s rather than 0.1 mm/s. These simulations were less sensitive and could be run at a faster rate than the sample 1 simulations. Note that all of the plots below are for boundary measurements. This was used instead of the central measurement sphere because of the fact that these simulations are validated by laboratory data.

4.2.1 Influence of Vertical Effective Stress on Response

The influence of vertical effective stress on shear response was investigated by comparing simulations with the same initial density and different vertical stresses. Fig. 4.32 presents the results for the medium dense prototype samples. Fig. 4.33 presents the results for the loose samples.

In terms of shear stress response, the trends are as expected. The samples tested at the highest vertical stress exhibit the highest peak shear stress. For the 50 and 100 kPa samples, the peak stress ratio is the highest for the simulation tested at the lowest vertical stress, although the difference is less marked than in the laboratory data. The 200 kPa sample, however, exhibits the highest stress ratio response of the three samples. This does not correlate with the laboratory results or previous research findings. The cause of this anomaly is unknown. All of the DEM simulations are dilative responses. One would expect the simulation at the lowest vertical stress to be more dilative and the sample at higher vertical effective stresses to contract more initially. This is not the case for these results. The volumetric responses are very similar for the three samples. The 200 kPa sample is more dilative which is not expected. It is also clear from the DEM results that volume change is still occurring at 15% shear strain and therefore, the samples are not yet at critical state. The expected trends are observed in the shear response, but overall the DEM data does not qualitatively match the observed laboratory response or previous research

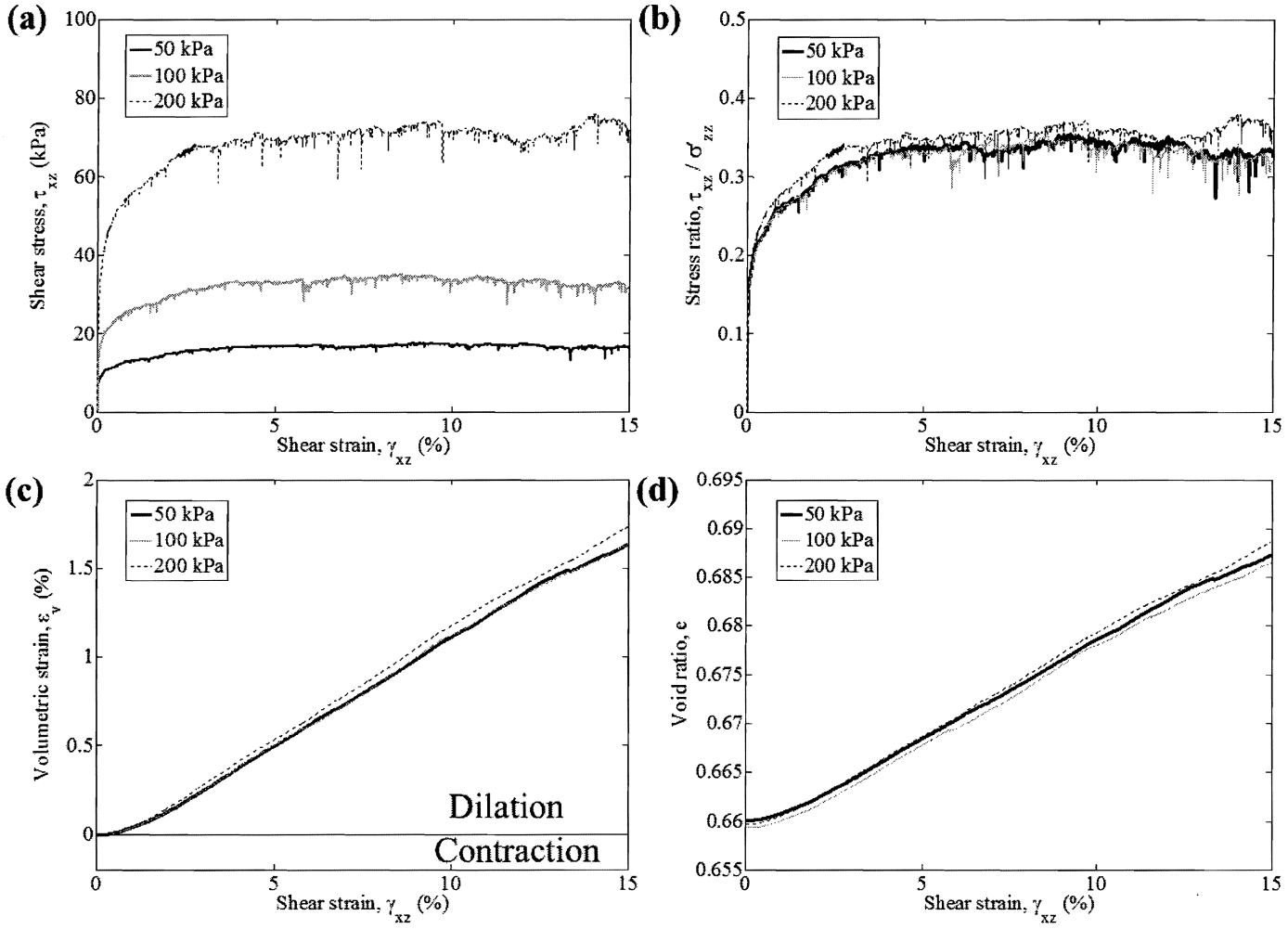

Fig. 4.32. Results for sample 1 dense simulations at different vertical stresses

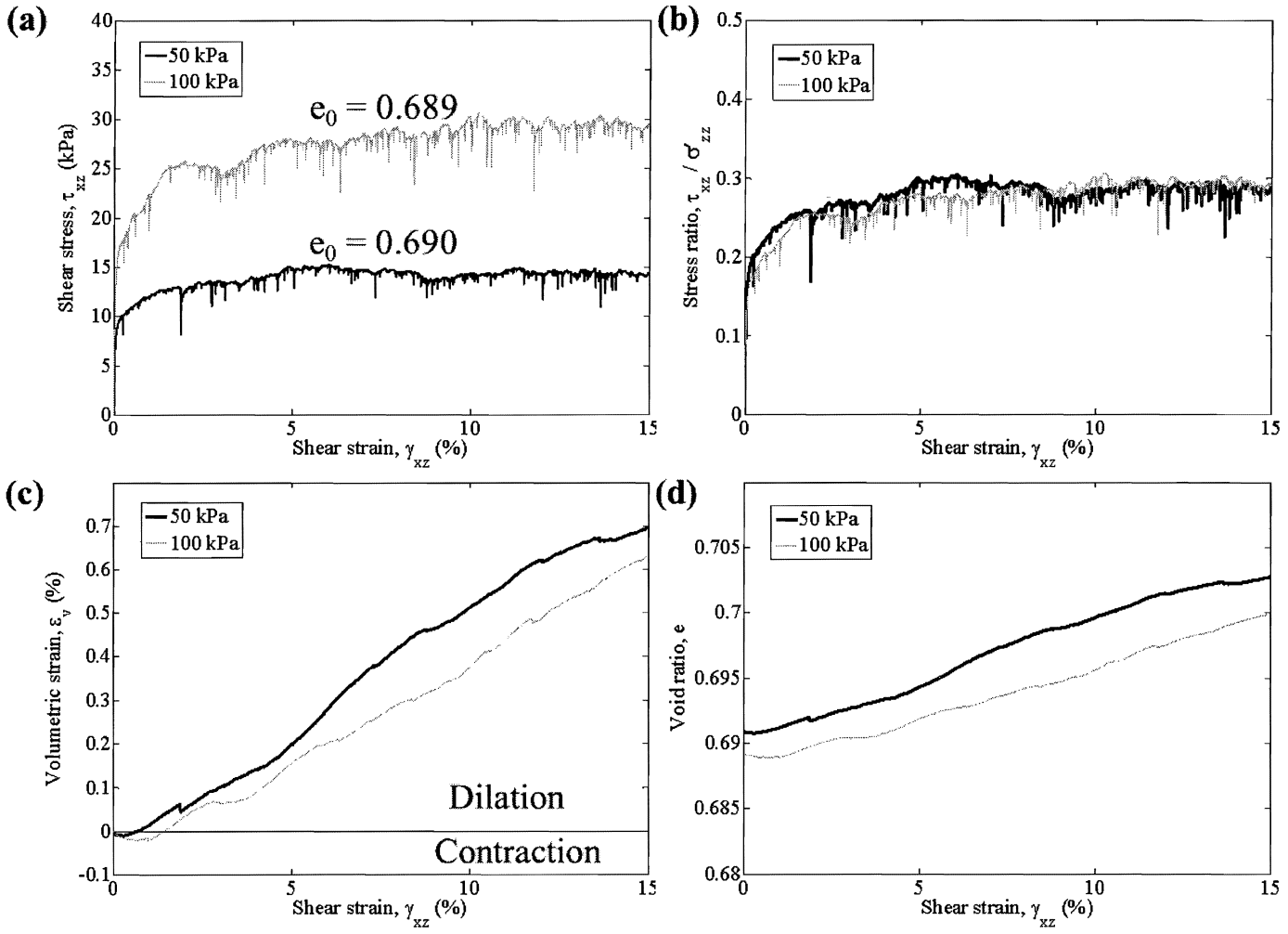

Fig. 4.33. Results for sample 1 loose simulations at different vertical stresses

findings of other authors. Further investigation is needed to determine possible causes for these differences.

4.2.2 Influence of Density on Response

Another factor that affects the behavior of granular materials is density. Figs. 4.34 and 4.35 give the results for samples tested at different densities and vertical effective stresses of 50 and 100 kPa, respectively.

As expected, the samples with the highest initial densities exhibit the highest peak stress ratio. One would expect the samples tested at similar vertical stresses to all approach a similar stress ratio at critical state. This is not evident in Fig. 4.34; however, the samples are also not yet at critical state because volume change is still occurring. The medium and loose sample appear to be slightly approaching one another at 15% shear strain, but it is difficult to draw a definite conclusion from the data. The samples tested at 100 kPa (Fig. 4.35), however, appear to be following this expected trend. Again, these samples are not at critical state, but the loose sample seems to be experiencing very little volume change and could be close to critical state. Overall, the DEM simulations qualitatively agree with the laboratory findings, as well as previous research on granular materials.

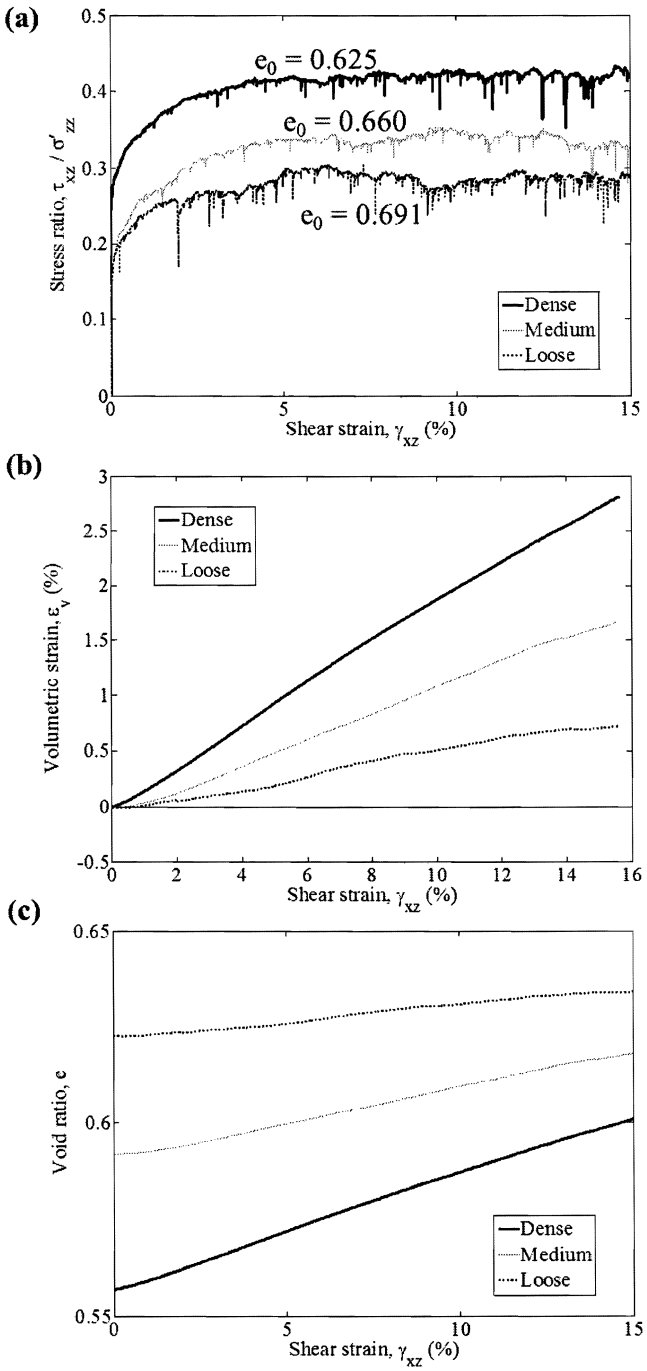

Fig. 4.34. Comparison of response for sample 1 at different densities and a vertical effective stress of 50 kPa

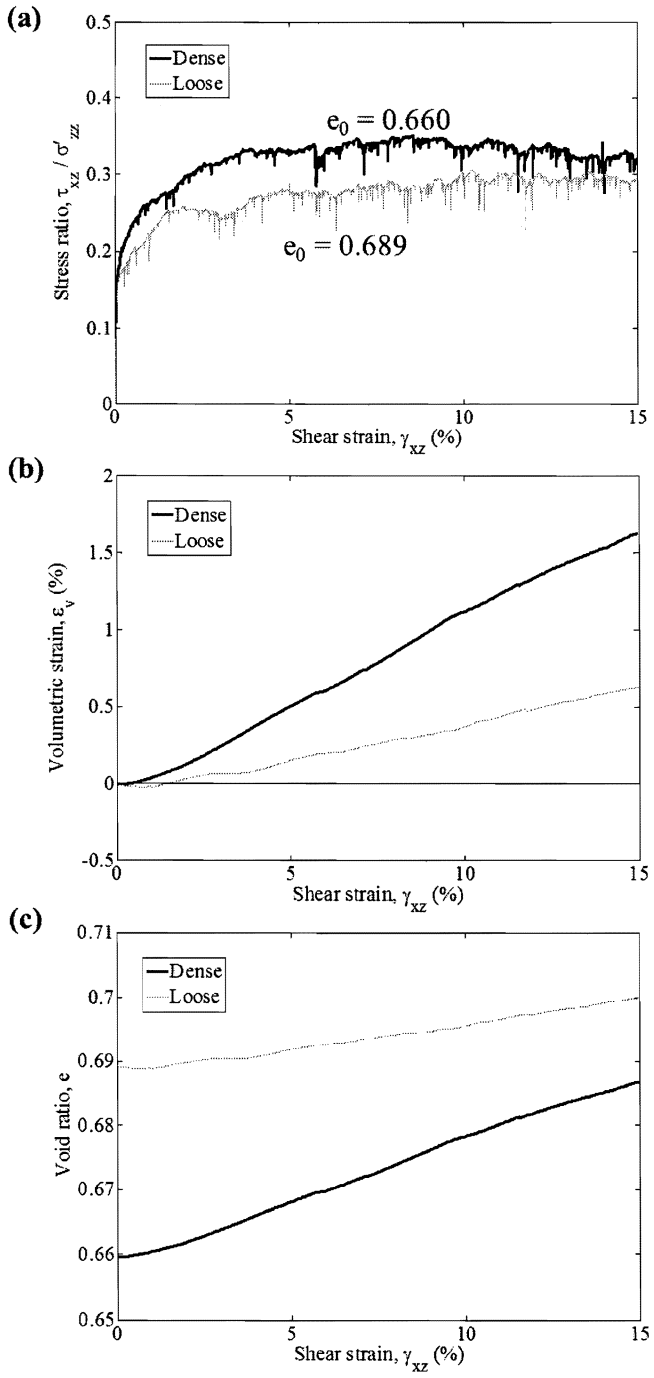

Fig. 4.35. Comparison of response for sample 1 at different densities and a vertical effective stress of 100 kPa

Table 4.13. DEM simulation computational time requirements

Sample Description	**Computational Time (hrs/1%γ_{xz})**
Basic Prototype, Sample 1, 10 rings, ϕ_μ=5.5°, Shear rate=1e-04	30.03
Sample 1, 35 rings, ϕ_μ=5.5°, Shear rate=1e-04	63.23
Sample 2, 10 rings, ϕ_μ=5.5°, Shear rate=1e-03	90.81
Sample 2, 35 rings, ϕ_μ=5.5°, Shear rate=1e-03	176.53
Sample 1, 10 rings, ϕ_μ=7.5°, Shear rate=1e-04	47.13
Sample 1, 10 rings, ϕ_μ=5.5°, Shear rate=5e-06	872.80
Basic Prototype, Sample 1 with ring wall friction angle set to 19.8°	52.90

4.3 Prototype Sensitivity Studies

Several sensitivity studies were also carried out to assess the influence of various parameters and testing conditions on the response. The prototype sample was developed as a simplified version of the actual physical specimen. For example, only 10 confining rings were used initially rather than the 35 rings used in the laboratory. Also, the friction on these rings was initially set to zero. These simplifications improved the runtime efficiency and provided a basic specimen to use during the development and debugging of the simple shear code. Running the simulations under the exact physical conditions was very time consuming. Table 4.13 lists the computational time required for several of the various test conditions. Because not all of the simulations were carried out the full 15%, the time is given per 1% shear strain. It was proposed that slight differences in the virtual sample, which greatly lowered the time required for the simulations, would not affect the response greatly. The findings are presented in the following sections.

4.3.1 Influence of Ring Size on Response

The laboratory sample uses a set of approximately 35 rings, each 0.7 mm high, to provide the required lateral confinement. Simulating this number of rings resulted

in extremely large computational times. The initial prototypes were developed using only 10 rings to reduce the simulation time during the debugging and initial analysis phases. It was also proposed that if the shear response was not greatly affected, the remainder of the simulations would also be conducted using only 10 rings. Fig. 4.36 shows a comparison of the shear results for the same sample 1 simulation conducted with 10 and 35 rings.

It appears that the number of rings has very little influence on the stress ratio and the volumetric response of the samples. The only difference observed is a slightly higher stress ratio and a slightly more dilative response for the 10 ring sample. These are not significant enough to justify the tremendous difference in computational time required. Therefore, all remaining simulations were conducted with only 10 confining rings.

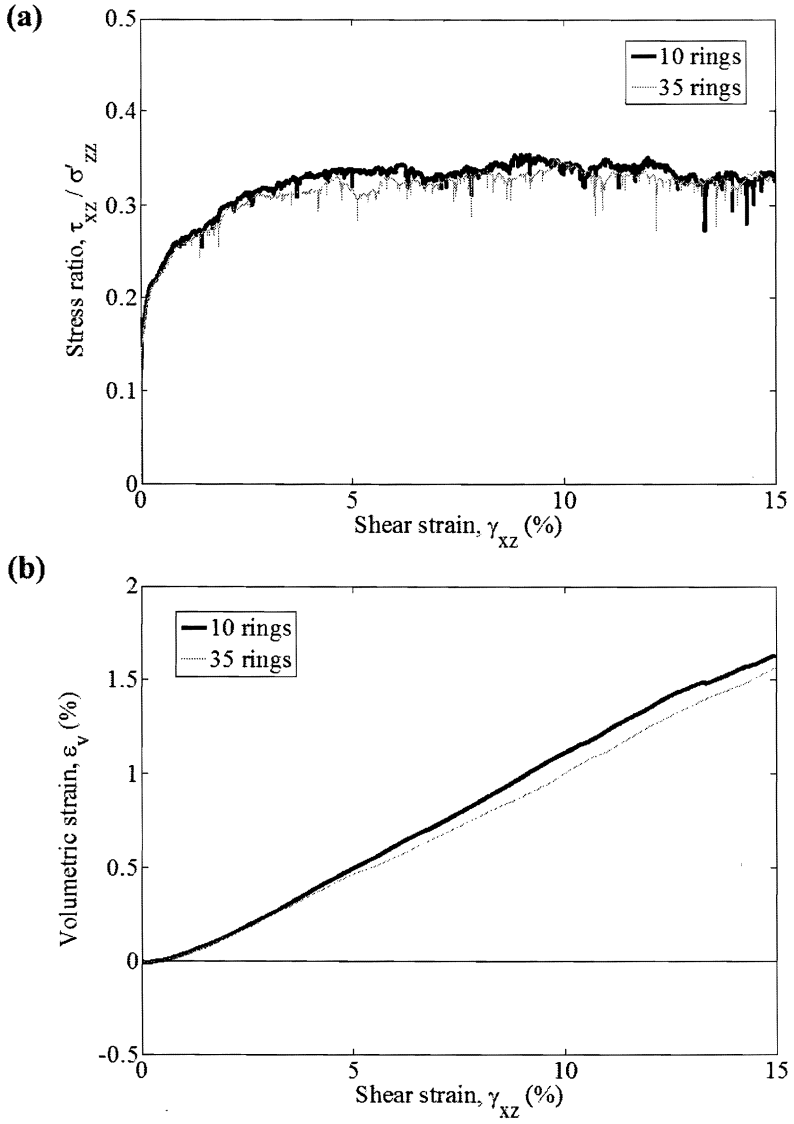

Fig. 4.36. Results for the sample 1 prototype with 10 and 35 rings

4.3.2 Influence of Number of Particles on Response

Shen (2013), as well as many other researchers have shown that the number of particles can affect the response observed in DEM simulations. This generally

occurs for assemblies with a number of particles below some threshold number which separates the responses. Above the threshold, no significant differences are noticed, but below the threshold, the shear response is not representative of the response obtained for the larger number of particles sample. The specific number of particles where this difference occurs is not known. For the 2D simulations presented in Shen (2013), significant differences were reported for the 5,000 and 20,000 particle samples. It was important for a similar comparison to be made in this study. Fig. 4.37 shows the results for the sample 1 and sample 2 prototype simulations, prepared and tested under similar conditions as listed above.

It is clear from the plot of normal stress that the sample 1 simulation is more sensitive to disturbances and force chain collapses. These oscillations are also visible in the stress ratio plot. The overall stress ratio at 15% is very similar for the two samples, although some differences are noticed in the lower stress ranges. The sample 2 simulation continuously gains strength, while sample 1 appears to level off at a low shear strain of about 5%. Sample 1 also exhibits a very slight strain-softening behavior at high shear strains. For the simulations presented by Shen, it was the larger number of particles (sample 2 in this case) that exhibited the strain-softening behavior.

The volumetric response is slightly different for the two samples. Sample 1 tends to exhibit a more dilative response. With only the DEM samples, it is difficult to determine relative density. The samples were prepared using the same pluviation techniques and it is likely that they have similar densities. The interparticle friction values determined in the laboratory, however, were different for the large and small particle sizes and so this theory is not guaranteed. A measure of relative density based on the laboratory data is made in the validation section and this issue is further discussed in the next chapter.

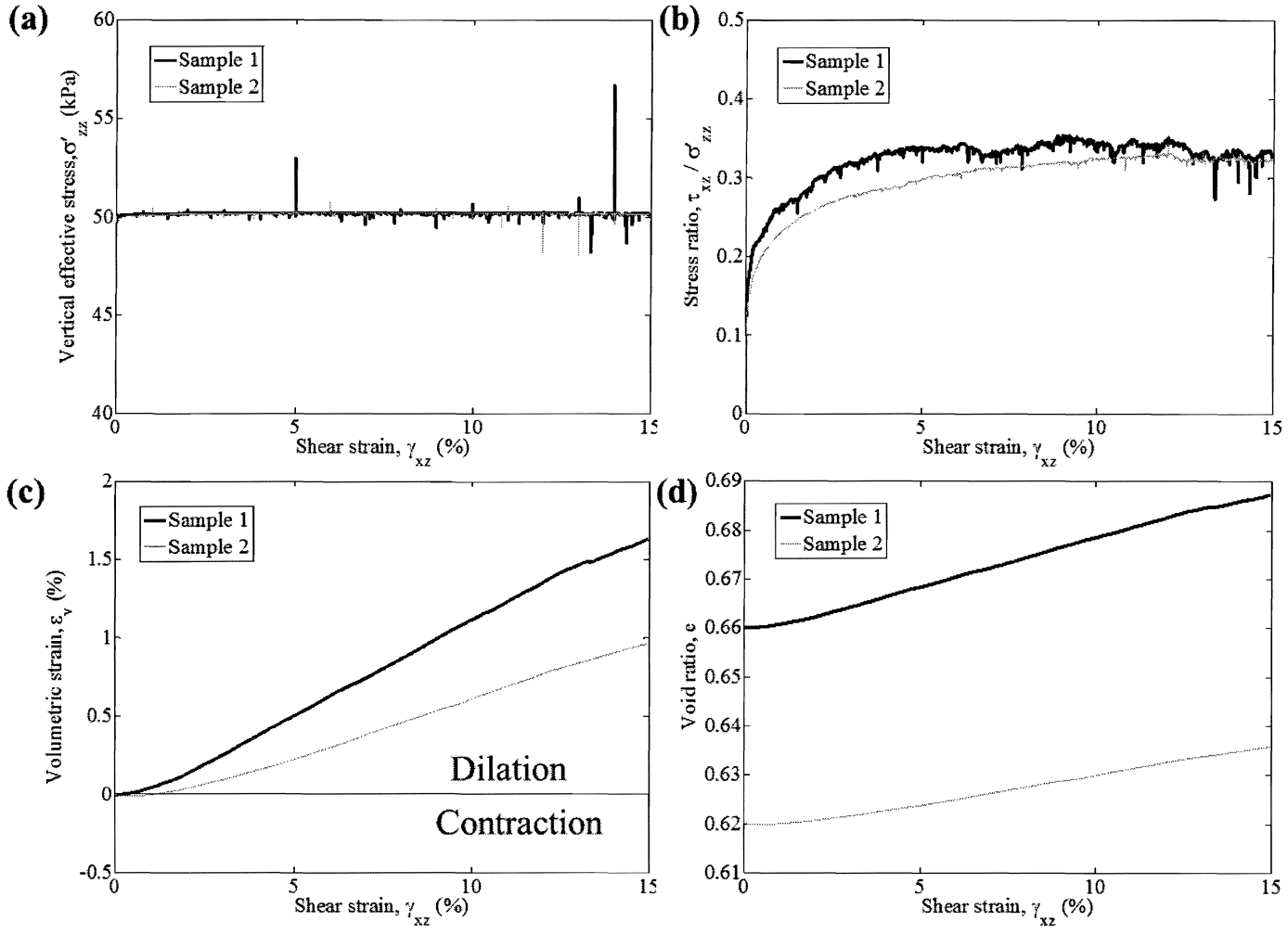

Fig. 4.37. Results for sample 1 and sample 2 Prototypes

4.3.3 Influence of Interparticle Friction on Response

Previous DEM studies have shown that interparticle friction influences the observed shear response. Although the physical particles were tested in the laboratory, there was still some variation in the values obtained. In order to better understand how sensitive the simple shear simulations were to this scatter, the densest sample ($e_0 = 0.628$) was tested with three different interparticle friction values. The densest sample was used in each case so that no density effects were present. The interparticle friction angles were set to 1.9, 5.5, and 7.7° just before shearing. The 5.5° value represents the original prototype and the 1.9 and 7.5° values represent the smallest and largest possible $\phi_\mu \pm \sigma$ value, respectively. Fig. 4.38 shows a comparison of the results.

The figure clearly shows that interparticle friction angle influences the peak stress ratio obtained. The sample with the highest friction angle exhibits the highest peak stress ratio. It also affects the volumetric response. The sample with the highest friction angle exhibits the most dilative response, while the sample with the lowest interparticle friction angle exhibits the least dilative response. This plot is compared with the laboratory data in the next chapter to compare the physical response with the possible envelope shown in the DEM study.

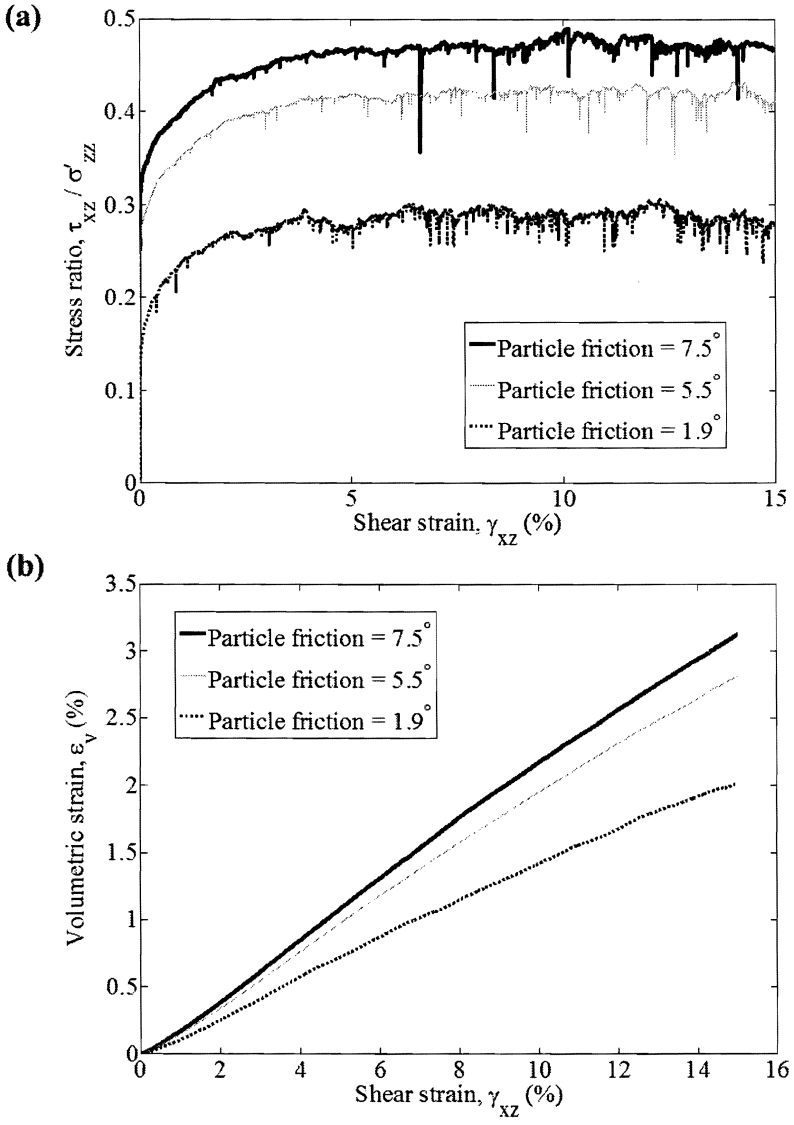

Fig. 4.38. Results for sample 2 prototype with 10 and 35 rings

4.4 Additional Studies

4.4.1 Influence of Ring Wall Friction on Response

In PFC, when two particles contact one another or when a particle contacts a wall, the lowest friction coefficient is used in the calculations. The ring walls in the simulations presented above had zero friction; however, the laboratory sample has a latex membrane interface between the rings and particles with a approximate friction angle of 19.8°. It was proposed that using zero wall friction in the DEM simulations might not accurately replicate the physical specimen. Two additional simulations were conducted using the 10 and 35 ring sample 1 prototypes. The wall friction angle was set to 19.8° and the "maxfric on" command was used. Specifying this command tells PFC to take the maximum friction coefficient value for ball-wall contacts. Fig. 4.39 shows the results for the 10 and 35 ring simulations with and without friction.

It is clear from the figures that the presence of friction on the ring walls influences both the shear and volumetric responses. For both the 10 and 35 ring samples, frictional walls result in higher stress ratios overall and more dilative responses. As discussed previously, the number of rings has little affect on the overall response. One exception is in the volumetric response above 5% shear strain where the 35 ring sample exhibits a less dilative response than the 10 ring sample. While only a short sensitivity study was conducted in this research, it is recommended that all future simulations are conducted with wall friction present.

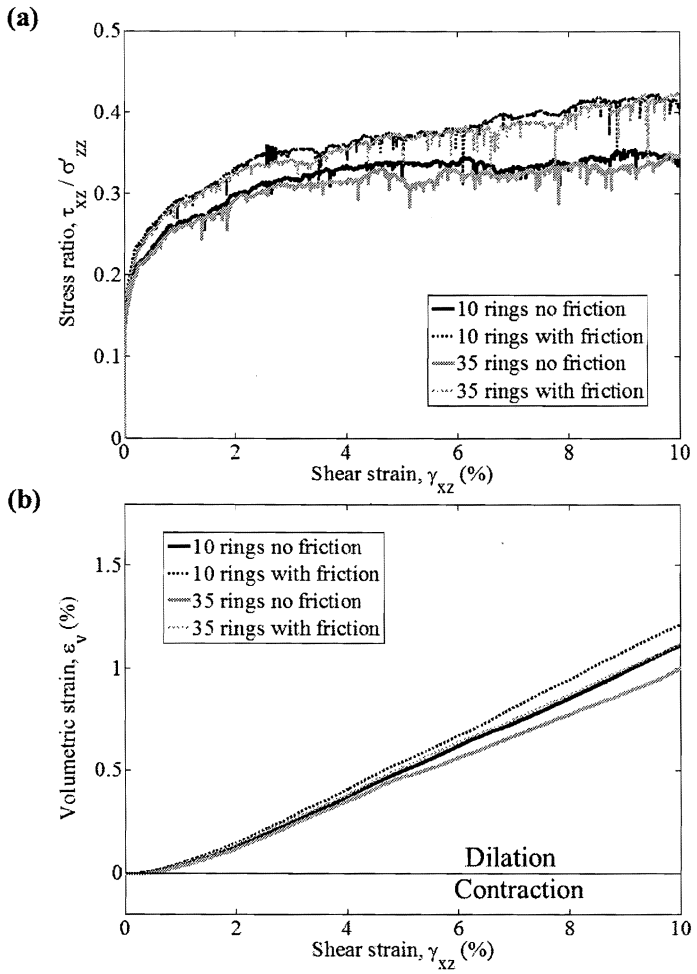

Fig. 4.39. Results for sample 1 prototypes for 10 and 35 rings with and without wall friction

4.4.2 Influence of DEM Sample Preparation Method on Response

As discussed previously, a study was conducted to assess the influence of DEM sample preparation methods on initial fabric. Samples were prepared using the three most common DEM sample preparation procedures. The void ratios obtained, as well as the micro-scale information was similar for all three methods. A followup

study was conducted to assess the influence of these procedures on the subsequent shearing response. Three preparation methods were conducted: pluviation, radius expansion, and rigid wall compression. Fig. 4.40 shows a comparison of the three monotonic simulations.

The initial response up to about 2% shear strain is similar for all three samples. Above 2%, the radius expansion sample increases to a higher peak stress ratio, while the other two samples exhibit stress ratios very close to one another. This could possibly due to the fact that the radius expansion sample begins with a slightly higher void ratio. Also, the peak stress ratio is at a higher percent shear strain (10%) for the radius expansion sample than it is for the other two (7%). The radius expansion sample also exhibits a greater strain-softening behavior. The pluviation sample does not appear to exhibit any strain-softening behavior, and the radius expansion sample appears to exhibit only slight, if any, strain-softening behavior.

In terms of volumetric response, all three samples exhibit very similar dilative behavior until approximately 11% shear strain, at which point the radius expansion sample begins to decrease the rate of volume change. The plot of void ratio response shows the radius expansion sample approaching the pluviation void ratio and becoming equal to it at approximately 14%. It is clear that these samples are not at critical state, but it is likely that the radius expansion sample will reach a condition of zero volume change at a lower strain percentage than the other two sample types. As mentioned in the sample preparation discussion, the slight differences in initial fabric, and the need to accurately replicate the experimental data warranted the use of the pluviation method in this study. This decision is reassured by the observed difference in shear response for the radius expansion and pluviation methods.

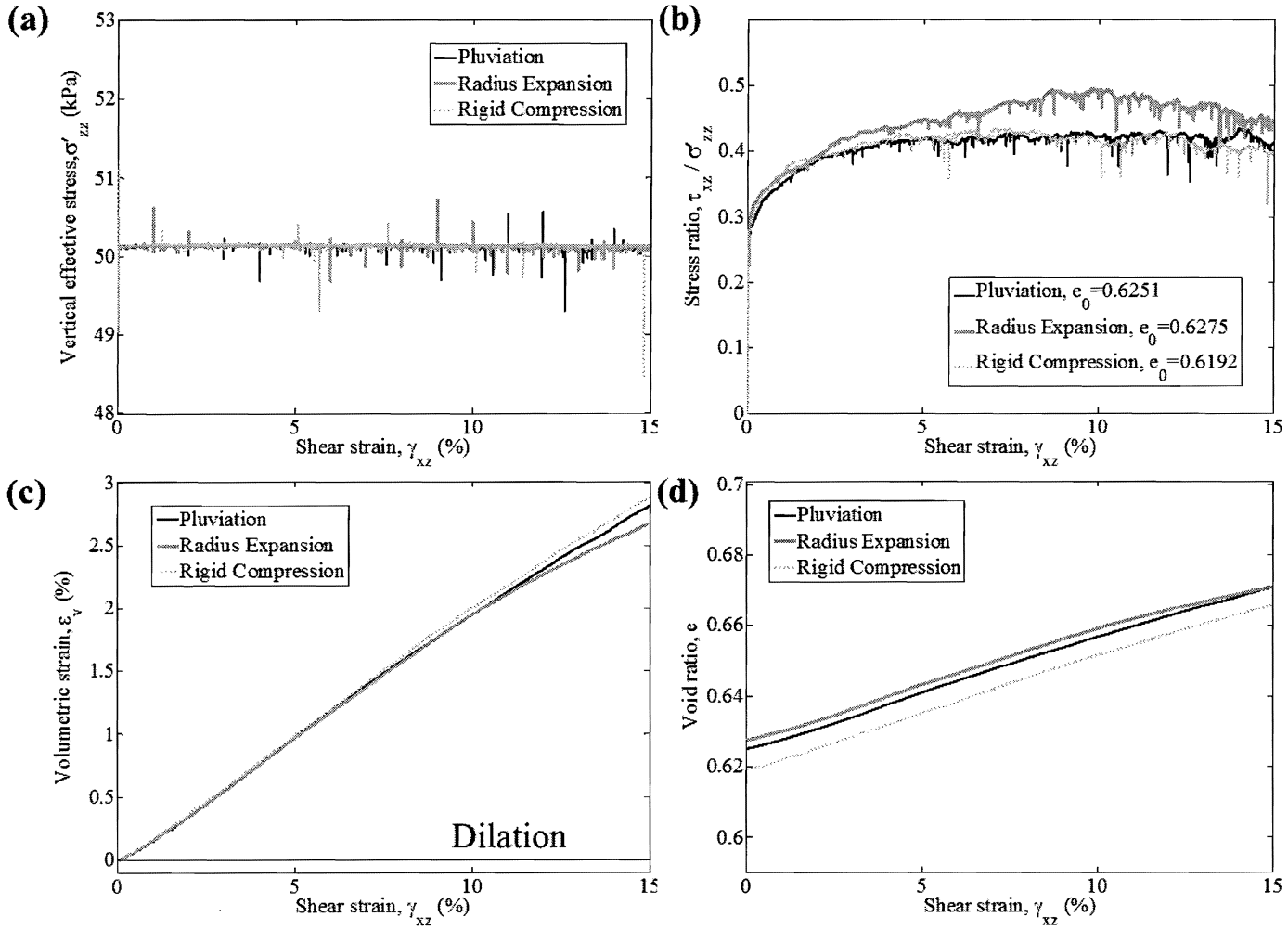

Fig. 4.40. Results for samples prepared with three different DEM sample preparation methods

4.5 Conclusions

The DEM simulations have shown to qualitatively match the experimental findings in this study, as well as the expected trends based on previous research. These DEM results are directly compared with the experimental results and validated in the next chapter. Also, the microscopic information for the validated simulations is examined in Chapter 6.

5. VALIDATION AND DISCUSSION OF RESULTS

5.1 Validation of DEM Simulations

As shown previously for the experimental and numerical results, density, and vertical stress affect the response of granular materials. Therefore, it was important for the simulations to be validated by experimental results for similar testing conditions. Table 5.1 lists a description of the discrete element method (DEM) simulations presented throughout this chapter and the corresponding experimental tests used in their validation. The DEM simulations and validation comparisons throughout this chapter will use the label designations corresponding to the similar laboratory tests. This labeling was not used in Chapter 4 because of the number of simulations and sensitivity studies conducted at different void ratios and test conditions. Only those corresponding to a specific experimental test are validated. A comparison of the experimental and DEM void ratios are given in Table 5.2. The experimental values are given as a range of void ratios for those conditions in which more than one test was conducted. The values are given for the void ratios after sample preparation, and at 50 and 100 kPa vertical effective stress.

Table 5.1. Description of DEM simulations and corresponding experimental tests used in validation

DEM Simulation	Experimental Validation Test
Sample 1 Prototype (Medium), $\phi_\mu = 5.5°$, $\sigma'_v = 50kPa$	MM-50-1
Sample 2 Prototype (Medium), $\phi_\mu = 5.5°$, $\sigma'_v = 50kPa$	MM-50-2
Sample 1 Dense, $\phi_\mu = 1.9, 5.5, and 7.5°$, $\sigma'_v = 50kPa$	MD-50-1
Sample 1 Loose, $\phi_\mu = 5.5, and 6.5°$, $\sigma'_v = 50kPa$	ML-50-1
Sample 1 Loose, $\phi_\mu = 5.5, and 6.5°$, $\sigma'_v = 100kPa$	ML-100-1

Table 5.2. Summary of void ratios for the dense, medium dense, and loose samples tested in the laboratory and replicated in DEM

Sample Density	**Laboratory** e_0	**Laboratory** e_{50kPa}	**Laboratory** e_{100kPa}	**DEM** e_0	**DEM** e_{50kPa}	**DEM** e_{100kPa}
MM-1	0.69	0.66	-	0.667	0.660	-
MM-2	0.65	0.62	-	0.623	0.620	-
MD-1	0.62-0.64	0.61-0.63	-	0.628	0.625	-
ML-1	0.73-0.74	0.67-0.68	0.66-0.68	0.709	0.690	0.689

The original prototype simulation had an initial void ratio equivalent to that of the medium dense laboratory tests. Both were prepared using the Method 6 type preparation techniques. Obtaining the medium dense samples in the lab was more difficult than preparing the dense and loose samples. Several tests were conducted at various intermediate void ratios. The experimental test with the closest void ratio is compared in Fig. 5.1 to the prototype simulation for validation.

The response is different for the two samples. The DEM prototype sample is extremely stiff initially and then levels off after reaching about 5% shear strain. The peak stress ratio of the DEM sample is approximately 0.35 at 9% shear strain, while the peak stress ratio of the laboratory sample is 0.42 at approximately 13% shear strain. This sample continues to gain strength until this point and then exhibits strain-softening behavior. The volumetric responses are also very different (Fig. 5.1b). The PFC sample dilates while the laboratory sample contracts initially. The laboratory sample begins to dilate at approximately 7% shear strain. This also corresponds to the location where the stress ratio begins to rapidly increase. This differing volumetric response also results in a different void ratio response. The DEM sample increases in void ratio due to the dilation while the experimental sample densifies and then only slightly increases in void ratio back to the original value. As stated previously, the samples were difficult to prepare and it was not guaranteed

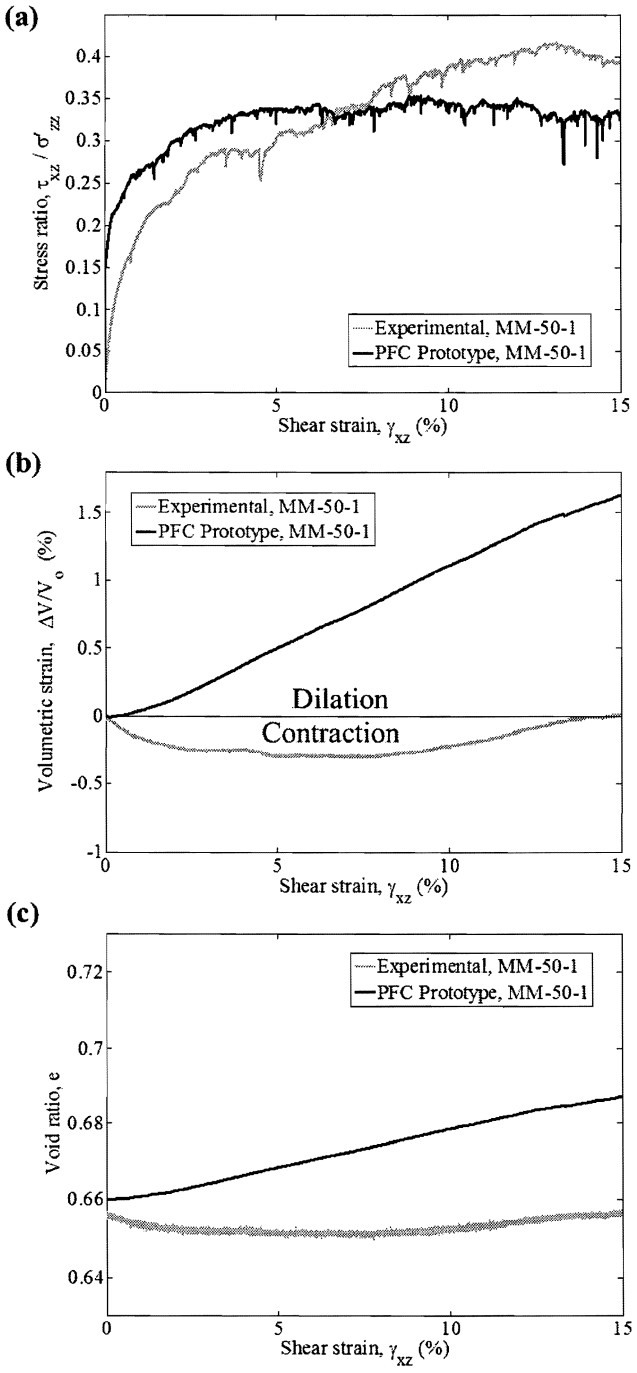

Fig. 5.1. Results for MM-50-1 experimental and PFC simulation results

that a uniform and homogeneous sample was generated in the laboratory. The differences in response could be due to localized differences in the samples even when the overall void ratios were similar. There are several differences in the responses that raise questions to the validation of the numerical results and the degree of accuracy required to reasonably consider the simulations valid.

A similar comparison was made for the sample 2 experimental and numerical results to determine if the two responses were within a reasonable range for validation (Fig. 5.2). The PFC results agree very well with the experimental response. The stress ratio curves are very similar. The laboratory sample is initially less stiff than the PFC sample, but it ultimately reaches higher stress ratio values. Although the samples start out with almost the same void ratio, the volumetric responses are slightly different. The PFC sample dilates for the entire test, while the laboratory sample initially contracts. The laboratory sample also begins to approach a state of zero volume change at the end of the test. Overall, the DEM results are reasonably close enough to consider them to be validated by the experimental data.

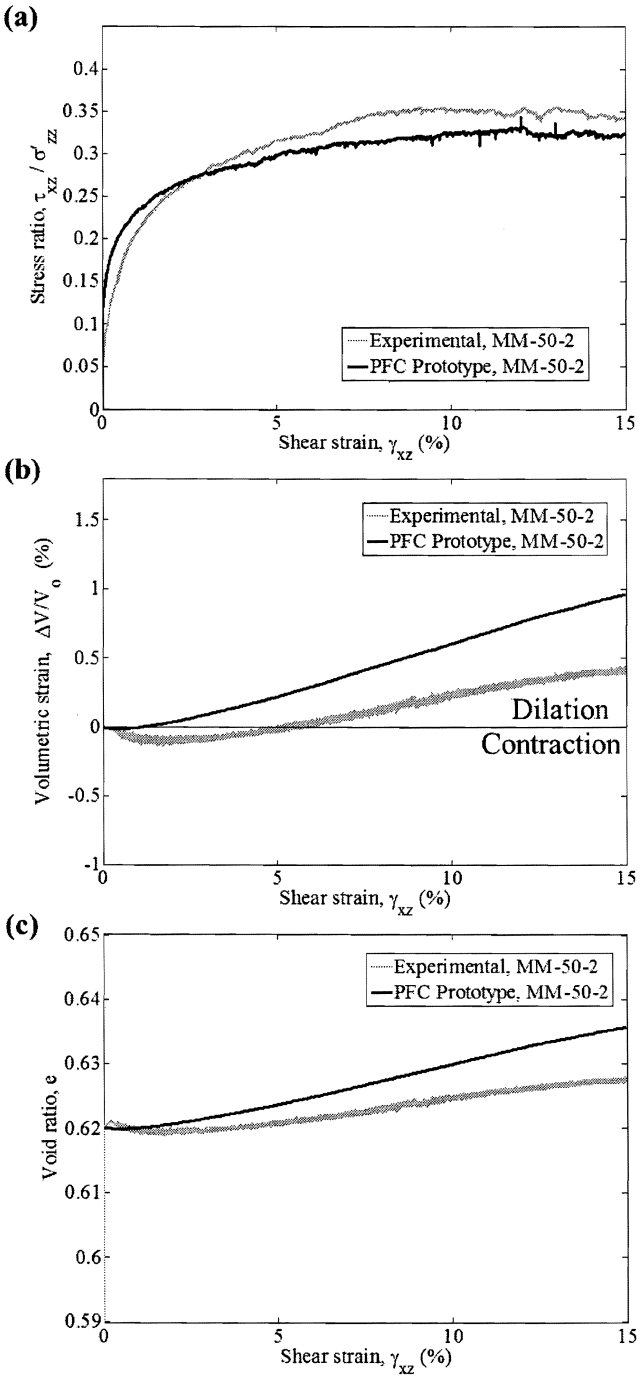

Fig. 5.2. Results for MM-50-2 experimental and PFC simulation results

For both of these initial prototype comparisons, the experimental data exhibits a higher overall peak stress ratio than the DEM simulation data. Two possible factors could explain this: experimental scatter, and differences in interparticle friction. As shown in Chapter 3, even when samples are prepared within a reasonably small range of void ratios, some experimental scatter is observed. Also, as presented in Chapter 4, the value of interparticle friction plays an important role on the peak stress ratio obtained. Based on the three simulations, it appears that higher interparticle friction values result in higher peak stress ratios. To examine the influence of these factors it was important to use samples that were repeatable in the laboratory. The dense samples (MD-50-1) were the easiest to prepare consistently and within a small range of void ratios. These tests also had very similar void ratios to the dense DEM simulation samples prepared. A total of eight tests were conduced to assess the expected experimental scatter, five of which are used in this initial comparison. These experimental results are compared directly with simulation results using various values of interparticle friction (Fig. 5.3). The prototype sample used an interparticle friction angle of 5.5°, but the values measured by Cavarretta showed a possible spread from 1.9 to 7.5°, representing $\phi_\mu \pm \sigma$. It should also be noted that the values determined in the laboratory were for virgin or un-sheared particles. It is likely that the surface roughness, and therefore, interparticle friction angles would increase after repeated shearing. A second set of plots is also shown with only three of the experimental results and the highest two interparticle friction values for clarity. The three experimental curves represent the tests with the best vertical control.

It is clear from the plots that the initial stiffness of the laboratory samples is much less than that of the PFC samples, irrespective of interparticle friction. It is also clear that the actual interparticle friction value is most likely higher than the 5.5° used in the prototype samples. A value of 7.5° appears to be a decent aver-

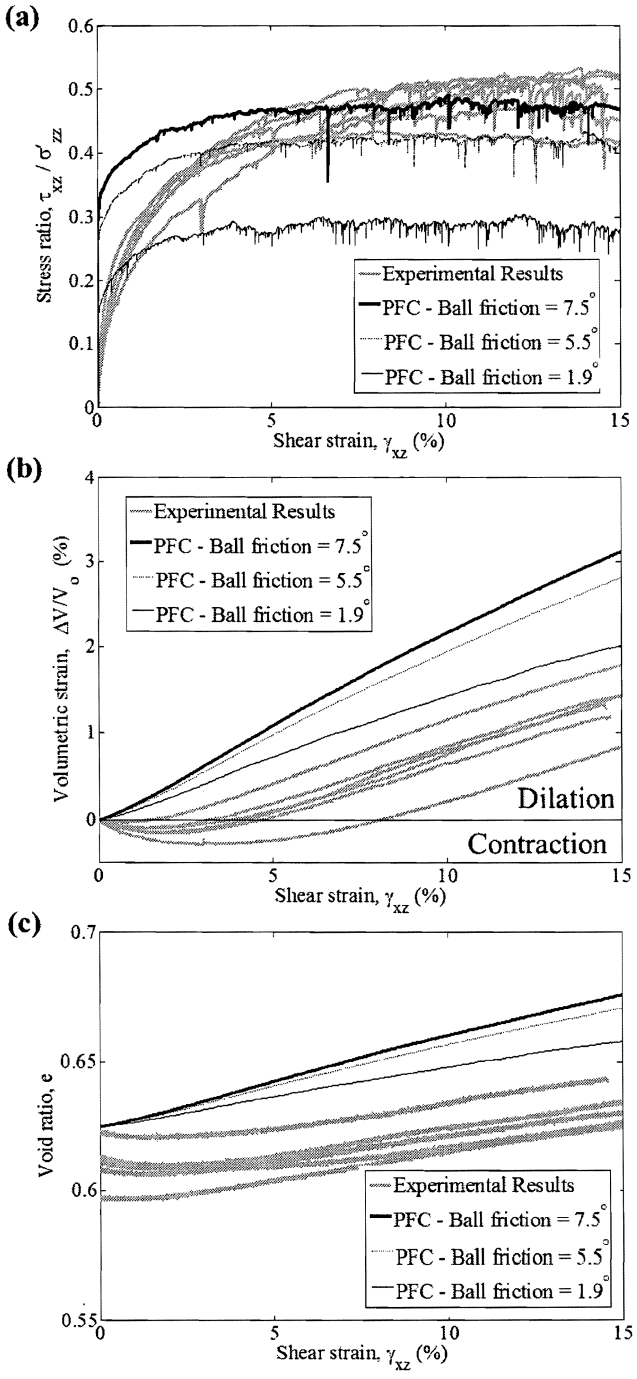

Fig. 5.3. Comparison of MD-50-1 experimental and PFC simulation results

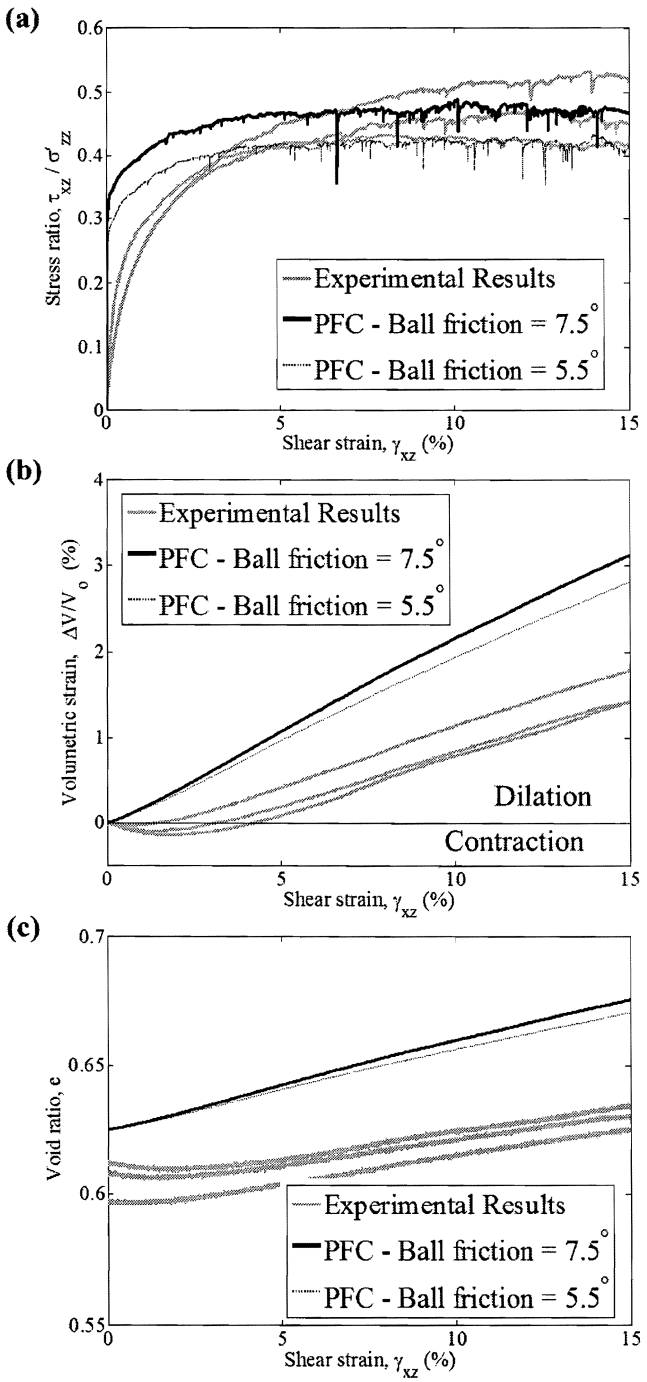

Fig. 5.4. Comparison of the three MD-50-1 experimental results with the best control and the PFC simulation results

age value for future use in subsequent simulations. In terms of volumetric response, the experimental samples exhibit initial contractive behavior while the PFC samples only exhibit dilative responses. If only the dilative portions of the curves are considered, the dilation rates are somewhat similar, although the actual values of volumetric strain observed are quite different. It is interesting in the fact that the experimental results begin with lower void ratios signifying samples that are more dense than the PFC samples, yet they exhibit a more contractive response. The laboratory samples were prepared at very high relative densities (96-99%) and it is likely that the contracting behavior may be caused by the settling of the top cap rather than contraction of the actual sample. Also, only slight differences in height measurements made a significant difference in the void ratio calculated. It is possible that measurement errors could lead to a lower estimation of the experimental void ratio than what is actually prepared. This would, however, contradict the fact that the experimental results exhibit higher stress ratio values as expected for denser samples.

A similar comparison was made for the loose samples at 50 and 100 kPa. Two experimental tests were conducted for each vertical stress. Figs. 5.5 and 5.6 show the experimental results along with the DEM results for interparticle friction angles of 5.5 and 6.5°.

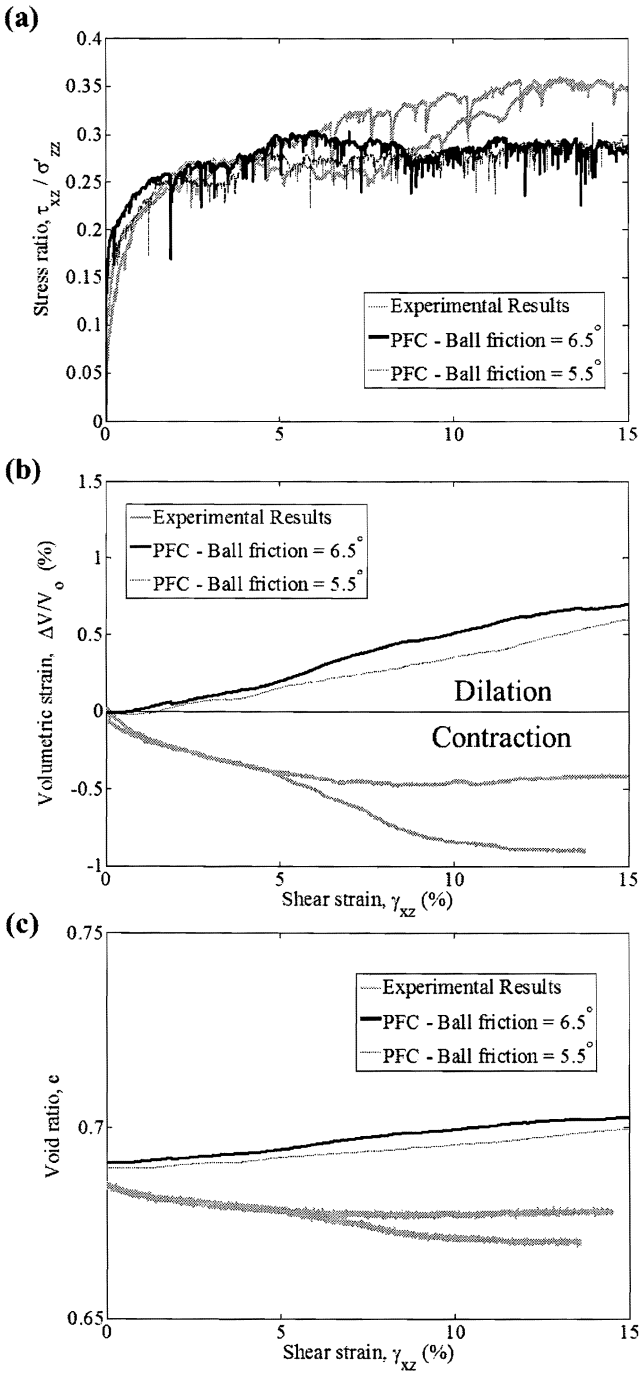

Fig. 5.5. Results for ML-50-1 experimental and PFC simulation results

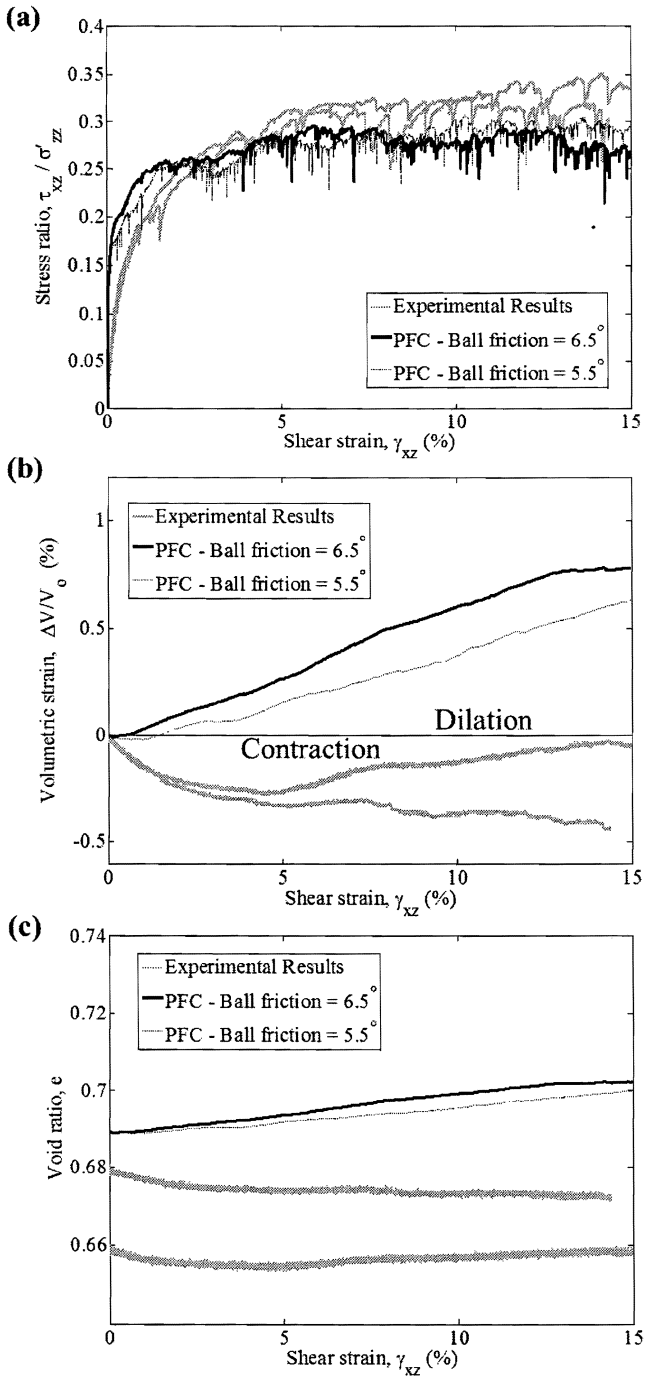

Fig. 5.6. Results for ML-100-1 experimental and PFC simulation results

At 50 kPa, both sets of data show very similar responses up to a peak stress ratio of 0.3 at approximately 6% shear strain, at which point the experimental results continue to gain strength while the DEM simulations level off. The initial stiffness of these tests is much closer than what was observed for the dense samples. At 100 kPa, the stress ratio responses are somewhat similar for the entire test duration, with the PFC samples exhibiting slightly higher stress ratios at larger shear strain percentages. In terms of volumetric response, however, the results are very different for the laboratory and DEM samples at both vertical effective stress conditions. The PFC samples exhibit mostly dilative responses while the laboratory samples exhibit mostly contractive behavior. The experimental samples have lower initial void ratios meaning the samples are initially more dense. In turn, one would expect the response to be more dilative than the PFC samples which is not seen in either case. Additionally, it appears from the volumetric response that interparticle friction angle has more of an influence on volumetric strain at higher vertical effective stresses.

From each of the validation comparisons presented, it appears that the experimental and numerical results agree reasonably well in terms of stress ratio response; however, they do not agree in terms of volumetric response. Also, it is clear that some differences in initial stiffness are present for the two data types. Several factors could cause this difference in stiffness both in the experimental testing and the modeling programs. Several sensitivity studies were conducted to assess the influence of these possible factors and are presented in the following section.

5.2 Validation Sensitivity Studies

Although the experimental and DEM results agree reasonably well, there are several factors that could influence the initial stiffness of the two sample types. Possible factors include: slippage or boundary effects due to the top cap placement,

machine compliance, and any differences due to the DEM prototype simplifications, such as shearing rate, and contact model. It is most likely a combination of these factors causing the differences.

5.2.1 Influence of Boundary Slippage on Response

To investigate possible slippage at the top cap boundary, a MD-50-1 test was conducted using flat porous stones in place of the fixed particle boundary caps used in the experimental testing program. A comparison of the flat and fixed particle boundary test results are given in Fig. 5.7.

Both curves begin with a very similar response in terms of stress ratio and volumetric strain. The samples contract at a similar rate until a point when the two curves separate and the fixed particle boundary test begins to dilate. After the initial contraction, the fixed particle boundary sample remains at the same volume for the remainder of the test. Because the flat boundary sample shows a similar initial contraction, it is not likely that the differences in initial stiffness are due to slipping or rearranging of the top boundary particles.

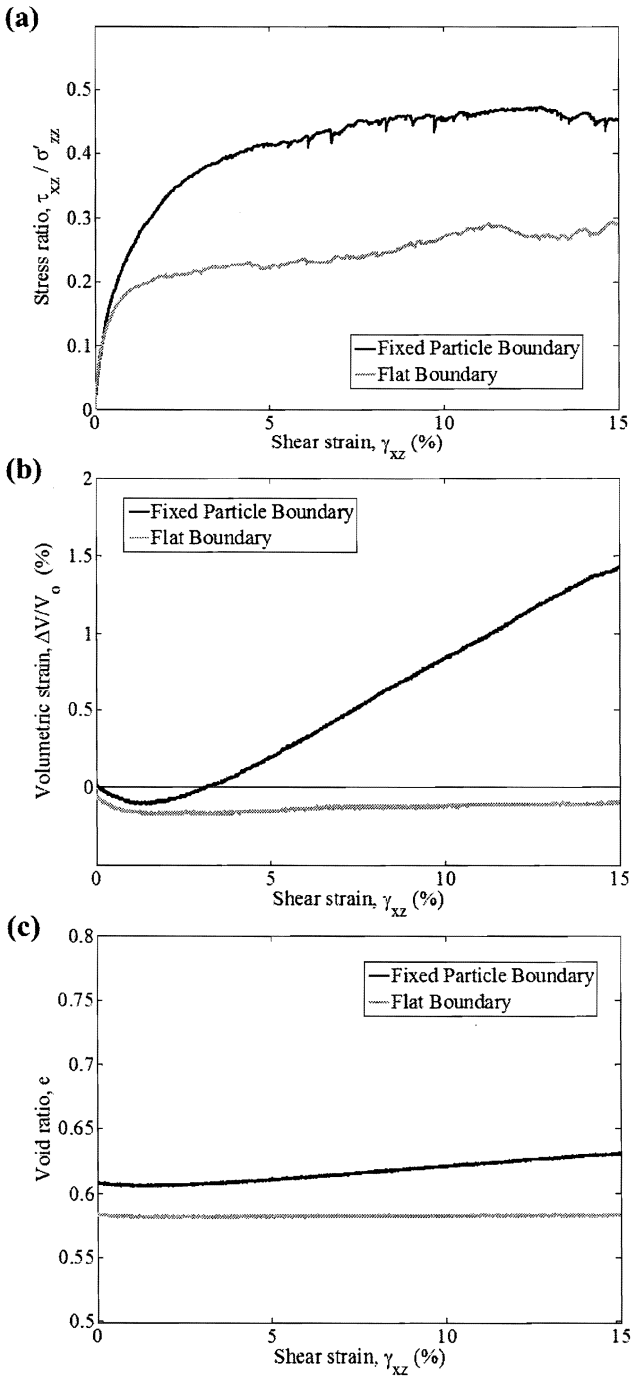

Fig. 5.7. Experimental results for MD-50-1 with flat and fixed particle boundaries

5.2.2 *Influence of Machine Compliance on Response*

Because the initial stiffness of the fixed and flat particles matched, it was proposed that compliance in the device could possibly cause the appearance of a less stiff response. An external linear strain conversion transducer (LSCT) was fixed to a stable frame and positioned so that it measured the bottom cap movement. A MD-50-1 test was conducted while recording the external and internal (feedback) displacement histories. Fig. 5.8 shows the shear stress response plotted using the internal and external displacement readings.

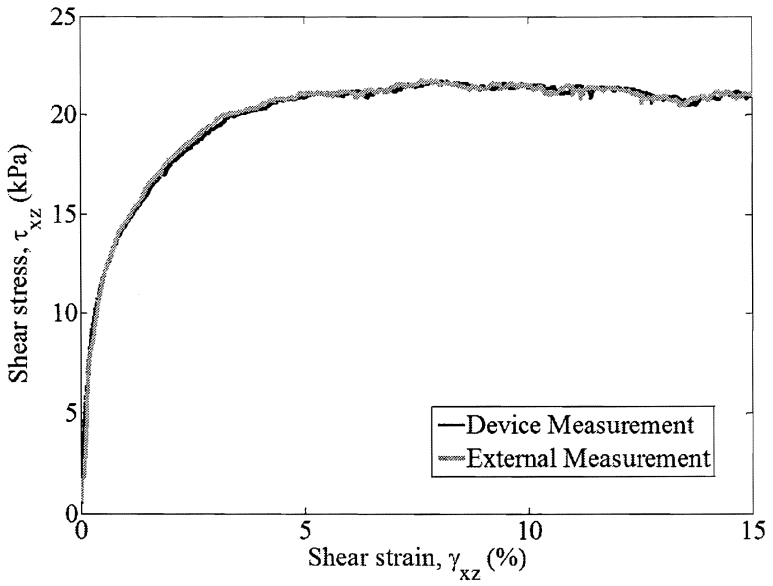

Fig. 5.8. Experimental results for MD-50-1 compliance check

It is very clear that no machine compliance is observed at this vertical effective stress. The lines plot virtually on top of one another. Overall, it appears that no significant changes in stiffness are observed for any of the possible experimental

factors investigated.

5.2.3 Influence of Shearing Rate on Response

In the laboratory, researchers have shown that shearing rate does not affect the response of dry granular material. Because the DEM simulations are not run in realtime, it was questioned whether the rate would have any influence on the response. Two simulations were sheared at different rates, both of which were quasi-static (Fig. 5.9). The slower simulation was only carried out to 1% due to the extremely large computational time demands for this shearing rate (872.8 hours of computational time per 1% shear strain versus 30 hours for the faster shearing rate).

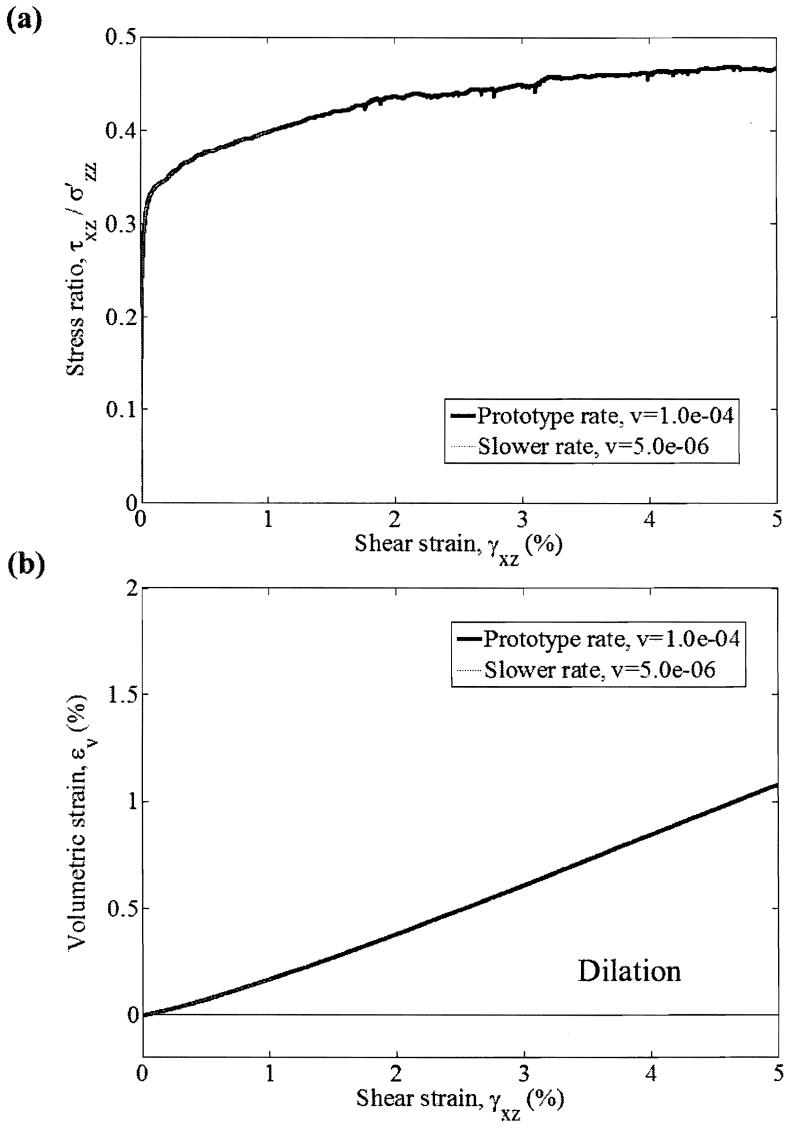

Fig. 5.9. Results for sample 1 prototypes sheared at different rates

It is somewhat difficult to see the difference in the two plots because the slower simulation essentially plots exactly on top of the faster prototype simulations. Therefore, no rate effects and no differences in initial stiffness are seen in the DEM simulations and the simulations can be carried out at the faster rate as long as they remain

in quasi-static conditions.

5.2.4 Influence of Contact Model on Response

One of the major simplifications in DEM modeling is the contact model used. Very simple contact models are used to capture the response of particles which, in reality, have very complex contact interface behaviors. For example, the simplified Hertz-Mindlin model used in this study assumes a perfectly smooth contact occurs in only one exact location. In reality, at the micro-scale, surfaces are rough and contacts occur in several locations, initially deforming asperities while building the frictional interaction. It was proposed that a different contact model, or a lower input stiffness would create a less stiff initial response. The Hertz-Mindlin model requires shear modulus, density, and Poisson's ratio to be input. A range of values was given for the 51200 alloy and the initial prototype simulations used mid-range values. An additional simulation was conducted using the lowest values to assess the effects of lowering the input stiffness within the given range. No differences were noticed.

A second study used a linear contact model with equivalent values of normal and shear stiffness calculated from the average overlaps and corresponding shear modulus and Poisson's ratios used in the Hertz simulations ($k_n = 11600kN/m$ and $k_s = 9560kN/m$). The relationship for equivalent stiffness was given in the PFC manual. An additional simulation was also conducted using a linear contact model with input stiffness values of one order of magnitude lower ($k_n = 1160kN/m$ and $k_s = 956kN/m$). Note that all of these simulations began with the same sample preparation file and therefore, all began at the same void ratio. Fig. 5.10 presents the results for the simulations conducted with different contact models.

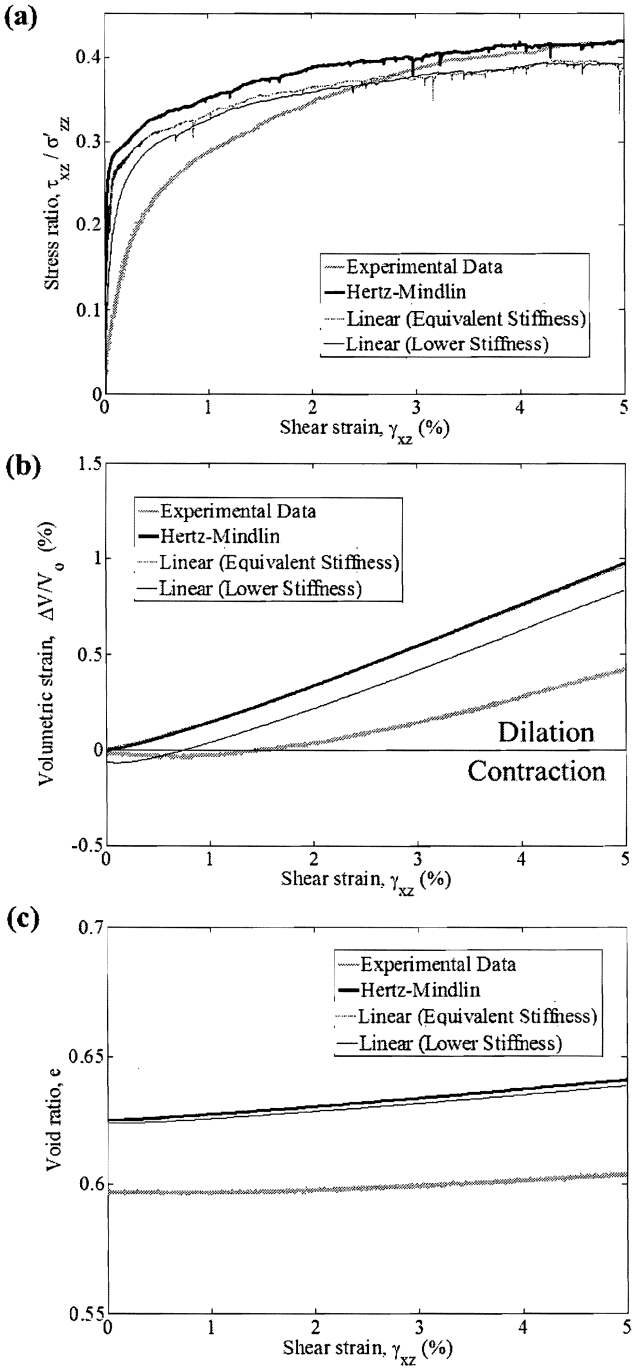

Fig. 5.10. Comparison of experimental data and sample 1 prototype using different contact models

Although the input values of stiffness were calculated to be equivalent for the Hertz and linear models, a slight difference in the overall stress ratio is noticed. The Hertz-Mindlin model exhibits higher initial stiffness as well as higher overall stress ratio values compared to the linear contact model. The volumetric responses for the two are exactly the same however. It is also clear from the plot that changing the stiffness parameters by an order of magnitude only slightly affects the resulting stress ratio, but it does have a marked affect on the initial stiffness when using the linear contact model. It also has a significant affect on the volumetric response. While the response is different using the linear contact model, it still does not solve the problem in initial stiffness differences even when a much lower stiffness is used.

5.3 Conclusions

The above comparisons show that the experimental results can be successfully used to validate the DEM simulation results. Differences in the initial stiffness were observed for the experimental and numerical results. A number of possible factors were assessed and none appear to have a major influence on the observed response at low shear strains. The overall shear response and behavioral trends, however, are accurately captured in the DEM simulations. The microscopic information obtained in the DEM simulations is analyzed in the following chapter.

6. DEM SIMULATION ANALYSIS

The major benefit of the DEM simulations is the ability to obtain micro- or particle-scale information about the assembly. The overall or macro-scale information about the sample is available, as well as the micro-scale information about each particle. Localized information is calculated using smaller volume measurement spheres throughout the sample. The following information is presented below as a means to examine the microscopic response of the validated DEM simulations:

- Sample void ratio and localized measurements of void ratio
- Sample and localized measurements of coordination number
- Boundary and internal stress measurements
- Boundary stress distribution
- Stress path
- Angle of shearing resistance
- Major principal stress orientation
- Angle of non-coaxiality
- Particle displacement with height profile
- Particle displacement and velocity vectors
- Contact force network
- Fabric tensor and orientation of major principal fabric

- Statistical analysis of fabric

Such information cannot be obtained in even the most sophisticated laboratory tests. The DEM simulations allow for examination of the microscopic differences seen in the samples under the various loading paths tested. These differences lead to a greater understanding of the overall response of the particulate assembly, as well as the improved ability to interpret the three dimensional laboratory results. Improved interpretation will be useful for existing and future similar laboratory testing on sands.

The five validated tests are compared below in terms of the micro-scale response. As before, the simulations are grouped in order to examine the effects of density, vertical stress, and number of particles on response. The entire suite of microscopic tools are presented for the first analysis; however, only pertinent data and figures are presented for the additional analyses.

6.1 Influence of Density on Microscopic Response

As shown in the experimental and macro-scale DEM results, density influences the shear response of granular materials. During validation, only the macro-scale information, such as overall void ratio and stress measurements were compared. It is important to also understand how the internal measurements relate to the measured boundary values. Figs. 6.1 through 6.4 show a comparison of boundary and sample core measurements for the dense, medium dense, and loose samples. The sample core values were determined from a central measurement sphere. PFC allows for various quantities to be measured and recorded throughout the sample. A short discussion of measurement spheres and the possible information obtained is given in Chapter 4.

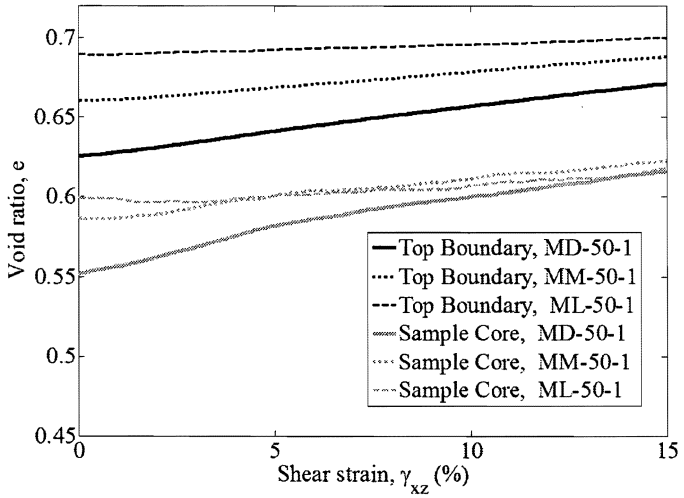

Fig. 6.1. Comparison of void ratios measured from the top boundary location and the sample core for MD-50-1, MM-50-1, and ML-50-1

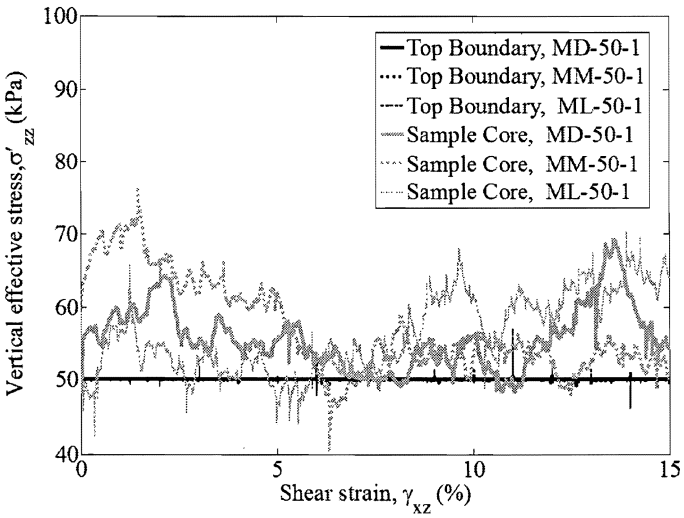

Fig. 6.2. Comparison of vertical stress measured on the top boundary and the sample core for MD-50-1, MM-50-1, and ML-50-1

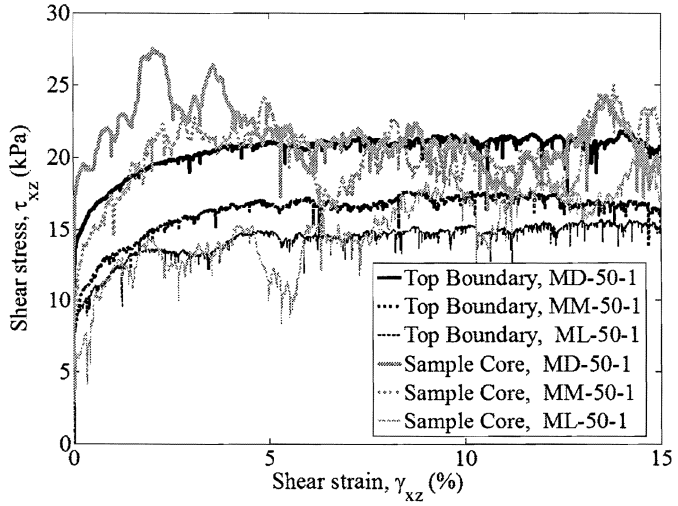

Fig. 6.3. Comparison of shear stress measured on the top boundary and the sample core for MD-50-1, MM-50-1, and ML-50-1

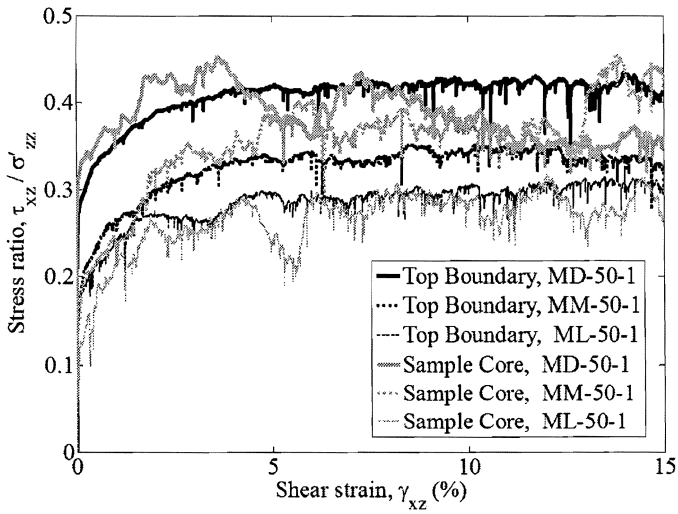

Fig. 6.4. Comparison of stress ratio measured on the top boundary and the sample core for MD-50-1, MM-50-1, and ML-50-1

For all three samples, the void ratio measured within the sample core is significantly less than the boundary value. The MM-50-1 sample appears to have the highest separation in boundary and sample core values and the dense sample appears to have the least. As mentioned in the sample preparation section, this measured difference is due to the fact that the void ratio is higher where the spheres are bounded by a flat surface.

Differences in boundary and sample core stress measurements are also observed. In accordance with previous research findings, both the normal and shear stresses are higher in the sample core than what is measured on the boundary. The vertical stress measured in the sample core of the medium dense sample is significantly higher initially and then approaches near the boundary value as shearing progresses. The loose sample, however, begins at somewhat similar values and then the internal vertical stress in the sample core begins to increases after approximately 7% shear strain. A similar trend is observed in the shear stress response. The ML-50-1 sample, overall, is the most similar in terms of boundary and internal stress measurements, while the medium and dense samples have significantly different measurements initially. When the shear stress is normalized by the vertical stress and the stress ratio is considered, the measurement locations have much less influence of the obtained value. The boundary and sample core stress ratio results are similar for all three sample densities. One slight exception is observed in the dense sample after approximately 8% shear strain. The internal core stress ratio appears to soften as shearing progresses.

Another way to analyze the internal and localized response of granular materials using DEM simulation data is to compare the average quantities from several different measurement spheres throughout the sample. The same five measurement volumes (Fig. 4.5) used in the DEM model development portion of this research

are used to obtain the localized micro-scale information. Figs. 6.5, 6.6, and 6.7 present localized values of void ratio for samples MD-50-1, MM-50-1, and ML-50-1, respectively.

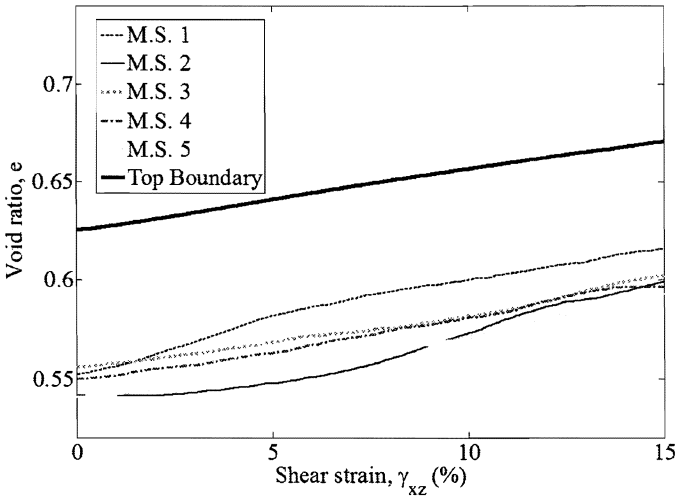

Fig. 6.5. Comparison of void ratio measured from the top boundary location and for various measurement sphere locations throughout sample for MD-50-1

As shown previously, the overall measurement of void ratio is much higher than the internal void ratios for the five volumes. It is also clear to see that there is scatter in the void ratios among the different sample locations. For the dense and medium dense samples, M.S. 2 (the measurement sphere located in the "advancing front" of the sample) exhibits the largest amount of dilation. This is not as notable in the loose sample.

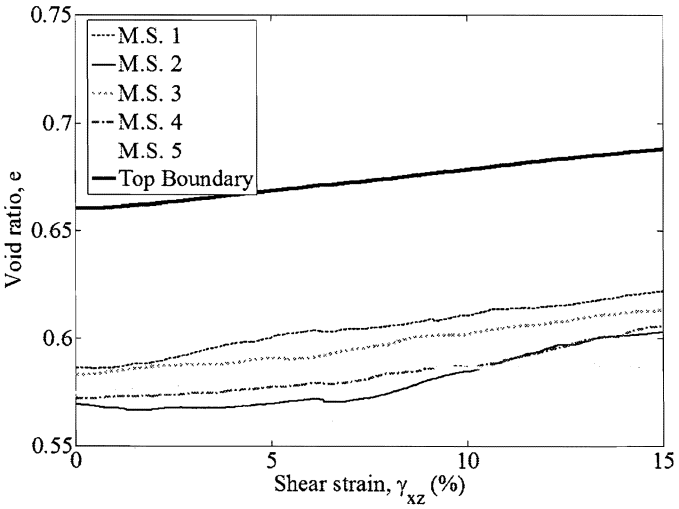

Fig. 6.6. Comparison of void ratio measured from the top boundary location and for various measurement sphere locations throughout sample for MM-50-1

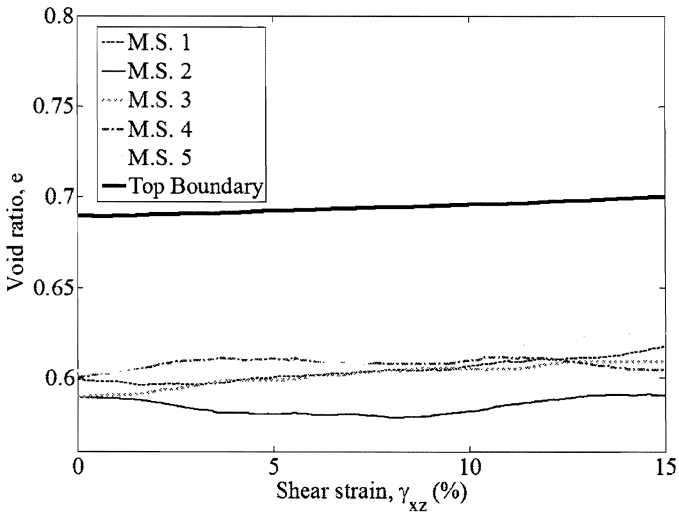

Fig. 6.7. Comparison of void ratio measured from the top boundary location and for various measurement sphere locations throughout sample for ML-50-1

A similar comparison can be made in terms of stress ratio. Fig. 6.8, Fig. 6.9, and Fig. 6.10 compare the measured boundary stress ratios with the localized measurements from the three measurement spheres along the x-axis. Three rather than five locations were plotted for clarity.

The dense sample exhibits the least spread. The M.S. 2 and M.S. 3 values are slightly lower than the measured boundary stress ratio. MM-50-1 exhibits similar measurements up to 5% shear strain, at which point M.S. 1 and M.S. 2 begin to highly separate from the boundary value. The loose sample exhibits similar behavior for the different locations, with the exception of M.S. 3, which largely deviates from the other quantities.

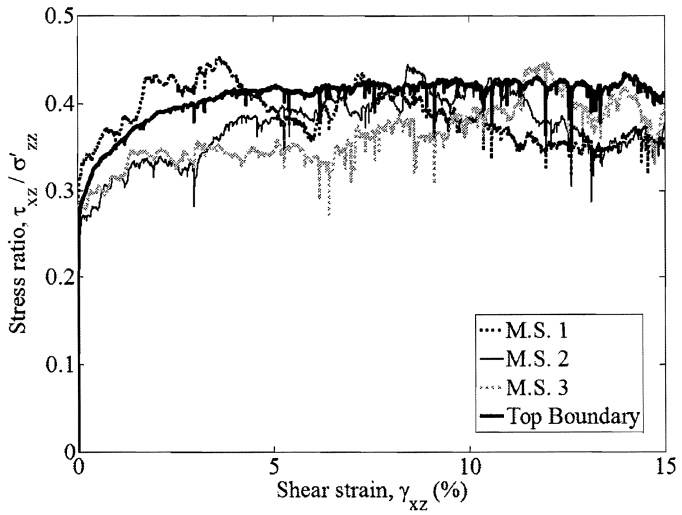

Fig. 6.8. Comparison of stress ratio measured on the top boundary and for various measurement sphere locations throughout sample for MD-50-1

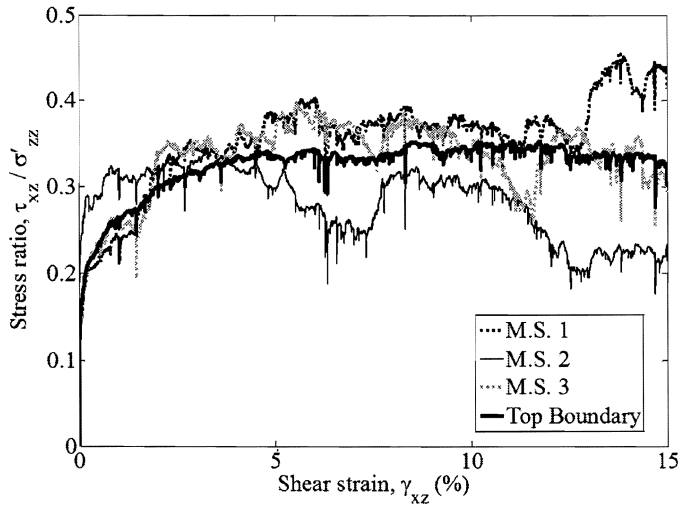

Fig. 6.9. Comparison of stress ratio measured on the top boundary and for various measurement sphere locations throughout sample for MM-50-1

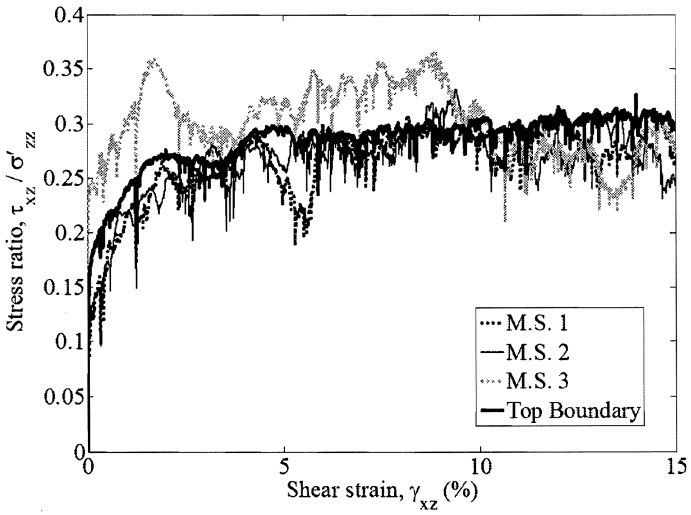

Fig. 6.10. Comparison of stress ratio measured on the top boundary and for various measurement sphere locations throughout sample for ML-50-1

The above comparisons of the macro- and micro-scale data show that there are definite differences in what is being measured at the boundary and what the majority of the sample is actually seeing. One of the additional shortcomings of the device is the inability to apply the complementary shear stresses. This leads to non-uniform normal and shear stress distributions across the sample caps. Based on laboratory data alone, there is little information regarding the severity of these non-uniformities. The DEM data can be used to plot contours of the the normal and shear contacts at the top boundary. Because the particles were glued, the corresponding contact forces included the sum of all of forces from adjacent particles, as well as the particle's out of balance force. The particle's contact magnitude and location was then plotted as a contour using the built-in MATLAB functions. Figs. 6.11, 6.12, and 6.13 show the top boundary normal stress distribution at 0, 5, and 10% shear strain for the dense, medium dense, and loose samples, respectively. Figs. 6.14, 6.15, and 6.16 show similar plots for the shear stress distributions.

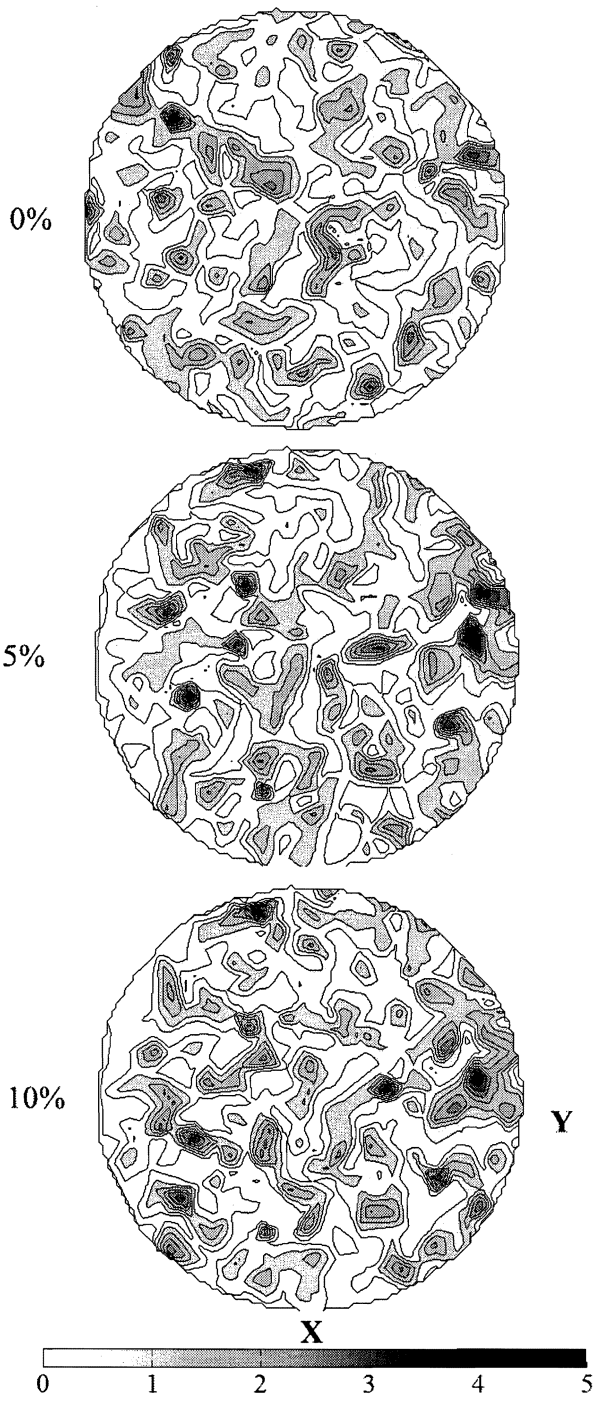

Fig. 6.11. Comparison of MD-50-1 vertical stress distributions on the top boundary for 0, 5, and 10% shear strain

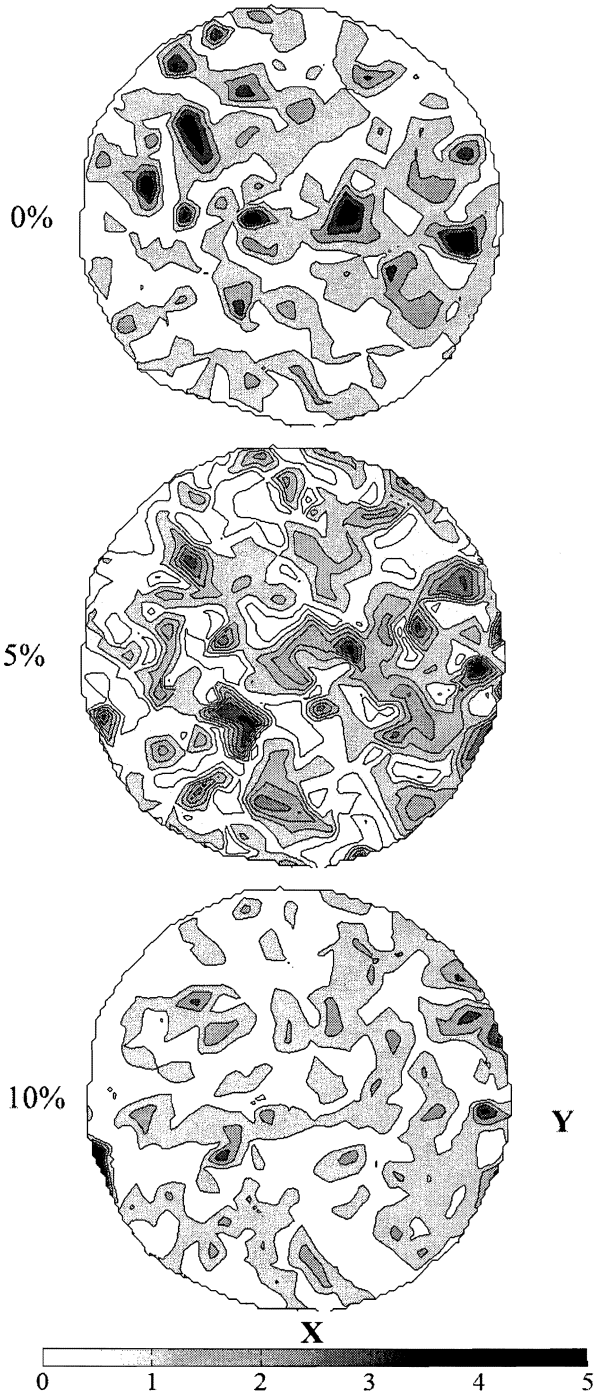

Fig. 6.12. Comparison of MM-50-1 vertical stress distributions on the top boundary for 0, 5, and 10% shear strain

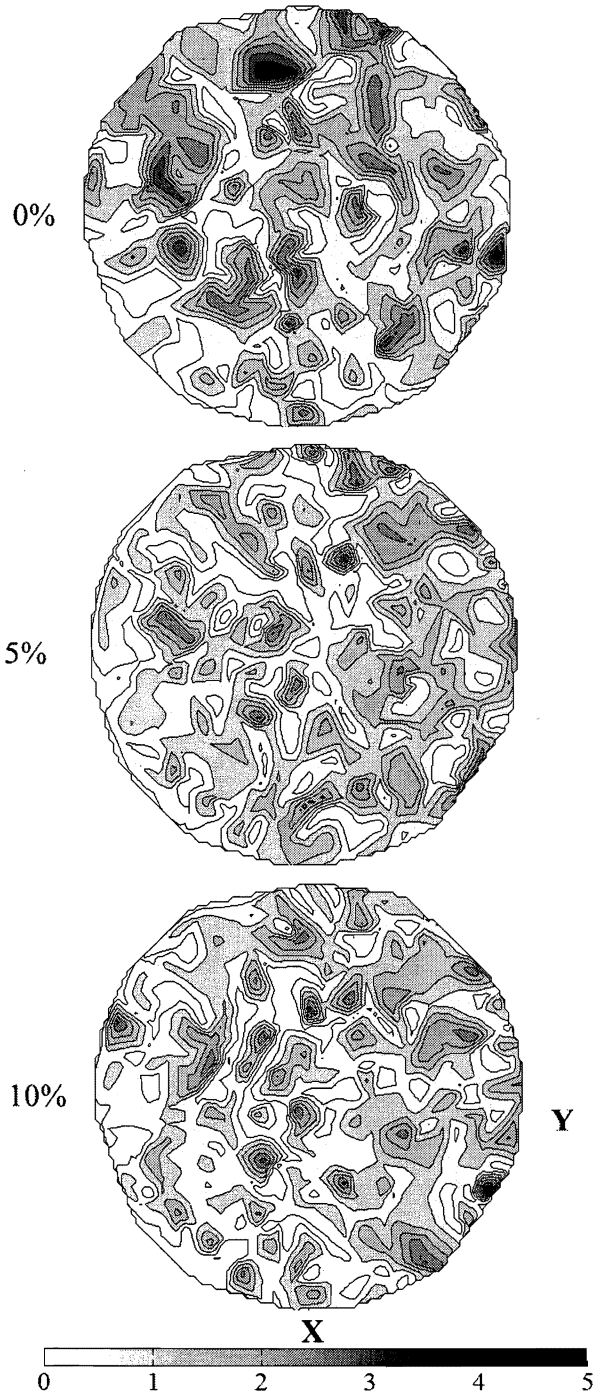

Fig. 6.13. Comparison of ML-50-1 vertical stress distributions on the top boundary for 0, 5, and 10% shear strain

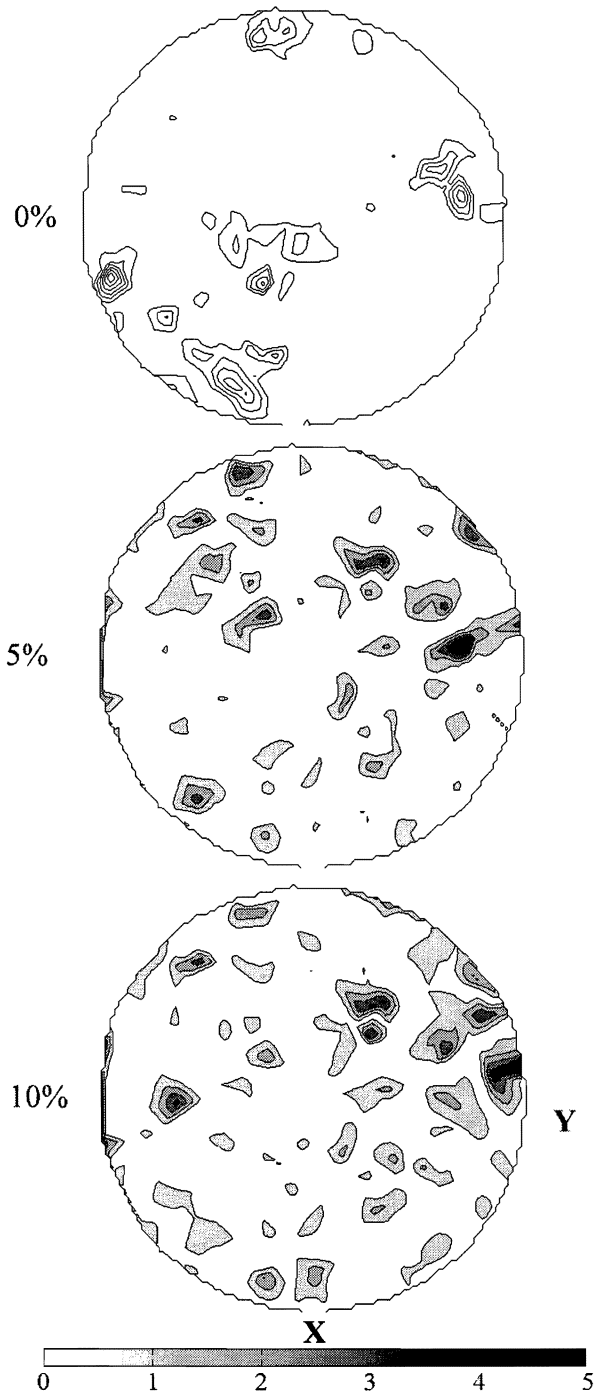

Fig. 6.14. Comparison of MD-50-1 shear stress distributions on the top boundary for 0, 5, and 10% shear strain

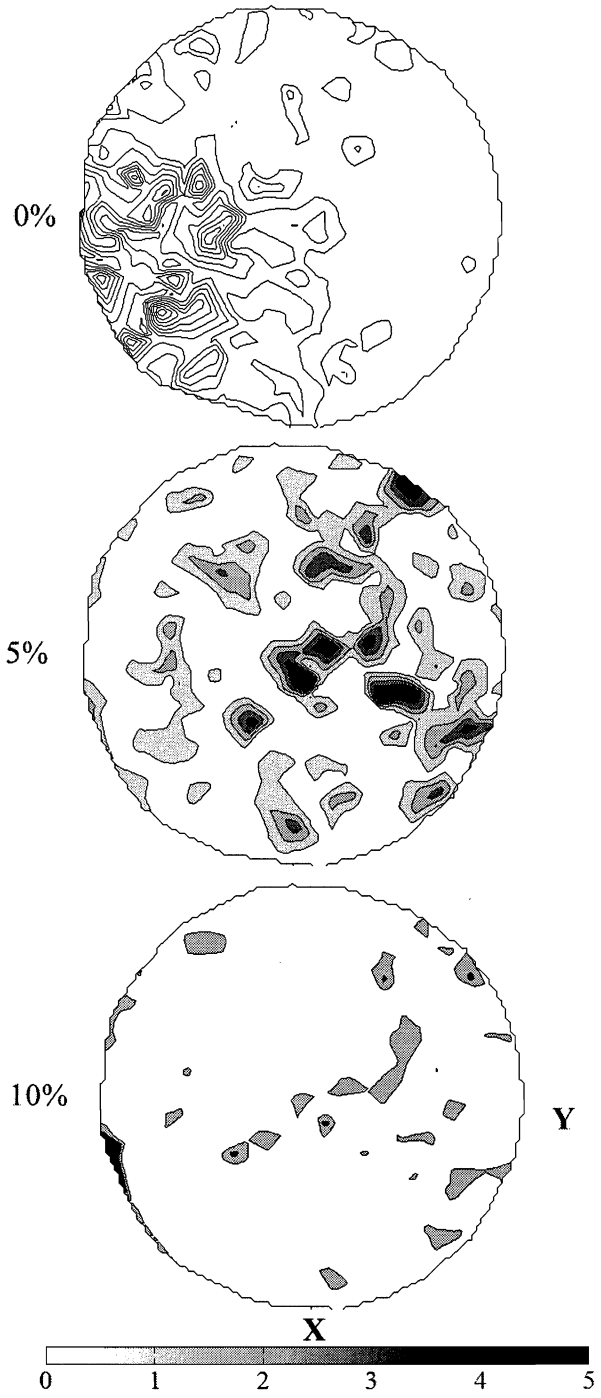

Fig. 6.15. Comparison of MM-50-1 shear stress distributions on the top boundary for 0, 5, and 10% shear strain

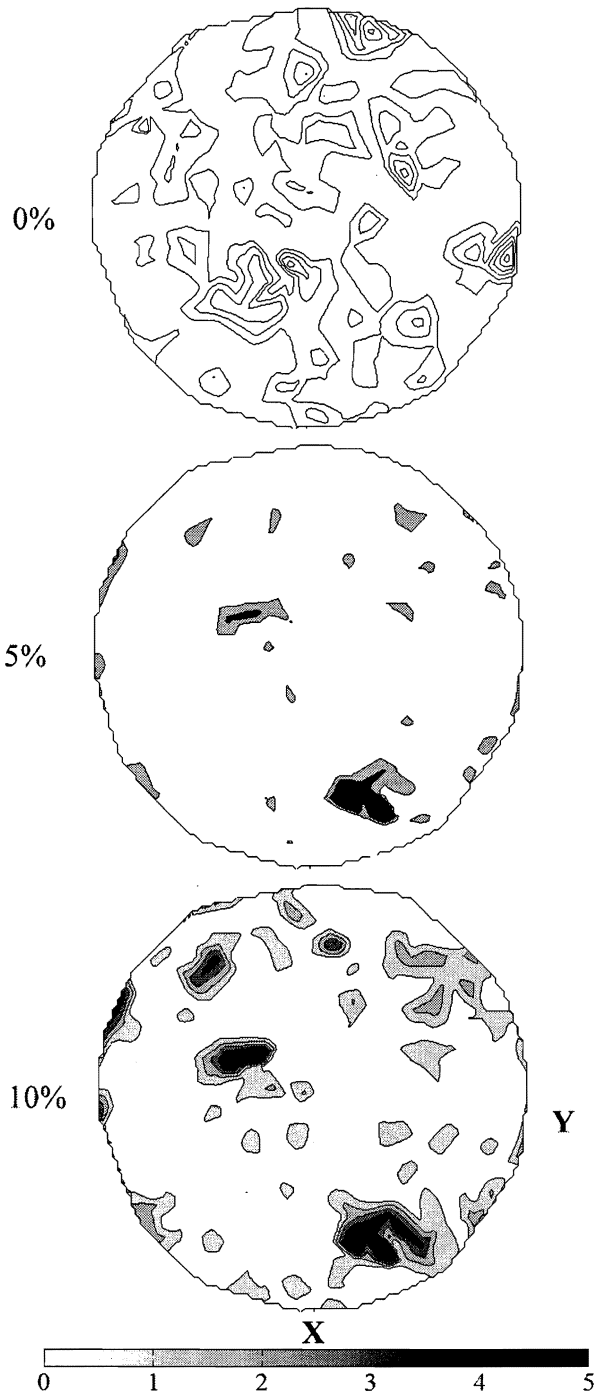

Fig. 6.16. Comparison of ML-50-1 shear stress distributions on the top boundary for 0, 5, and 10% shear strain

It is difficult to see any clear trends using these contour plots due to the low number of contacts per area; however, several observations can still be made. In terms of normal stress distributions, it appears that a higher number of normal contacts, as well as contacts with higher magnitudes develop on the advancing edge (right side of sample). In other words, more white space is seen on the left side of the sample indicating more zero normal contacts. This trend is less marked in the loose sample where several large contacts exist initially and then are redistributed once shearing begins. In terms of shear stresses on the top boundary, all three samples essentially begin with zero shear stresses. As shearing progresses to 5 and 10%, several particles appear to pick up the majority of the shear stress load. The medium dense sample seems to have the most distributed shear stress distribution at 5% because it shows the most non-white area of the contours. It is interesting that high shear stresses are shown at 5%, but they disappear at 10% or are picked up by a small location along the left edge. It is unclear why this would occur. It is possible that some separation could have occurred between the top cap and top ring because of sample dilation, allowing a particle to "lodge" into the space and carry large shear loads. Although it is not as notable, similar concentrations are also seen on the back edge of the other two samples. With the large particle to surface size ratio, it is difficult to easily visualize the stress distributions on the boundary cap. A better indicator is the sample 2 simulation results where 60,000 particles are used. The results for this simulation are presented below.

Another limitation of the direct simple shear device is the inability to measure the horizontal normal stresses and therefore, define the stress state of the sample during shearing. DEM simulations allow for the stress path and various state parameters to be directly calculated. PFC enables the stress tensor of each individual particle, as well as an average stress tensor of a measurement volume to be moni-

tored and recorded. The eigenvectors of the tensors give the principal stresses and the eigenvalues describe their orientations. The stress path can then be defined by q and p' where:

$$q = \sqrt{\frac{(\sigma'_1 - \sigma'_2)^2 + (\sigma'_2 - \sigma'_3)^2 + (\sigma'_3 - \sigma'_1)}{2}} \tag{6.1}$$

$$p' = \frac{\sigma'_1 + \sigma'_2 + \sigma'_3}{3} \tag{6.2}$$

These values are defined in terms of all three principal stresses, which are not attainable in even the most sophisticated cylindrical direct simple shear devices. Note that alternative equations for q and p exist. Fig. 6.17 compares the stress paths for the three samples. These stress paths are calculated based on the stress tensor for the entire cell.

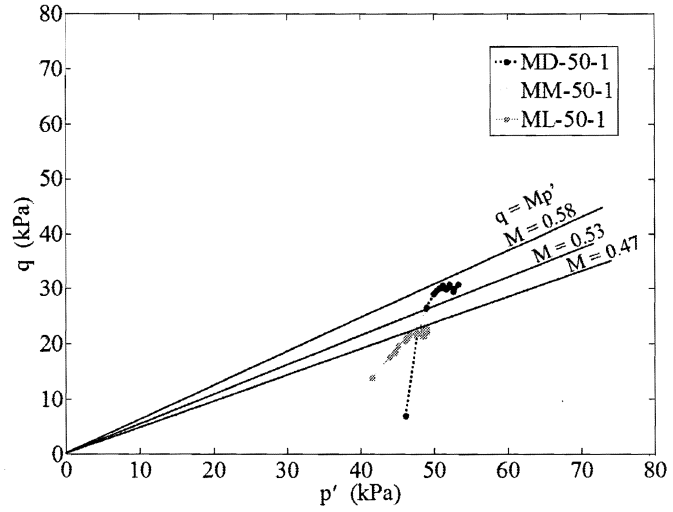

Fig. 6.17. Comparison of stress paths for MD-50-1, MM-50-1, and ML-50-1

A critical state parameter, M, representing the slope of the critical state line, can also be determined from the relationship of q and p' as shown in the figure. It

should be noted, however, that the samples are not yet at critical state at 15% shear strain and it is expected that all three samples would eventually reach a common critical state condition. This is simply shown as an example of information that can be obtained using DEM which cannot be obtained in the laboratory.

The angle of shearing resistance, ϕ', is also calculated using the principal stresses as follows:

$$\phi' = \frac{\sigma_1 - \sigma_3}{\sigma_1 + \sigma_3} \tag{6.3}$$

Fig. 6.18 and Fig. 6.19 show comparisons of the angle of shearing resistance for the three samples based on the entire sample and the sample core data, respectively.

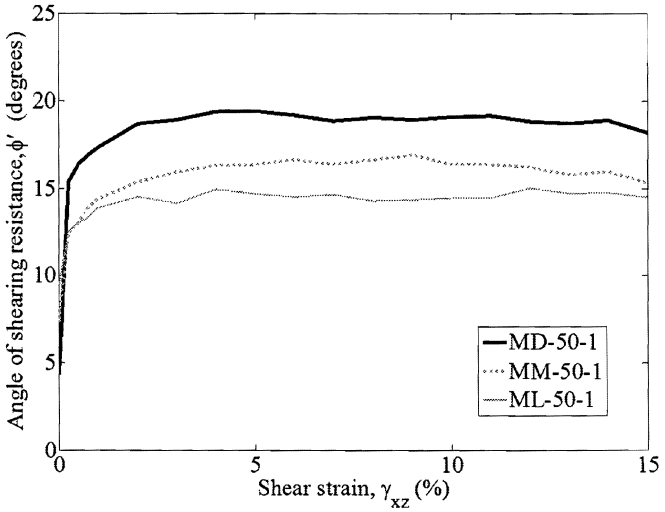

Fig. 6.18. Comparison of angle of shearing resistance based on entire cell data for MD-50-1, MM-50-1, and ML-50-1

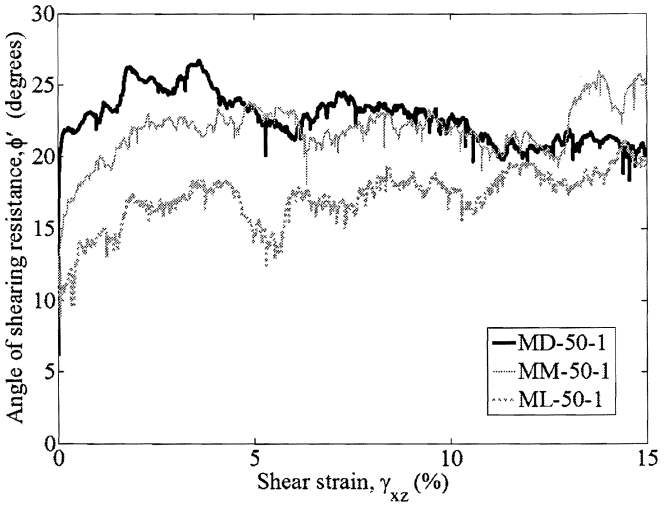

Fig. 6.19. Comparison of angle of shearing resistance based on central measurement sphere data for MD-50-1, MM-50-1, and ML-50-1

It is clear from the figures that the angle of shearing resistance is influenced by the density at shear strain percentages less than 15%. Based on the data for the entire cell, the dense sample has the highest peak friction angle of 19.5°, while the medium dense and loose samples have peak friction angles of 16.9 and 15.0°, respectively. The information for the entire sample is calculated at 0, 0.25, 0.5, 0.75, 1, and then at 1% intervals until 15%. Therefore, the data is much more smooth compared to the internal core measurements, which are recorded every 100 cycles. Several differences are noted in the two. Based on the sample core data, the dense sample reaches the peak friction angle of 26.7° at low strains and then slowly reduces to 20.6° at 15%. The MM-50-1 sample increases to a peak of approximately 24° for the majority of the curve, but then sharply increases to a higher peak of 25.9° at approximately 13.5%. In both of the data sets, one would expect these curves to approach a common value once the sample reached critical state conditions. It

should be noted that these samples are not at critical state at 15% shear strain. The medium dense and loose samples appear to be approaching a common value based on the entire sample and the dense and loose samples appear to be approaching a common value based on the sample core data, but it is difficult to draw conclusions, especially regarding shear strains above 15%. One conclusion that can be drawn from the two figures is that the angles measured in the sample core are significantly higher than those calculated based on the entire sample.

Simple shear testing is the optimal method for replicating in situ stress conditions because it allows for rotation of the principal axes. The limitations of cylindrical direct simple shear devices, however, make measuring the principal stresses and quantifying the actual principal stress rotation difficult and impossible in most cases. The rotation of the principal axes can be easily tracked in the DEM simulations. The orientation of the principal stress planes are given by calculating the eigenvectors of the stress tensor. These eigenvectors are unit normals that can be further described by defining their orientation in spherical coordinates by the angles they make with the x, y, and z axes. Figs. 6.20 and 6.21 show comparisons of α, the angle of the major principal stress axes with the vertical, for calculations based on the entire cell and sample core, respectively.

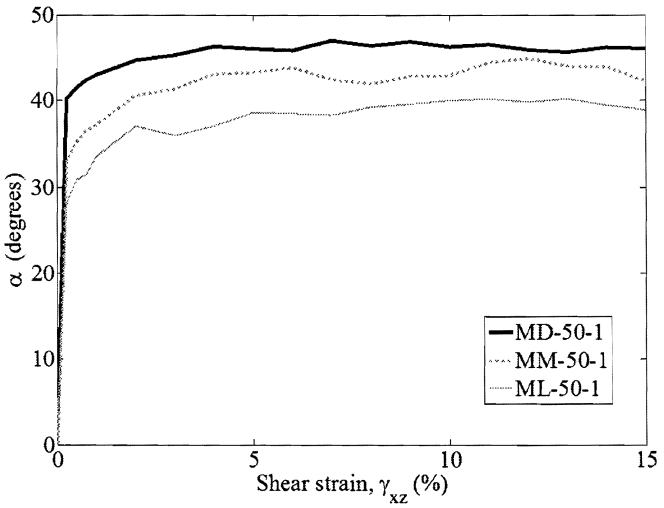

Fig. 6.20. Comparison of major principal stress orientation with the vertical based on entire cell data for MD-50-1, MM-50-1, and ML-50-1

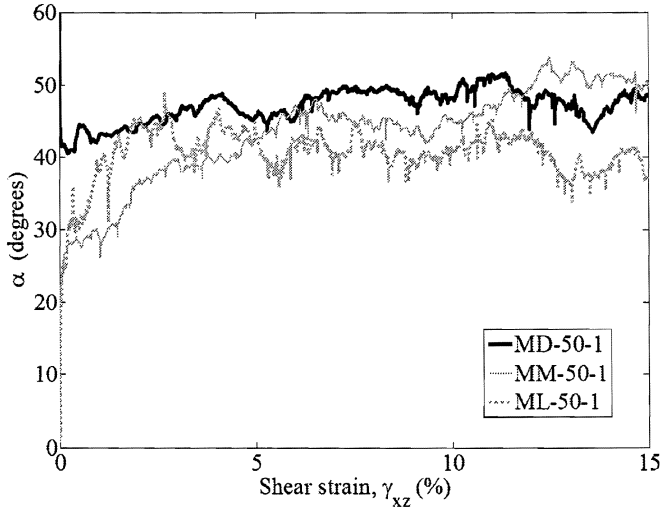

Fig. 6.21. Comparison of major principal stress orientation with the vertical based on central measurement sphere data for MD-50-1, MM-50-1, and ML-50-1

Based on both figures, the degree and magnitude of principal stress rotation is density dependent. The densest sample has the highest angle of principal stress axis rotation. Similar to the angle of shearing resistance, the principal stress rotation angles measured in the sample core are larger than those measured for the entire sample. Within the sample core, the loose sample increases initially to an angle of approximately 43° at a shear strain of 3% and then slowly rotates back to an angle around 40° for the majority of the shearing. Also, the medium dense sample appears to increase substantially after approximately 9% shear strain. For the calculations using the entire cell, all three samples appear to rotate rapidly at very low strains and then remain relatively constant for the remainder of the simulation.

A short summary of non-coaxial behavior was given in Chapter 2. Non-coaxiality is defined as the non-coincidence of the major principal stress and major plastic principal strain rate directions. PFC3D allows for tracking both the stress tensor and the strain rate tensor within a measurement sphere. The method used to measure local strain rate is different than the method described for local stress. As outlined in Potyondy and Cundall (2004) and the PFC3D user manual, the strain rate tensor is determined based on a best-fit approach which minimizes the error between the predicted and actual particle velocities within the measurement volume. The velocity-gradient tensor or strain rate tensor, $\dot{\alpha}_{ij}$, is determined by the following least-square procedure. The average velocity and average position of the particles within the measurement volume are given by:

$$\overline{V}_i = \frac{\sum_{N_p} V_i^{(p)}}{N_p} \quad and \quad \overline{x}_i = \frac{\sum_{N_p} x_i^{(p)}}{N_p} \tag{6.4}$$

where $V_i^{(p)}$ and $x_i^{(p)}$ are the translational velocity and centroid location of each particle

(p). The relative velocities and relative displacements are then given by:

$$\tilde{V}_i^{(p)} = V_i^{(p)} - \overline{V}_i \quad and \quad \tilde{x}_i^{(p)} = x_i^{(p)} - \overline{x}_i \tag{6.5}$$

For a given strain-rate-tensor, $\dot{\alpha}_{ij}$, the predicted relative velocities and displacements are simply:

$$\tilde{v}_i^{(p)} = \dot{\alpha}_{ij}\tilde{x}_j^{(p)} \tag{6.6}$$

The sum of the squares of the deviations between the predicted and actual measured velocities gives the measured error for these predictions:

$$z = \sum_{N_p} |\tilde{v}_i^{(p)} - \tilde{V}_i^{(p)}|^2 = \sum_{N_p} (\tilde{v}_i^{(p)} - \tilde{V}_i^{(p)})(\tilde{v}_i^{(p)} - \tilde{V}_i^{(p)}) \tag{6.7}$$

The minimum error is then determined by the condition:

$$\frac{\partial z}{\partial \dot{\alpha}_{ij}} = 0 \tag{6.8}$$

Eq. 6.6 is then subbed into Eq. 6.7 and differentiated to get nine linear equations:

$$\begin{bmatrix} \sum_{N_p} \tilde{x}_1^{(p)}\tilde{x}_1^{(p)} & \sum_{N_p} \tilde{x}_2^{(p)}\tilde{x}_1^{(p)} & \sum_{N_p} \tilde{x}_3^{(p)}\tilde{x}_1^{(p)} \\ \sum_{N_p} \tilde{x}_1^{(p)}\tilde{x}_2^{(p)} & \sum_{N_p} \tilde{x}_2^{(p)}\tilde{x}_2^{(p)} & \sum_{N_p} \tilde{x}_3^{(p)}\tilde{x}_2^{(p)} \\ \sum_{N_p} \tilde{x}_1^{(p)}\tilde{x}_3^{(p)} & \sum_{N_p} \tilde{x}_2^{(p)}\tilde{x}_3^{(p)} & \sum_{N_p} \tilde{x}_3^{(p)}\tilde{x}_3^{(p)} \end{bmatrix} \begin{bmatrix} \dot{\alpha}_{i1} \\ \dot{\alpha}_{i2} \\ \dot{\alpha}_{i3} \end{bmatrix} = \begin{bmatrix} \sum_{N_p} \tilde{V}_i^{(p)}\tilde{x}_1^{(p)} \\ \sum_{N_p} \tilde{V}_i^{(p)}\tilde{x}_2^{(p)} \\ \sum_{N_p} \tilde{V}_i^{(p)}\tilde{x}_3^{(p)} \end{bmatrix} \tag{6.9}$$

These equations are then solved using a LU-decomposition for the 3×3 matrix and performing three back-substitutions for i=1, 2, and 3 to obtain the nine strain rate tensor components.

The angle the major principal strain rate axes makes with the vertical is calculated in a similar manner as described above for the major principal stress angle.

The angle of non-coaxiality, $\triangle\alpha$, is then defined as the difference in the major plastic principal strain rate and major principal stress directions. Fig. 6.22 gives the angle of non-coaxiality for the three samples.

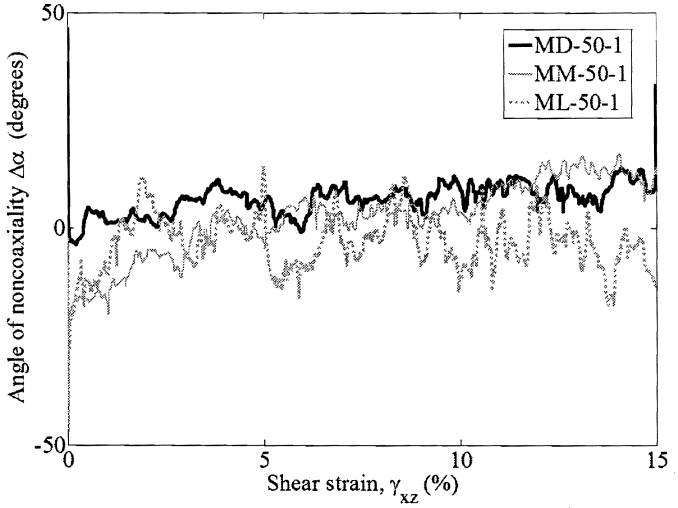

Fig. 6.22. Comparison of the angle of non-coaxiality based on central measurement sphere data for MD-50-1, MM-50-1, and ML-50-1

Initially at low strains, the principal strain rate and principal stress axes for the MM-50-1 and ML-50-1 samples are not coincident. The strain rate orientation lags behind the principal stress until a shear strain of approximately 2% for the loose sample and 5% for the medium dense sample.

Another method of examining non-coaxial behavior and the movement of the individual particles in general is to plot the incremental displacements with height for each individual particle. Figs. 6.23, 6.24, and 6.25 show the x, y, and z directional displacement of the particles from 0 to 15% shear strain plotted at their sample height.

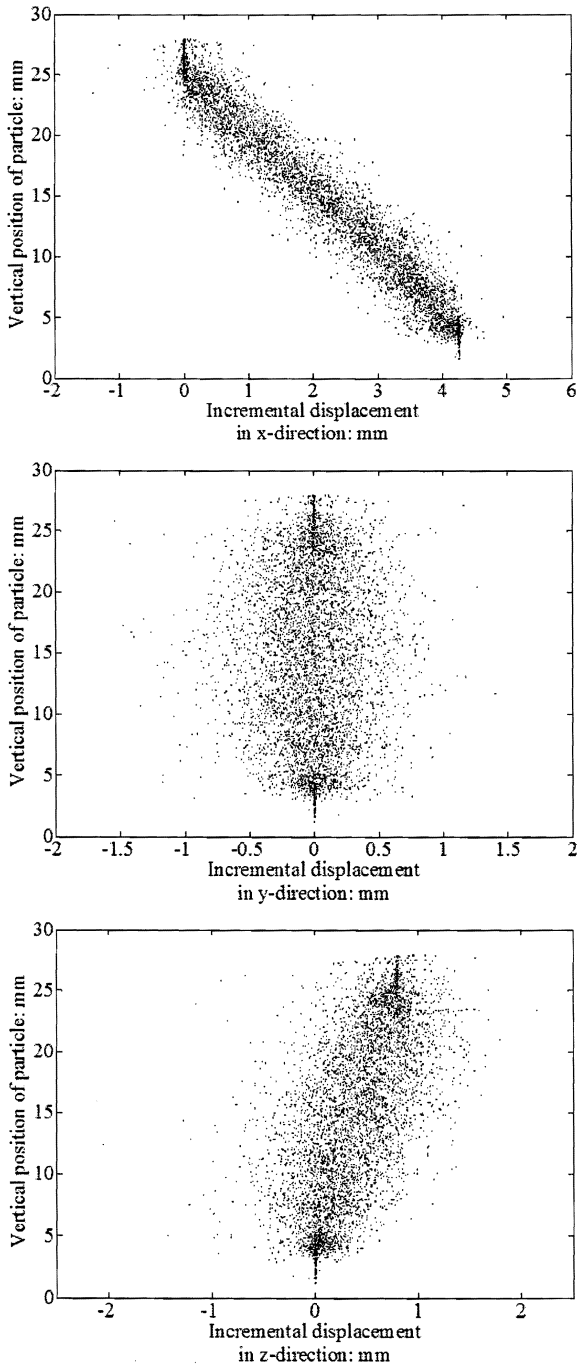

Fig. 6.23. Comparison of x, y, and z particle displacements with height for MD-50-1

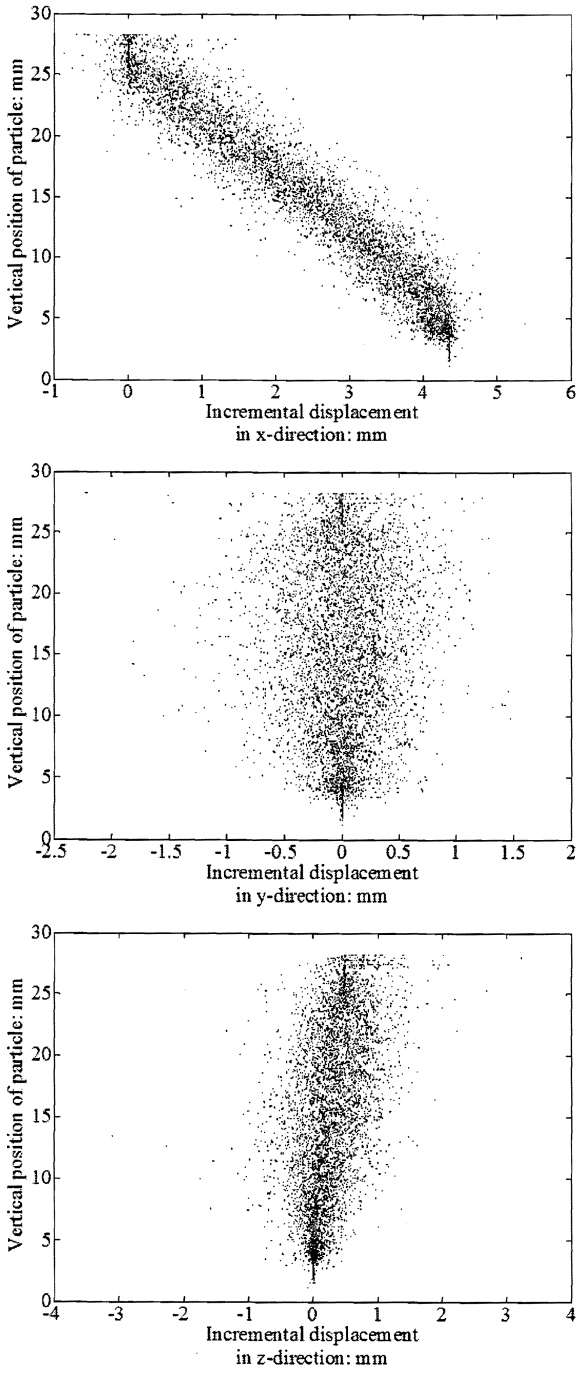

Fig. 6.24. Comparison of x, y, and z particle displacements with height for MM-50-1

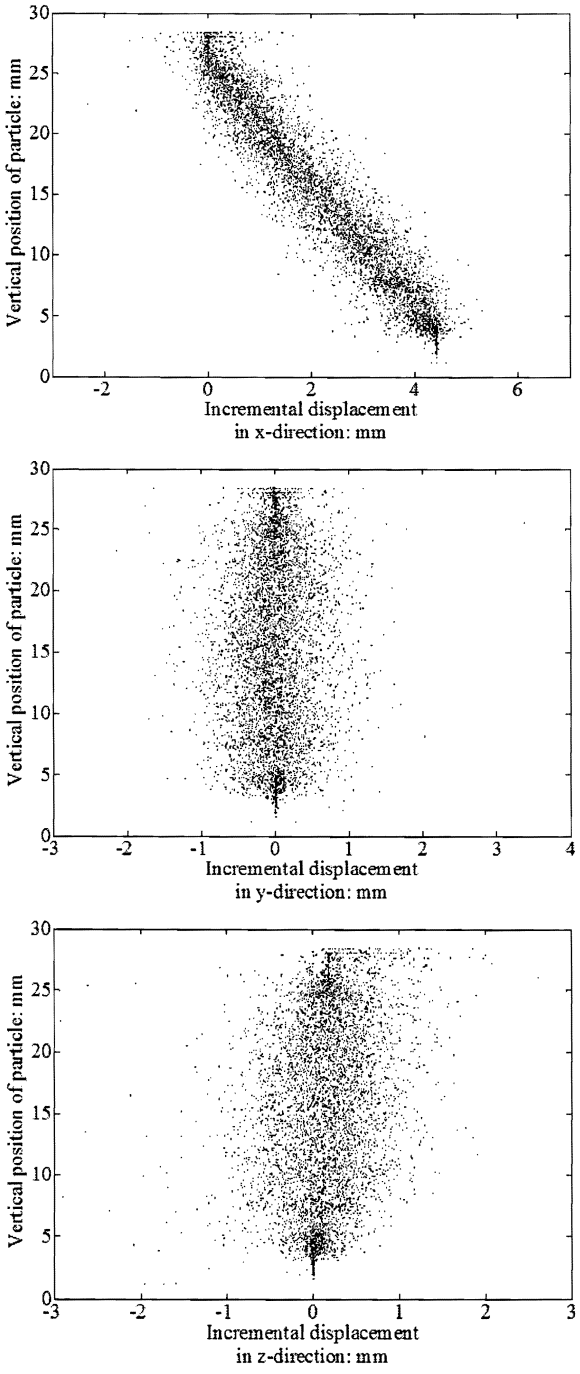

Fig. 6.25. Comparison of x, y, and z particle displacements with height for ML-50-1

For each figure, the displacement in the x-direction is as expected for simple shear. The particles glued to the top and bottom caps displace with the caps with no scatter. The profile is linear between these two locations with some scatter observed. The plot of the y displacements displays the non-coaxial behavior. The shearing is only occurring in the x-direction; however, there is displacement in the y-direction for the majority of the particles. The plot of z displacements shows the dilative nature of the DEM samples. The particles near the top of the sample move in the positive z-direction, representing dilation. It is also interesting that many of the particles in this top section move downward in the negative direction even though the sample overall is dilating.

The particle displacements can also be plotted as vectors. This allows for the movement of each particle to be tracked through the various increments of strain. Figs. 6.26, 6.27, and 6.28 show the displacements for the three samples at various increments of shear strain. These figures display the displacements of the particles located within a slice through the middle of the sample along the x-axis. The vector lengths represent the magnitude of the corresponding particle displacement.

It is apparent from each of the figures that there are essentially three zones within the sample. The top portion of the sample is a dilative zone where most of the particles are only moving upwards in the z-direction. The bottom portion is a shearing zone where most of the particles are only shearing in the x-direction with very little if any vertical motion. The third zone in the middle of the sample is an intermediate zone where particles are moving both horizontally and vertically. When a granular sample is sheared, particles move up and over one another or around each other. The above displacement point plots showed that many of the particles move horizontally around one another, as well as move vertically over one another. Plotting the displacement vectors for a slice through the sample isolates and shows

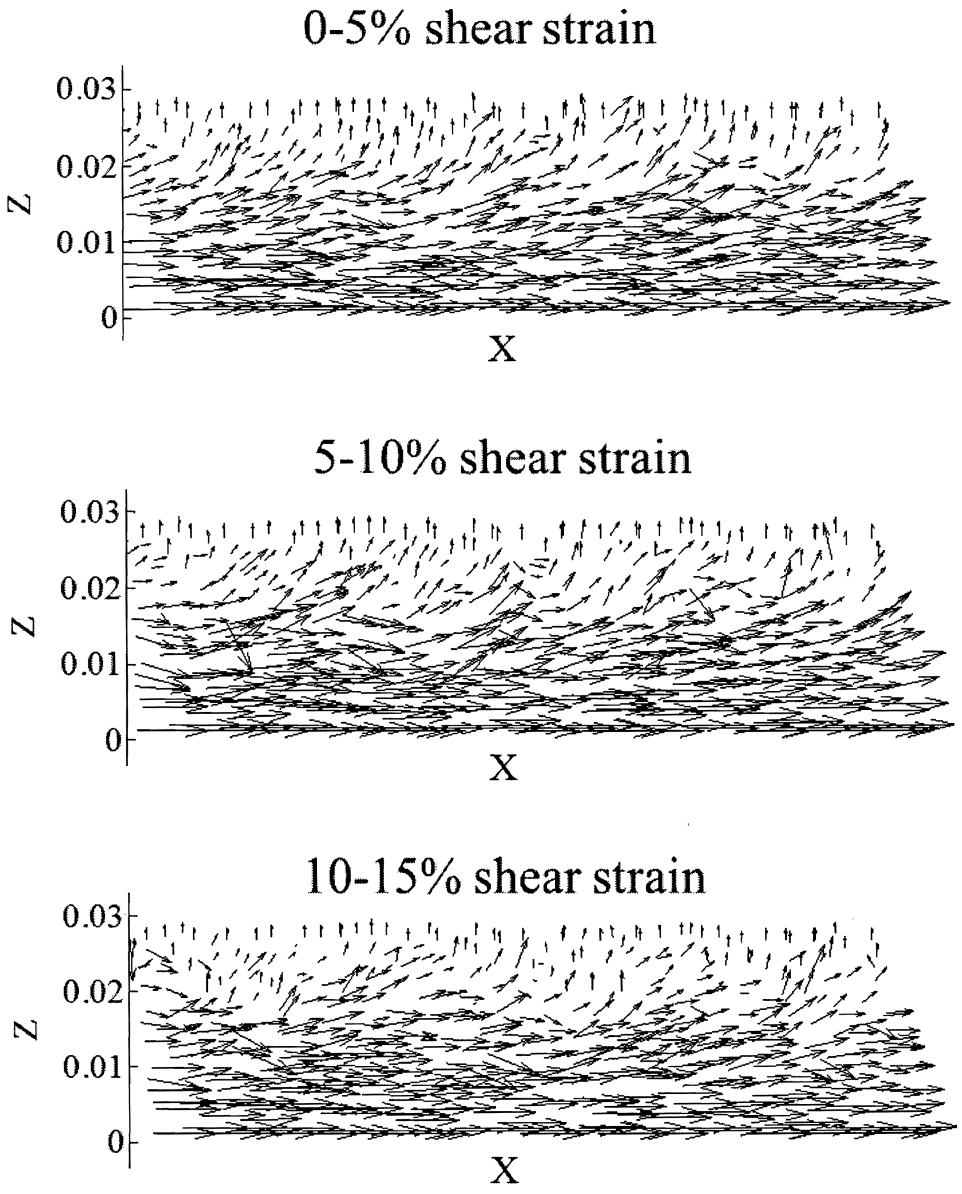

Fig. 6.26. Comparison of particle displacement vectors for slice through MD-50-1 sample along x-axis

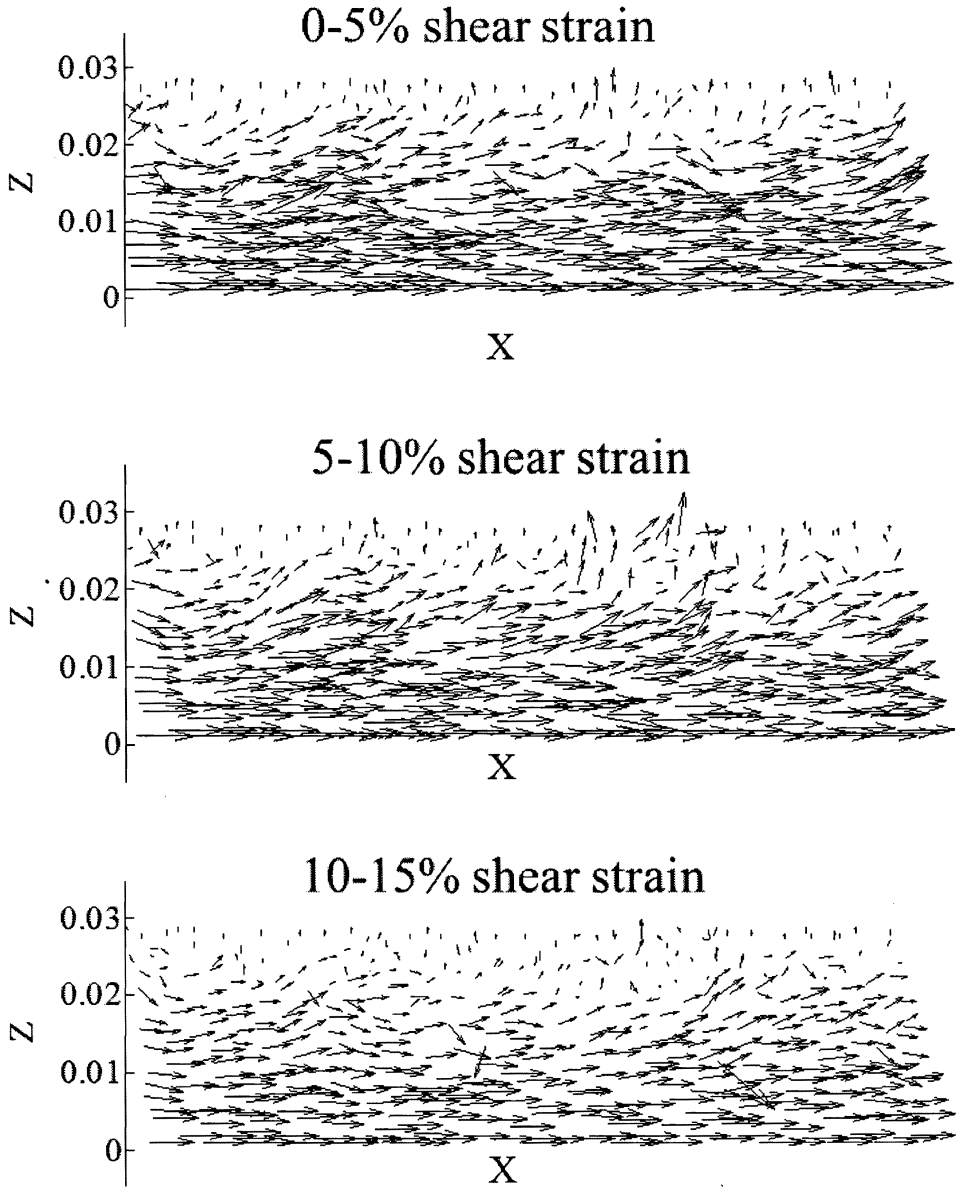

Fig. 6.27. Comparison of particle displacement vectors for slice through MM-50-1 sample along x-axis

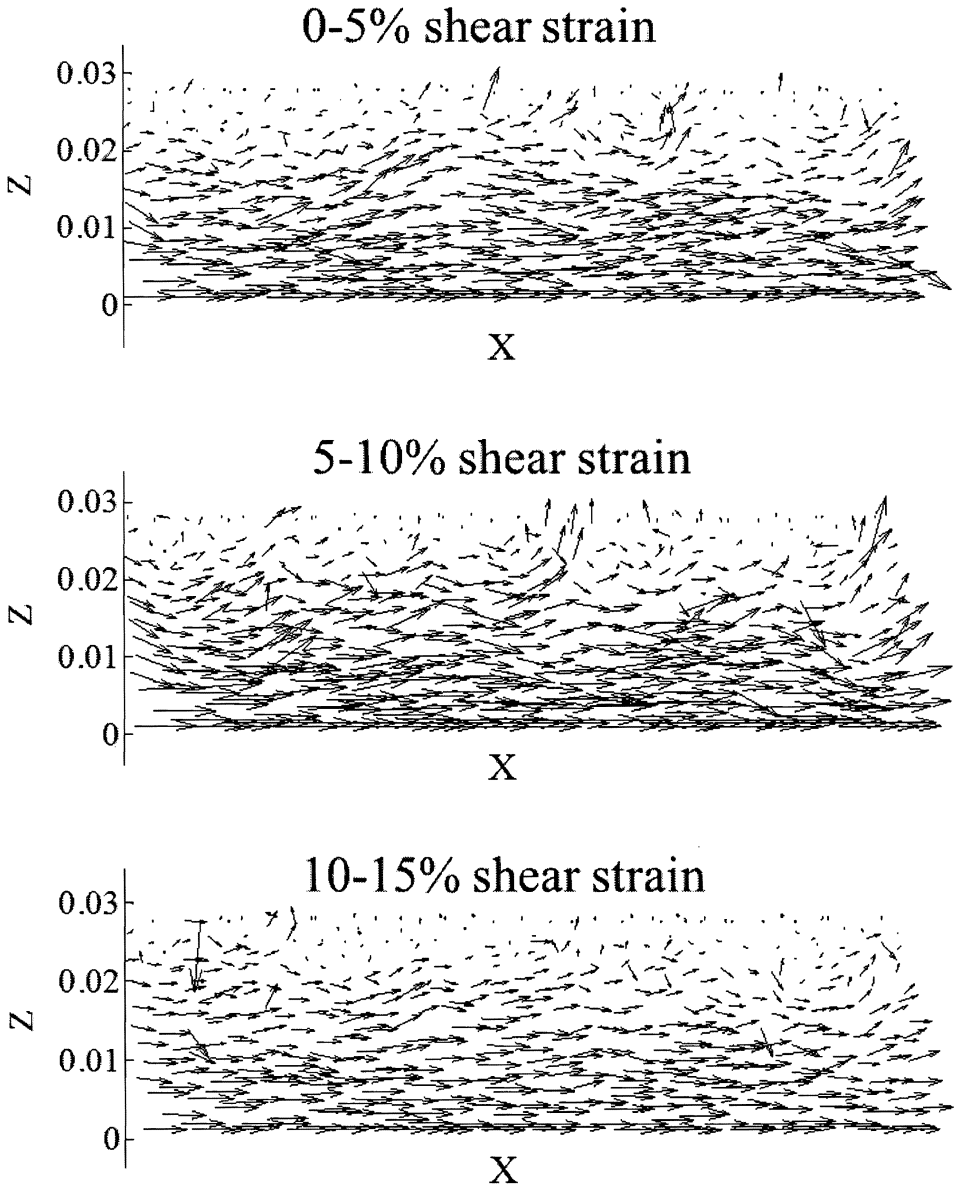

Fig. 6.28. Comparison of particle displacement vectors for slice through ML-50-1 sample along x-axis

the movement in the plane. It is clear to see the particles in the mid-zone move up and over an adjacent particle and then move downward into the void space. For the dense sample, the majority of this type of behavior occurs at shear strains above 5%. From 0 to 5%, the particles are mostly moving upward and the sample is dilating. The displacement of the particles in the mid-zone of the medium and loose samples is more erratic than that of the dense sample. These particles appear to re-arrange more easily and displace greater distances. This is also confirmed by the above displacement point plots which show more scatter in the displacements for these two samples.

Along with plotting displacement vectors, instantaneous velocity vectors also give an indication of particle movements throughout the sample. Similar plots showing the instantaneous velocities for a vertical slice through the samples along the x-axis are given in Figs. 6.29, 6.30, and 6.31.

The findings from these plots are similar to the incremental displacement vector plots. Three zones are present within the sample. Also, the instantaneous velocities show the particles within the center zone moving up and over one another during shearing. One interesting feature is that the instantaneous velocities of the loose sample at 5% shear strain are very small indicating the particles are relatively still. The majority of the particle movement appears to occur in the first 5% shear strain and then there is a still point before the particles begin to move again.

One of the major advantages of DEM simulations is the ability to quantify fabric in several different ways. One indication of fabric is void ratio which was presented above. A second component involves the contacts and the distribution of forces throughout the sample. A short introduction to coordination number was given in Chapter 4. The coordination number, calculated as in Eq. 4.1, quantifies the number of contacts per particle and gives a way of measuring packing density

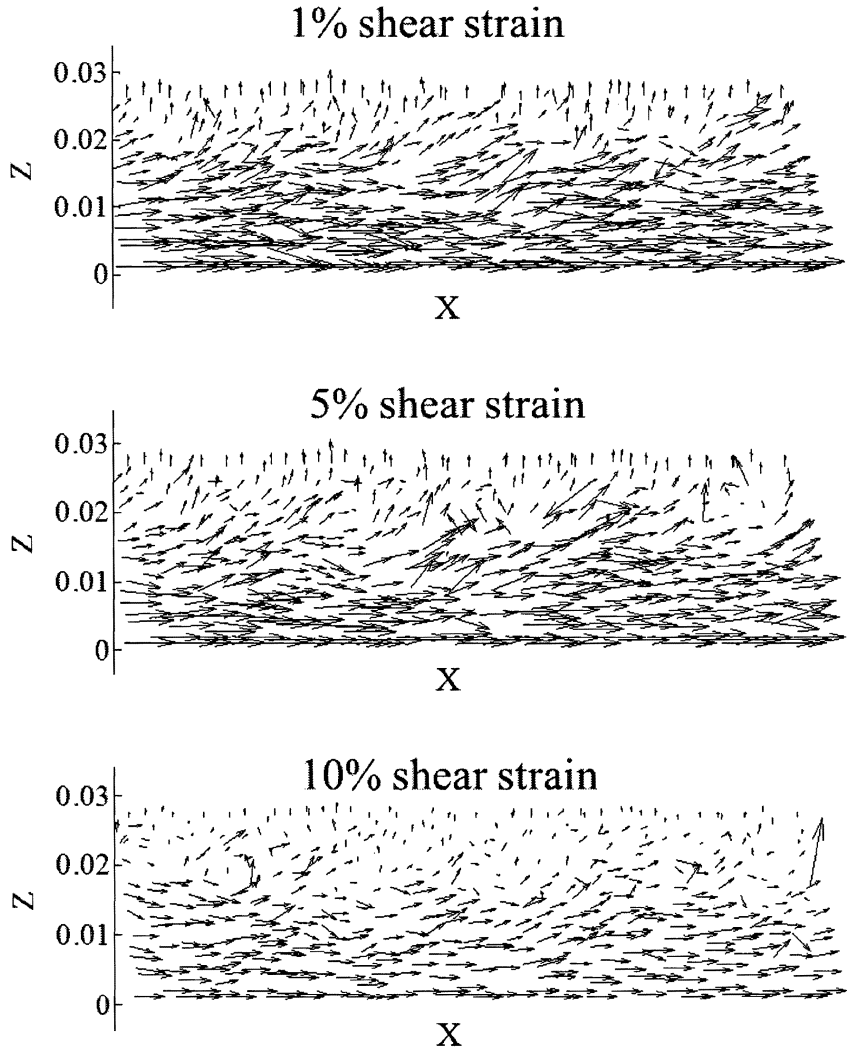

Fig. 6.29. Comparison of particle instantaneous velocity for slice through MD-50-1 sample along x-axis

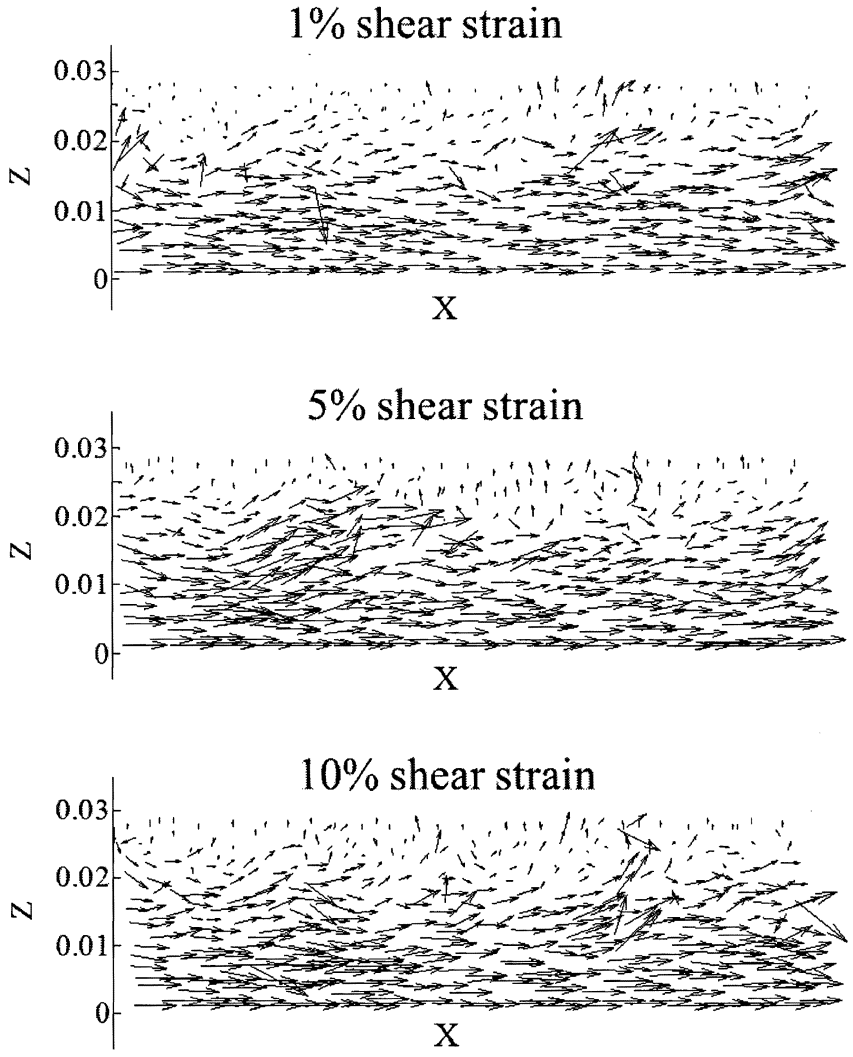

Fig. 6.30. Comparison of particle instantaneous velocity for slice through MM-50-1 sample along x-axis

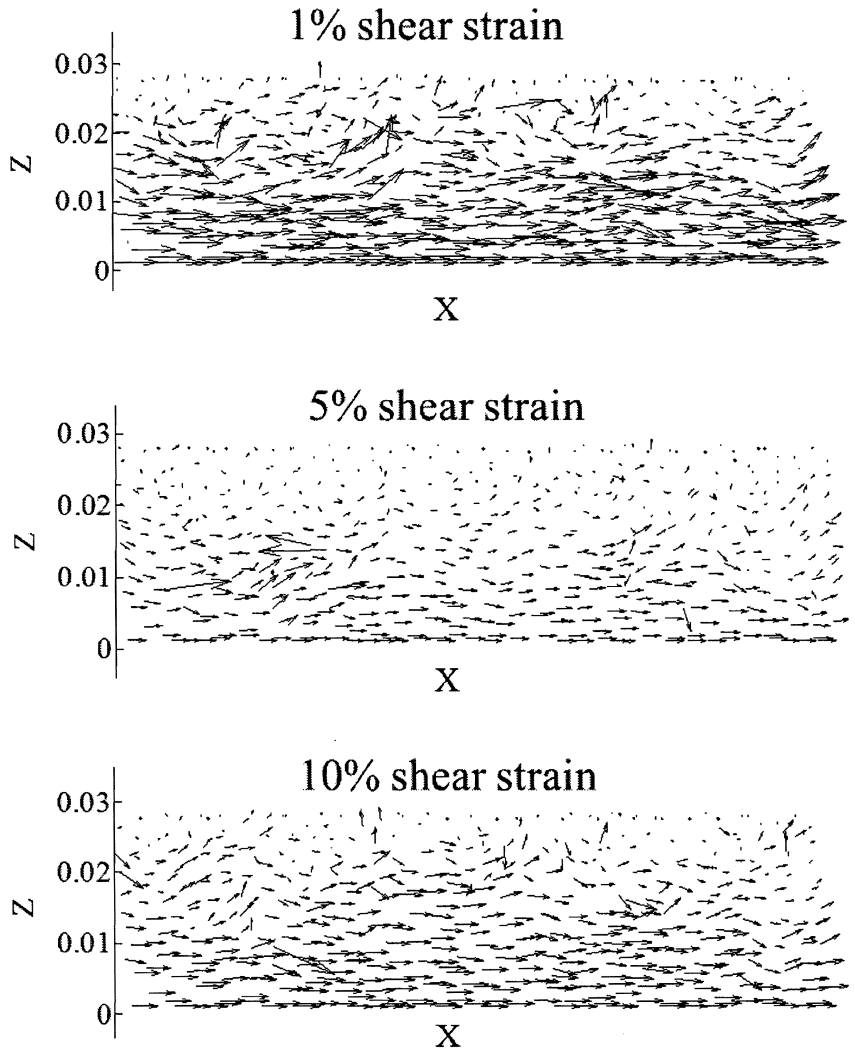

Fig. 6.31. Comparison of particle instantaneous velocity for slice through ML-50-1 sample along x-axis

and contact intensity. Plots of coordination number calculated for the entire cell and sample core are given in Fig. 6.36. Additional plots of coordination number for the five measurement sphere locations are also given in Figs. 6.37, 6.38, and 6.39. The built in PFC function uses a different definition of coordination number. Therefore, the particle output files at each strain interval were used in a user-written MATLAB code to calculate the average coordination number within the measurement spheres.

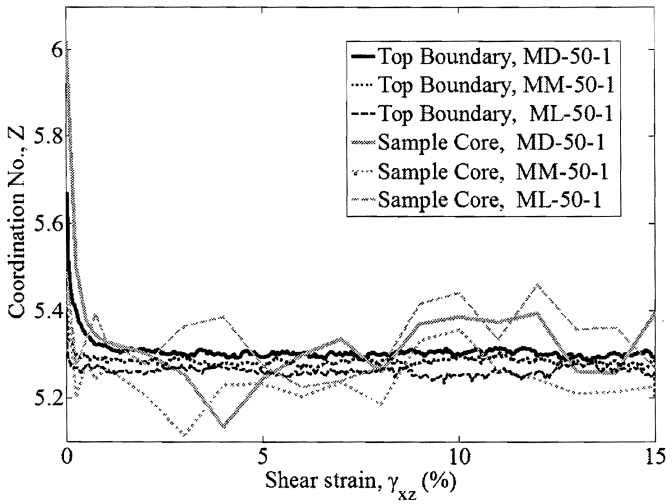

Fig. 6.32. Comparison of coordination number measured for the entire cell and the sample core for MD-50-1, MM-50-1, and ML-50-1

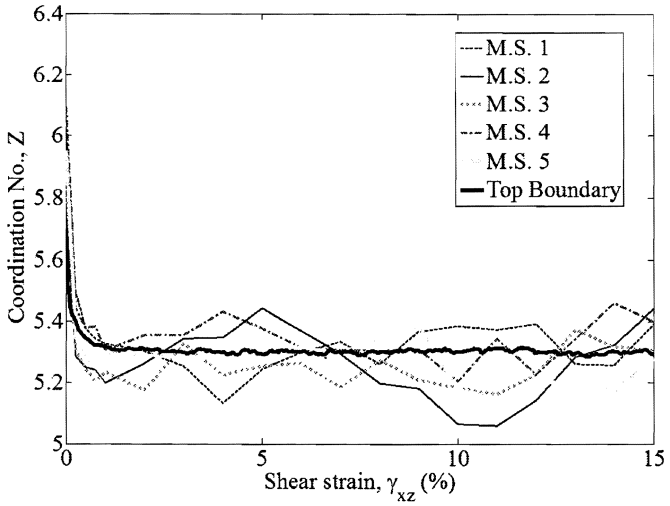

Fig. 6.33. Comparison of coordination number measured for the entire cell and for various measurement sphere locations throughout sample for MD-50-1

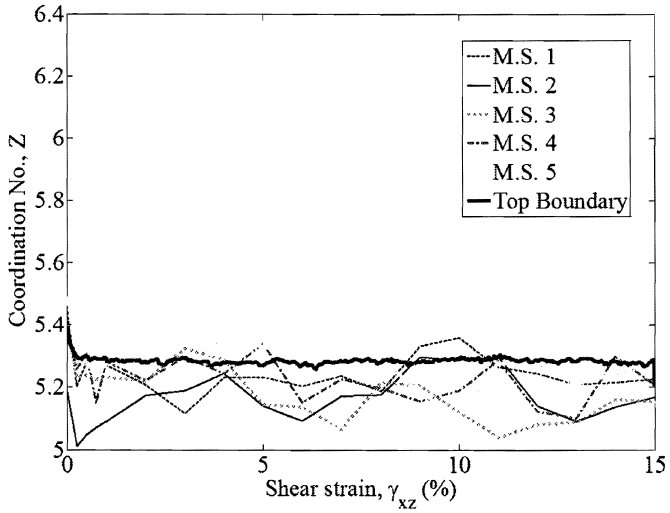

Fig. 6.34. Comparison of coordination number measured for the entire cell and for various measurement sphere locations throughout sample for MM-50-1

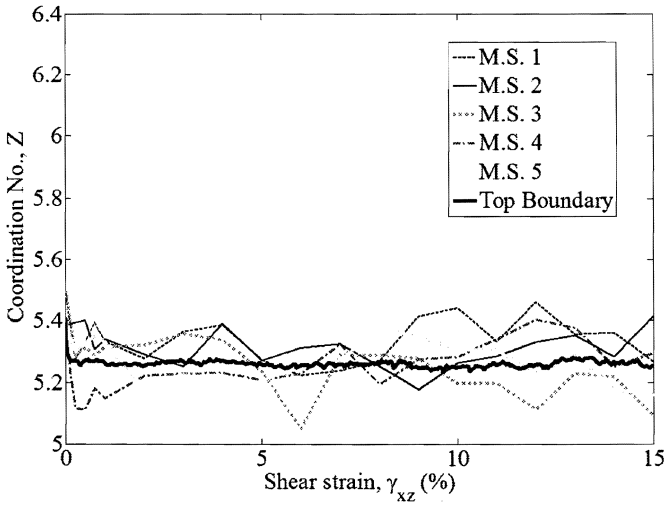

Fig. 6.35. Comparison of coordination number measured for the entire cell and for various measurement sphere locations throughout sample for ML-50-1

In each case, the coordination number starts at a higher value and then lowers immediately as shearing begins. The coordination number then reaches a stable and consistent value for the boundary measurements. The measurement sphere values oscillate about the boundary measurements, but stay within a relatively narrow range of the boundary measurement. No major differences are noted for any of the samples.

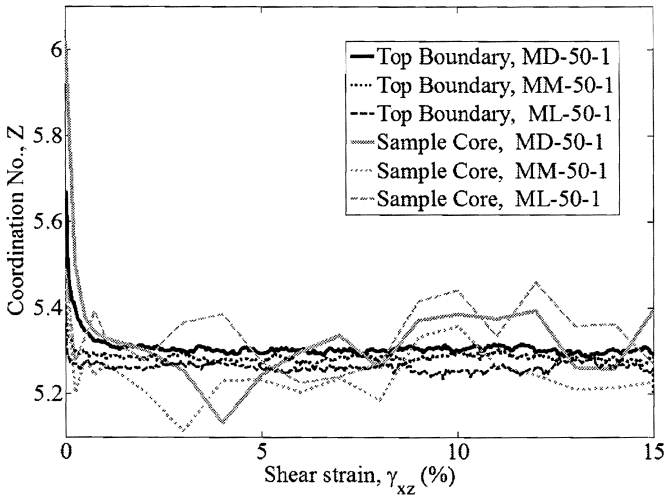

Fig. 6.36. Comparison of coordination number measured for the entire cell and the sample core for MD-50-1, MM-50-1, and ML-50-1

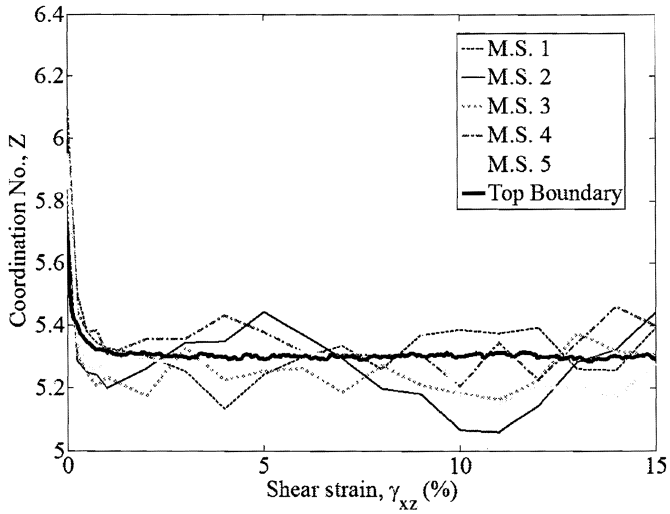

Fig. 6.37. Comparison of coordination number measured for the entire cell and for various measurement sphere locations throughout sample for MD-50-1

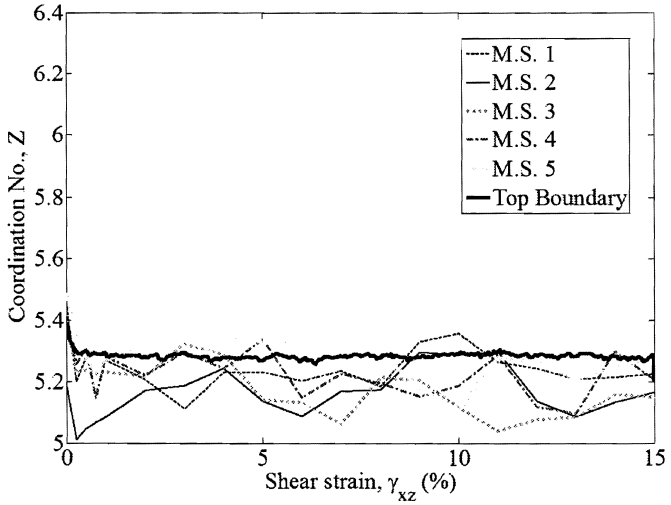

Fig. 6.38. Comparison of coordination number measured for the entire cell and for various measurement sphere locations throughout sample for MM-50-1

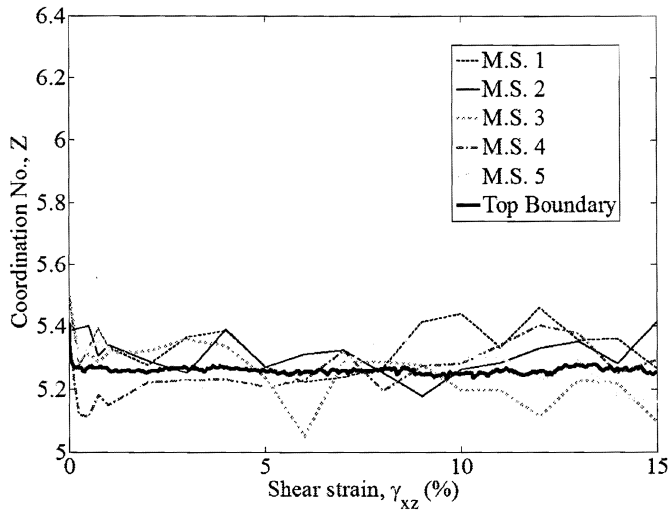

Fig. 6.39. Comparison of coordination number measured for the entire cell and for various measurement sphere locations throughout sample for ML-50-1

Similar to the above displacement and velocity plots for a slice through the sample, the contact force branches can be plotted to show the contact force network. The contact force network is created by plotting the branch vectors of the corresponding particles. In other words, the centroids of the adjacent contacting particles are connected by a line. The thickness of the line is proportional to the magnitude of the contact. This allows a way to visualize how the forces are transmitted throughout the sample. Fig. 6.40 presents the contact force networks for the samples at 0, 5, and 10% shear strain. Figs. 6.41 and 6.42 compare each sample's contact force network at 5% and 10% for the ease of viewing and comparison.

At 0% shear strain, the only loading is the top cap and one would expect the majority of the contact force chains in all three samples to be oriented vertically. One of the interesting features of granular soils is the fact that a large portion of the load is carried by a relatively small number of force chains. This is more visible at the higher shear strain percentages. At 5 and 10% shear strain, the force chains are oriented diagonally extending from the top right corner of the sample to the lower left.

As introduced in Chapter 4, the fabric tensor for a granular material can be defined as in Eq. 4.4. The eigenvalues of the fabric tensor then define measures of the principal fabric and the eigenvectors define their orientations. The angle the major principal fabric makes with the vertical, α_{fab}, is defined in the same manner as α and is shown in Fig. 6.43 for the three samples. These values are determined using the tensor for the entire sample.

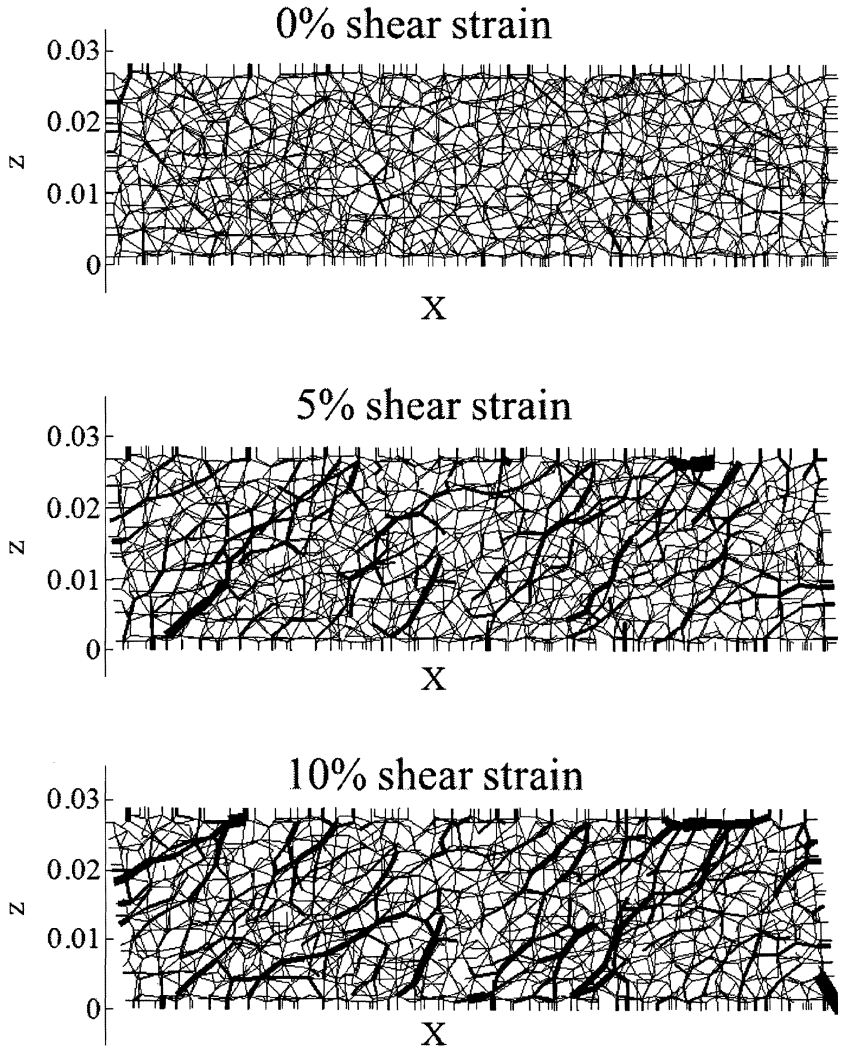

Fig. 6.40. Comparison of contact force network for slice through MD-50-1 sample along x-axis

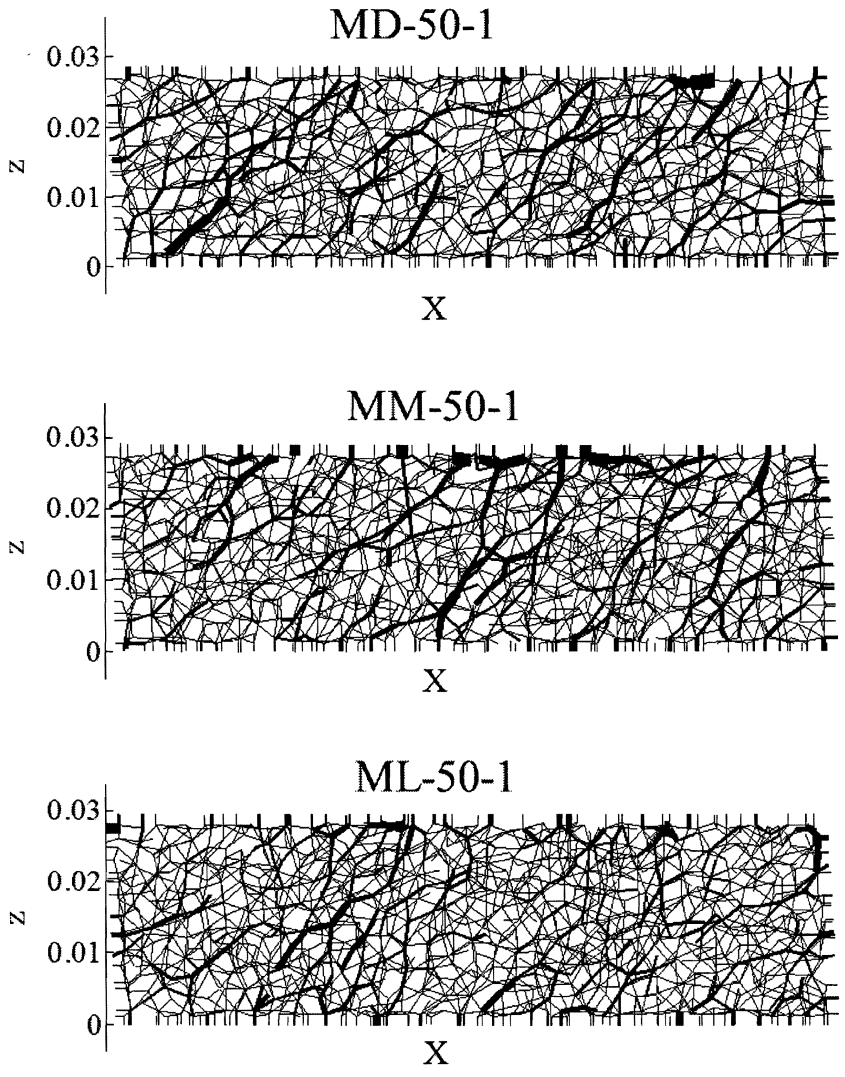

Fig. 6.41. Comparison of contact force networks at 5% shear strain for MD-50-1, MM-50-1, and ML-50-1

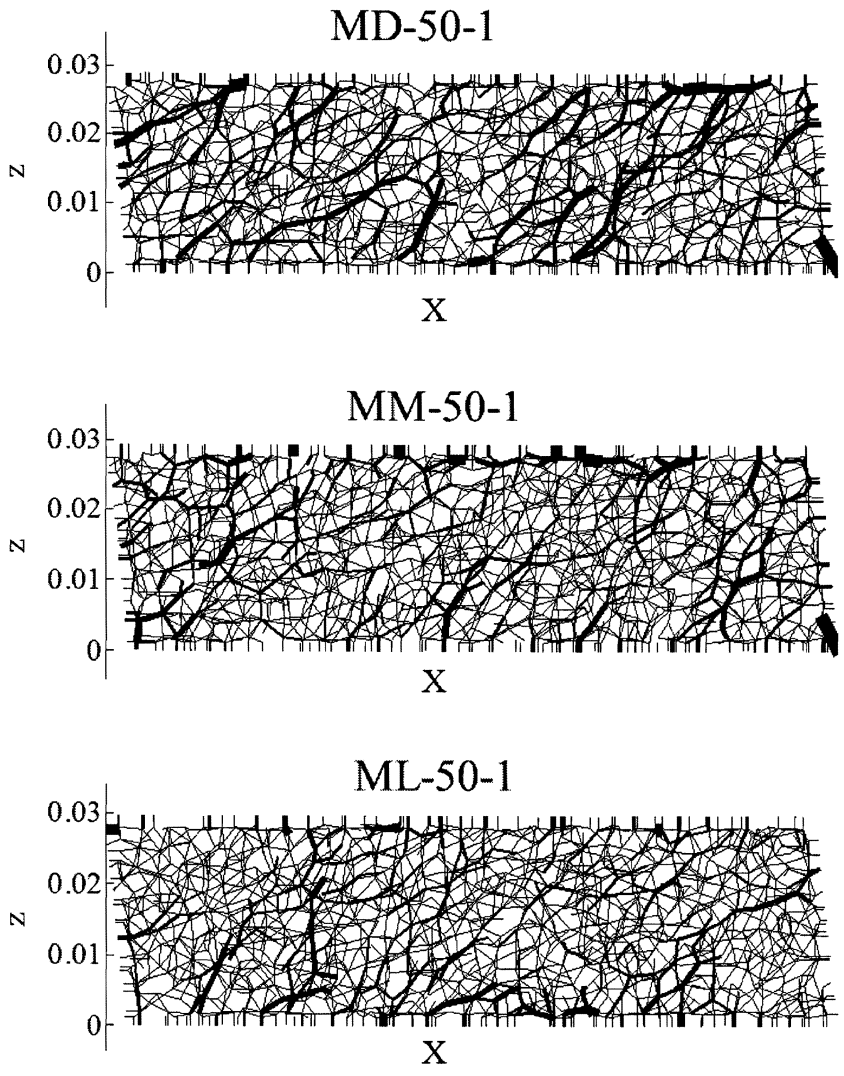

Fig. 6.42. Comparison of contact force networks at 10% shear strain for MD-50-1, MM-50-1, and ML-50-1

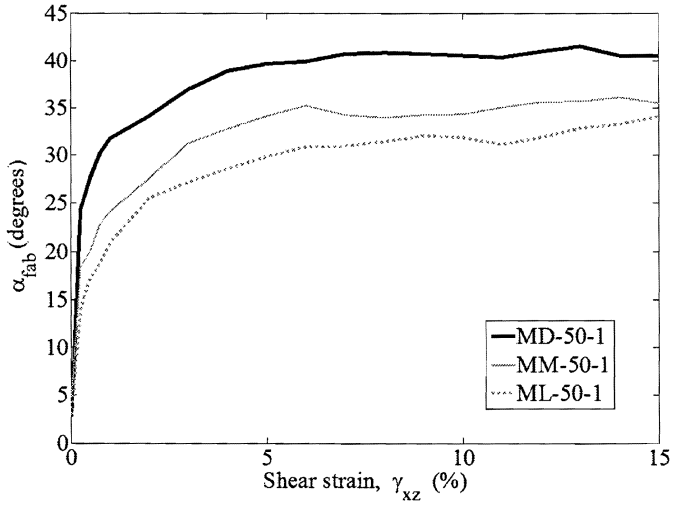

Fig. 6.43. Comparison of major principal fabric orientation with the vertical for MD-50-1, MM-50-1, and ML-50-1

For each of the samples, the major fabric is oriented very near vertical before shearing begins. This is as expected. It is clear that the angle of major fabric orientation with the vertical is density dependent. The densest sample exhibits the largest rotation and the highest overall angle of major fabric orientation. The loose sample exhibits the least. For each of the cases, $\alpha_{fab} < \alpha$. This is due to the fact that the larger contact forces contribute to the stress tensor, while all forces contribute equally in the fabric tensor.

A second measure of fabric is the deviator fabric, or the difference in the major and minor principal fabrics. This gives a way of quantifying the anisotropy of the fabric (i.e. isotropic samples have a difference of zero). Fig. 6.44 compares the deviator fabric for the three samples.

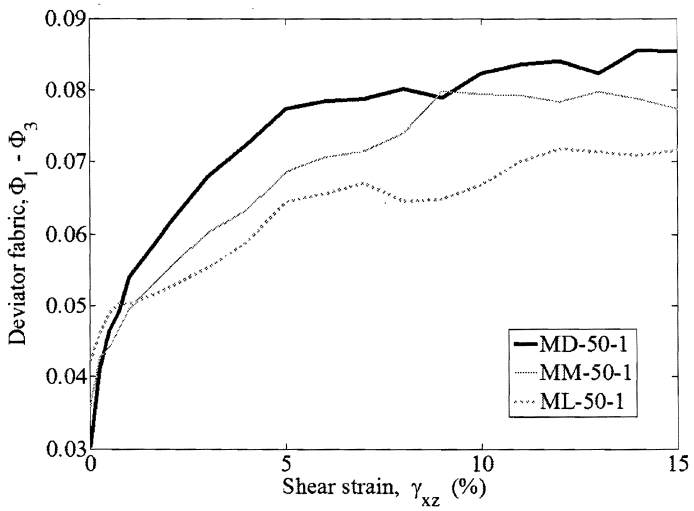

Fig. 6.44. Comparison of deviator fabric for MD-50-1, MM-50-1, and ML-50-1

The deviator fabric also appears to be density dependent. The densest sample has the largest difference in the major and minor principal fabrics and the loose sample has the least. For each of the samples, the deviator fabric begins low and then increases as shearing progresses.

As shown in the analysis above, many of the microscopic parameters are influenced by density. The densest sample exhibits the largest degree of principal stress rotation, the highest angle of shearing resistance, and the highest deviator fabric. It is also apparent from the figures that a number of the measured parameters are underestimated by the boundary measurements taken on the top cap. This is an important factor that should be considered in the laboratory and design parameter determination.

6.2 Influence of Vertical Stress on Microscopic Response

Another factor influencing granular behavior is confining stress or the vertical effective stress the sample is tested at. The following section relates the loose samples at 50 and 100 kPa, ML-50-1 and ML-100-1. While the entire suite of information was presented above to show the capabilities of DEM, only pertinent plots are shown in this section. The void ratios of the two samples are very close. This was important in order to isolate the effects from differing vertical stresses. Fig. 6.45 shows a comparison of void ratios measured by the top cap boundary location and in the sample core of the two samples. Fig. 6.46 compares the boundary value with the void ratios determined in the five measurement spheres for sample ML-100-1.

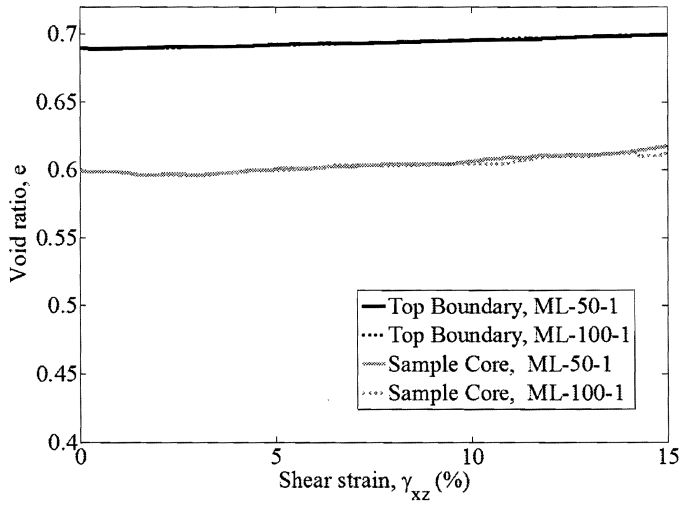

Fig. 6.45. Comparison of void ratios measured from the top boundary location and the sample core for ML-50-1 and ML-100-1

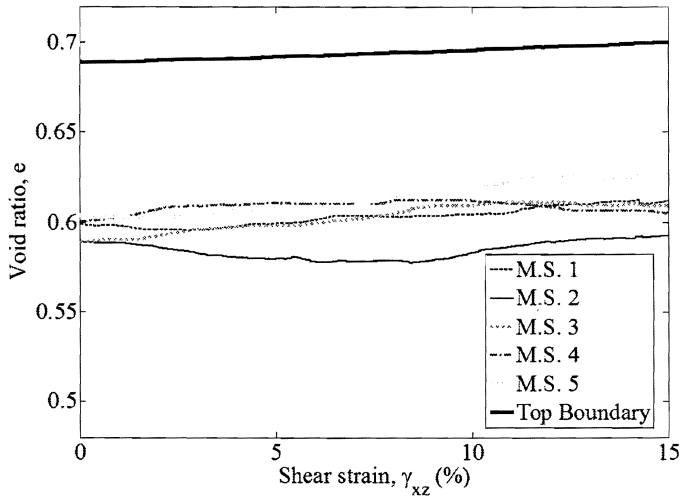

Fig. 6.46. Comparison of void ratio measured from the top boundary location and for various measurement sphere locations throughout sample for ML-100-1

The void ratio measured within the internal portion of the sample is much lower than that measured by the location of the top cap. The sample core measurements are very similar for the samples tested at 50 and 100 kPa vertical effective stress. The scatter in the void ratio values among the five measurement spheres is within a similar range for the two samples. M.S. 2 appears to be the densest in both samples, while M.S. 5 is the loosest zone.

A comparison of stress ratio is also given for the samples. Fig. 6.47 gives the stress ratios with shear strain measured at the boundary and sample core. Fig. 6.48 compares the boundary measured stress ratio with three of the measurement sphere locations for ML-100-1. Only the three measurements spheres located along the x-axis are plotted for clarity.

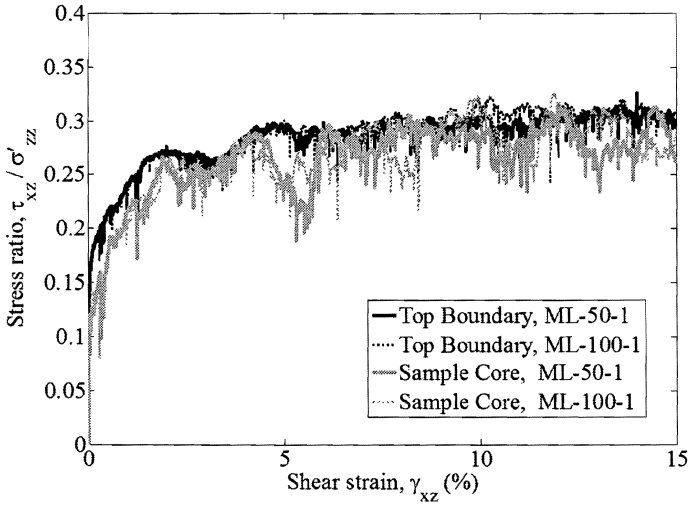

Fig. 6.47. Comparison of stress ratio measured on the top boundary and the sample core for ML-50-1 and ML-100-1

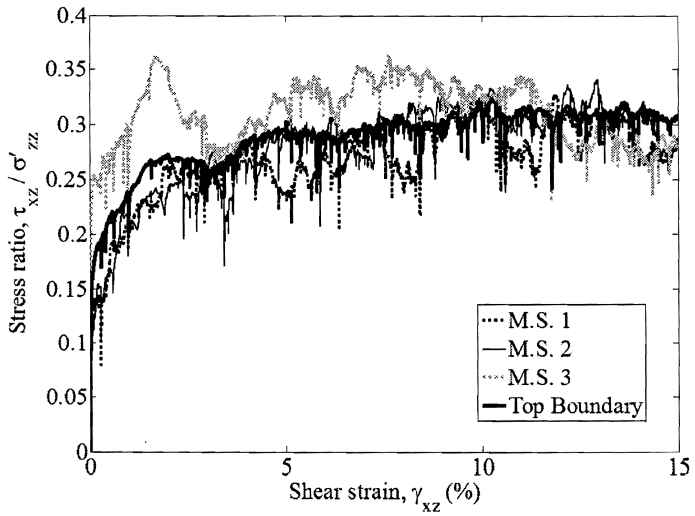

Fig. 6.48. Comparison of stress ratio measured on the top boundary and for various measurement sphere locations throughout sample for ML-100-1

For both samples, the boundary measurement is representative of the internal stresses in the sample core. The curve also follows the expected trend for granular materials tested at different vertical stresses in that the sample tested at the lower vertical stress exhibits a higher stress ratio. M.S. 1 and M.S. 2 plot relatively close to the boundary measured curve. M.S. 3, however, exhibits a significantly higher peak stress ratio and exhibits a higher value for the majority of shearing. This is unexpected, but it does agree with the results for the loose sample tested at 50 kPa (Fig. 6.10). The 50 and 100 kPa samples were prepared with the same file and only differ in the ultimate stress the top cap was lowered to reach. This is most likely the reason why these samples exhibit very similar results.

The stress contours measured on the top boundary cap of ML-100-1 are also similar to the stress contours observed for the 50 kPa sample. Figs. 6.49 and 6.49 show contours of the vertical and shear stress distributions on the top boundary.

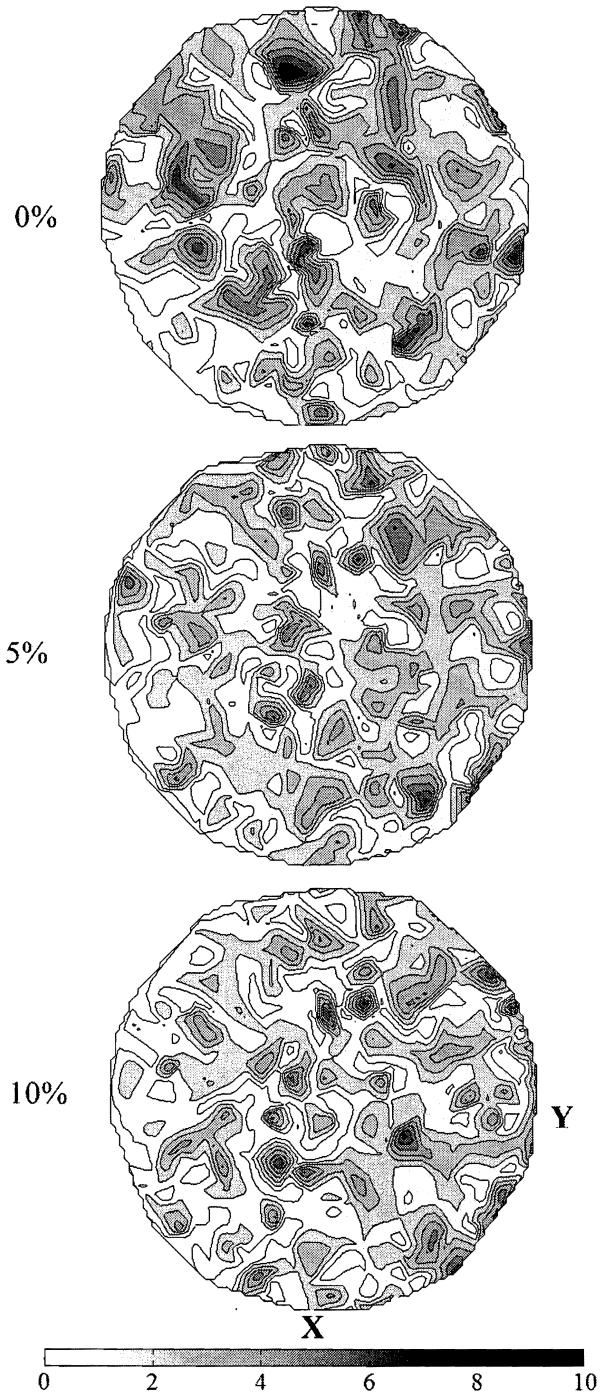

Fig. 6.49. Comparison of ML-100-1 vertical stress distributions on the top boundary for 0, 5, and 10% shear strain

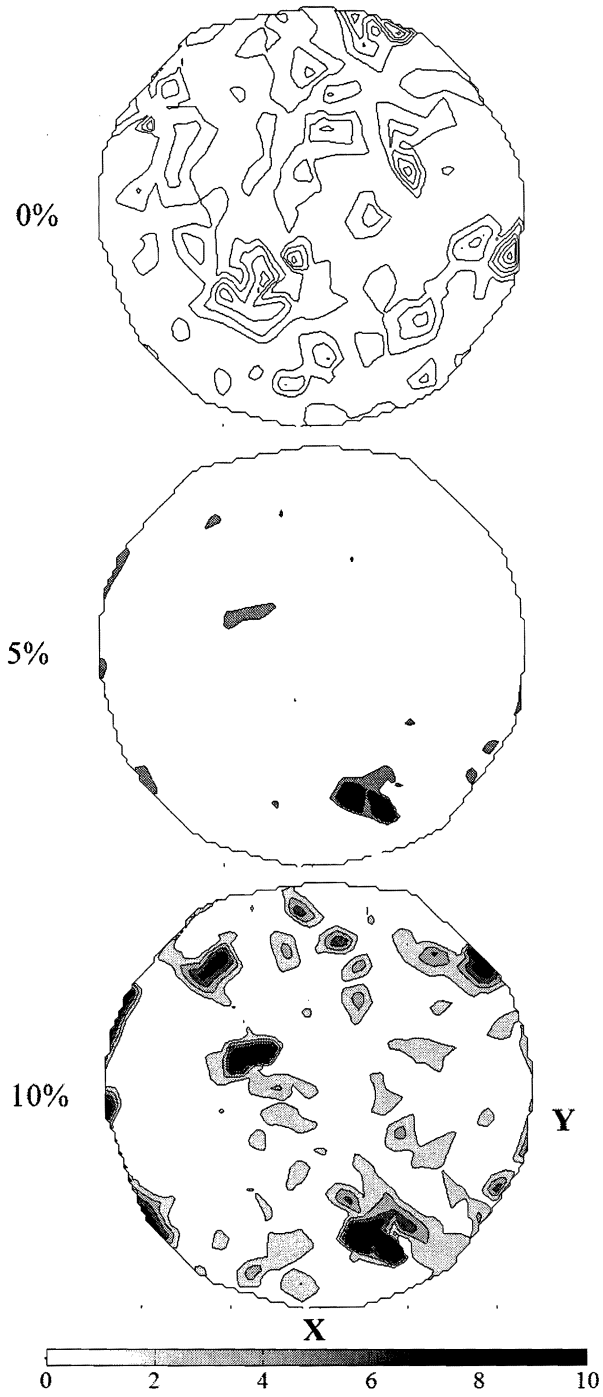

Fig. 6.50. Comparison of ML-100-1 shear stress distributions on the top boundary for 0, 5, and 10% shear strain

One exception is the shear stress at 5% shear strain. The ML-100-1 sample appears to have a small concentration of only a few particles that are carrying the majority of the shear stress. The ML-50-1 sample is much more uniformly distributed (Fig. 6.16). For both samples it appears that the right portion of the sample (the advancing side) has higher concentrations of normal stress, while the left edge carries more of the shear stresses.

The stress paths for the 50 and 100 kPa sample are plotted together in Fig. 6.51. Again, these samples are not at critical state, but the plot shows that the slope of the critical state line is similar for both samples.

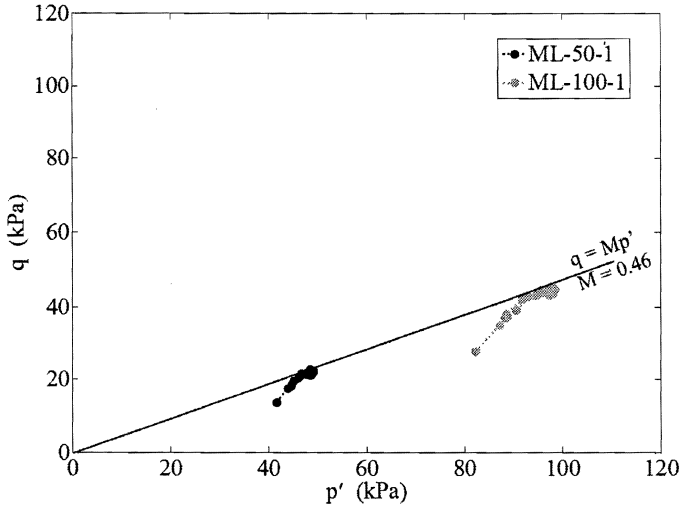

Fig. 6.51. Comparison of stress paths for ML-50-1 and ML-100-1

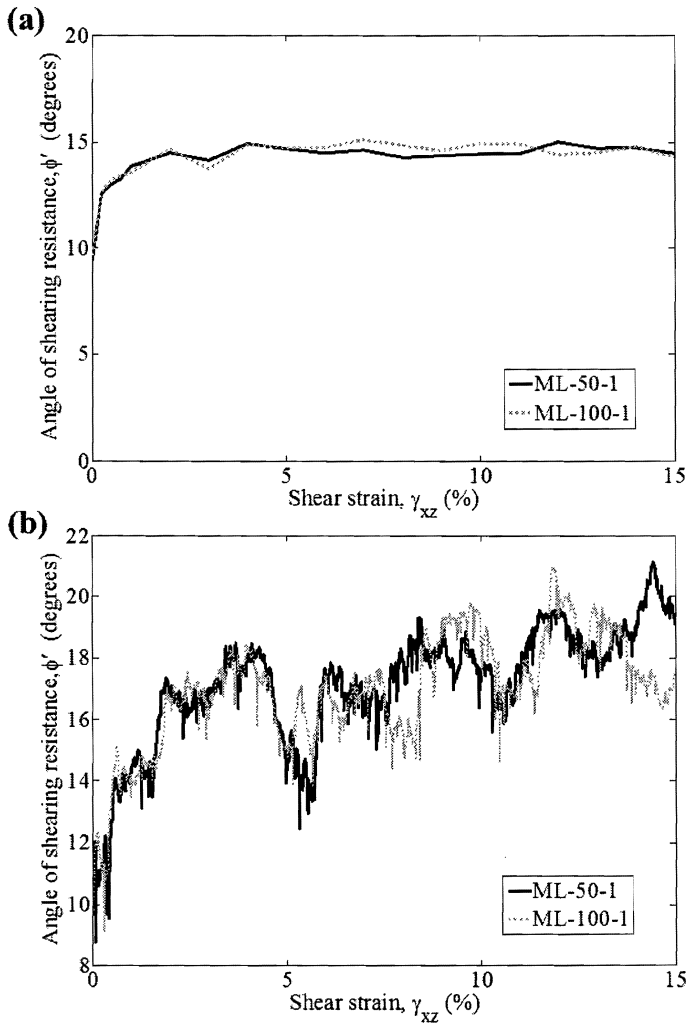

Fig. 6.52. Comparison of angles of shearing resistance for ML-50-1 and ML-100-1 measured for (a) the entire cell and (b) central measurement sphere

Fig. 6.52 shows a comparison of the angle of shearing resistance for the two samples based on measurements taken for the entire cell and for the sample core. Similar plots of the major principal stress orientation (Fig. 6.53) and the angle of non-coaxiality (Fig. 6.54) also show no influence from vertical effective stress.

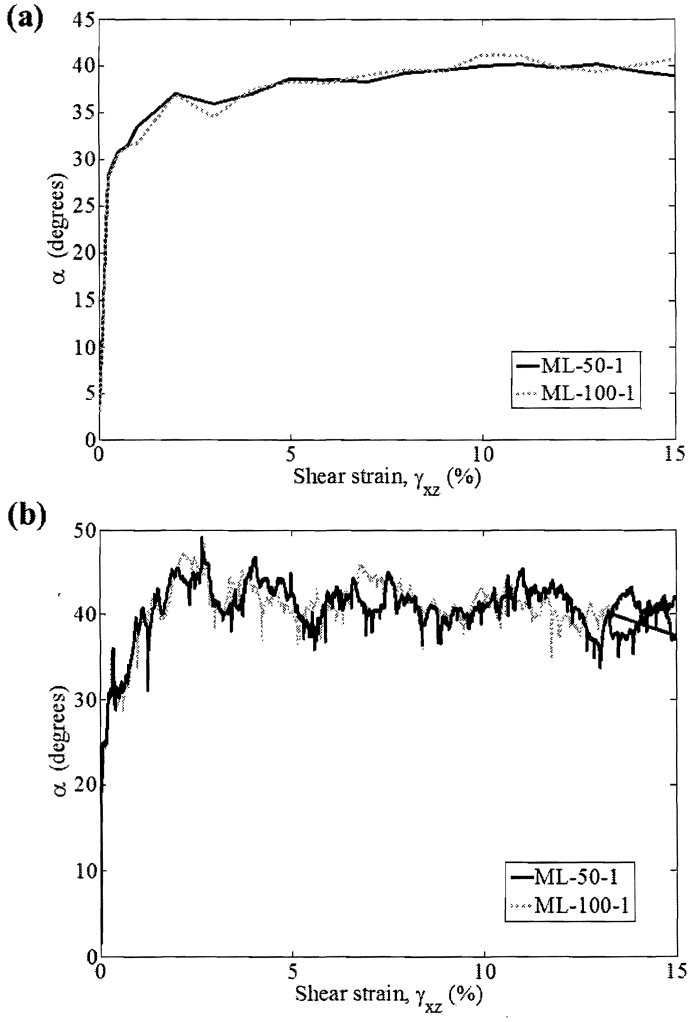

Fig. 6.53. Comparison of major principal stress orientation to the vertical for ML-50-1 and ML-100-1 measured for (a) the entire cell and (b) central measurement sphere

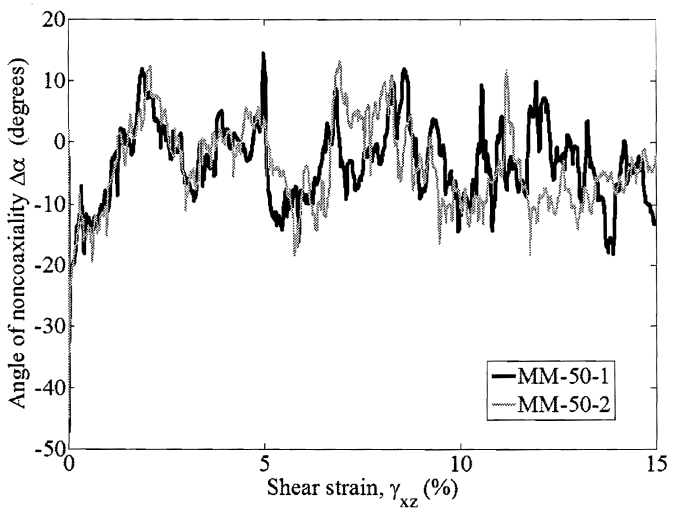

Fig. 6.54. Comparison of angles of non-coaxiality for ML-50-1 and ML-100-1 based on central measurement sphere data

The particle displacements are similar for the two samples. No real differences are observed in the ML-100-1 sample in terms of magnitudes of displacements or scatter (Fig. 6.55 and Fig. 6.25). The non-coaxial behavior can also be seen in the scatter in the y displacement plots.

The fabric of the two samples are compared by plotting the contact force networks, as well as the deviator fabric and the orientation of the major principal fabric. Figs. 6.56 and 6.57 show the contact force networks for the two samples at 5 and 10% shear strain, respectively.

It is somewhat difficult to directly compare the networks because the sample tested at the higher vertical stress naturally has higher magnitude force chains and therefore, thicker lines. It is interesting to see that similar force chains are generated in each sample. This, in turn, shows that the initial fabric created during the sample generation phase strongly influences the way the forces are transmitted during shear-

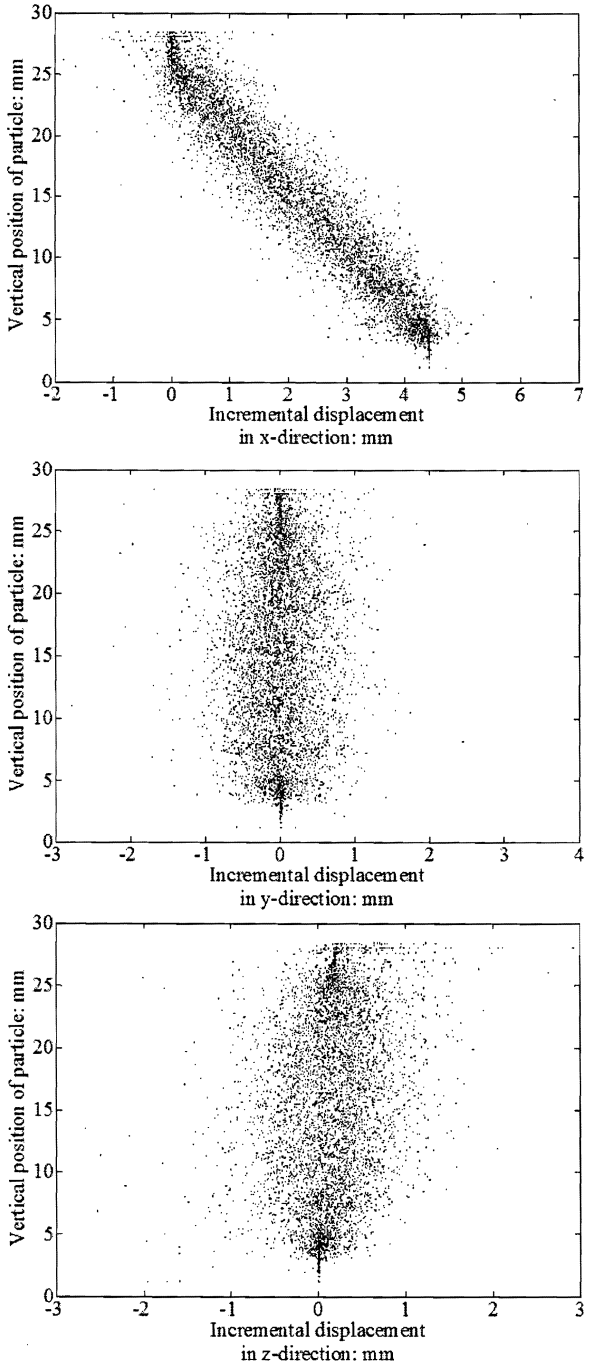

Fig. 6.55. Comparison of x, y, and z particle displacements with height for ML-100-1

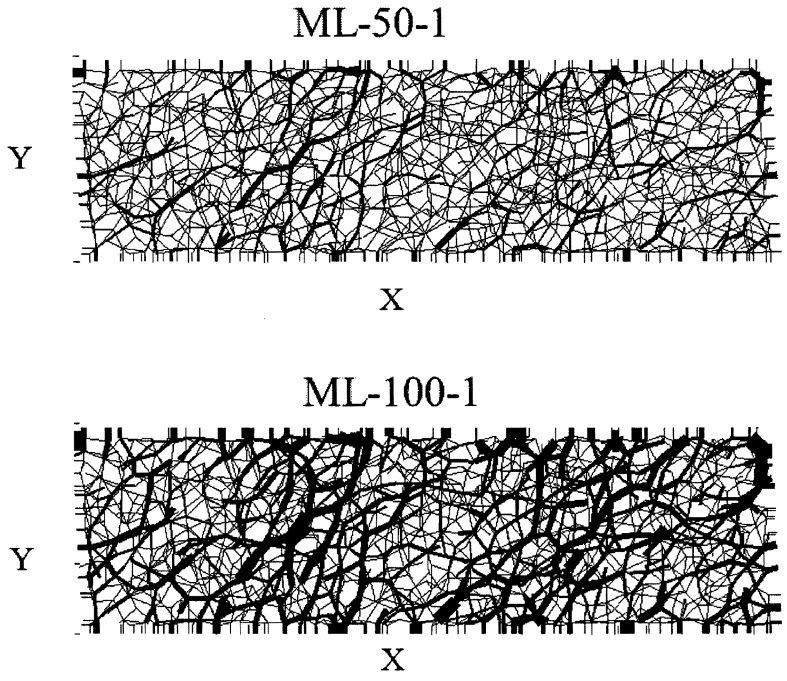

Fig. 6.56. Comparison of contact force networks at 5% shear strain for ML-50-1 and ML-100-1

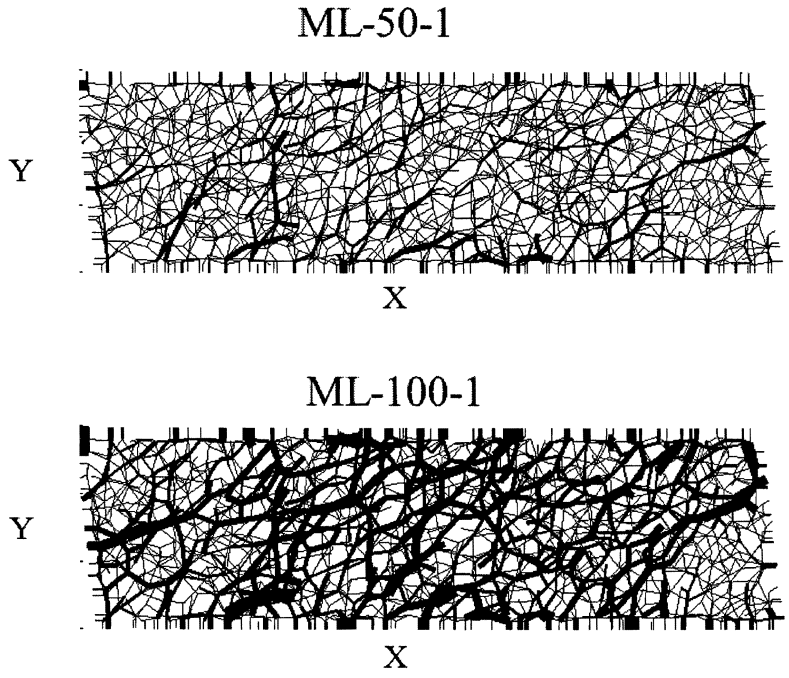

Fig. 6.57. Comparison of contact force networks at 10% shear strain for ML-50-1 and ML-100-1

ing and that vertical effective stress only affects the magnitude of the force chains rather than their development during shearing.

As with the previous samples, the initial coordination numbers in both the ML-50-1 and ML-100-1 drops quickly at very low strains and then is relatively constant for the remainder of shearing (Fig. 6.58). The boundary measurements are also similar for the two samples with the 100 kPa sample having a slightly higher coordination number. Therefore, vertical effective stress only marginally influences the coordination number. The measurement sphere values of coordination number oscillate about the boundary measurement (Fig. 6.59).

The orientation of the major principal fabric and the deviator fabric also appear to be virtually unaffected by the vertical effective stress (Figs. 6.79 and 6.80). Although there are slight differences noted, they are negligible at these stress differences. It should be noted that this is a relatively low range of stresses used to compare vertical stress effects, but was chosen based on laboratory load cell capacity and control.

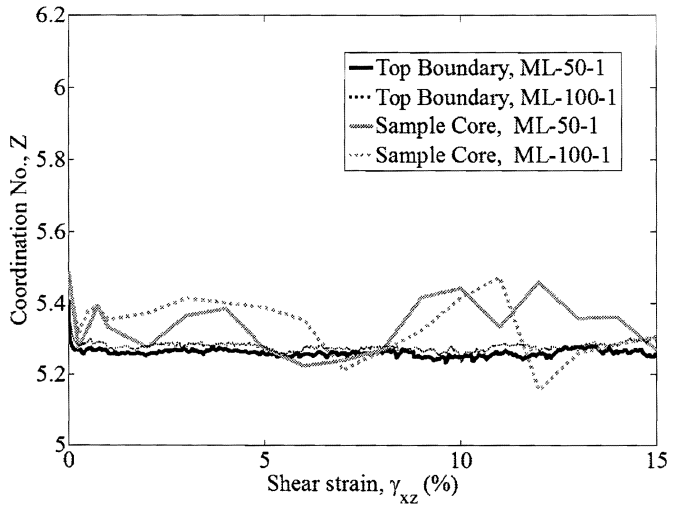

Fig. 6.58. Comparison of coordination number measured for the entire cell and the sample core for ML-50-1 and ML-100-1

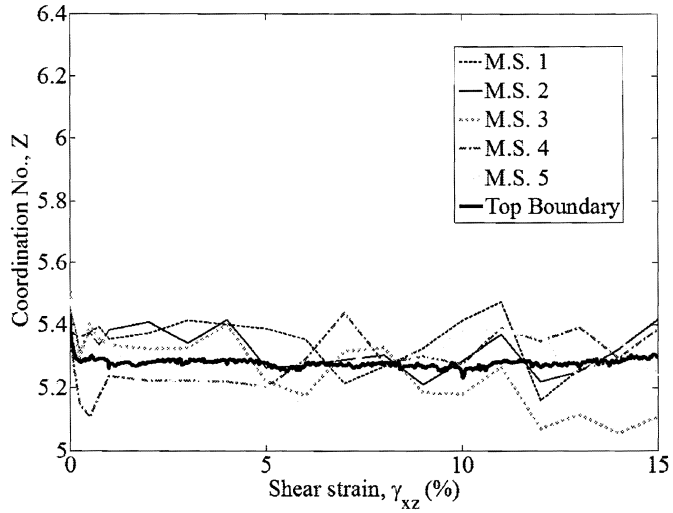

Fig. 6.59. Comparison of coordination number measured for the entire cell and for various measurement sphere locations throughout sample for ML-100-1

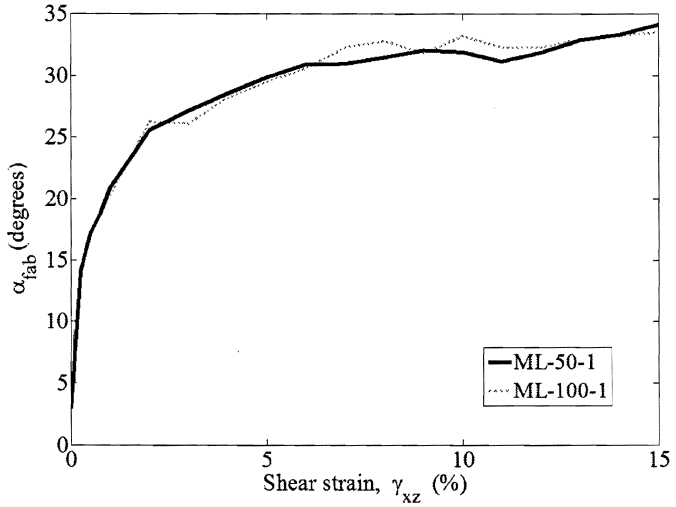

Fig. 6.60. Comparison of major fabric orientation measured for the entire cell for ML-50-1 and ML-100-1

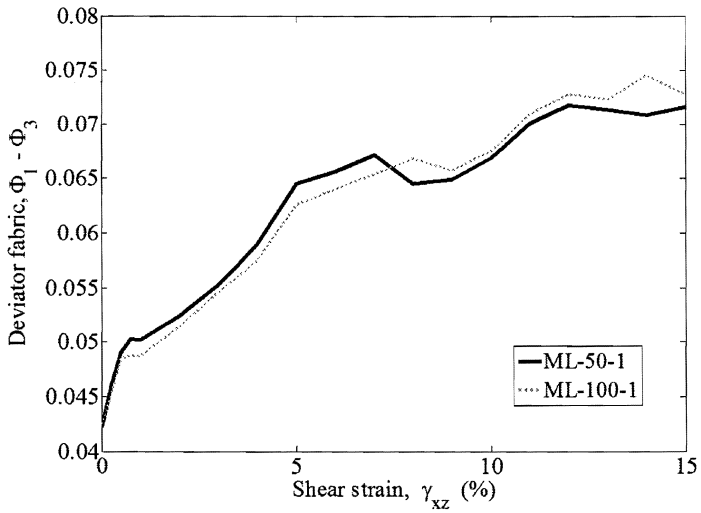

Fig. 6.61. Comparison of deviator fabric measured for the entire cell for ML-50-1 and ML-100-1

6.3 Influence of Number of Particles on Microscopic Response

Several differences in the stress-strain and volumetric responses of the MM-50-1 and MM-50-2 samples were noted in Chapter 4. The void ratios are different for the two samples and cannot be directly compared. The difference in the void ratio calculated using the top cap boundary and the void ratio taken in the sample core is higher for MM-50-1 (Fig. 6.62). While the boundary and core measurements are closer for sample 2, they are still significantly different. The values measured within the five measurement spheres is very similar in the MM-50-2 sample (Fig. 6.63). Very little variation is noted.

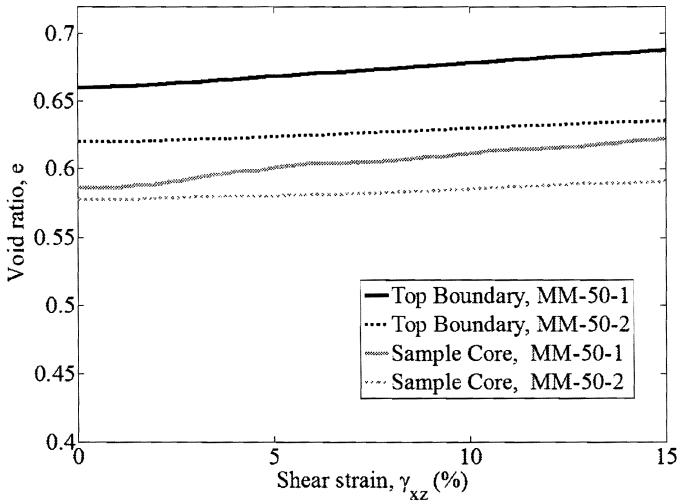

Fig. 6.62. Comparison of void ratios measured from the top boundary location and the sample core for MM-50-1 and MM-50-2

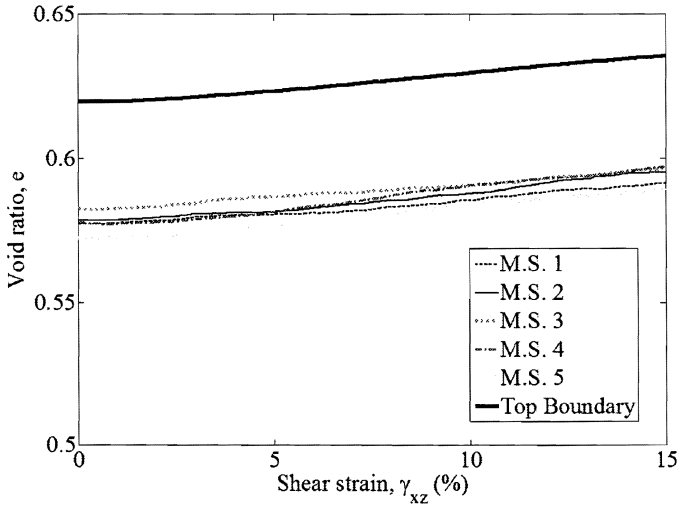

Fig. 6.63. Comparison of void ratio measured from the top boundary location and for various measurement sphere locations throughout sample for MM-50-2

In terms of the stress response, the MM-50-2 sample exhibits a lower overall stress ratio response. While the top boundary underestimates the stress ratio present in the internal sample core for the MM-50-1 sample, the boundary stress ratio overestimates the internal stress ratio response for the MM-50-2 sample. The boundary and sample core measurements are very similar for the two samples. The stress ratios for the MM-50-2 sample measured in the three spheres in Fig. 6.65 are very similar and are slightly less than the boundary value for the majority of shearing. An additional plot of all five measurement spheres (Fig. 6.65) shows that all of the measurement locations fall within a very narrow range of stress ratio values.

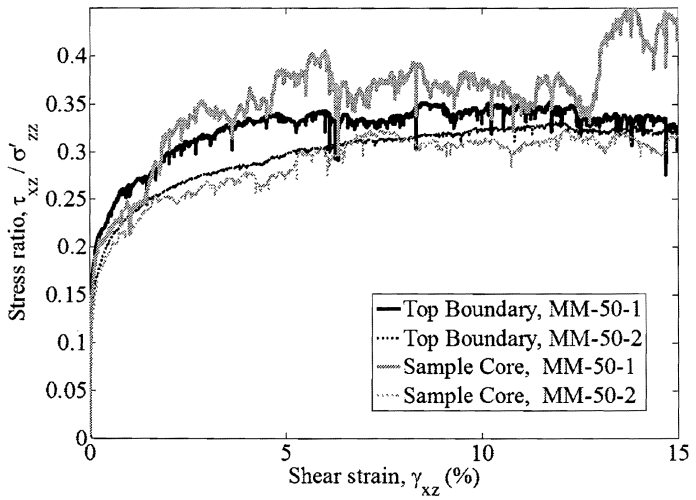

Fig. 6.64. Comparison of stress ratio measured on the top boundary and the sample core for MM-50-1 and MM-50-2

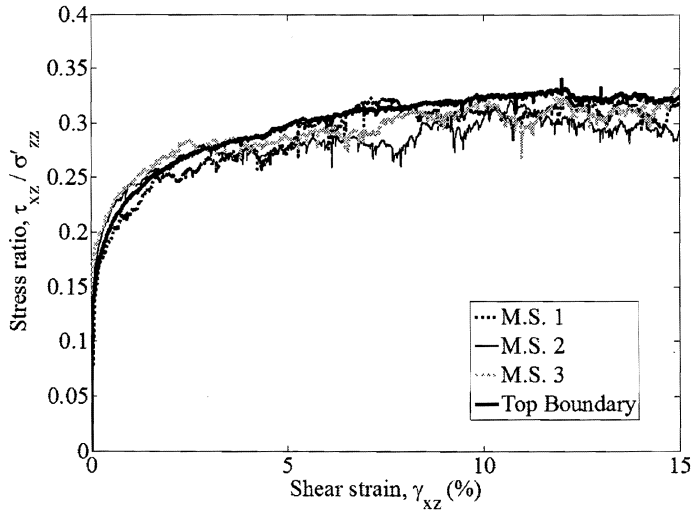

Fig. 6.65. Comparison of stress ratio measured on the top boundary and for three measurement sphere locations along x-axis for MM-50-2

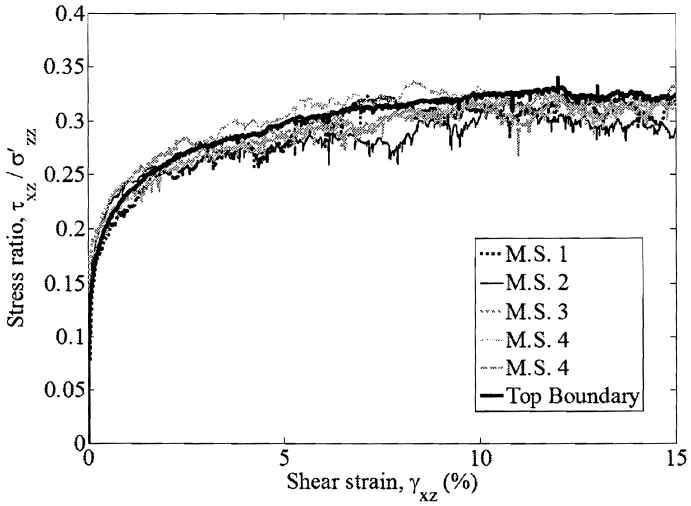

Fig. 6.66. Comparison of stress ratio measured on the top boundary and for all five measurement sphere locations throughout sample for MM-50-2

The stress contours for sample MM-50-1 gave some indication of the of the top boundary stress distributions, but the data was somewhat limited because of the few number of contacts with the top cap. The MM-50-2 sample, comprised of 60,000 particles, had approximately 1,500 particles contacting the top cap whereas the MM-50-1 sample only had 360. The stress contours for sample MM-50-2 are shown in Figs. 6.67 and 6.68.

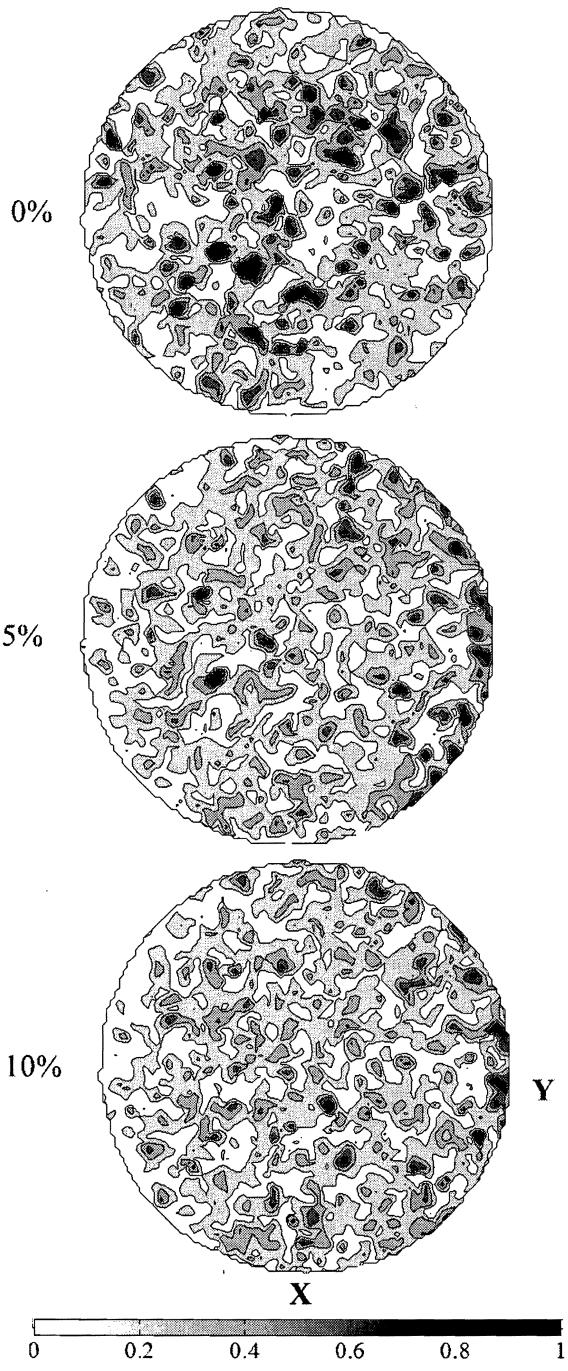

Fig. 6.67. Comparison of MM-50-2 vertical stress distributions on the top boundary for 0, 5, and 10% shear strain

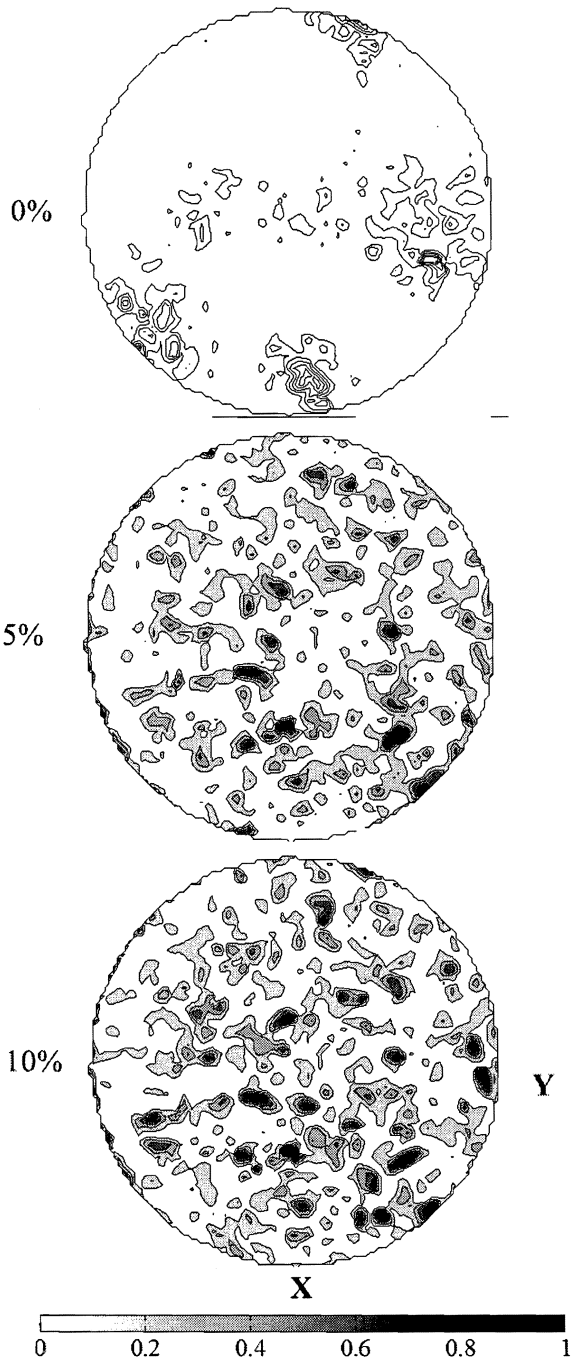

Fig. 6.68. Comparison of MM-50-2 shear stress distributions on the top boundary for 0, 5, and 10% shear strain

The non-uniformities in the vertical stress distribution at 5 and 10% are more clear in the MM-50-2 contour plots. Originally, the higher vertical stresses are evenly distributed within the center of the sample. The right side of the sample sees higher vertical stresses than the left side of the sample. The shear stress distribution is more uniform than for the MM-50-1 sample. There is still a slight concentration of stresses along the left edge of the sample, but the majority of the shear stress is carried by contacts distributed uniformly across the top cap. The stress paths for the two samples are plotted together in Fig. 6.69. The two paths are similar, but have slightly different critical line slopes according to the values up to 15%. As noted previously, these samples are not at critical state.

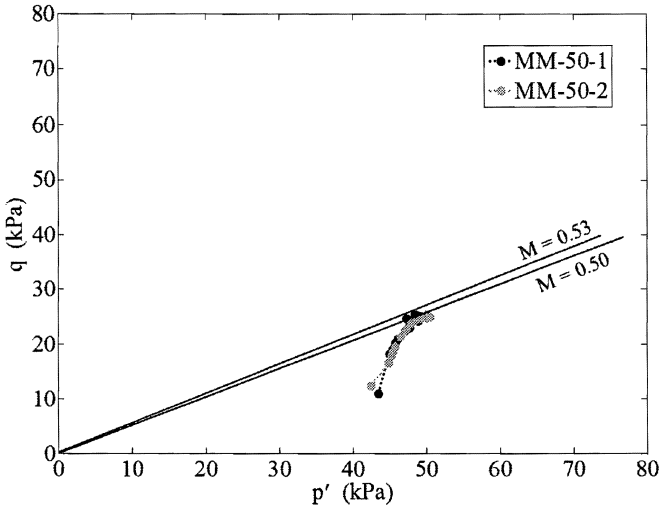

Fig. 6.69. Comparison of stress paths for MM-50-1 and MM-50-2

Fig. 6.70 presents a comparison of the angle of shearing resistance based on measurements for the entire cell and measurements for the sample core. The measurements using the entire sample are similar with only slight differences observed

below 10% shear strain. The peak friction angles are 16.9° and 16.5° for samples MM-50-1 and MM-50-2, respectively.

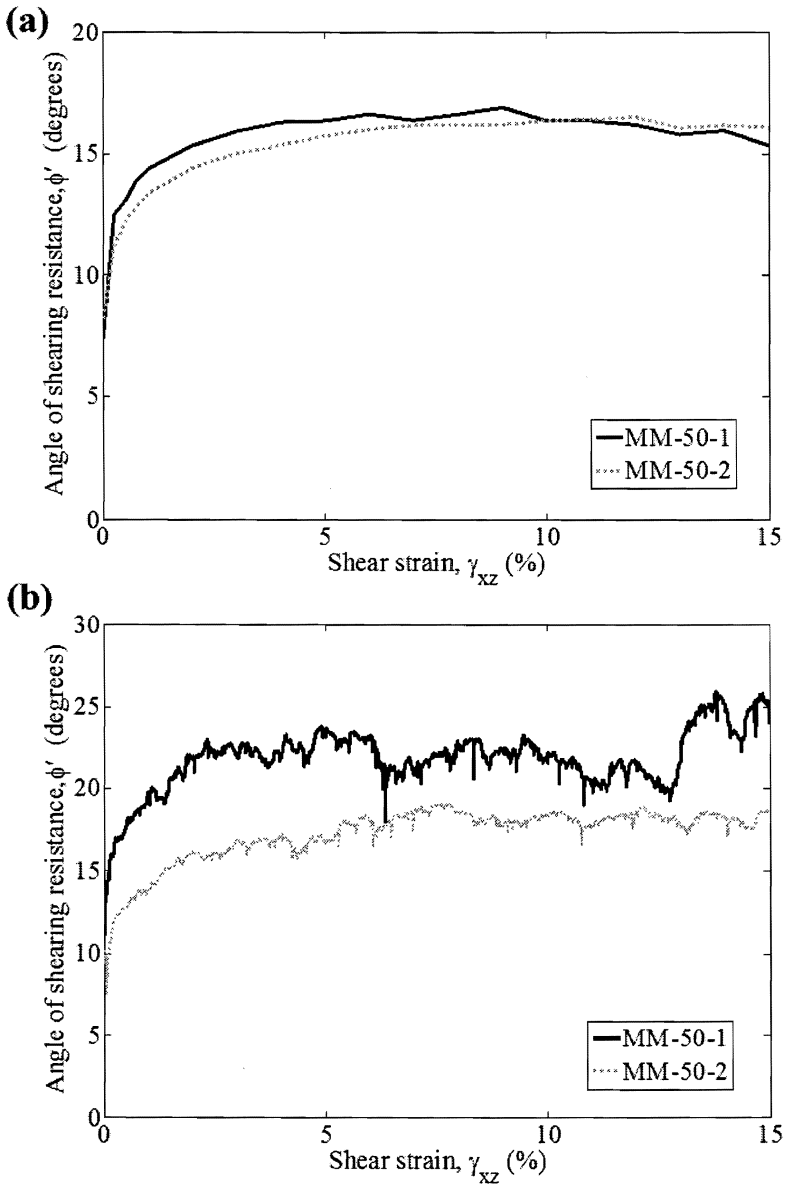

Fig. 6.70. Comparison of angles of shearing resistance for MM-50-1 and MM-50-2 measured for (a) the entire cell and (b) central measurement sphere

The sample core values are substantially different from the two samples. The sample core peak friction angle for the MM-50-2 sample ($\phi' = 19.0$), however, is similar to the values calculated for the entire cell. This indicates that the measurement sphere volume is likely too small to be representative of the actual sample conditions for this parameter. In other words, the values obtained within the measurement spheres are influenced by the size/number of particles within them. A larger number of particles gives an average value which is more representative of the sample as a whole. While the measurement volume effect is more clear for this comparison, it likely influences the measurements of several of the other parameters. It does not appear, however, to influence the angle of the major principal stress orientation (Fig. 6.71) or the angle of non-coaxiality (Fig. 6.72). The values are similar for both measurement types. One exception is for the major principal stress orientation calculated for MM-50-1 above 10%. It is likely that this also influences the angle of non-coaxiality above this strain percentage.

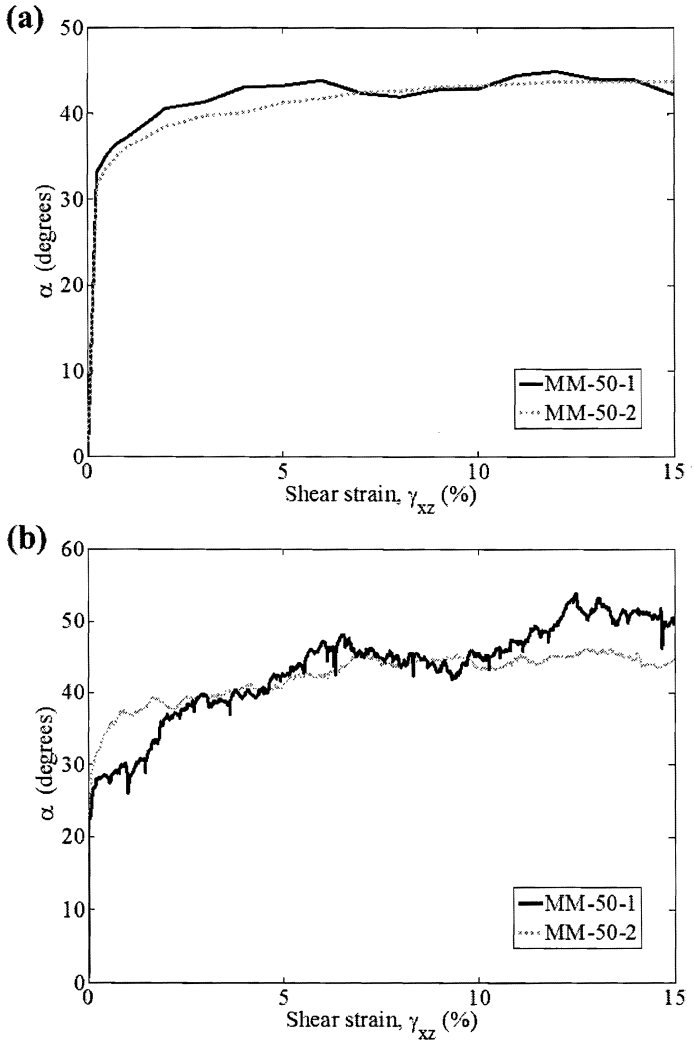

Fig. 6.71. Comparison of major principal stress orientation to the vertical for MM-50-1 and MM-50-2 measured for (a) the entire cell and (b) central measurement sphere

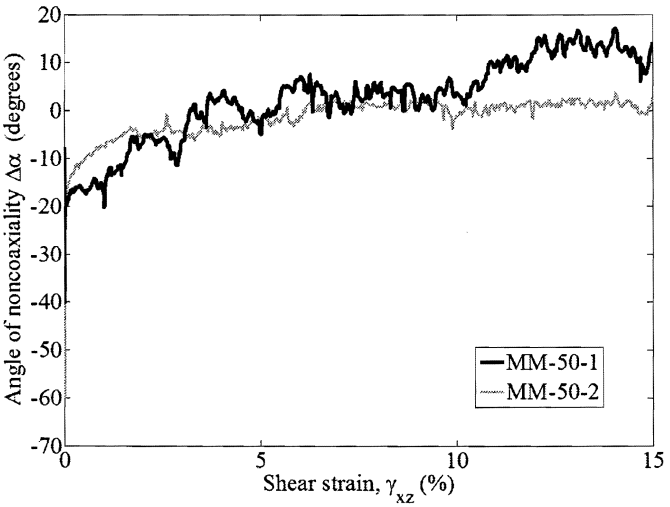

Fig. 6.72. Comparison of angles of non-coaxiality for MM-50-1 and MM-50-2 based on central measurement sphere data

It is clear that the major principal stress and the major principal strain rate are non-coincident at the beginning of the test. Based on the MM-50-2 sample data, the axes become aligned at approximately 7% shear strain and remain aligned for the remainder of shearing.

Fig. 6.73 shows the particle displacements in three directions plotted versus their initial vertical location. The x displacements show a more "curved" response than what was observed for the sample type of plot for MM-50-1. The central portion of the sample is still a linear type response as expected. The sections joining the central core and the glued particles on the boundary, however, plot as a curve. This agrees with the deformation fields from experiments with plasticene presented by Finn et al. (1971). Finn showed that the actual boundary conditions do not agree with the simple shear strain assumption causing distortions along the sample sides (Fig. 6.74).

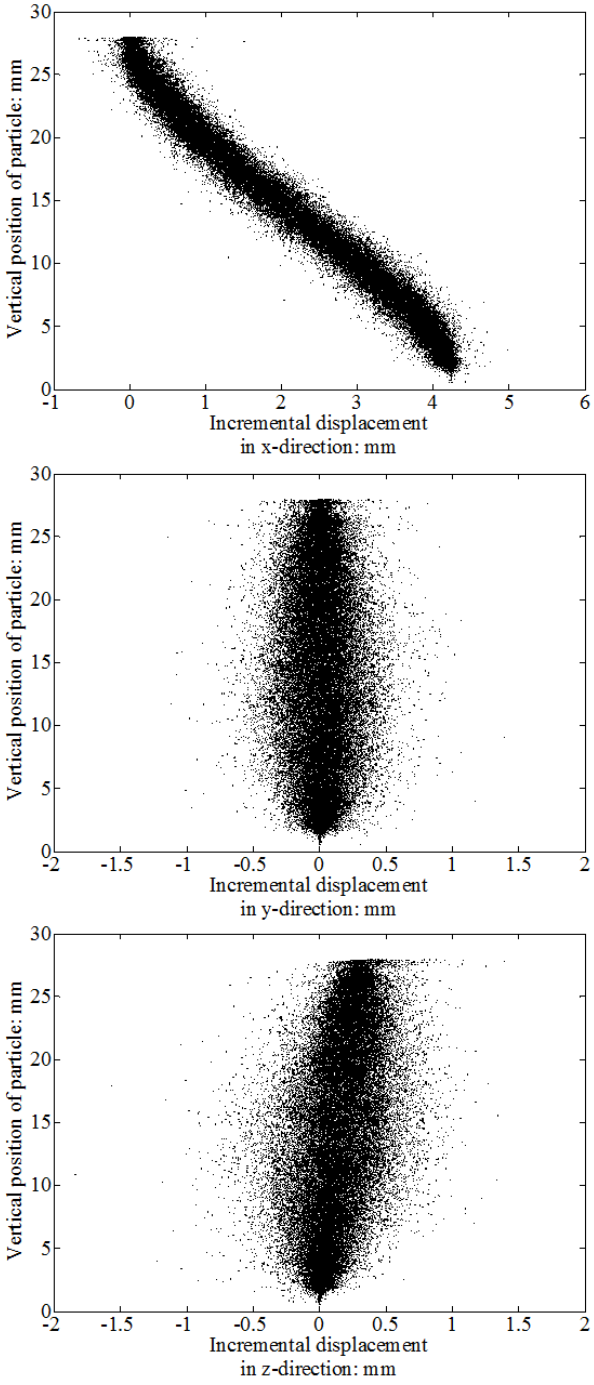

Fig. 6.73. Comparison of x, y, and z particle displacements with height for MM-50-2

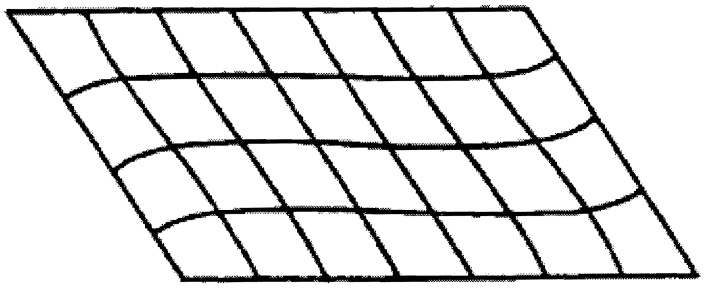

Fig. 6.74. Deformation field schematic in simple shear experiments on plasticene

In terms of fabric for the two samples, the coordination number for the MM-50-2 sample is higher than that of the MM-50-1 sample (Fig. 6.75). The measurement sphere values shown in Fig. 6.76 are more representative of the entire sample for the MM-50-2 sample.

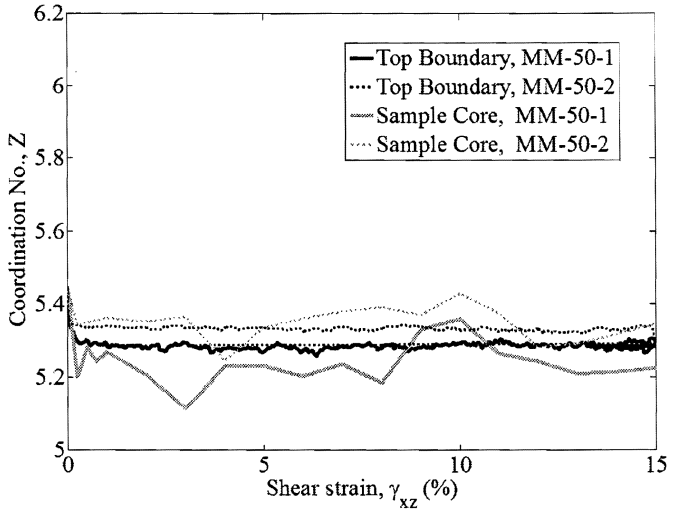

Fig. 6.75. Comparison of coordination number measured for the entire cell and the sample core for MM-50-1 and MM-50-2

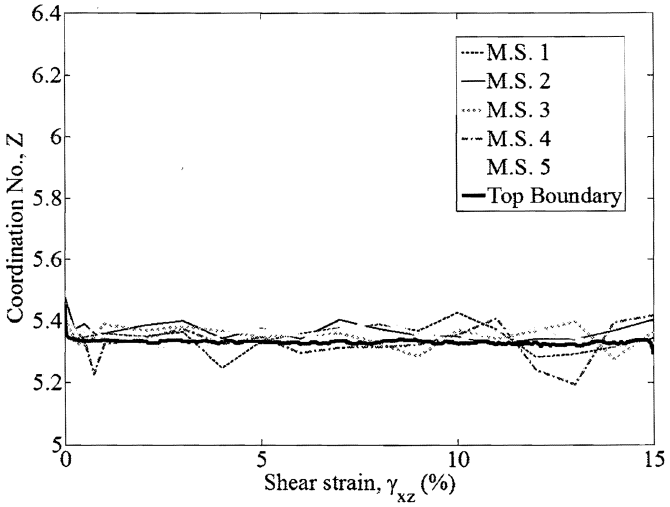

Fig. 6.76. Comparison of coordination number measured for the entire cell and for various measurement sphere locations throughout sample for MM-50-2

The contact network plots for samples MM-50-1 and MM-50-2 at 5 and 10% shear strain are given in Figs. 6.77 and 6.78.

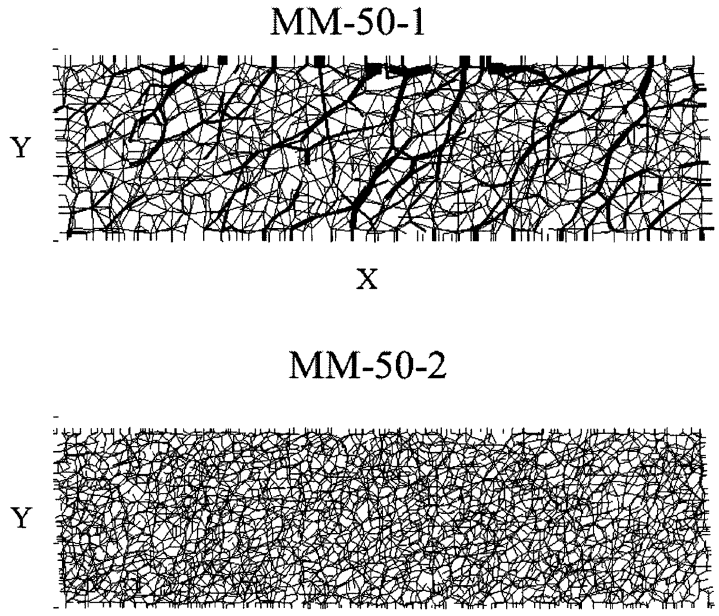

Fig. 6.77. Comparison of contact force networks at 5% shear strain for MM-50-1 and MM-50-2

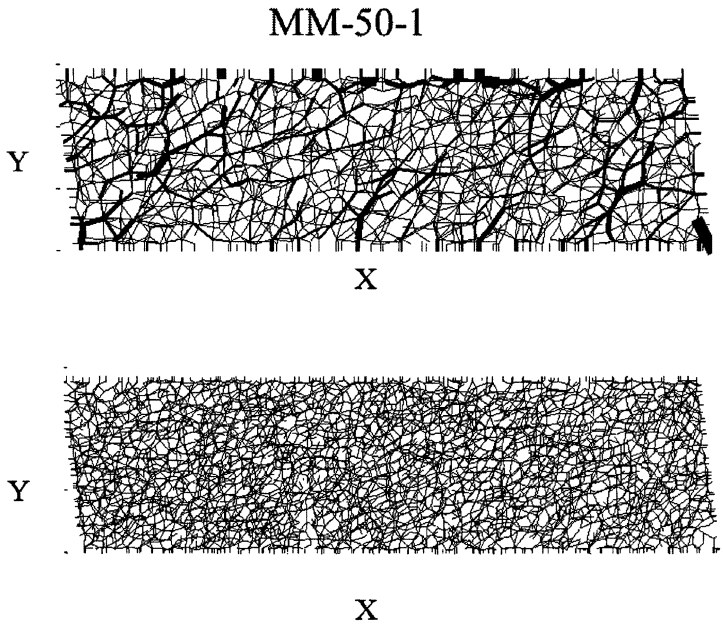

Fig. 6.78. Comparison of contact force networks at 10% shear strain for MM-50-1 and MM-50-2

For the ease of viewing, the sample 2 contact force networks are shown for a smaller slice through the center of the sample and only consider contacts that are larger than the average contact force value. For the 5% and 10% plots, the MM-50-2 network has many more contacts and less strong force chains than the MM-50-1 sample. In other words, the stresses are more uniformly distributed throughout the sample and the collapse of a single force chain is not as likely to disrupt the sample. This gives indication to why the sample 2 tests are much more stable during shearing.

The orientation of the major principal fabric is similar for the two samples up to approximately 6% shear strain, at which point the MM-50-2 angle continues to gradually rise and the MM-50-1 value drops slightly. At 15% shear strain the orientation angles differ by approximately 5°. In terms of the deviator fabric, the

MM-50-1 sample is slightly higher than the MM-50-2 sample. Both samples follow a similar trend as shearing progresses.

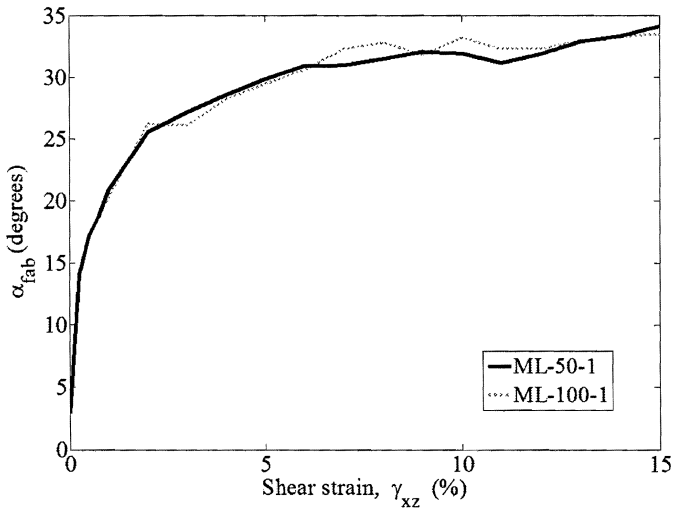

Fig. 6.79. Comparison of coordination number measured for the entire cell and the sample core for ML-50-1 and ML-100-1

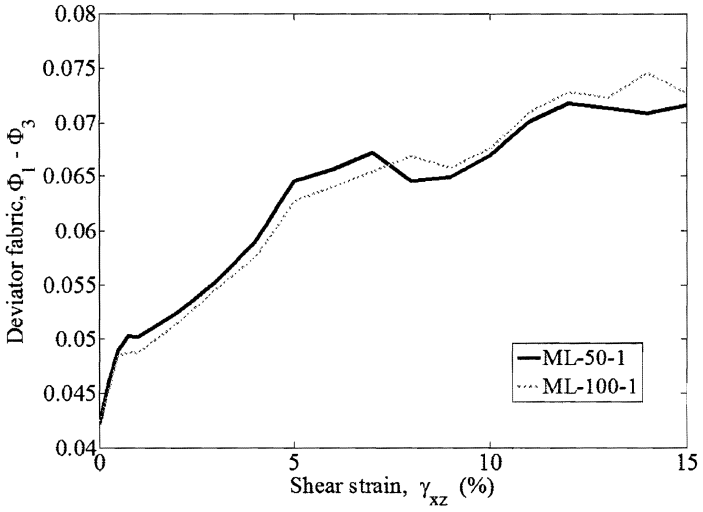

Fig. 6.80. Comparison of coordination number measured for the entire cell and for various measurement sphere locations throughout sample for ML-100-1

6.4 Conclusions

Many of the trends observed in the macro-scale laboratory and DEM results are also reflected in the microscopic responses. The boundary stress measurements appear to underestimate the internal stresses significantly in the sample 1 tests; however, it is also possible that these measurements are influenced by the particle size and measurement sphere volume. The sample 2 stress measurements are very similar for the two measurement types. Differences in the measured values for several other parameters were observed in the MM-50-2 sample, indicating actual differences in the response rather than the measurement precision. It is recommended to conduct additional studies to simulate a number of other testing conditions using sample 2.

7. CONCLUSIONS AND FUTURE WORK

7.1 Conclusions

While simple shear has been studied in the past using Discrete element method (DEM) models, this study represents the first time that laboratory validated three-dimensional DEM simulations have been used to study the behavior of granular soils in the laminar-type devices. This research showed that the DEM simulations could be successfully validated by laboratory data and that the the overall trends observed agreed with the experimental data from this study, as well as previous studies by other researchers. There were several differences in the DEM and laboratory responses which limited the validation to only a portion of the curve, most notably the differences in initial stiffness. Several attempts were made, both in the laboratory and in the DEM models, to assess possible causes for the disagreement in initial stiffness. While some differences were noticed for the linear and Hertzian contact models, neither model matched the initial portion of the curve obtained in the laboratory. The DEM simulations did agree well with the laboratory response at higher strain levels, capturing the expected granular soil behavior. Volumetric differences were also noted for the DEM and laboratory samples and no clear explanation was derived to explain these differences. Also, it is most likely that due to roughening of the surface during repeated shearing, the interparticle friction of the current assembly is higher than the original tested particles. Overall, the laboratory response and DEM simulation response agreed reasonably well for the various test conditions.

The major findings from this work come from the micro-scale information obtained from the validated DEM simulations. As noted by previous researchers, the internal sample core measurements were higher for many of the parameters than

what was measured on the boundary. Boundary measurements underestimate the internals stresses, as well as the density of the majority of the sample. The size of the measurement sphere compared to the size of the particles also plays an important role in the values obtained. The 60,000 particle sample had internal measurements which were more representative of the entire sample due to the fact that a larger number of particles were contained within the measurement volume and provided a better average value. When the entire sample was used for calculations, however, the values obtained were similar for sample 1 (7,500 particles) and sample 2 (60,000 particles) tests. One advantage of using DEM is the ability to obtain localized measurements throughout the sample. The measurement spheres also allowed observation of the spatial distribution and variability of several of the parameters. It is clear that the right side of the sample, or the zone advancing in the direction of shearing, sees different conditions in terms of packing and stress levels than the trailing zone. Stress contours also showed slightly non-uniform conditions across the top cap.

Several factors have shown to contribute to both the macro- and micro-scale responses of granular materials. Density not only influences shear strength of a sample, it also affects the angle of shearing resistance, the magnitude of principal stress rotation, the angle of non-coaxiality, and the orientation of the principal fabrics for strains below those needed to reach critical state. Vertical effective stress on the other hand, has very little influence on these parameters. The initial fabric appears to play a greater role in the behavior of samples tested at different vertical stresses.

For each of the simulations, the non-coaxial behavior of the granular samples was observed. The major principal strain rates lagged behind the rotation of the major principal stress during the initial shearing. This non-coaxiality was also shown in the displacement plots. Scatter in the y-displacements shows that particles not only dilate to move across one another, they also move horizontally around one

another.

Overall, the DEM simulation data has provided additional understanding and explanation of the observed macro-scale response. This research provided a beginning look into the three-dimensional response of the laminar-type direct simple shear apparatus. Future work is needed to fine-tune the DEM models and further examine the influence of the various testing/modeling conditions on the microscopic response.

7.2 Future Work

Although the findings show that DEM can successfully capture the stress response of granular simple shear behavior, the volumetric responses were quite different for the laboratory and DEM samples. Only dilative samples were created in the DEM simulations, while even the densest laboratory samples showed some initial contraction. Further work is needed to better understand sample preparation within DEM and the corresponding initial state obtained.

Also, several of the modeling simplifications used in this research have shown to influence the macro-scale response and should be included in future simulations. These simplifications were implemented in the initial prototype simulations because of computational time constraints; however, including them in future simulations will give a more accurate representation of the observed laboratory response. Sensitivity studies showed that the wall friction coefficient affected the overall stress response. Future simulations should include wall friction, or further studies should be conducted to assess the overall influence.

In terms of macro-scale response, the 7,500 and 60,000 particle samples behaved similarly. The response for the 60,000 particle sample was much less sensitive when compared to the 7,500 particle sample. Observations of the micro-scale information were also more representative of the actual sample conditions for the 60,000 particle

sample. It is recommended that further studies be conducted on sample 2 at the various testing conditions. This will likely give a better indication of the sample conditions present in a smaller particle size sand sample.

As mentioned previously, true field conditions are extremely complex. Understanding the monotonic behavior of granular materials is an important first step in the overall goal of understanding granular behavior under cyclic and multi-directional simple shear loading. Slight adjustments and further validation of the simulations presented in this dissertation will allow for future simulations to consider more complex loading schemes. The microscopic information gained from this study, as well as future similar studies will aid in the development and verification of future DEM and constitutive models.

REFERENCES

Acheampong, K. B. (1996). "Evaluation of discrete element analysis for the mechanics of granular assemblies." Ph.D. Thesis, University of Massachusetts, Amherst.

Airey, D., Budhu, M., and Wood, D. (1985). "Some aspects of the behaviour of soils in simple shear." *Developments in soil mechanics and foundation engineering: Vol. 2: Stress-strain modeling of soils*, P. K. In Banerjee and R. Butterfield, eds., Elsevier, London, UK, Chapter 6, 185–213.

Airey, D. and Wood, D. (1987). "An evaluation of direct simple shear tests on clay." *Géotechnique*, 37(1), 25–35.

Amer, M. I., Kovacs, W. D., and Aggour, M. S. (1987). "Cyclic simple shear size effects." *J. Geotech. Eng.*, 113(7), 693–707.

Ansell, P. and Brown, S. F. (1978). "A cyclic simple shear apparatus for dry granular materials." *Geotech. Test. J.*, 1(2), 82–92.

Arthur, J. R. F., Al-Ani, Q. H. J. L., Dunstan, T., and Assadi, A. (1977a). "Plastic deformation and failure in granular media." *Géotechnique*, 27 (1), 53–74.

Arthur, J. R. F., Chua, K. S., and Dunstan, T. (1977b). "Induced anisotropy in a sand." *Géotechnique*, 27, 13–30.

Arthur, J. R. F., Koenders, M. A., and Wong, R. K. S. (1986). "Anisotropy in particle contacts associated with shearing in granular media." *Acta Mech.*, 64, 20–29.

Arthur, J. R. F. and Menzies, B. (1972). "Inherent anisotropy in a sand." *Géotechnique*, 22, 115–128.

Arthur, J. R. F., Rodriguez, J. D. C., Chua, K. S., and Dunstan, T. (1980). "Principal stress rotation: a missing parameter." *J. Geotech. Eng.*, 106, 419–433.

Assadi, A. (1975). "Rupture layers in granular materials." Ph.D. Thesis, University

of London.

Bagi, K. (2005). "An algorithm to generate random dense arrangements for discrete element simulations of granular assemblies." *Granul. Matter*, 7, 3143.

Bashir, Y. and Goddard, J. (1991). "A novel simulation method for the quasi-static mechanics of granular assemblages." *J. Rheol.*, 35(5), 849–885.

Bassett, R. H. (1967). "The behaviour of granular materials in the simple shear apparatus." Ph.D. Thesis, University of Cambridge.

Bathurst, R. J. and Rothenburg, L. (1989). "Investigation of micromechanical features of idealized granular assemblies using dem." *In Proceedings of 1st U.S. Conference on Discrete Element Methods, Golden, CO.*

Bjerrum, L. and Landva, A. (1966). "Direct simple shear test on a Norwegian quick clay." *Géotechnique*, 16(1), 1–20.

Bolton, M. D. (1986). "The strength and dilatancy of sands." *Géotechnique*, 36 (1), 65–78.

Bolton, M. D., Nakata, Y., and Cheng, Y. P. (2008). "Micro- and macro-mechanical behavior of dem crushable materials." *Géotechnique*, 58 (6), 471–480.

Boulanger, R. W. (1990). "Liquefaction behavior of saturated cohesionless soils subjected to uni-directional and bi-directional static and cyclic loads." Ph.D. Thesis, University of California, Berkeley.

Boulanger, R. W., Chan, C. K., Seed, H. B., Seed, R. B., and Sousa, J. (1993). "A low compliance bi-directional cyclic simple shear apparatus." *Geotech. Test. J.*, 16(1), 36–45.

Boulanger, R. W. and Seed, R. B. (1995). "Liquefaction of sand under bi-directional monotonic and cyclic loading." *J. Geotech. Eng.*, 121 (12), 870–878.

Budhu, M. (1979). "Simple shear deformation of sands." Ph.D. Thesis, University of Cambridge.

Budhu, M. (1984a). "Nonuniformities imposed by simple shear apparatus." *Can. Geotech. J.*, 20, 125–137.

Budhu, M. (1984b). "On comparing simple shear and triaxial test results." *J. Geotech. Eng.*, 110 (12), 1809–1814.

Budhu, M. (1985). "Lateral stresses observed in the simple shear apparatus." *J. Geotech. Eng.*, 111(6), 698–711.

Budhu, M. (1988). "Failure state of a sand in simple shear." *Can. Geotech. J.*, 25, 395–400.

Budhu, M. and Britto, A. (1987). "Numerical analysis of soils in simple shear devices." *Soils Found.*, 29(2), 31–41.

Cai, Y. (2010). "An experimental study of non-coaxial soil behavior using hollow cylinder testing." Ph.D. Thesis, The University of Nottingham.

Casagrande, A. (1976). "Liquefaction and cyclic deformation of sands - a critical review. proc. of the 5th Pan Amarican conf. on soil mechanics and foundation engineering." *Harvard soil mechanics series No. 88.*

Cavarretta, I., Rocchi, I., and Coop, M. R. (2011). "A new interparticle friction apparatus for granular materials." *Can. Geotech. J.*, 48, 1829–1840.

Cheung, G. and O'Sullivan, C. (2008). "Effective simulation of flexible lateral boundaries in two- and three-dimentional dem simulations." *Particuology*, 6, 483–500.

Christian, J. T. (1981). "Discussion of 'state of the art: laboratory strength testing of soils',." *Laboratory Shear Strength of Soil, ASTM STP 740*, R. N. Yong and F. C. Townsend, eds., American Society for Testing and Materials, 638–640.

Cole, E. R. (1967). "The behaviour of soils in the simple-shear apparatus." Ph.D. Thesis, University of Cambridge.

Cornforth, D. H. (1964). "Some experiments on the influence of strain conditions on the strength of sand." *Géotechnique*, 14 (2), 143–167.

Cui, L. (2002). "Developing a virtual test environment for granular materials using discrete element modeling." Ph.D. Thesis, University College Dublin.

Cui, L. and O'Sullivan, C. (2006). "Exploring the macro- and micro-scale response of an idealized granular material in the direct shear apparatus." *Géotechnique*, 56, 455–468.

Cui, L., O'Sullivan, C., and O'Neil, S. (2007). "An analysis of the triaxial apparatus using a mixed boundary three-dimentional discrete element model." *Géotechnique*, 57(10), 831–844.

Cundall, P. (1971). "A computer model for simulating progressive large scale movements in blocky rock systems." *Proc. ISRM Symp., Nancy, France*, Vol. 2, 129–136.

Cundall, P. (2001). "A discontinuous future for numerical modelling in geomechanics? geotech. eng. proc. of the institution of civil engineers." 149(1), 41–47.

Cundall, P., Drescher, A., and Strack, O. (1982). "Numerical experiments on granular assemblies: measurements and observations." *IUTAM Conference on Deformation and Failure of Granular Materials*, 355–370.

Cundall, P. and Strack, O. (1978). "The distinct element methods as a tool for research in granular media, part 1." *Report no.*, Report to NSF.

Cundall, P. and Strack, O. (1979). "A discrete numerical model for granular assemblies." *Géotechnique*, 29(1), 47–65.

Dabeet, A., Wijewickreme, D., and Byrne, P. M. (2011). "Discrete element modeling of direct simple shear response of granular soils and model validation using laboratory element tests." *Proc. 2011 Pan-Am CGS Geotechnical Conference*, Canadian Geotechnical Society.

Dafalias, Y. F., Papadimitriou, A. G., and Li, X. S. (2004). "Sand plasticity model accounting for inherent fabric anisotropy." *J. Eng. Mech.*, 130 (11), 1319–1333.

Davis, E. H. (1968). *Theories of plasticity and the failure of soil masses.* Soil Me-

chanics: Special Topics. Butterworth, London, 1 edition.

de Josselin de Jong (1968). "Discussion proceedings of geotechnical conference, oslo." Vol. 2, 199–200.

de Josselin de Jong, G. (1971). "The double sliding, free rotating model for granular assemblies." *Géotechnique*, 21, 155–162.

de Josselin de Jong, G. and Verrujit, A. (1969). "Etude photo-elastique d'un empilement de disques." *Cah. Grpe fr. Etud. Rheol.*, 2, 73–86.

DeGroot, D. J. (1989). "The multidirection direct simple shear apparatus with application of design to offshore artic structures." Ph.D. Thesis, Massachusetts Institute of Technology.

DeGroot, D. J., Ladd, C. C., and Germaine, J. T. (1996). "Undrained multidirectional direct simple shear behavior of cohesive soil." *J. Geotech. Eng.*, 122(2), 91–98.

Dounias, G. T. and Potts, D. M. (1993). "Numerical analysis of drained direct and simple shear tests." *J. Geotech. Eng.*, 119 (12), 1870–1891.

Drescher, A. and de Josselin de Jong, G. (1972). "Photoelastic verification of a mechanical model for the flow of a granular material." *J. Mech. Phys. Solids*, 20, 337–351.

Duncan, J. M. and Dunlop, P. (1969). "Behavior of soils in simple shear. proc. 7th icsmfe, mexico.

Feng, Y. T., Han, K., and Owen, D. (2003). "Filling domains with disks: an advancing front approach." *Int. J. for Numer. Meth. Eng.*, 56(5), 699–731.

Finn, W. D. L., Pickering, D. J., and Bransby, P. L. (1971). "Sand liquefaction in triaxial and simple shear tests." *J. Soil Mech. Found. Div.*, SM4, 639–659.

Franke, E., Kiekbusch, M., and Schuppener, B. (1979). "A new direct simple shear device." *Geotech. Test. J.*, 2(4), 190–199.

Graton, L. C. and Fraser, H. J. (1935). "The systematic packing of spheres; with particular relation to porosity and permeability." *J. Geol.*, 43, 785–909.

Gutierrez, M. (1989). "Behavior of sand during rotation of principal stress directions." Ph.D. Thesis, Tokyo University.

Gutierrez, M., Ishihara, K., and Towhata, I. (1991). "Flow theory for sand during rotation of principal stress direction." *Soils Found.*, 31, 121–132.

Gutierrez, M., Ishihara, K., and Towhata, I. (1993). "Flow theory for sand during rotation of principal stress direction." *SoilsFound.*, 31 (4), 121–132.

Gutierrez, M., Wang, J., and Yoshimine, M. (2009). "Modeling of the simple shear deformation of sand: effects of principal stress rotation." *Acta Geotech.*, 4, 193–201.

Hight, D. W., Gens, A., and Symes, M. J. (1983). "The development of a new hollow cylinder apparatus for investigating the effects of principal rotation in soils." *Géotechnique*, 33 (4), 355–383.

Idriss, I. M. and Boulanger, R. W. (2007). *Earthquake Geotechnical Engineering: SPT- and CPT-based relationships for the residual shear strength of liquefied soils.* Springer.

Ishihara, K. and Yamazaki, F. (1980). "Cyclic simple shear tests on saturated sand in multi-directional loading." *Soils Found.*, 20(1), 45–59.

Itasca (2004). *PFC2D 3.10 Particle Flow Code in Two Dimensions, Theory and Background volume.* Minneapolis, Minnesota, third edition.

Itasca (2008). *PFC3D 4.0 Particle Flow Code in Three Dimensions, Theory and Implementation Volume.* Minneapolis, Minnesota.

James, R. G. and Bransby, P. L. (1970). "Experimental and theoretical investigations of a passive earth pressure problem." *Géotechnique*, 20 (1), 17–37.

Jardine, J. R. and Menkiti, C. O. (1999). "The undrained anisotropy of ko consoli-

dated sediments." *Proc. ECSMGE, Amsterdam, The Netherlands.*

Jefferies, M. and Been, K. (2006). *Soil Liquefaction: A Critical State Approach.* Taylor and Francis, New York, NY.

Jiang, M., Konrad, J., and Leroueil, S. (2003). "An efficient technique for generating homogeneous specimens for dem studies." *Comput. Geotech.*, 30, 579–597.

Jiang, M. J. and Yu, H. S. (2006). *Application of the discrete element method to modern geomechanics.* Modern Trends in Geomechanics. Springer.

Joer, H. A., Lanier, J., and Fahey, M. (1998). "Deformation of granular materials due to rotation of principal axes." *Géotechnique*, 48, 605–618.

Kammerer, A. (2002). "Undrained response of cohesionless soils under multi-directional cyclic simple shear conditions." Ph.D. Thesis, University of California, Berkeley.

Kim, Y. S. (2009). "Static simple shear characteristics of nak-dong river clean sand." *KSCE J. Civ. Eng.*, 13 (6), 389–401.

Kishino, Y. (1999). *Mechanics of Granular Materials: An Introduction.* A. A. Balkema, Brookfield, VT, USA, Chapter Physical and mathematical backgrounds, 149–155.

Kjellman, W. (1951). "Testing the shear strength of clay in sweden." *Géotechnique*, 2(3), 225–232.

Kolbuszewski, J. (1965). "Sand particles and their density. Lecture delivered at Materials Science Club Symposium, London. Cited from Stroud (1971).

Kozicki, J. and Donze, F. V. (2008). "A new open-source software developed for numerical simulations using discrete modelling methods." *Comput. Method Appl. M.*, 197, 4429–4443.

Lacasse, S., Dyvik, R., and Hoeg, K. (1988). "Discussion on the behavior of normally consolidated clay as observed in undrained direct shear tests by wroth (1987)."

Géotechnique, 38 (1), 144–146.

Lacasse, S. and Vucetic, M. (1981). "Discussion of 'state of the art: laboratory strength testing of soils',." *Laboratory Shear Strength of Soil, ASTM STP 740*, R. N. Yong and F. C. Townsend, eds., American Society for Testing and Materials.

Ladd, R. (1978). "Preparing test specimens using undercompaction." *Geotech. Test. J.*, 1 (1), 16–23.

Ladd, R. S. (1974). "Specimen preparation and liquefaction of sands." *J. Soil Mech. Found. Div. ASCE*, 100 (GT10), 1180–1184.

Lade, P. V. (1975). "Torsion shear test on cohesionless soil." *Proc., 5th Panamerican Conf. on Soil Mech. and Found. Engrg.*

Lade, P. V. and Duncan, J. M. (1973). "Cubical triaxial tests on cohesionless soils." *J. Soil Mech. Found. Div. ASCE*, 99 No. SM10, 793–812.

Lade, P. V., Nam, J., and Hong, W. P. (2008). "Shear banding and cross-anisotropic behavior observed in laboratory sand tests with stress rotation." *Can. Geotech. J.*, 45 (1), 74–84.

LaRochelle, P. (1981). "Limitations of direct simple shear test devices." *Laboratory Shear Strength of Soil, ASTM*, STP 740, 653–658.

Lashkari, A. and Latifi, M. (2007). "A simple plasticity model for prediction of non-coaxial flow of sand." *Mech. Res. Commun.*, 34, 191–200.

Li, X. and Yu, H. (2010). "Numerical investigation of granular material behaviour under rotational shear." *Géotechnique*, 60(5), 381–394.

Li, X. and Yu, H. S. (2009). "Influence of loading direction on the behavior of anisotropic granular materials." *Int. J. Eng. Sci.*, 47, 1284–1296.

Lucks, A., Christian, J., Brandow, G., and Hoeg, K. (1972). "Stress conditions in NGI simple shear test." *J. Soil Mech. Found. Div.*, 98(SMI), 155–160.

Macky, T. A. and Saada, A. S. (1984). "Dynamics of anisotropic clays under large

strain." *J. Geotech. Eng.*, 110 (4), 487–504.

Malek, A. M. (1987). "Cyclic behavior of clay in undrained simple shearing and application to offshore tension piles." Ph.D. Thesis, MIT.

Marketos, G. and Bolton, M. D. (2010). "Flat boundaries and their effect on sand testing." *Int. J. Numer. Anal. Meth. Geomech.*, 34, 821–837.

Masson, S. and Martinez, J. (2001). "Micromechanical analysis of the shear behavior of a granular material." *J. Eng. Mech.*, 127(10), 1007–1016.

Matsuoka, H., Sakakibara, K., and Suzuki, Y. (1988). "A constitutive model for granular materials evaluating principal stress rotation." *Micromechanics of Granular Materials*, 287–296.

McGuire, S. T. (2011). "Comparison of direct simple shear confinement methods on clay and silt specimens." M.S. Thesis, University of Rhode Island.

Menkiti, C. O. (1995). "Behaviour of clay and clayey-sand with particular reference to principal stress rotation." M.S. Thesis, Imperial College of Science, Technology and Medicine, University of London.

Miura, K., Miura, S., and Toki, S. (1986). "Deformation behavior of anisotropic sand under principal stress axes rotation." *Soils Found.*, 26 (1), 36–52.

Mulilis, J. P., Seed, H. B., Chan, C. K., Mitchell, J. K., and Arulanandan, K. (1977). "Effects of sample preparation on sand liquefaction." *J. Geotech. Eng.*, 103(GT2), 91–108.

Nakata, Y., Hyodo, M., and Murata, H. (1998). "Flow deformation of sands subjected to principal stress rotation." *Soils Found.*, 38 (2), 115–128.

Nemat-Nasser, S. and Tobita, Y. (1982). "Influence of fabric on liquefaction and densification potential of cohesionless sand." *Mech. Mater.*, 1(1), 43–62.

Ng, K. K. and Donald, I. B. (1988). "A hydraulic servo-controlled cyclic simple shear device." *Proceedings Fifth Austrailia-New Zealand Conference on Geomechanics.*

Ng, T. T. (1989). "Numerical simulation of granular soils under montonic and cyclic loading: A particulate mechanics approach." Ph.D. Thesis, Rensselaer Polytechnic Institute.

Ng, T.-T. (2004). "Shear strength of assemblies of ellipsoidal particles." *Géotechnique*, 54(10), 659–670.

Ng, T. T. and Dobry, R. (1994). "Numerical simulations of monotonic and cyclic loading of granular soil." *J. Geotech. Eng.*, 120(2), 388–403.

Oda, M. (1972). "Initial fabrics and their relations to mechanical properties of granular materials." *Soils Found.*, 1, 17–36.

Oda, M. and Konishi, J. (1974). "Microscopic deformation mechanism of granular materials in simple shear." *Soils Found.*, 14, 25–38.

Ohsaki, Y. (1969). "The effects of local soil conditions upon earthquake damage." *Proc. of Specialty Session 2, 7th International Conference on Soil Mechanics and Foundation Engineering, Mexico City.*

Osinov, V. A. and Wu, W. (2006). "Simple shear in sand with an anisotropic hypoplastic model." *Geomech. Geoeng.*, 1 (1), 43–50.

O'Sullivan, C. (2002). "The application of discrete element modelling to finite deformation problems in geomechanics." Ph.D. thesis, University of California, Berkeley.

O'Sullivan, C. (2011). *Particulate Discrete Element Modeling.* Spoon Press/Taylor & Francis, New York, NY.

O'Sullivan, C., Bray, J., and Riemer, M. (2004). "An examination of the response of regularly packed specimens of spherical particles using physical tests and discrete element simulations.." *ASCE J. Eng. Mech.*, 130(10), 1140–1150.

O'Sullivan, C., Bray, J. D., and Riemer, M. F. (2002). "The influence of particle shape and surface friction variability on macroscopic frictional strength of rod-shaped

particulate media." *Journal of Engineering Mechanics*, 128(11), 1182–1192.

O'Sullivan, C., Cui, L., and O'Neil, S. (2008). "Discrete element analysis of the response of granular materials during cyclic loading." *Soils Found.*, 48, 511–530.

Parikh, P. V. (1967). "The shearing behavior of sand under axisymmetric loading." Ph.D. Thesis, University of Manchester.

Peacock, W. H. and Seed, H. B. (1968). "Sand liquefaction under cyclic loading simple shear conditions." *J. Soil Mech. Found. Div.*, 94 (SM3), 689–708.

Potyondy, D. O. and Cundall, P. A. (2004). "A bonded-particle model for rock." *Int. J. Rock Mech. Min.*, 41(8), 1329–1364.

Powrie, W., Ni, Q., Harkness, R. M., and Zhang, X. (2005). "Numerical modelling of plane strain tests on sands using a particulate approach." *Géotechnique*, 55(4), 297–306.

Prevost, J. H. and Hoeg, K. (1976). "Reanalysis of simple shear soil testing." *Can. Geotech. J.*, 13 (4), 418–429.

Pyke, R. M. (1973). "Settlement and liquefaction of sands under multi-directional loading." Ph.D. Thesis, University of California, Berkeley.

Pyke, R. M., Chan, C. K., and Seed, H. B. (1974). "Settlement and liquefaction of sands under multi-directional shaking." *Report No. 74-2*, University of California, Berkeley.

Randolph, M. F. and Wroth, C. P. (1981). "Application of the failure state in undrained simple shear to the shaft capacity of driven piles." *Géotechnique*, 31 (1), 143–157.

Roscoe, K. (1953). "An apparatus for the application of simple shear to soil samples." *Proc. of the 3rd Int. Conf. in Soil Mechanics and Foundation Engineering.*

Roscoe, K. (1970). "The influence of strains in soil mechanics." *Géotechnique*, 20, 129–170.

Roscoe, K., Bassett, R. H., and Cole, E. R. (1967). "Principal axes observed during simple shear of a sand." *Proc. of the Geotechnical Conference on Shear Strength Properties of Natural Soils and Rocks, Oslo*, 231–237.

Roscoe, K., Schofield, A. N., and Wroth, C. P. (1958). "On the yielding of soils." *Géotechnique*, 8 (1), 22–53.

Rothenburg, L. and Kruyt, N. (2004). "Critical state and evolution of coordination number in simulated granular materials." *Int. J. Solids Struct.*, 41, 5763–5774.

Rowe, P. (1962). "The stress-dilatancy relation for static equilibrium of an assembly of particles in contact.." *Proc. of the Royal Society of London. Series A, Mathematical and Physical Sciences*, 269(1339), 500–527.

Rowe, P. W. and Peaker, K. (1965). "Passive earth pressure measurement." *Géotechnique*, 15 (1), 57.

Rutherford, C. J. (2012). "Development of a multi-directional simple shear testing device for characterization of the cyclic shear response of marine clay." Ph.D. Thesis, Texas A&M University.

Saada, A. S. and Baah, A. K. (1967). "Deformation and failure of a cross anisotropic clay under combined stresses." *Proc. 3rd Panamerican Conf. on Soil Mech. and Found. Engrg.*

Saada, A. S., Fries, G., and Ker, C. C. (1983). "An evaluation of laboratory testing techniques in soil mechanics." *J. Geotech. Eng.*, 123(3), 379–398.

Saada, A. S. and Macky, T. A. (1985). "Integrated testing and properties of a Gulf of Mexico clay." *Strength Testing on Marine Sediments: Laboratory and In-situ Measurements, ASTM*, STP 883, 363–380.

Saada, A. S. and Townsend, F. C. (1981). *State of the art: laboratory strenth testing of soils. Laboratory shear strength of soil.* American Society for Testing and Materials, Baltimore, MD.

Sadrekarimi, A. and Olson, S. M. (2012). "Effect of sample-preparation method on critical-state behavior of sands." *Geotech. Test. J.*, 35 (4), 1–15.

Salot, C., Gotteland, P., and Villard, P. (2009). "Influence of relative density on granular materials behavior: DEM simulations of triaxial tests." *Granul. Matter*, 11(4), 221–236.

Satake, M. (1982). "Fabric tensor in granular materials." *Proc. IUTAM Symp. on Deformation and Failure of Granular Materials*, P. Vermeer and H. Luger, eds., A.A. Balkema, 63–68.

Sayão, A. and Vaid (1996). "Effect of intermediate principal stress on the deformation response of sand." *Can. Geotech. J.*, 33, 822–828.

Seed, H. B. (1979). "Soil liquefaction and cyclic mobility evaluation for level ground during earthquakes." *J. Geotech. Eng. Div.*, 105 (2), 201–255.

Seed, H. B. and Silver, M. L. (1972). "Settlement of dry sand during earthquakes." *Proceedings ASCE*, 98 (SM4).

Shaw, P. and Brown, S. F. (1986). "Cyclic simple shear testing of granular materials." *Geotech. Test. J.*, 9 (4), 213–220.

Shen, C. K. (2013). "A micromechanical investigation of drained simple shear tests on dense sand using discrete element simulations." Ph.D. Thesis, Imperial College London.

Shen, C.-K., O'Sullivan, C., and Jardine, R. (2010). "A michromechanical investigation of drained simple shear tests." *Proc. of Int. Symp. on Deformation Characteristics of Geomaterials*, Seoul, Korea.

Shen, C. K., Sadigh, K., and Herrmann, L. R. (1978). "An analysis of ngi simple shear apparatus for cyclic load testing." *Dynamic Geotechnical Testing, ASTM STP 654, ASTM International*, West Conshohocken, PA, 148–162.

Shibuya, S. and Hight, D. W. (1987). "A bounding surface for granular materials."

Soils Found., 27 (4), 123–136.

Sitharam, T. G., Vinod, J. S., and Ravishankar, B. V. (2009). "Post-liquefaction undrained monotonic behaviour of sands: experiments and dem simulations." *Géotechnique*, 59 (9), 739749.

Stroud, M. (1971). "The behavior of sand at low stress levels in the simple shear apparatus." Ph.D. Thesis, University of Cambridge.

Symes, M. J., Gens, A., and Hight, D. W. (1984). "Undrained anisotropy and principal stress rotation in saturated sand." *Géotechnique*, 34 (1), 11–27.

Symes, M. J., Gens, A., and Hight, D. W. (1988). "Drained principal stress rotation in saturated sand." *Géotechnique*, 38 (1), 59–81.

Symes, M. J., Hight, D. W., and Gens, A. (1982). "Investigating anisotropy and the effects of principal stress rotation and of the intermediate principal stress using a hollow cyclinder apparatus." *IU-TAM Conference on Deformation and Failure of Granular Materials, Delft*, 441–449.

Talesnick, M. and Frydman, S. (1991). "Simple shear of an undisturbed soft marine class in NGI and torsional shear equipment." *Geotech. Test. J.*, 14 (2), 180–194.

Tatsuoka, F. and Hara, K. (1987). "Undrained shear strength of clay by torsional shear test." *Proc., 8th Asian Regional Conference on Soil Mechanics and Foundation Engineering.*

Tatsuoka, F., Pradhan, T. B. S., and Yoshi-ie, H. (1989). "A cyclic undrained simple shear testing method for soils." *Geotech. Test. J.*, 12 (4), 268–280.

Thomas, P. (1997). "Discontinuous deformation analysis of particulate media.." Ph.D. thesis, University of California, Berkeley.

Thornton, C. (1979). "The conditions for failure of a face-centered cubic array of uniform rigid spheres." *Géotechnique*, 29 (4), 441–459.

Thornton, C. (1997). "Force transmission in granular media." *KONA Powder Part.*

J., 15, 81–90.

Thornton, C. (2000). "Numerical simulations of deviatoric shear deformation of granular media." *Géotechnique*, 50 (1), 43–53.

Thornton, C. and Antony, S. (1998). "Quasi-static deformation of particulate media." *Phil. Trans. R. Soc. Lond. A*, 356, 2763–2782.

Thornton, C. and Antony, S. (2000). "Quasi-static shear deformation of a soft particle system." *Powder Technol.*, 109, 179–191.

Thornton, C. and Lanier, J. (1997). "Uniaxial compression of granular media: numerical simulations and physical experiments." *Powders and Grains*, 97, 223–227.

Thornton, C. and Sun, G. (1993). "Axisymmetric compression of 3d polydisperse systems of spheres." *Powders and Grains*, 93, 129–134.

Thornton, C. and Zhang, L. (2001). "A DEM comparison of different shear testing devices." *Powders and Grains 01*, Y. Kishino, ed., Rotterdam, The Netherlands, A.A. Balkema, 183–190.

Thornton, C. Zhang, L. (2010). "On the evolution of stress and microstructure during general 3d deviatoric straining of granular media." *Géotechnique*, 60, 333–341.

Ting, J. M., Corkum, B. T., Kauffman, C. R., and Greco, C. (1989). "Discrete numerical model for soil mechanics." *J. Geotech. Eng.*, 3, 379–398.

Towhata, I. and Ishihara, K. (1985). "Undrained strength of sand undergoing cyclic rotation of principal stress axes." *Soils Found.*, 25 (2), 135–147.

USGS, U. G. S. (2010). "Earthquake information by year." Department of the Interior, <http://earthquake.usgs.gov/earthquakes/eqarchives/year/> (April).

Vaid, Y. P., Byrne, P. M., and Hughes, J. M. O. (1981). "Dilation angle and liquefaction potential." *J. Geotech. Eng.*, 107, 1003–1008.

Vaid, Y. P. and Negussey, D. (1984). "Relative density of air and water pluviated sand." *Soils Found.*, 4 (2), 101–105.

Vaid, Y. P., Sayão, A., Enhuang, H., and Negussey, D. (1990). "Generallized stress-path-dependent soil behaviour with a new hollow cylinder torisional apparatus." *Can. Geotech. J.*, 27, 601–616.

Vaid, Y. P. and Sivathayalan, S. (1996). "Static and cyclic liquefaction potential of fraser delta sand in simple shear and triaxial tests." *Can. Geotech. J.*, 33, 281–289.

Vaid, Y. P. and Sivathayalan, S. (2000). "Fundamental factors affecting liquefaction susceptibility of sands." *Can. Geotech. J.*, 37(3), 592606.

Vaid, Y. P., Sivathayalan, S., and Stedman, D. (1999). "Influence of specimen-reconstituting method on the undrained response of sand." *Geotech. Test. J.*, 22 (3), 187–195.

Vesic, A. (1973). "Discussion on bearing capacity theory from experimental results." *J. Soil Mech. Found. Div.*, 99 (SM7), 575–577.

Vucetic, M. (1981). "The influence of height versus diameter ratio on the behaviour of haga clay in the ngi simple shear device, internal report 56204-9." *Report no.*, Norwegian Geotechnical Institute, Oslo, Norway.

Vucetic, M. and Lacasse, S. (1982). "Specimen size effect in simple shear test." *J. Geotech. Engrg. Div.*, 108 (2), 1567–1585.

Vucetic, M. and Lacasse, S. (1984). "Specimen size effect in simple shear test: closure." *Geotech. Test. J.*, 110 (GT3), 439–453.

Walton, O. R. (1982). "Explicit particle dynamics model for granular materials." *Numerical methods in geomechanics*, Z. Eisenstein, ed., A. A. Balkema, Rotterdam, The Netherlands, 1261–1268.

Wang, J. and Gutierrez, M. (2010). "Discrete element simulation of direct shear specimen scale effects." *Géotechnique*, 60(5), 395–409.

Wang, Y.-H., Xu, D., and J., T. K. Y. (2008). "Discrete element modeling of contact creep and aging in sand." *ASCE J. Geotech. Geoenviron.*, 134(9), 1407–1411.

Wijewickreme, D., Dabeet, A., and Byrne, P. M. (2013). "Some observations on the state of stress in the direct simple shear test using 3d discrete element analysis." *Geotech. Test. J.*, 36 (2), 1–8.

Wijewickreme, D., Sriskandakumar, S., and Byrne, P. M. (2005). "Cyclic loading response of loose air-pluviated fraser river sand for validation of numerical models simulating centrifuge tests." *Can. Geotech. J.*, 42, 550–561.

Wijewickreme, D. and Vaid, Y. P. (1993). "Behavior of loose sand under simulataneous increase in stress ratio and principal stress rotation." *Can. Geotech. J.*, 30, 353–364.

Wood, D. M. (1990). *Soil Behaviour and Critical State Soil Mechanics.* Cambridge University Press, Cambridge, UK.

Wood, D. M. (2004). *Geotechnical Modeling.* Spoon Press, New York, NY, USA.

Wood, D. M., Drescher, A., and Budhu, M. (1979). "On the determination of the stress state in the simple shear apparatus." *Geotech. Test. J.*, 2 (4), 211–222.

Wood, F. M. and Yamamuro, J. A. (1999). "The effect of depositional method on the liquefaction behavior of silty sand." *Proc. 13th ASCE Engrg. Mech. Conf., The Johns Hopkins University, Baltimore, MD.*

Wright, D. K., Gilbert, P. A., and Saada, A. S. (1978). "Shear devices for determining dynamic soil properties." *Proc. Earthquake Engineering and Soil Dynamics, ASCE Specialty Conference, Pasadena, Calif.*

Wroth, C. P. (1958). "The behavior of soils and other granular media when subjected to shear." Ph.D. Thesis, University of Cambridge.

Yamada, Y. and Ishihara, K. (1979). "Anisotropic deformation characteristics of sand under three dimensional stress conditions." *Soils Found.*, 19 (2), 79–94.

Yang, Y. and Yu, H. S. (2006). "Numerical simulations of simple shear with non-coaxial soil models." *Int. J. Num. Anal. Meth. Geomech.*, 30 (1), 1–19.

Yang, Z. X., Li, X. S., and Yang, J. (2007). "Undrained anisotropy and rotational shear in granular soils." *Géotechnique*, 57 (4), 371–384.

Yimsiri, S. and Soga, K. (2010). "DEM analysis of soil fabric effects on behaviour of sand." *Géotechnique*, 60 (6), 483–495.

Yoshimine, M., Robertson, P. K., and Wride, C. E. (1999). "Undrained shear strength of clean sands to trigger flow liquefaction." *Can. Geotech. J.*, 36, 891–906.

Yu, H. S. (2006). *Plasticity and Geotechnics*. Springer, New York, NY, USA.

Yu, H. S. (2008). "Non-coaxial theories of plasticity for granular materials." *Keynote The 12th International Conference of International Association for Computer Methods and Advances in Geomechanics (IACMAG)* (October).

Yu, H. S. and Yuan, X. (2006). "On a class of non-coaxial plasticity models for granular soils." *Proc. R. Soc. A*, 462, 725–748.

Zeghal, M. and El Shamy, U. (2008). "Liquefaction of saturated loose and cemented granular soils." *Powder Technol.*, 184(2), 254–265.

Zhang, J., Tong, Z., and Yu, H. (2008). "Effects of cyclic rotation of principal stress axes and intermediate principal stress parameter on the deformation behavior of sands." *Geotechnical Earthquake Engineering and Soils Dynamics*, IV, 1–10.

Zhang, L. (2003). "The behaviour of granular material in pure shear, direct shear, and simple shear." Ph.D. Thesis, Aston University, UK.

Zhang, L. and Thornton, C. (2007). "A numerical examination of the direct shear test." *Géotechnique*, 57(4), 343–354.

Zhuang, X. (1993). "Computer simulation and experiments on the quasi-static mechanics and transport properties of granular materials." Ph.D. Thesis, University of California, San Diego.